ELSEVIER

Progress in Nuclear Magnetic Resonance Spectroscopy 52 (2008) 197–269

PROGRESS IN NUCLEAR MAGNETIC RESONANCE SPECTROSCOPY

www.elsevier.com/locate/pnmrs

Mobile single-sided NMR

B. Blümich *, J. Perlo, F. Casanova

Institute of Technical and Macromolecular Chemistry, RWTH Aachen University, D-52056 Aachen, Germany

Received 22 August 2007; accepted 30 October 2007
Available online 28 December 2007

Contents

* Corresponding author. Tel.: +49 241 80 26420.
E-mail address: bluemich@mc.rwth-aachen.de (B. Blümich).

0079-6565/$ - see front matter
doi:10.1016/j.pnmrs.2007.10.002

1. Introduction

Mobile, single-sided NMR has its origin in inside-out NMR, where NMR spectrometers are lowered into bore holes for analysis of fluids in the surrounding rock matrix. Similar equipment can be used for measurement of product streams and product quality, and for medical diagnostics. Although this idea has been formulated over three decades ago, mobile NMR has remained a niche largely unnoticed by the NMR community until systematic investigations of NMR in inhomogeneous fields appeared in the scientific literature with the commercialization of well-logging instruments and the development of the NMR-MOUSE®. This review summarizes the development of instrumentation, methods, and applications of mobile NMR, with particular attention to single-sided NMR.

Nuclear magnetic resonance (NMR) [1] is well known from diagnostic medical imaging [2] and analytical chemical spectroscopy [3]. In either case, the object or the sample is brought into the laboratory to be investigated with radio-waves inside stationary magnets. This procedure is followed to obtain high magnetic fields, for example, $B_0 > 20$ T, for good signal strength and homogeneous magnetic fields, for example, $\Delta B_0/B_0 < 10^{-7}$ across the sample, for good spectroscopic resolution [4]. As the resultant magnets are made from superconducting wires and require cooling, they are large and heavy, and cannot be moved.

By reducing the magnet size, field strength and homogeneity deteriorate. This has seemed to be unacceptable for a long time, although the oil industry has demonstrated that robust and mobile sensors can be built from permanent magnets that can be lowered into the bore hole of an oil-well for relaxation time analysis of the fluids in the surrounding, porous rock formation [5,6]. Such sensors employ low and inhomogeneous magnetic fields, for example, $B_0 = 0.03$ T with gradients of the order of 0.1 T/m to measure the decay of the transverse magnetization. Echo techniques, which had been discovered already in 1949, are used to overcome the effects of field inhomogeneity [7–10]. Driven by the oil industry, the principle of inside-out NMR was introduced in this way [11–13], where the magnet sits inside the object, in this case the earth, as opposed to conventional NMR which then may be called outside-in NMR with the sample inside the magnet.

Inside-out NMR [14–16] is a form of single-sided or unilateral NMR, where an NMR sensor much smaller than the object is placed near the object to acquire signals from the object volume near the sensor. This concept has been accepted largely by the developers of well-logging NMR and some engineers at the Southwest Research Institute [17] in San Antonio, Texas, to be of use also for other purposes (Fig. 1). Examples are the detection of moisture [18] in soil (Fig. 1b) [19–23], concrete bridge decks (Fig. 1a) [19,24], building materials (Fig. 1d) [24,25] and food [26–32], explosives detection [33–40], quality and product control [41–44], medical diagnostics [16] and on-line monitoring (Fig. 1c) [16,18,26,27,30,45] well before the commercialization of well-logging NMR in the mid 1990s. Yet the single-sided sensors then used were large and heavy (Fig. 1a and b), designed with the understanding, that the magnetic field should be as homogeneous as possible to excite as large a volume as possible. Also, the electronics at that time were bulky due to the state of the art, so that this type of NMR is better called transportable than mobile.

It was not until the NMR-MOUSE (MObile Universal Surface Explorer) was built in 1995 (Fig. 1e) [46], that a small single-sided NMR sensor weighting of the order of 1 kg with a field gradient higher than 10 T/m at a field

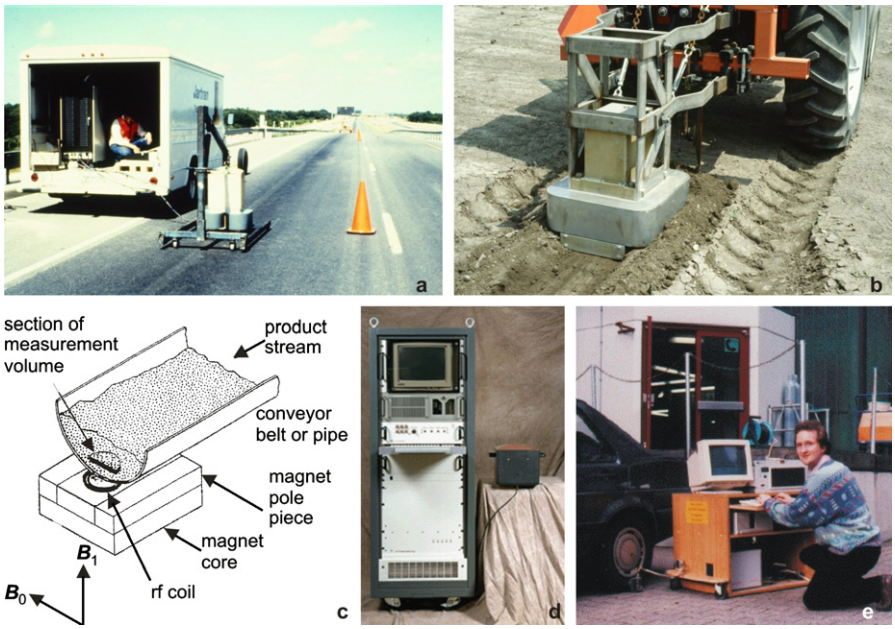

Fig. 1. Early NMR sensors for unilateral NMR. (a) Transportable electromagnet for measuring moisture in bridge decks (photo with permission from G.A. Matzkanin). (b) Permanent magnet to measure moisture in soil (photo with permission from G.A. Matzkanin). (c) Online sensor to measure moisture in a product stream [18]. (d) Sensor to measure moisture in building materials [17,25]. (e) Gunnar Eidmann measuring a car tire with the first NMR-MOUSE (photo by B. Blümich) [46].

strength of 0.5 T was discovered to be useful for materials testing. This is somewhat surprising, in so far as the acquisition of NMR data in very strong field gradients had been pioneered previously in stray-field imaging and provides good spatial resolution even for solid objects [47–51]. Based on the insight, that most contrast parameters exploited in medical and more so in materials imaging require neither a homogeneous magnetic polarization field $\boldsymbol{B}_0$ nor a homogeneous radio-frequency (rf) field $\boldsymbol{B}_1$, the NMR-MOUSE was designed to provide the NMR information maintained in a single pixel of a magnetic resonance image by imposing the spatial resolution in real space $\boldsymbol{r}$ and not in its conjugate space $\boldsymbol{k}$, which the established Fourier imaging methods prefer in order to make use of the multiplex advantage [52].

As the NMR-MOUSE appeared at about the same year as the commercial well-logging instruments [12,53], new methods were rapidly developed for both, logging tools and the NMR-MOUSE, that could acquire more and more information in inhomogeneous magnetic fields. In addition to T_2 measurements by single echoes [7,54] and echo trains [9,10,55–58], the most important ones are measurements of other relaxation times [59] such as T_1 [60–64], diffusion coefficients D [7,9,65–69], spin modes like double-quantum coherences and their relaxation times [70,71], velocities $\boldsymbol{v}$ [72], images [73–76] which assign signal to position $\boldsymbol{r}$ by Fourier techniques, velocity distributions [77] and velocity images [78], two- and multi-dimensional schemes that correlate distributions of different relaxation times [79] and diffusion coefficients [80], and last but not least even chemical-shift resolved spectra [81]. The latter is a fundamental turning point in the development of NMR, as inhomogeneous magnetic fields had been avoided in the previous 50 years because of the false understanding that chemical-shifts cannot be resolved in a polarization field $\boldsymbol{B}_0$ that is inhomogeneous across the sample [82].

Today the plethora of ideas of multi-dimensional NMR formulated 30 years ago [3,83] is explored with mobile sensors and inhomogeneous fields, and extended to include correlations of NMR parameters other than the frequencies of spectra or space coordinates in images (Fig. 2). In

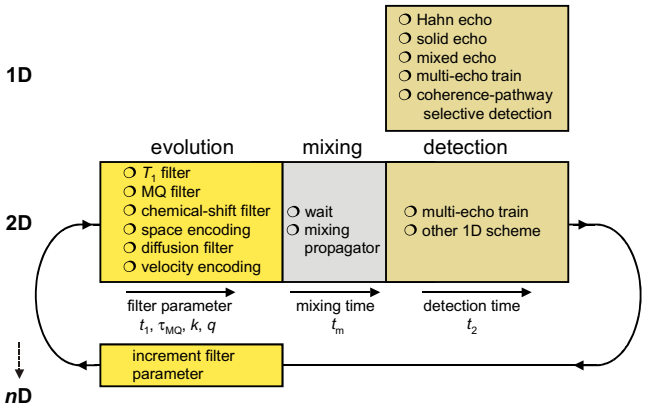

Fig. 2. Data acquisition in inhomogeneous fields. Multi-dimensional methods are incorporated in the same way as in NMR spectroscopy. The directly detected dimension may encode relaxation times, diffusion constants, flow velocity components and chemical-shifts. The indirectly detected dimensions can encode either of these as well as for example multi-quantum coherences and position. A fixed mixing time t_m for scrambling of magnetization components may be used to connect evolution and detection periods.

fact, the direct acquisition domain today can encode one of many NMR parameters such as transverse relaxation, space, diffusion, velocity, or frequency in the sense of chemical-shift. The indirect dimensions are interrogated in a repetitive fashion by filtering the magnetization detected directly and varying a filter parameter in a systematic fashion [4,84]. A fixed mixing time t_m for dynamic magnetization exchange can be used to connect evolution and detection periods. The generalization of this concept is referred to as *ex situ* NMR, originally denoting NMR of a sample outside the homogeneous field of a magnet, where the methodical scenario is explored in all aspects to conduct not only relaxometry, but also imaging and spectroscopy preferably outside the geometrical limitations of a magnet bore [85]. Today, *ex situ* NMR is understood as the toolbox of NMR in inhomogeneous fields inside and outside the magnet.

Yet mobile NMR is more than NMR with small magnets and inhomogeneous fields. Also light-weight magnets with homogeneous fields and simple field profiles can be built. One example is the series of Halbach magnets [86,87]. One of them is a cylinder magnet constructed from many magnet blocks in such a way that the magnetic field is largely homogeneous inside the cylinder, transverse to the cylinder axis, and zero outside [88]. Quasi homogeneous fields are conventionally generated by the classical C-shaped magnet geometry, but can even be generated in the stray field of a modified horse-shoe magnet [89]. Alternatively the magnetic stray field of the earth can be exploited [90–92]. Here the field comes for free, and the objects investigated are very much smaller than the magnet. In areas a bit remote from city civilization, the earth's magnetic field is extremely homogeneous in space so spectra with ultra-high spectroscopic resolution can be acquired [93,94], and indirect couplings bearing chemical information can be resolved with unprecedented accuracy [94]. But disadvantages are the time fluctuations of the magnetic field due to sunspot activities and motion of the core of the earth [92,95], and the low value of the nuclear magnetization in such low fields, so that the initial magnetization must be enhanced by prepolarization techniques or ultra-high sensitivity is needed for signal detection [96].

As the response bandwidth is small at low and homogeneous field, the sensitivity can be boosted by detecting the nuclear induction signal with narrow-band receivers [97]. This fails for inhomogeneous fields, where the bandwidth is wide. Here super-conducting quantum interference devices (SQUIDs) [96,98,99] and optical sensors [100–102] bear great promise as novel low-frequency detectors, or the nuclear magnetization must be increased by prepolarization techniques such as the use of prepolarization fields [92,93,96,103], hyperpolarized gases [104–107] including the subsequent magnetization transfer to other nuclei [108], the generation of chemically selective hyperpolarization by fast reaction with para-hydrogen [109–112], and dynamic nuclear polarization [113–115]. If transport phenomena are investigated, for example, in chemical engineering, the concept of remote detection can be applied [116–119], where the magnetization is encoded in a diluted state and subsequently transported to and detected in a compacted state with improved sensitivity.

Mobile NMR holds great promise in a variety of fields [120], in particular in medicine, materials science [121], chemical engineering [122] and space science [123]. In fact, many experiments can be conducted with far greater ease at low fields including the earth's magnetic field [123], where water reservoirs can be located at depths up to about 100 m with large-diameter surface coils [124] and spectra can be acquired with milli-Hertz resolution [94,6]. A very promising area of application of mobile NMR is process control by sensors installed in the production line [32,125–127]. The original ideas refer back mainly to the Southwest Research Institute in San Antonio, Texas, and concern the detection of moisture [17,18,30,128] in agricultural applications [19,31,32], in reduction grade aluminum oxide as it leaves the kiln [45], in food products like cereals and grains [27,28] and in building materials like concrete [19,24,129]. Today, NMR sensors are used in a variety of industrial processes, such as oil refining [130] and polymer processing [131]. These [24,132–149] and novel applications are continuously being explored, for example, in screening diverse food products [150] including bottled wine [151,152] and monitoring extrusion processes [153,154], and novel principles of NMR with stationary sensors measuring bypassing products are being investigated [155].

2. Hardware

The evolution of NMR is driven by the advances in electronics, computer and magnet technology leading to more and more sensitive instruments with higher, more stable and more homogeneous fields. The quest for high fields is rationalized by the fact that both the nuclear magnetization and the frequency range of the chemical-shift are proportional to the strength of the polarizing field. Consequently large molecules which give rise to many lines and low concentrations of chemical groups, typical in the bio-sciences, necessitate NMR at high fields. Yet what is good for one area of research may not be good for another, and low and inhomogeneous fields turn out to provide many methodical challenges and novel solutions to conduct nuclear magnetic resonance with an abundance of new applications to be conquered. In fact NMR in homogeneous fields is only an asymptotic limit of NMR in different field profiles, which is preferably explored for chemical-shift resolved NMR spectroscopy. Another limit is NMR in linear field profiles which are characterized by constant gradients. This limit is preferably explored in imaging. All other field profiles are also amenable to NMR. For example, one could derive a whole concept of NMR in quadratic field profiles which are characterized by linear gradients [156,157].

Taking NMR in homogeneous fields as one extreme case, and NMR in highly inhomogeneous fields as the

opposite extreme case, then NMR in linear fields is somewhere in between, and so is NMR with an infinite number of other field profiles. As the limiting case of NMR in homogeneous fields has extensively been explored in the past 60 years, NMR in inhomogeneous fields was restricted largely to relaxometry in the context of well-logging [12,13] and later extended to imaging [73]. So many opportunities for discovery and innovation can be expected for NMR in inhomogeneous fields. Examples of emerging techniques are chemical-shift resolved NMR spectroscopy [82,89,158], NMR force microscopy [159–161], and mobile NMR which is the focus of this review.

2.1. Homogeneous and inhomogeneous polarization fields

The most prominent features of the two extreme cases of NMR with respect to the homogeneity of the polarizing magnetic field $\boldsymbol{B}_0$ across the object are illustrated in Fig. 3. NMR in homogeneous fields (Fig. 3a) is an asymptotic limit of NMR in inhomogeneous fields (Fig. 3d–g). As the ratio of sample size over magnet size increases, the field inhomogeneity increases and the magnet geometry becomes more open. The most inhomogeneous fields across the object are produced by magnets small compared to the object corresponding to open magnets such as those used for single-sided NMR devices like well-logging sensors (Fig. 3d) [6], the NMR-MOUSE (Fig. 3e) [46], the endovascular NMR endoscope (Fig. 3f) [162] and the magnetic resonance force microscope (Fig. 3g) [159,161]. NMR imagers (Fig. 3b) [163] and dedicated open access imagers [164–167] such as the MagneVue 1000 limb imager (Fig. 3c) [166] are grouped in between single-sided NMR devices and closed magnets including small mobile [150,168] and transportable systems [169–171], as well as conventional superconducting magnets (Fig. 3a) for high field NMR spectroscopy.

When the sample is small compared to the magnet, the field across the sample can be made high and homogeneous. An extreme example is Earth's field NMR [94–96]. For samples large compared to the magnet, the field can at best be homogeneous in a small region of the sample, but not across the whole sample. As a rule of thumb for single-sided NMR devices, the more homogeneous the field should be across the sample, the lower is the field strength. Given a 1 μs rf pulse from a practical point of view, the maximum excitation bandwidth is about 1 MHz, and the excitation is always selective for single-sided NMR devices and large objects (Fig. 4) [172–174]. The size and shape of the sensitive volume can be tailored by the profiles of the polarization field $\boldsymbol{B}_0(\boldsymbol{r})$ and the rf field $\boldsymbol{B}_1(\boldsymbol{r})$, and by the choice of the rf excitation. For battery-operated instruments, low rf power is an advantage, and noise modulation of the rf carrier frequency may be an interesting form of excitation [172,173].

2.2. Well-logging sensors: inside-out NMR

When the magnet is introduced into the object through an opening, one speaks of inside-out NMR. This concept has been developed in the oil industry to overcome the problem of low sensitivity associated with the earth's field and to eliminate the contribution of the borehole fluid from the measured data [175]. As boreholes have a circular cross-section, a sensitive volume of suitable symmetry has the shape of a hollow cylinder or an annulus. The latter is realized by the ingenious inside-out-NMR sensor of Jackson (Fig. 5a) [16]. Two axially aligned cylinder magnets facing each other with the same poles produce a

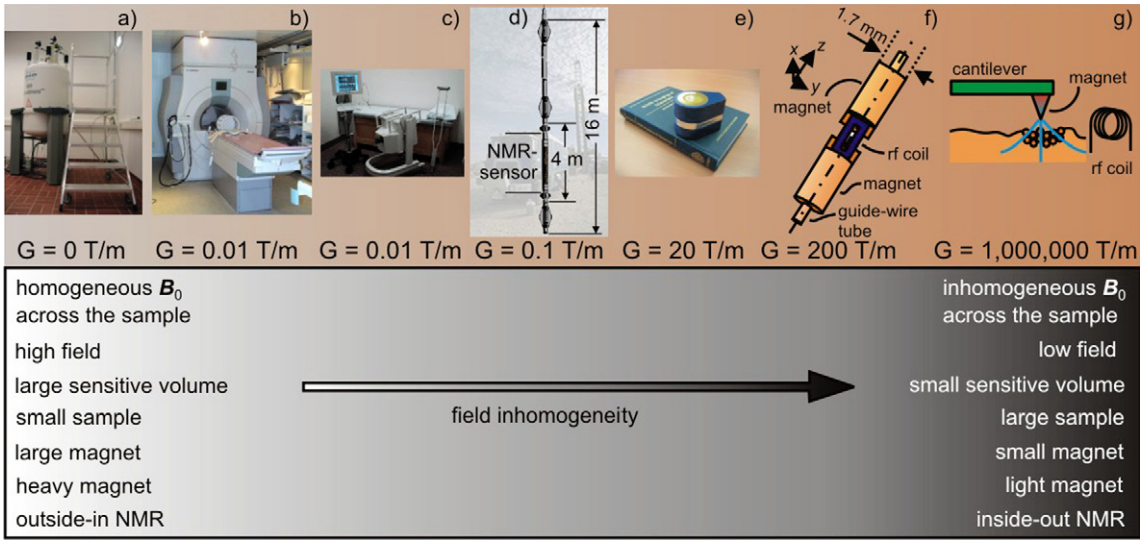

Fig. 3. NMR magnets and associated field homogeneity specified in terms of a characteristic gradient G. As the field inhomogeneity increases, the magnet geometry becomes more open, and the limitations on the sample size compared to the magnet size are reduced. The most inhomogeneous fields across the object are produced by small and open magnets used for single-sided NMR devices like the NMR-MOUSE (e), well-logging sensors (d), the endovascular NMR endoscope (f), and the magnetic resonance force microscope (g). NMR imagers (b) and dedicated open access imagers (c) are grouped in between single-sided NMR devices at one end and conventional superconducting magnets (a) for high field NMR spectroscopy at the other end.

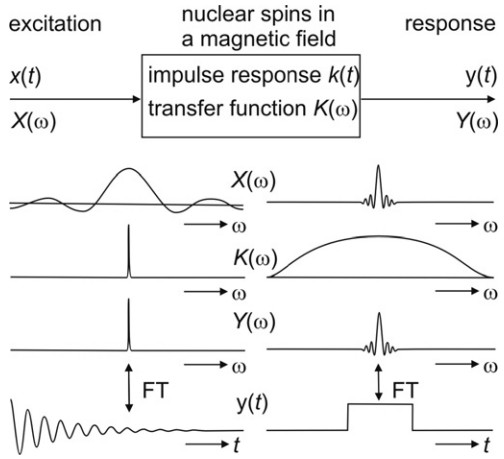

Fig. 4. Selective and non-selective excitation in the linear approximation [4,174]. The nuclear spins in a magnetic field form a system which transforms the rf excitation $x(t)$ into the response or transverse magnetization $y(t)$. The system is characterized by the impulse response function $k(t)$ which corresponds to the free induction decay. When approximated by a linear system, the NMR response spectrum $Y(\omega)$ is given by the product of the excitation spectrum $X(\omega)$ and the transfer function $K(\omega)$, which is the Fourier transform of the impulse response function $k(t)$, $Y(\omega) = K(\omega)\ X(\omega)$. For pulsed excitation in homogeneous fields, the transfer function is narrow compared to the excitation spectrum of the rf impulse, so that the response spectrum is the transfer function or the 1D NMR spectrum (left). For large objects in inhomogeneous fields, the excitation spectrum is narrow compared to the transfer function, so that the response spectrum is the excitation spectrum, which is the Fourier transform of the impulse used for excitation (right).

radial stray field in the transverse plane through the gap, with a nearly constant magnitude $|\boldsymbol{B}_0|$ of the magnetic field in an annular region around the gap. A simple solenoidal coil in the gap aligned with the magnets produces a $\boldsymbol{B}_1$ field orthogonal to $\boldsymbol{B}_0$ in the annulus. As the axial extension of the annulus is narrow, the use of such a sensor for wire-line applications with the sensor in axial motion is limited to slow speeds, but the circular symmetry is of great advantage in logging-while-drilling applications [176], where the entire NMR assembly rotates with the drill string.

The early Schlumberger sensor is based on a design by Kleinberg (Fig. 5b) [6,177], which provides a sensitive volume localized at a given sector but with an axial extension defined by the length of the magnets. This sensor is far better suited for wire-line NMR as the residence time of the spins in the sensitive volume under axial motion of the sensor is far longer than with the Jackson sensor. A conceptually related sensor with angular resolution but narrow axial resolution has been designed from opposing cylinder magnets magnetized along their diameters [178,179].

The Halliburton sensor (Fig. 5c) [6,175,180] explores the fact that the magnitude of a dipolar field is constant at a given radius r in a plane perpendicular to the axis of the dipole. An axially extended $\boldsymbol{B}_0$ dipole is obtained by a long magnet magnetized perpendicular to its long axis. An rf coil is wound around it which produces a dipolar $\boldsymbol{B}_1$ field

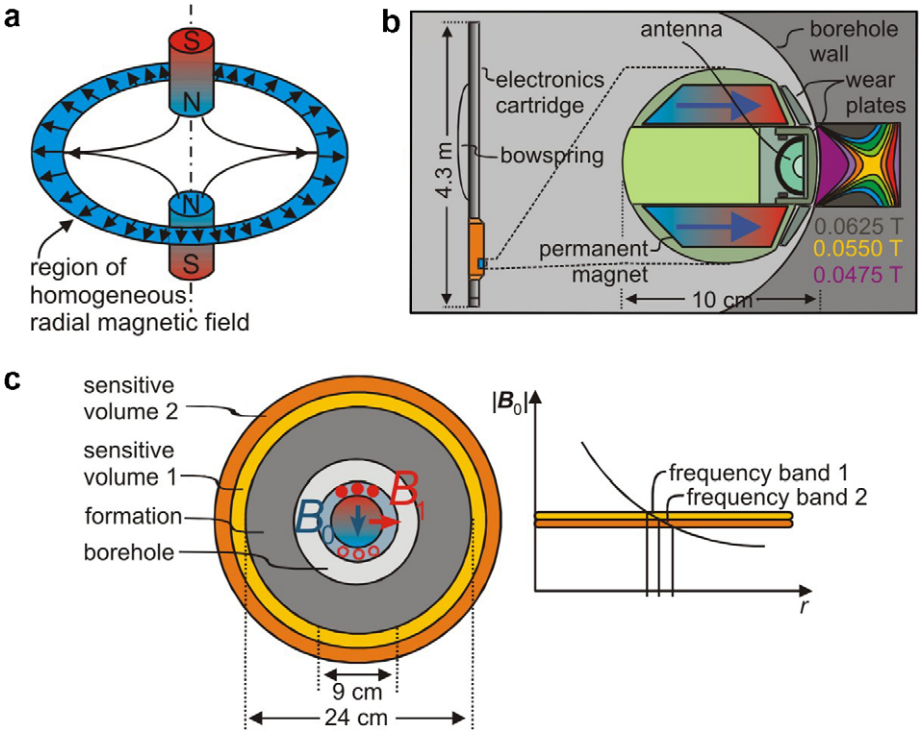

Fig. 5. Well-logging sensors. (a) Original design by Jackson with a sensitive volume of high homogeneity in the shape of an annulus [16]. (b) Schlumberger sensor by Kleinberg with the sensitive volume localized at a given sector but axially extended [6,177]. (c) Halliburton sensor with a radial sensitive volume and a radial gradient for selection of different depths [6,180].

perpendicular to $\boldsymbol{B}_0$ at all positions and again with a constant value at a given radius. As the dipolar $\boldsymbol{B}_0$ and $\boldsymbol{B}_1$ fields decay radially with $1/r^2$, the signal can be collected from annular shells selected by the transmitter frequency in the radially decaying $\boldsymbol{B}_0$ field. In this way, measurements can be done at different depths and the sensitivity towards diffusion be adjusted by the echo-time in the CPMG sequence.

The inside-out-NMR sensor geometries are suitable in principle as well for miniaturization to use as endoscopes. A cardiovascular endoscope with an outer diameter smaller than 1.7 mm has been developed in Israel and is in the clinical testing phase (Fig. 3f) [162,181,182]. Such sensors can also be employed for example as moisture sensors in industrial drying processes [183].

2.3. Magnets for unilateral NMR

Unilateral NMR sensors derive from well-logging sensors. Apart from sensor geometries particularly suited to the cylindrical boreholes of oil wells, single-sided sensors suited for diverse other applications have been tested. A classical geometry for such a single-sided sensor employs a magnet in the shape of a "u" or a horseshoe (Fig. 6b) [25,42,43,46,184,185]. This shape is obtained by opening up a conventional c-shaped magnet with a homogeneous field between its poles (Fig. 6a) [186,187]. While in conventional NMR devices (Fig. 6a), the sample rests inside the rf coil and between the magnet poles to achieve maximum strength and homogeneity, in unilateral NMR the sample rests near the sensor in the inhomogeneous stray fields of the magnet and the rf coil. This lifts the constraints on the sample size, but introduces variations in magnitude and orientation of the polarization and rf fields $\boldsymbol{B}_0$ and $\boldsymbol{B}_1$, respectively, across an extended sample.

Once inhomogeneous fields are admitted for the NMR measurement, the most simple NMR sensor is obtained as the simple bar magnet (Fig. 6c) [188,189]. If the rf coil is placed on one of the faces, the orientation of the $\boldsymbol{B}_0$ field is perpendicular to the sensor surface, and an rf coil which produces a field parallel to the surface needs to be employed. Such a coil is the figure-eight coil [185,190] where the current flow follows the path of the figure eight. Sensors less open than unilateral ones can be constructed by exploring the principle of ferro-refraction that is, mirroring of magnetic dipoles by suitably placed iron plates [191].

The different orientations of $\boldsymbol{B}_0$ parallel and perpendicular to the sensor surface may be important in the analysis of objects with preferential orientational order in that plane such as a tendon [192–195] or a sample of strained rubber [196,197]. If the direction $\boldsymbol{n}$ of preferential order is parallel to the sensor surface, the angle between $\boldsymbol{B}_0$ and $\boldsymbol{n}$ varies with rotation of the u-shaped magnet, while it remains at a value of 90° with the bar-magnet sensor. The two geometries, the u-shaped (Fig. 6b) and the single bar (Fig. 6c) magnets, are the basic forms of many different magnet designs for single-sided NMR reported in the last decade. Several u-shaped magnets have been built either with different aspect ratios and additional magnetic material placed in some strategic positions to generate stronger fields, or by combining concentric u-shaped magnets to reduce the gradient strength. However, all have the common feature, that the polarizing magnetic field is oriented parallel to the sensor surface. The case of the single bar magnet is not less diverse. Although magnets with cylindrical and square cross-sections, single cylinders with a hole giving the barrel magnet, barrel magnets with an additional single bar placed in the hole, etc., have been constructed, they share as a common feature the generation of a polarizing field perpendicular the sensor surface. As the direction of the polarizing field imposes strong restrictions to the rf coil and gradient coil system designs, magnets with $\boldsymbol{B}_0$ parallel and perpendicular to the sensor surface are differentiated. Furthermore, magnets with a strong gradient in the depth direction are differentiated from those with a largely homogeneous field distribution within the sensitive volume. The former provides natural slice selectivity and high depth resolution, and the latter minimizes the attenuation of signals from fluids by diffusive signal attenuation and provides better conditions for volume imaging. The region of magnetic field with a low gradient is often referred to as the sweet spot.

Pulyer has worked out a strategy to compare various magnet geometries composed of simple permanent or electro-magnet blocks [198,199]. To obtain a sweet spot, more than one elementary magnet block is needed. These can be arranged next to each other in different numbers and with

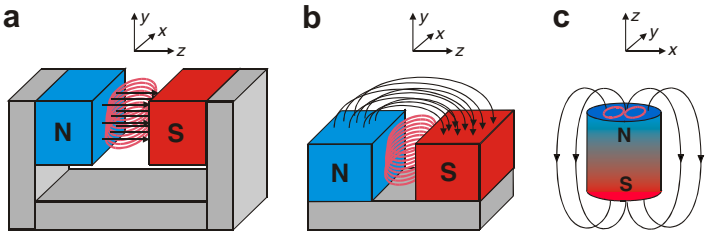

Fig. 6. Simple geometries of permanent magnets and rf coils used for NMR. (a) Conventional c-shaped geometry where the sample is positioned in the homogeneous field inside the gap and inside the rf coil. (b) u-shaped open magnet. The sample is positioned above the gap in the stray fields of the magnet and the rf coil. The magnetic polarization field is parallel to the sensor surface. (c) Simple bar magnet with a figure-eight coil on one of the faces. The magnetic polarization field is perpendicular to the sensor surface.

different orientations of their magnetizations. As a rule of thumb, a sweet spot is obtained where the magnetic field is different from zero and at least the first derivative with respect to space vanishes. The more higher-order derivatives that vanish in all three directions of space, the larger is the sweet spot. This principle is used in mechanical shimming, but not only by incorporating additional magnets where needed, but also magnetic metal pieces.

The field profiles are often optimized with the help of numerical simulations [200–207], for example, to arrive at a magnet with a maximum sensitive volume in a linear gradient field [200–203], to reduce the weight of such a magnet [201], and to arrive at a large region of homogeneous field [202]. Such optimizations can focus on identifying suitable pole caps [208,202,203] or finding proper magnet shapes and orientations. In some cases analytical expressions can be derived [86] as for the GARfield (Gradients At Right angles to field) magnet. This is a c-shaped magnet with a strong gradient at right angle to the magnetic field for depth profiling of thin samples [209–211] quite similar in performance to the profile NMR-MOUSE when small samples are used [212].

2.3.1. Magnets with $\boldsymbol{B}_0$ parallel to the surface

The basic u-shaped magnet geometry (Fig. 6b and 7a) [25,32,42,43,46,129,184,213] produces a field, with approximately quadratic profiles along x and z and with a main gradient along the depth direction y [46]. A similar field distribution is obtained in the stray-field of a Halbach magnet close to its face [214]. The field variation with depth can be used to resolve depth profiles into the object simply by varying the excitation frequency. However, the one-to-one relationship between resonance frequency and depth requires the lateral field variations to vanish within the sensitive volume. But, for simple magnets, these variations are severe and introduce a curvature to the sensitive slice which depends on the distance from the magnet surface [57]. The sensitive slice has the cross-sectional shape of a soup dish which flattens out with increasing distance from the coil [215]. This curvature limits the depth resolution to a few points across a representative accessible depth of 10 mm.

Several attempts have been made to improve the spatial resolution. One approach is to vary the thickness of the magnet blocks across the gap (Fig. 7c) [200,216] or to close the sides of the gap (Fig. 7b) [145,217] in order to reduce the curvature of the selective slice over a range of depths. The same concept has been employed to shape the field of a bar magnet to generate a sweet spot along its side by placing a constriction in the center [208]. Another approach is to extend the lateral dimensions of the magnet, for example, by chaining u-shaped magnet elements. This results in the planar Halbach magnet [218] which has been combined with suitably placed rf coils centered above the gaps, so that an extended sensitive volume of constant magnetic field is obtained in a plane above the magnet [210,212,219].

The typical depth resolution attainable by frequency variation with such sensors is of the order of some tens of millimeters. Yet the curvature of the sensitive plane can be minimized at one given depth, and much higher depth resolution can be obtained by shifting this sensitive plane though the object for acquisition of a depth profile

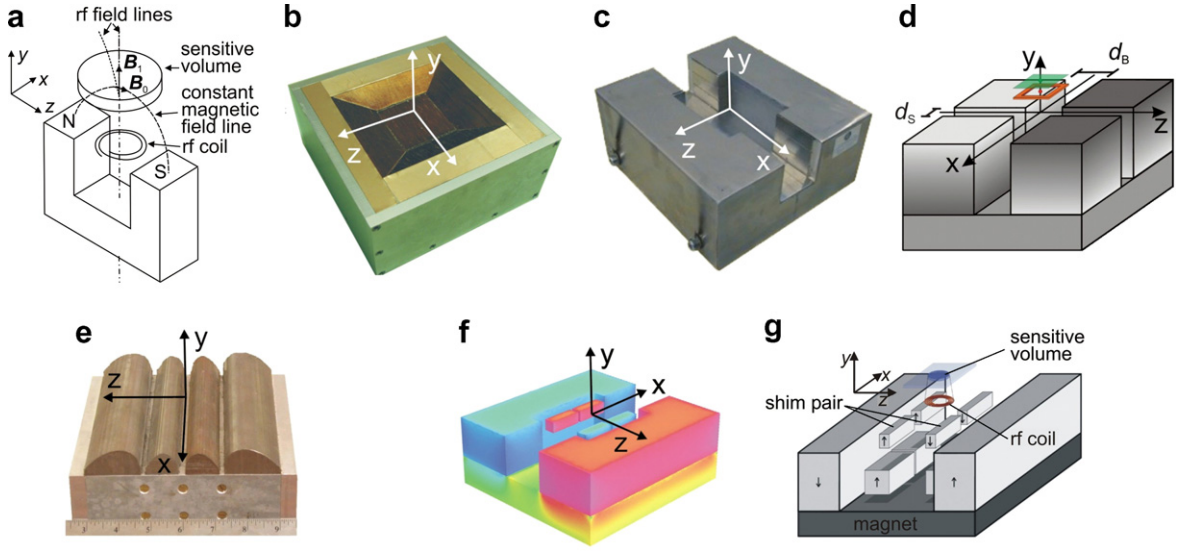

Fig. 7. Magnets for unilateral NMR sensors with the magnetic field parallel to the sensor surface. (a) Early drawing of a u-shaped one-sided access NMR sensor (adapted from [41]). (b) Magnet designed for slice selective imaging [146,217]. (c) Single-sided u-shaped magnet optimized for a linear field profile in the depth direction and for improved homogeneity along the direction of the gap [200,216]. (d) Magnet arrangement for the Profile NMR-MOUSE which provides a constant gradient in y-direction and a constant field $|\boldsymbol{B}_0|$ in the xz-plane at one particular depth y [220]. (e) Planar arrangement of magnets with shaped pole shoes optimized for a large sensitive volume at low field [202,203]. The magnet design is based on the same approach as the GARfield magnet [209]. (f) Magnet array generating a sweet spot. The small magnet blocks are used to establish matching conditions for spectroscopy in inhomogeneous fields [158]. (g) Single-sided magnet generating highly homogenous fields for ^{1}H spectroscopy [89].

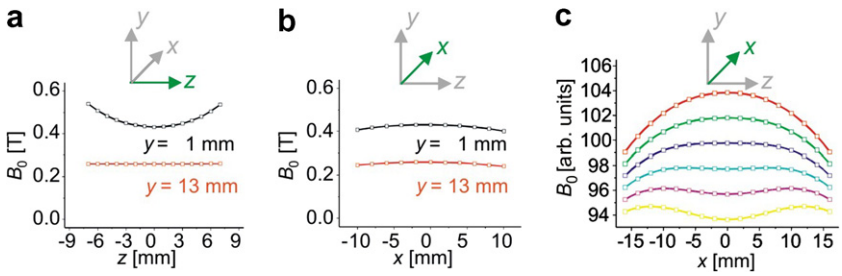

Fig. 8. Magnetic field profiles for u-shaped magnet geometries. (a) Profiles across the gap at two different depths (cf. Fig. 6b). As the profiles change from concave to convex, a flat region is obtained at one particular depth. (b) Profiles along the gap direction (cf. Fig. 6b). The profile remains convex at all depths. (c) Profiles along the gap direction to for two identical u-shaped sensors next to each other with the spacing between them increasing from top to bottom (cf. Fig. 7d). A flat region is obtained at one particular depth.

at constant frequency [220]. This is much easier to achieve than a linear gradient-field variation over an extended range of depths such as with the GARfield magnet [209]. An effect similar to enforcing the ends of the u-shaped magnet across the gap is obtained by arranging two simple u-shaped magnets in parallel leaving a small gap along the x-direction (Fig. 7d). An extremely flat sensitive slice can be generated in this way with a curvature of only a few micrometers over a region of about one square centimeter (Fig. 8). This sensor is known as the Profile NMR-MOUSE, and suitable methods are discussed in Section 3. The trick with introducing a gap for flattening the field profile has also been demonstrated with the Halo magnet, an imaging magnet made from two axially magnetized rings with an adjustable gap between them [221] and with the Halbach magnet [222].

A favorable way to design unilateral magnets with particular field profiles including a sweet spot is by shimming the field using pole shoes or additional small magnets (Fig. 7e–g). Single-sided low-gradient magnets have a larger sensitive volume, but typically also lower field strength. The size increase of the sensitive volume more or less compensates for the sensitivity loss associated with the field reduction, hardly leading to any improvement in the signal-to-noise ratio. It is worth noting that single-sided NMR sensors with a sweet spot are often referred to in the literature as sensors that generate a homogenous field, although the inhomogeneities are of the order of 1000–10,000 of parts per million across the sensitive volume.

The concept of shimming by generating compensation fields with additional permanent magnets has been refined to include higher-order derivatives of the field to improve the homogeneity within an extended sensitive volume (Fig. 7g). The main u-shaped magnet is equipped with several magnet-block pairs that form a shim unit. By controlling the positions of the pairs, first and second order derivatives of the field can be adjusted to zero to generate a sweet spot external to the magnet sufficiently homogeneous for chemical-shift resolved NMR spectroscopy with a resolution of a few parts in 10^7 [89]. The first order shim components x, y and z are generated by displacing two magnet pairs along the x, y and z directions, respectively. The second order terms x^2 and z^2 are adjusted by varying the distance between magnets in a pair while keeping their centers fixed. The cross terms xy, xz and yz can be generated by displacing the magnets as described in Table 1.

Table 1
Shim components and associated magnet displacements

Shim component	Magnet (cf. Fig. 7g)			
	1	2	3	4
X	Δx	Δx	Δx	Δx
Y	Δy	Δy	Δy	Δy
Z	Δz	Δz	Δz	Δz
X^2	Δx	Δx	$-\Delta x$	$-\Delta x$
Z^2	Δz	$-\Delta z$	Δz	$-\Delta z$
xy	$-\Delta y$	$-\Delta y$	Δy	Δy
zy	Δy	$-\Delta y$	Δy	$-\Delta y$
xz	Δx	$-\Delta x$	Δx	$-\Delta x$

2.3.2. Magnets with $\boldsymbol{B}_0$ perpendicular to the surface

The simplest magnet geometry is a bar magnet homogeneously polarized along its axis (Fig. 6c). This geometry provides a more generous ratio of sensitive volume to sensor size than the u-shaped geometry. For the latter the sensitive volume scales with the size of the gap while for the former it scales with size of the pole face. The field lines generated by the bar magnet approximate those of a dipole. They emanate from one pole face and curl back to enter at the opposite pole face. Such geometry produces a magnetic field (Fig. 9b) which, compared to that of the original u-shaped magnet (Fig. 9a) [185], exhibits much weaker lateral variations and similar strength of the gradient (~20 T/m) in depth direction [188,189]. This simple geometry is quite well suited for slice selective scanning of depth profiles.

The bar-magnet geometry is also suited to generate a sweet spot [223–227]. Two concentric tube magnets with different diameters and opposite polarization can be employed to generate a point at certain distance from the sensor surface where the gradient is zero. The same effect can be produced by drilling a hole in the center of a cylinder. Such a hole can be considered as negatively polarized material inside a positively polarized magnet. This is the idea underlying the barrel magnet (Fig. 10a). The particular depth where the sweet spot is generated, its size, and the magnitude of the magnetic field can be modified by choos-

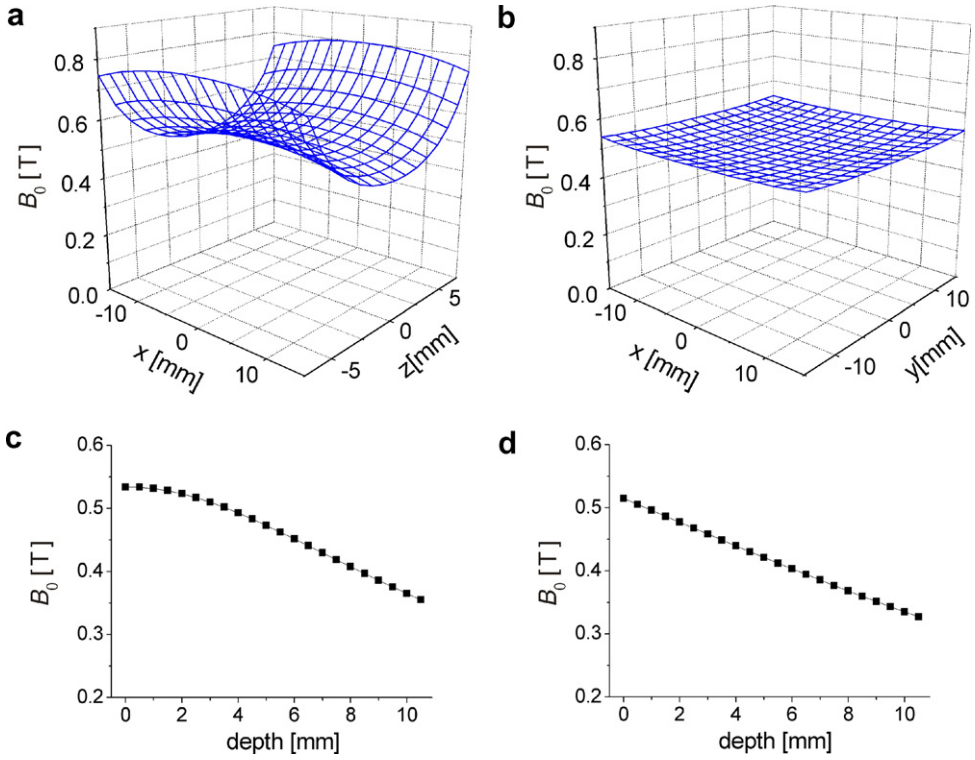

Fig. 9. Field (top: a and b) and gradient (bottom: c and d) profiles of the original u-shaped NMR-MOUSE (left: a and c) [184] and the bar-magnet NMR-MOUSE (right: b and d) [188] at 1 mm depth. In a given plane above the sensor, the magnetic field varies approximately linearly with depth for either sensor. The lateral gradient is approximately linear for the u-shaped sensor and zero for the bar-magnet sensor.

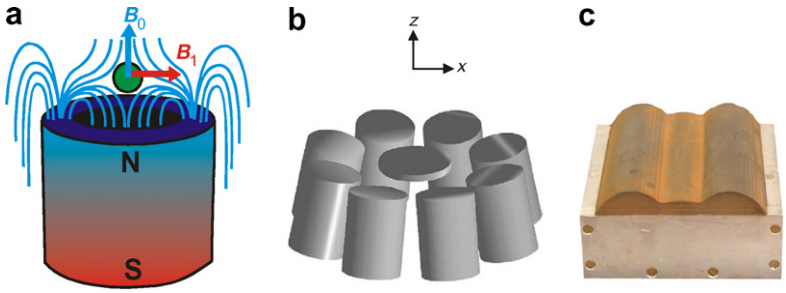

Fig. 10. Magnets for unilateral NMR with the magnetic field perpendicular to the sensor surface. (a) Barrel magnet with a sensitive volume thicker than that of the simple bar-magnet NMR-MOUSE (Fig. 6c) [223,224,226]. (b) Magnet of the NMR-MOLE, a variant of the barrel magnet from discrete magnet cylinders [229]. (c) Simple bar magnet combined with a shaped pole shoe optimized for depth profiling in low gradients [203].

ing different ratios between the outer and inner diameters. As the inner diameter approaches the outer one the depth and the size of the sweet spot increase while the field strength tends to zero. Instead of a hole a second magnet can be placed in the hole and its position varied [224]. This concept has been used some time ago in the design of electromagnets for unilateral NMR [228]. A discrete version of the barrel magnet is the NMR-MOLE (MObile Lateral Explorer, Fig. 10b) [229]. It consists of axially magnetized cylinder magnets arrange on a circle. By changing the inclination angle, the field profile can be fine tuned.

The principle of generating a sweet spot with the barrel magnet has also been used to reduce the gradient so as to excite a thicker slice while maintaining the possibility for sample profiling [227]. Another approach combines a simple bar magnet with a high permeability material like iron (Fig. 10c) [203]. The shape of the iron piece has been optimized to produce a main gradient of 0.3 T/m which, in principle, allows excitation of a depth region up to 1 cm. Although the slice thickness is increased in this way from tens of millimeters to several millimeters compared to high-gradient magnets, the improvement is bought at the expense of a reduction of the average field and a changing efficiency of the rf coil across the slice thickness [203]. Furthermore, to maintain the spatial resolution when reducing the gradient strength, the lateral field variations must be scaled down accordingly to flatten the curvature of the sensitive slice.

Most of the recent magnets for unilateral NMR have been built from permanent magnet blocks. Alternatively, electromagnets can be used [198,230]. Electromagnets provide a more homogeneous magnetic field at tighter tolerances as the inhomogeneity associated with the granular structure of magnet material is not an issue, and one can more easily compensate for temperature drifts. On the other hand, they are far more bulky than permanent magnets and have high power requirements that so far have prevented their use for field applications.

2.4. RF coils

Several different radio-frequency coils have been investigated for single-sided NMR. Similar to the magnets that provide the polarization and detection field $\boldsymbol{B}_0$ (Figs. 7 and 10), rf coils are distinguished that produce $\boldsymbol{B}_1$ fields largely perpendicular and largely parallel to the surface of the coil (Fig. 11). Those with a field perpendicular to the face of the coil are based on a single current loop in the plane (Fig. 11a). They are suitable only for use with u-shaped magnets that produce a $\boldsymbol{B}_0$ field parallel to the magnet face. Coils with a field parallel to their face are built from at least two opposed current loops in the plane (Fig. 11b and c) and can be employed for either bar or u-shaped magnets. The simplest coil of this type is the figure-eight coil (Fig. 11b). Figure-eight coils are gradiometer coils by their very nature. They are insensitive to far field noise, while simple current loops are not, but two and more can be arranged coaxially to form gradiometer coils with $\boldsymbol{B}_1$ perpendicular to the face of the coil [231–234].

In addition to the basic requirement for a coil to generate a $\boldsymbol{B}_1$ field perpendicular to $\boldsymbol{B}_0$, there are other requirements such as high sensitivity and spatial selectivity. The latter is important when analyzing objects larger than the coil, to restrict the extension of the sensitive volume by the geometry of the coil, and when implementing $\boldsymbol{B}_0$–$\boldsymbol{B}_1$ matching techniques. Important parameters that determine the sensitive volume are the rf coil efficiency B_1/i, the coil resistance R, the coil inductance L and the spatial variations of $\boldsymbol{B}_1$. These parameters can be optimized for maximum signal-to-noise ratio by maximizing the size of the sensitive volume and the detection sensitivity $B_1/(i\sqrt{R})$.

2.4.1. Coils for depth-profiling magnets

For unilateral depth profiling sensors, the rf coil must be designed to generate and detect signals only from the region where the $\boldsymbol{B}_0$ field is best for obtaining high depth resolution. In this case the lateral selectivity provided by the rf coil is crucial. As a rule of thumb the size of the selected region is of the order of the diameter of the rf coil. The variation of $\boldsymbol{B}_1$ across the selected region strongly depends on the particular rf coil geometry (Fig. 11). Any $\boldsymbol{B}_1$ inhomogeneity results in a sensitivity loss, as well-

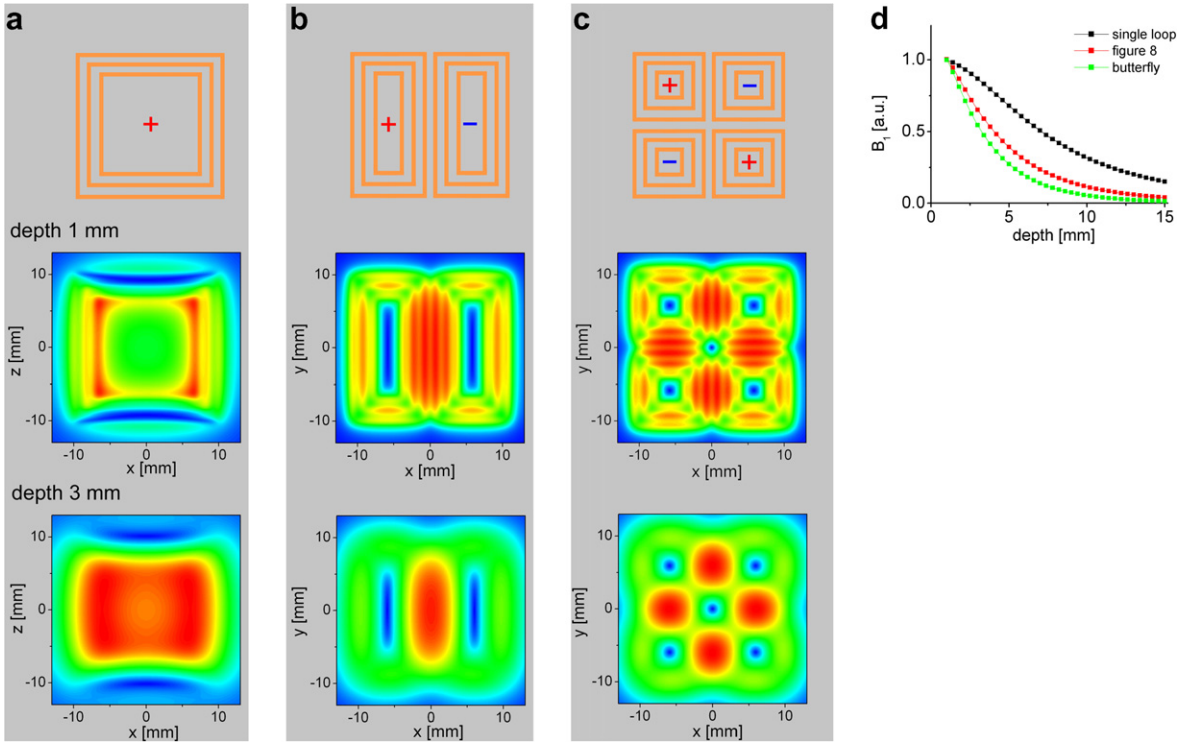

Fig. 11. Radio-frequency coils used in single-sided NMR (top) and field maps at different depths (middle and bottom). (a) Simple current loop coil for single-sided NMR. The $\boldsymbol{B}_1$ field is essentially perpendicular to the coil surface. The coil is well suited for use with a u-shaped magnet. (b) Figure-eight coil composed of two current loops with opposite current directions. The $\boldsymbol{B}_1$ field is essentially parallel to the coil surface. (c) Butterfly coil from two figure-eight coils. (d) $\boldsymbol{B}_1$ as a function of depth for the three rf coils. At 1 mm depth (middle), the 2D $\boldsymbol{B}_1$ maps closely reproduce the current paths while at 3 mm depth (bottom), the current paths are washed out.

defined 90° and 180° pulses cannot be generated even for on-resonance spins. Notice that each point in the profile is defined by the response of all spins inside the sensitive volume, and that there is no lateral localization other than that provided by the coil.

When slice selection is combined with 2D lateral imaging by pulsing gradient fields, any $\boldsymbol{B}_1$ variation manifests itself as an intensity modulation across the image. A contiguous sensitive volume is provided by the current loop (Fig. 11a) while the multiple current loops of the figure-eight coil (Fig. 11b) and the butterfly coil (Fig. 11c) generate multiple sensitive spots in the plane [188]. Close to the coil, the $\boldsymbol{B}_1$ field maps the current paths of the coil (Fig. 11, middle), while further away, the fine structure in the sensitive volume is washed out (Fig. 11, bottom). This dependence of the $\boldsymbol{B}_1$-field close to the coil has been explored for analysis of thin samples by use of meander coils where current flows in neighboring parallel conductors, straight [235] or wiggled [189] in alternating directions.

The field maps in Fig. 11 show the $\boldsymbol{B}_1$variations along the lateral directions only as they apply to high-gradient devices where changes across the thickness of the sensitive volume are quite small (Fig. 11d) [220]. As the gradient in depth direction is reduced [203,227] and the thickness of the sensitive volume becomes comparable to the size of the coil, the variation of $\boldsymbol{B}_1$ along the depth direction must be taken into account. In this case, rf coils like the figure-eight and the butterfly coils that generate $\boldsymbol{B}_1$ parallel to the coil surface, exhibit inferior performance compared to single loop coils. The issue of $\boldsymbol{B}_1$ variations along the depth direction is critical for sensors intended to access a large range of depths by changing the distance between the sensitive volume and the rf coil fixed at the object either by retuning to different frequencies [145] or by moving the magnet and not the coil with respect to the sample [219]. The latter approach is advantageous when measuring lossy samples because the loading of the rf coil remains constant during acquisition of the profile.

2.4.2. Coils for sweet-spot magnets

The requirements for rf coils to be used with magnets that generate a sweet spot mostly relate to maximizing the signal-to-noise ratio. There is no need for coils that provide lateral selectivity of the sensitive volume. In fact, the optimum coil is the one that does not restrict the size of the sensitive volume at all. In general, the rf coils are larger than the size of the sensitive volume which is mainly determined by the 3D spatial variation of the $\boldsymbol{B}_0$ field. As the size of the coil becomes bigger, the $\boldsymbol{B}_1$ variations along the depth direction become smaller, and rf coils like the figure-eight coil can be used when accepting some sensitivity loss. It has been shown that the $\boldsymbol{B}_1$ variations inside the sensitive volume can be reduced by proper design of the rf coil [226,236,237]. However, as in the depth profiling case, coils based on a single current loop are more sensitive than those producing $\boldsymbol{B}_1$ fields parallel to the sensor surface.

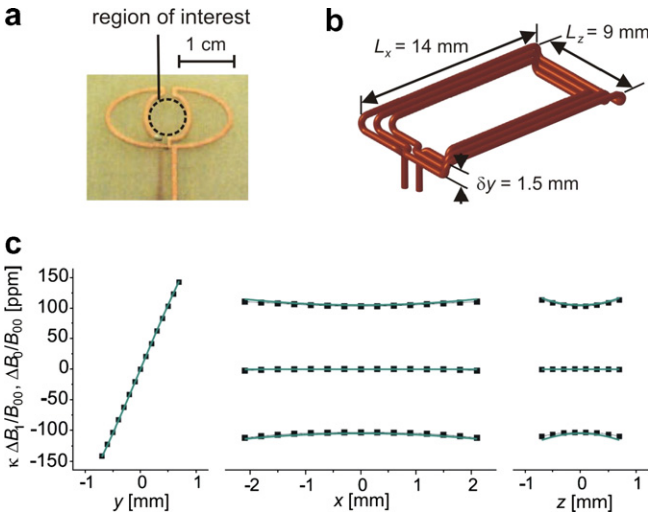

Fig. 12. Radio-frequency coils for matching $\boldsymbol{B}_1$ and $\boldsymbol{B}_0$ field profiles in *ex situ* NMR. (a) Figure-eight type open saddle coil with a $\boldsymbol{B}_1$ field essentially parallel to the surface of the coil [230]. The matching region is encircled. (b) Single-loop coil with a $\boldsymbol{B}_1$ field essentially perpendicular to the surface of the coil designed to match the $\boldsymbol{B}_0$ profile of the magnet depicted in Fig. 7f [81]. (c) Relative field variations as a function of space for the rf coil of Fig. 7b and the magnet of Fig. 7f.

2.4.3. Coils for field matching

A situation, where the requirements of the rf coil are exceptional is NMR with matching of $\boldsymbol{B}_0$ and $\boldsymbol{B}_1$ inhomogeneities, for example, for high-resolution spectroscopy in inhomogeneous fields [85,158,238–240]. More specifically, the term matching refers to the fact that the spatial variations of the corresponding vector components of the $\boldsymbol{B}_0$ and $\boldsymbol{B}_1$ fields exhibit the same space dependence across the sensitive volume while the vector orientations are required to be perpendicular. Radio frequency coils with spatial properties suitable for tensorial field matching that generate $\boldsymbol{B}_1$ fields parallel and perpendicular to the coil surface are shown in Fig. 12a and b, respectively. The open saddle coil (Fig. 12a) is a figure-eight coil that has been optimized to reproduce the field variations of a bar-type electro-magnet in a limited region of interest [230]. A tailored spatial dependence (Fig. 12c) of the field perpendicular to the coil surface is generated by the single current-loop coil shown in Fig. 12b which has been optimized to match the field profile of a u-shaped magnet (Fig. 7f). This coil was used in the first measurements of chemical-shift resolved spectra outside the magnet [158].

2.5. Gradient coils

Pulsed magnetic fields with gradients constant in space are conventionally referred to as pulsed field gradients (PFG). They are widely used for space encoding in imaging and flow NMR in homogeneous polarization fields [4,245–247] although much of the same information can also be obtained with field profiles other than linear [156]. In single-sided NMR the polarization field is inhomogeneous, and typical static gradients can easily be one or two orders

of magnitude larger than PFG. In spite of that, pulsed gradients can be used for space and displacement encoding in single-sided NMR by use of suitable NMR techniques which are primarily pure phase encoding methods [73–77]. However, to generate PFG with single-sided coils several challenges are encountered which mostly relate to the efficiency of the gradient coils. For instance, the gradient strength changes with depth which introduces variations of the field of view (FoV). Another issue relates to the signal attenuation observed in liquid samples due to molecular self-diffusion in the presence of strong background gradients. As the minimum encoding times used in imaging or velocity measurements are determined by the maximum strength of the pulsed gradient, a weak pulsed gradient nevertheless is associated with strong signal attenuation.

As for the rf coils, the direction of the polarizing field plays a determining role in the design of gradients coils. In the high-field limit, only the component of field generated by gradient coils parallel to $\boldsymbol{B}_0$ needs to be considered. For example, the z component of the field generated by two solenoids arranged as in Fig. 13a generates a linear variation along the gap direction x, which makes them appropri-

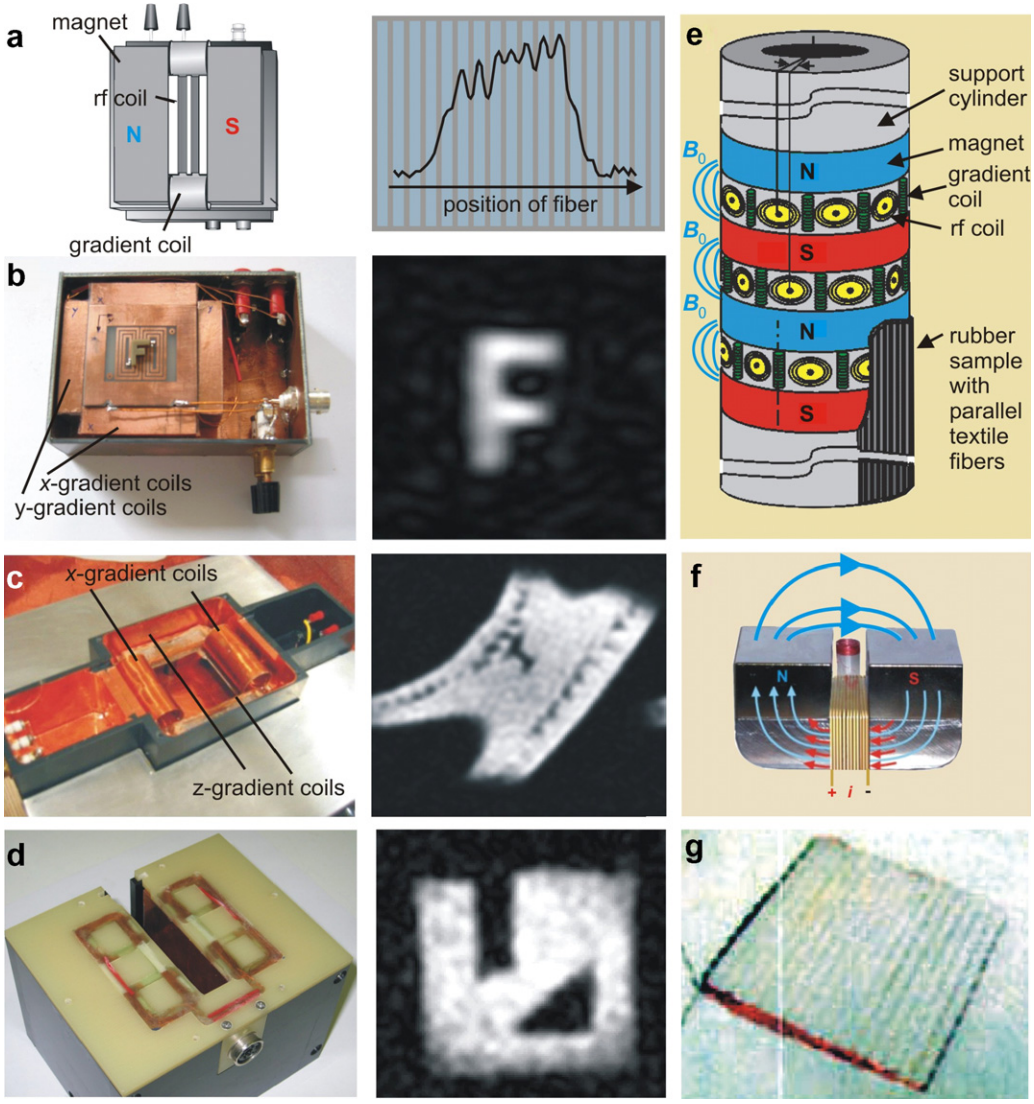

Fig. 13. Different approaches used to achieve spatial resolution with single-sided sensors. (a) NMR-MOUSE for 1D lateral imaging [73] with gradient coils in the magnet gap and an elongated rf coil. Drawing (left) and profile of fibre positions in an air-spring bellows (right). The fibres are centered on a 1 mm grid. (b) Small unilateral MRI scanner with a bar-magnet (left) and image (right) of the rubber letter F on top of the rf coil [74]. (c) Gradient coil arrangement mounted in the gap of the unilateral MRI magnet of Fig. 7c (left) and slice-selective NMR image of a defect in a textile fibre reinforced rubber tube (right) [76,216,241,242]. The acquisition time for the 50 × 50 pixel image with a field of view of 4 cm × 4 cm was 2 h [241]. (d) Flat gradient coil system built to fit on the Profile NMR-MOUSE (left) and slice-selective NMR image of a silicon rubber phantom. (e) Drawing of an MRI scanner for identifying the fibre positions in an air spring bellows for on-line quality control [243]. (f) Depth resolution by the MOUSE Refined for imaging (MRI) [244]. The position of the sensitive slice at a given rf frequency is shifted by a current $\boldsymbol{i}$ which changes the magnetic flux in the yoke to scan depth profiles. (g) Planar ladder gradient coil that generates a magnetic field in the z-direction with a gradient in the x-direction suitable for field-matching in *ex situ* NMR [230].

ate for imaging along the gap of a u-shaped magnet. In this set-up an ill-defined sensitive volume together with changes of the FoV with depth degrade the spatial resolution. This problem is solved by shaping the sensitive volume into a flat thin slice. In that case the variations of the coil efficiency with the depth can be neglected when the thickness of the sensitive volume is limited to a few tenths of a millimeter. Several set-ups based on this approach have been built to produce 2D images in planes parallel to the sensor surface (Fig. 13b–e) [74,76,217,243,244]. For example, a planar *xy* gradient system has been combined with a bar magnet to produce 2D images with sub millimeter resolution in a plane about 2 mm distant from the sensor (Fig. 13b) [74]. As $\boldsymbol{B}_0$ is normal to the sensor surface, the *x* and *y* gradient coils are identical but rotated by 90°. Fig. 10c shows an *xz* gradient system used in combination with a large u-shaped magnet (Fig. 7c) for 3D imaging [76]. The gradient coils were designed to work in a depth range from 0 to about 2 cm. To cover this range, the sensor is retuned and the gradient currents are adjusted accordingly to maintain a constant FoV at all depths. In this case the gradient system is accommodated in the gap of the u-shaped magnet [73,76,216,243]. However, this is not possible for similar sensors with a smaller gap. One solution is to place the gradient coils at the outside of the magnet at the expense of a serious loss in efficiency. A better choice is a planar gradient coil system, which has been used with the Profile NMR-MOUSE (Fig. 13d). Based on the same approach as the magnet, the *zx* gradient system was optimized to work at a fixed depth thus alleviating constrains to its dimensions.

An interesting variant of PFG-NMR is to shift the entire space-dependent field profile by generating a bias field with an electromagnet. This has been explored in stray-field MRI with a superconducting magnet to shift the sensitive plane through the sample [248] and with the original u-shaped NMR-MOUSE to scan depth profiles (Fig. 13f) [244]. Another use of gradient coils is for profiling the detection field $\boldsymbol{B}_0$ to establish field matching conditions in *ex situ* NMR (Fig. 13g) [230]. Such planar surface gradient coils are also of interest for shim-pulse techniques [249] in diverse applications of *ex situ* NMR, in particular for *ex situ* spectroscopy and imaging [238]. The advanced design of such flat gradient coils will benefit from the techniques developed in the context of medical MRI [250].

2.6. Spectrometers

During the last few years small commercial spectrometers have appeared on the market. Some of them can be battery operated and include an rf amplifier. The fore-runner of this development are desk-top NMR spectrometers for product and quality control of mostly food and polymer products. Desk-top NMR instruments come with a magnet for routine analysis mostly in terms of relaxation and diffusion NMR [125,126,135,251]. Well known among several suppliers are Bruker Optics (Fig. 14a) [252], Oxford Instruments (Fig. 14b) [253] and Resonance Instruments [254] which is now part of Oxford Instruments. For example, the Bruker Minispec spectrometer has variable frequency and can be used together with other NMR sensors such as the NMR-MOUSE® [255] or the Bruker Profiler. The MQC desk-top instrument by Oxford Instruments consists of a magnet and a spectrometer which includes the PC.

Small start-up companies are producing low-cost NMR instruments for educational purposes like Teachspin, Buffalo, USA [256], and Magritek, Wellington, New Zealand with its earth-field NMR spectrometer Terranova (Fig. 14c) [257]. Also the field cycling relaxometer by Stelar has been reduced to desk-top size (Fig. 14d) [258]. The NMR-MOUSE became truly mobile first with the Bruker Minispec console, which conveniently fits into a pilot's alu-

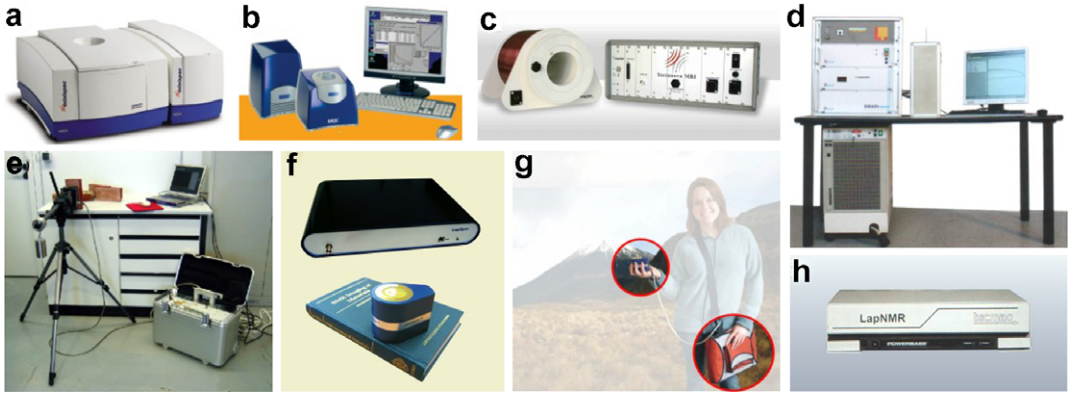

Fig. 14. Spectrometers for desk-top use and mobile NMR. (a) Bruker Minispec spectrometer and magnet (on left hand side) [252]. The spectrometer has variable frequency and can be used together with other NMR sensors like the NMR-MOUSE® [255] or the Bruker Profiler. (b) MQC desk-top instrument by Oxford Instruments consisting of a magnet and a spectrometer which includes the PC [253]. (c) Low-cost earth-field NMR spectrometer Terranova by Magritek, Wellington, New Zealand [257]. (d) Desk-top field cycling spectrometer SMARtracer by Stelar, designed to measure relaxation times as a function of field strength [258]. (e) NMR-MOUSE mounted on a tripod and Bruker Minispec console in a pilot's aluminum travelling case by RWTH Aachen University [259]. (f) Variable frequency spectrometer LapSpec for mobile NMR by ACT GmbH, Roetgen [260] and Magritek [257] together with the Easy NMR-MOUSE® [188]. (g) Lap-top size variable frequency NMR spectrometer with a battery pack for out-door's operation by Magritek [257] and ACT GmbH [260] and Easy NMR-MOUSE. (h) Variable frequency NMR spectrometer LapNMR by Tecmag [261].

minum travelling case (Fig. 14e) [259]. Later on, a compact, laptop-size, variable-frequency NMR spectrometer was developed together by ACT GmbH, Roetgen [260], and Magritek [257] (Fig. 14f and g) which includes the rf amplifier and can be connected to mobile NMR sensors to be operated out-door with a battery pack. Tecmag has come out at the same time with a small-size variable-frequency NMR spectrometer LapNMR which can readily be interfaced with available preamplifiers and rf amplifiers (Fig. 14h) [261]. It is fair to conclude, that the commercial NMR instruments are heading towards smaller sizes, driven by the pioneering work of individuals [90,93,150,168–170,262–269] and the challenges in mobile NMR, and the single-chip spectrometer with micro-coil probes is already on the horizon [270,271].

3. Methods

The development of NMR methods for mobile NMR is driven by two sources. One is the need for more information from, and better accuracy of, well-logging instruments. The other is scientific curiosity about doing NMR in low and inhomogeneous fields with inexpensive instrumentation and with it the drive for expanding the range of applications of NMR. A major part of the contributions on NMR in inhomogeneous fields has been published by the groups at Schlumberger, at UC Berkeley, and at RWTH Aachen University. With reference to the methods scheme of Fig. 2, the Schlumberger group is known for its well-logging oriented work on multi-echo trains with the analysis and exploitation of coherence transfer pathways [58,272] that leads to fast measurement schemes not only of relaxation but also of diffusion and flow and for their advancement of 2D NMR based on the inverse Laplace transformation [79,80,273,274]. The Aachen group is known for the development of the NMR-MOUSE [46] sensor and methods such as multi-quantum NMR [70,71], single-sided NMR imaging [73–76], single-sided flow NMR [77,78] with pulsed gradient fields, single-sided spectroscopy [81,89], and applications of mobile NMR to a diverse range of materials [241,275,276]. The Berkeley group has introduced novel concepts of obtaining spectroscopic resolution in inhomogeneous fields via field matching [85,158,238–240] and shimming the spins instead of the fields [249], and it has introduced innovations in enhancing the sensitivity by novel excitation and detection methods (see Section 1), a concept that it is referred to as *ex situ* NMR. The number of publications concerning NMR in inhomogeneous fields appears to be steadily increasing as more and more researchers are attracted by the challenging perspectives of novel applications, instrument design, and the exploration of new experimental strategies. The following sections attempt to review the guiding principles of NMR methods in inhomogeneous fields ranging from simple 1D CPMG-type relaxation measurements to methods with increasing complexity all the way to 2D NMR and high-resolution spectroscopy at this stage.

3.1. Relaxation

Relaxation denotes the loss of nuclear magnetization by energy dissipation from the spin system to the molecular environment as well as the loss of coherence in a large number of precessing spins. In simple spin-1/2 systems, the time scales of these two processes are described by one relaxation time each, i.e., by T_1 and T_2, respectively, within the simple formalism of the Bloch equations [277]. In higher-order spin systems, more relaxation times exist. The value of the relaxation time in a particular spin system depends on the spin interactions and the geometry and time scale of molecular motion [278]. Both change with the state of the matter studied. The relaxation times and their changes when compared to reference values are sensitive indicators for the state of materials. For most practical purposes, such a comparison relies on empirical rules and the use of reference data bases. Providing relaxation models to quantify material properties is a demanding topic of academic studies [4].

An area of great importance for relaxation analysis is the study of fluids in porous media [279,280]. For example, detailed knowledge about the properties of oil and water in porous rock and the properties of the rock matrix are of great importance for oil recovery from geophysical formations [5,175]. In the fast diffusion limit, the molecules explore the entire space of one pore within the characteristic diffusion time of the experiment by moving across the pore several times. The analysis of experimental data based on the validity of this limit has been shown to give good results in most geophysical applications of NMR. In this case the relaxation rates $1/T_1$ and $1/T_2$ are sums of the bulk relaxation rates $1/T_{i\mathrm{b}}$ and a surface-mediated relaxation term which is proportional to the surface relaxivity ρ_i and the surface-to-volume ratio S/V of the pore. In large volumes, $1/T_1$ is unaffected by diffusion, but $1/T_2$ is also influenced by coherence loss from displacements in field gradients G, so that one obtains for the relaxation rates

$$1/T_1 = 1/T_{1\mathrm{b}} + \rho_1 S/V, \tag{1}$$

$$1/T_2 = 1/T_{2\mathrm{b}} + \rho_2 S/V + D_0\gamma(Gt_\mathrm{E})^2/12, \tag{2}$$

where D_0 is the bulk self-diffusion coefficient and t_E the echo time. In rock, the pore sizes are distributed and the so are the NMR relaxation rates. The distribution of relaxation times can be used to obtain the pore-size distribution [281]. The derivation of distributions of relaxation times and other NMR parameters is a powerful way of describing heterogeneous media. When narrow slices are excited in strong field gradients, diffusive transport in and out of the slice modifies the apparent longitudinal relaxation time [282].

3.1.1. Measurement of transverse relaxation

The measurement of transverse relaxation in NMR involves the generation of spin echoes to refocus coherent magnetization dephasing in the presence of inhomogeneous fields. For spin-1/2 systems, such echoes are generated by

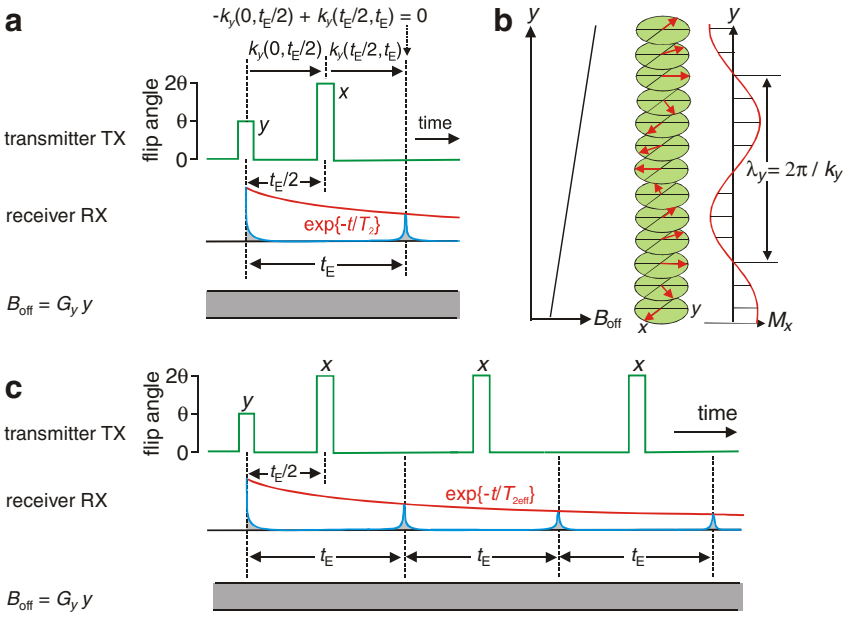

Fig. 15. NMR echoes for isolated spins 1/2. (a) Hahn echo and magnetization evolution in terms of the wave number k of a magnetization helix evolving in a linear offset field B_{off} with gradient G_y. In inhomogeneous fields, the flip angles θ are distributed. Ideally $\theta = 90°$. The refocusing pulse with flip angle 2θ changes the phases of the magnetization components by π in the transverse plane, which is equivalent to a sign change of the wave number k built up prior to the pulse, so that the helix formed in the interval between the first two pulses starts to unwind. The Hahn echo forms at $k_y(0, t_E) = 0$. (b) Helix of transverse magnetization, which forms in a linear field with gradient G_y. The wave number k_y is proportional to the integral of the gradient function: $k_y(t_i, t_f) = \gamma_{ti}\int^{tf} G_y(t)\,dt$. (c) Multi-echo CPMG sequence for stroboscopic observation of the magnetization decay. The envelope of the echo train is obtained at each echo centre by integrating the central part of the echo or by fitting the echo shape.

the Hahn-echo sequence (Fig 15a) [7,8]. A single echo is generated by applying two rf pulses. The formation of the echo can be understood in terms of winding and unwinding a magnetization helix with wave number k which tightens during the time following the first pulse and unwinds after the refocusing pulse (Fig. 15b). The echo forms when the wave number approaches zero. Upon repeating the measurement with changing echo time t_E, the decay time of the transverse magnetization can be extracted from the attenuation of the echo maxima. This procedure is time consuming, and in liquids, the signal decay is enhanced by translational diffusion in a magnetic field with gradient G (Eq. (2)). These shortcomings are alleviated by the CPMG-type (Carr, Purcell, Meiboom, Gill [9,10]) sequence with short echo times t_E. The CPMG sequence generates a multi-echo train (Fig. 15c) in a single shot for stroboscopic observation of the signal decay at the times of the echo maxima. However, the relaxation time extracted from the envelope of the echo train is not the T_2 measured in homogeneous field but an effective $T_{2\text{eff}}$ which is modified by off-resonance effects and flip angle variations in the inhomogeneous $\boldsymbol{B}_0$ and $\boldsymbol{B}_1$ fields [57,58].

3.1.2. Non-ideal rotations of magnetization

In the inhomogeneous magnetic stray fields of single-sided NMR devices, $\boldsymbol{B}_0$, $\boldsymbol{B}_1$, and with it the resonance offset vary with the position $\boldsymbol{r}$ of the spins inside the object. Any rotation of magnetization is around the effective field defined by the resonance offset and the acting $\boldsymbol{B}_1$ field. Ideal rotations by 90° and 180° about well defined axes are achieved at best for a small number of spins in the sensitive volume. Most spins experience rotations about other angles. As a consequence, the first echo in a CPMG echo train is a pure Hahn echo, but already the second one has components of a Hahn echo refocused by a Hahn echo, which is a direct echo, and of an indirect or stimulated echo [283], so that two different types of coherence pathways contribute to the formation of the second echo (Fig. 16a) [57,58,65,272,283]. The direct echo at time 2 t_E involves only transverse magnetization, and the stimulated echo at 2 t_E involves longitudinal magnetization which existed from time $t_E/2 < t < 3\ t_E/2$. In a CPMG sequence, the phases of the direct and indirect echoes are the same, and the signals add coherently. Typically $T_2 < T_{2\text{eff}}$, as $T_{2\text{eff}}$ includes contributions from stimulated echoes which relax with $T_1 > T_2$ during the second and the third pulses [57,58,63]. Thus in the end, $T_{2\text{eff}}$ depends on the $\boldsymbol{B}_1$ and $\boldsymbol{B}_0$ field profiles and therefore on the sensor geometry. Echoes with different coherence pathways can be separated by variable echo times and by suitable phase cycles [57,58]. This is of interest in practice, as each echo is affected differently by transverse and longitudinal relaxation as well as by diffusion in gradient fields [65,272]. In fact, the echo shape bears a characteristic signature of diffusion (Fig. 16b) [65,284].

Disentangling echoes from different coherence pathways and analyzing their shapes is the fundamental concept upon which novel schemes for single-shot measurements

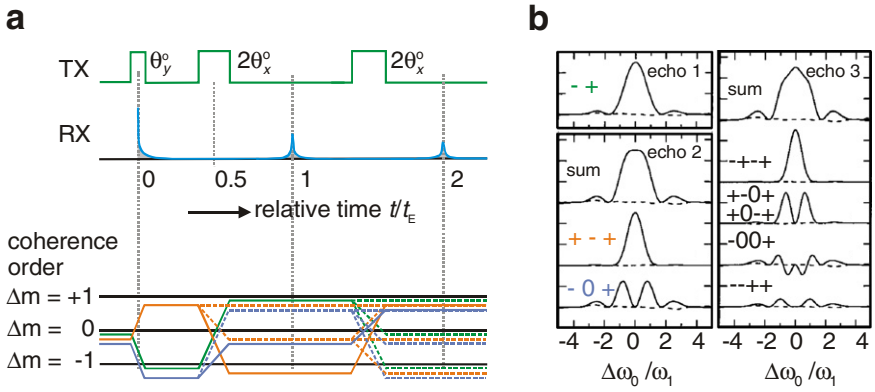

Fig. 16. Coherence transfer pathways for a system of uncoupled spins 1/2 (a) and echo shapes (b, adapted from [65]) for the first echoes generated with a pulse-width modulated CPMG sequence in a strongly inhomogeneous $\boldsymbol{B}_0$ field. The fully drawn lines in the coherence transfer diagram (a) correspond to the echo components (b) which add up to the corresponding sum echoes. The coherence orders Δm followed along the excitation pulse train are indicated for each echo component. The broken lines indicate pathways that lead to contributions in later echoes. T_2 relaxation and magnetization dephasing from diffusion act when orders $\Delta m = \pm 1$ are active, and T_1 relaxation acts when coherence order $\Delta m = 0$ is active.

[284] of relaxation [58,285], diffusion [68,285–288], velocity [72,289] and imaging [290] are designed. From a combinatorial analysis it is clear, that the number of contributions from different coherence pathways increases dramatically with the echo number. A cumbersome, but straightforward analysis based on resonance offset can only be done for $\boldsymbol{B}_1$ fields which are homogeneous in the sensitive volume [272].

As the first echo in a CPMG train measured in a strongly inhomogeneous field is just a direct echo, while the second and further echoes are sums of direct and stimulated echoes, the first echo is typically lower than the second echo [65,291–293]. A detailed analysis of the CPMG echo train further reveals that the pulse spacing between the first two pulses should be decreased by a time $2\ t_{90}/\pi$, where t_{90} is the duration of the 90° pulse to optimize the bandwidth and with it the signal-to noise ratio, as the beginning of the evolution of transverse magnetization effectively starts at $t_{90}\ (1 - 2/\pi)$ after the beginning of the 90° pulse [294]. In fact the echo shape changes with the timing of the first pulse spacing, an effect that has been attributed to a change in the bandwidth of the sequence. Similarly, different echo shapes are observed for CPMG sequences where the 180° refocusing pulses are produced by amplitude modulation as compared to those produced by pulse-width modulation. For amplitude modulation with identical excitation bandwidths for all pulses, the echo shape hardly changes, but it changes more strongly for pulse width modulation, where the bandwidths of excitation and refocusing pulses differ. Modified CPMG-like sequences with composite pulses [295,296] have been designed that maintain the error-correcting properties of the original CPMG sequence and exhibit increased signal-to-noise ratio in inhomogeneous fields as a result of a larger sensitive volume [297]. While the first few echoes show an oscillatory behavior, later echoes decay with the relaxation time characteristic to the sample, so that these sequences can be used to measure relaxation times. As composite pulses are longer than regular pulses and require more demanding hardware to generate, they have hardly been used so far.

The nominal flip angle $\theta = \gamma\ B_1\ t_p = 90°$ is defined on resonance where the rf frequency equals the Larmor frequency, $\omega_{rf} = \gamma\ B_0$. If θ is adjusted to different values, the echo contributions from the different coherence pathways are weighted differently and the signal decay is modified. This may be exploited to optimize the contrast to discriminate objects made from similar materials, like the same rubber formulation but differing in processing conditions [61,62]. As the flip angle of the refocusing pulse approaches 90°, solid echoes are obtained, and the CPMG sequence turns into a multi solid-echo sequence [62,292] with partial averaging of the homo-nuclear dipole–dipole interactions between the protons in solids. This concept can be generalized to search for different pulse sequences such as time-suspension sequences and others known from line-narrowing in solid-state NMR with stroboscopic observation of the transverse magnetization and an adequate description in terms of average Hamiltonians to move the observed magnetization decay into a time window where the contrast for discrimination of different materials is best [4,298]. Work along these lines has not yet been explored systematically for NMR in inhomogeneous fields apart from a proof of principle study by Miller and Garroway [299].

3.1.3. Evaluation of the echo decay envelope

To obtain parameters from the train of decaying echo amplitudes, different approaches can be taken. The clean approach is to fit the measured signal by a model function and extract the fit parameters. As the decay of the CPMG signal typically is non-exponential, model functions consisting of a sum of two exponentials, a sum of a Gaussian and an exponential function or some other suitable fitting function [300] are used. A sum of functions is intuitively appealing, as the different components can be assigned to different structural components of an object which is heterogeneous within the sensitive volume of the sensor. For

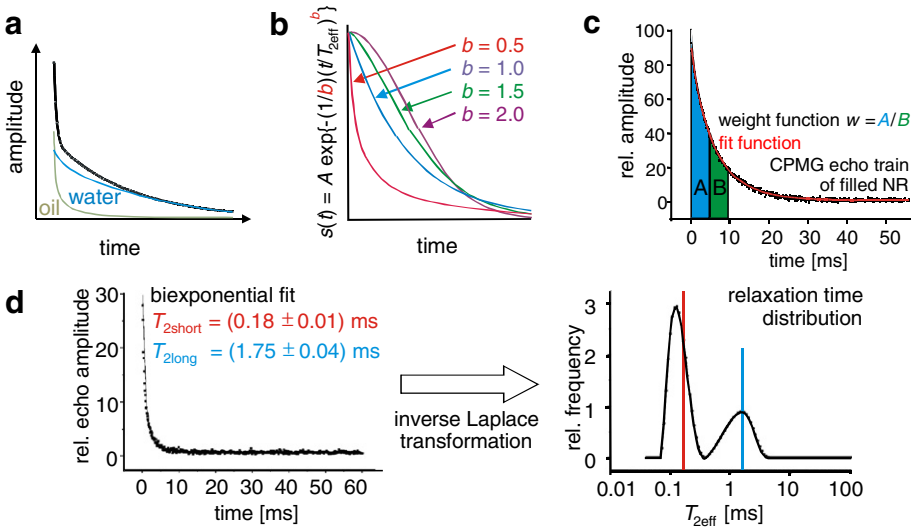

Fig. 17. Acquisition and evaluation of relaxation data. (a) Decomposition of the relaxation signal of water and oil in terms of a sum of two fitting functions. (b) Stretched exponential fitting function. (c) Definition of the NMR parameter w as the ratio of two definite integrals of the echo envelope. (d) A bi-exponential relaxation decay produces a bimodal distribution of relaxation times with peak widths determined by the particular regularization procedure used. The inverse Laplace transform of the echo envelope is typically displayed on a logarithmic scale to give the distribution of relaxation times.

example, water and oil signals can be separated (Fig. 17a), and a semi-crystalline polymer will show a rapidly relaxing component from the crystalline and rigid amorphous chain segments and a slowly relaxing component from the mobile amorphous segments, so that an NMR crystallinity can be defined as the relative amplitude $A_{\text{fast}}/(A_{\text{fast}}+A_{\text{slow}})$ of the rapidly relaxing component [301]. While such a fit requires four parameters, two amplitudes A_{fast} and A_{slow} and two relaxation times $T_{2\text{eff,fast}}$ and $T_{2\text{eff,slow}}$, in many cases a stretched exponential function gives an equally good fit with only three parameters, an amplitude A, a relaxation time $T_{2\text{eff}}$ and a stretched exponential b (Fig. 17b)

$$f(t) = A\exp\{-(t/T_{2\text{eff}})^{b}/b\}. \tag{3}$$

The normalization of the exponent ensures, that an exponential function is obtained for $b=1$ and a Gaussian for $b=2$. The value of $T_{2\text{eff}}$ in Eq. (3) then closely matches $T_{2\text{eff,long}}$ of a bi-exponential fit. It measures the characteristic decay time of the echo envelope for all shapes b and retains its meaning as an overall relaxation time for the material under investigation [276]. Its interpretation in terms of a material model, however, is not straightforward. Yet as only three parameters are required, the reproducibility of the parameters with different noise contributions in the same signal is better than for a four-parameter fit by a sum of two simple relaxation functions.

When comparative measurements are made, then an evaluation of the measured data by fitting a model function may not be necessary and empirical parameters instead of fitting parameters can be extracted from the signal. For example, the total signal may be normalized and integrated. When approximating the signal by a sum of exponential functions

$$s(t) = \sum\nolimits_i A_i \exp\{-t/T_{2\text{eff},i}\}, \tag{4}$$

the sum of all echoes [302] is proportional to the signal integral which corresponds to an amplitude-weighted average of the relaxation time $T_{2\text{eff}}$ after normalization of $s(t)$,

$$\int_0^\infty s(t)/s(0)\,\mathrm{d}t = \sum\nolimits_i w_i T_{2\text{eff},i} = \langle T_{2\text{eff}}\rangle, \tag{5}$$

where $w_i = A_i/(\sum_i A_i)$ is the relative amplitude of component i. Alternatively ratios and sums of partial integrals can be defined to produce suitable parameters which are sufficiently sensitive to differentiate variations in material properties. For example, the parameter w (Fig. 17c)

$$w = \int_0^{t1} s(t)\,\mathrm{d}t \Big/ \int_{t1}^{t2} s(t)\,\mathrm{d}t \tag{6}$$

has been used to characterize morphology variations in semi-crystalline polymers [301].

While an evaluation by a fitting function relies on a proper choice of this function, an integration or integration by parts does not. The most general fitting function is the sum (Eq. (7)) of many exponentials, from which the distribution of relaxation times can be extracted by inverse Laplace transformation [303–310],

$$S(p) = \int_0^\infty s(t)\exp\{tp\}\,\mathrm{d}t. \tag{7}$$

Strictly speaking, the distribution $S(p)$ of relaxation rates $p = 1/T_{2\text{eff}}$ is obtained. But as the relaxation time is usually plotted on a logarithmic scale (Fig. 17d), the difference between $\ln\{1/T_{2\text{eff}}\}$ and $\ln\{T_{2\text{eff}}\}$ is just a change in sign. As long as 1D transformations are handled this way, one representation is as good as the other. But once 2D transformations are explored more systematically, the additive

property of the relaxation rates may become significant, and distributions of effective relaxation rates may be preferred over distributions of relaxation times. In the presence of measurement noise in the signal to be transformed, the inverse Laplace transformation needs to be regularized to avoid instabilities in the algorithm. One way out is to transform a fitting function of something like 32 exponentials.

3.1.4. Longitudinal relaxation

Relaxation times other than T_2 and $T_{2\text{eff}}$ are also accessible in inhomogeneous fields but the corresponding signal properties need to be measured indirectly by modulating the initial state of the signal to be detected directly in the manner of multi-dimensional NMR. Some relevant pulse sequences are summarized in Fig. 18. For example, T_1 can be measured by inversion recovery (a) [60,65], saturation recovery (b) [61,62,184], and by hole-burning experiments (c) [311]. For detection, a single echo is sufficient, but a multi-echo train boosts the signal when all echoes are summed up [302]. Also detection of an echo train provides a signal with which the indirectly monitored evolution can be correlated with in the sense of two-dimensional time-domain NMR [312,313] or inverse Laplace transform NMR (cf. Section 3.4). This is why CPMG detection is the preferred procedure for NMR in inhomogeneous fields. Nevertheless, one should be aware of the fact that the CPMG signals may differ for example for magnetization components from fluids experiencing restricted diffusion in different size pores, so that simple addition of echoes may lead to incorrect amplitudes. Schemes for rapid measurement of combined T_1 and T_2 have been published, which avoid long recovery delays and explore the inversion recovery scheme [61] and the saturation recovery scheme [61,62,184]. Also other relaxation times like $T_{1\rho}$ (Fig. 18d) [314,315], the multi-solid echo decay time T_{2e} [62,314], and multi-quantum relaxation times (see Section 3.2) can be acquired in strongly inhomogeneous fields [71].

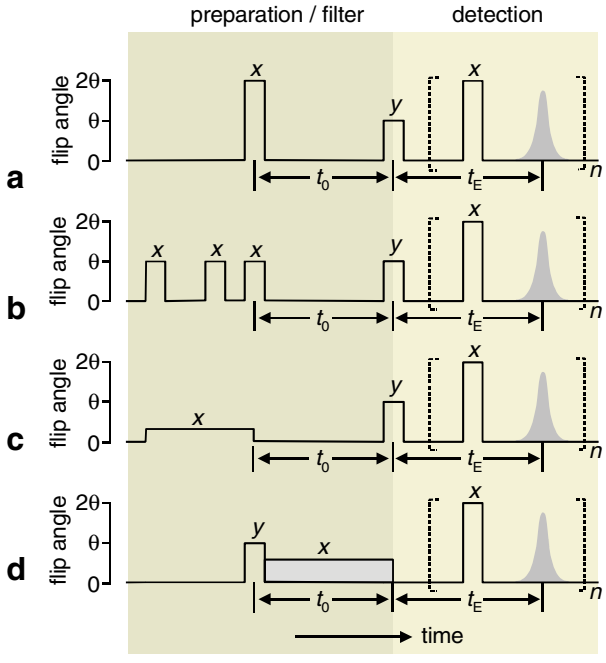

Fig. 18. Pulse sequences for measuring longitudinal relaxation times in an inhomogeneous magnetic field. The longitudinal magnetization evolves for a variable time t_0 during the preparation period, which acts as a filter that passes part of the total magnetization for detection. It is detected by a Hahn echo ($n = 1$) or a CPMG echo train ($n > 1$). (a) Inversion recovery sequence. (b) Saturation recovery sequence with aperiodic saturation of the initial longitudinal magnetization. (c) Hole burning sequence. (d) Sequence for detecting the longitudinal relaxation time $T_{1\rho}$ in the rotating frame. The magnetization is locked in the rotating frame with a spin-lock pulse of duration t_0.

Most practical applications of the NMR-MOUSE concern measurements with the CPMG sequence and the flip angle θ adjusted to maximize the echo amplitudes. As it takes longer to measure T_1, it is only measured in cases where $T_{2\text{eff}}$ fails to produce the sufficient contrast or when effects of diffusion are to be eliminated. As in conventional NMR, the saturation recovery sequence is the least error prone for T_1 measurements while the inversion recovery sequence provides the better dynamic range. A concept for rapid determination of T_1 in inhomogeneous fields is based on the signal decomposition at short recovery times [316]. A simple and very old method to probe T_1 is hole burning [278] which can readily be adapted to measurements in the strong and time-invariant gradient fields of the NMR-MOUSE [311]. From the evolution of the shape of the hole, T_1 relaxation can be separated from translational diffusion. Although $T_{1\rho}$ measurements require spin locking with an rf pulse, they can successfully be conducted in the $\boldsymbol{B}_0$ and $\boldsymbol{B}_1$ stray fields of single-sided NMR sensors [314].

3.2. Multi-quantum NMR

Multi-quantum NMR concerns transitions in spin systems where magnetic spin states with coherence orders different from ± 1 are generated with the exception of longitudinal magnetization [3,4,317]. For spins 1/2, such states require a coherent coupling, for example, by indirect coupling or direct dipole–dipole coupling [156]. The former is weak among protons in liquids and is difficult to observe by single-sided NMR. The latter is strong among protons but is averaged to zero by isotropic molecular reorientation, so that it vanishes in liquids. Weak dipolar couplings of a few Hertz from molecules partially oriented in anisotropic environments are an invaluable source in structural analysis of bio-molecules [318]. Stronger residual dipolar couplings of about 1 kHz and more are found in soft matter like biological tissues and rubber. They provide information on the molecular dynamics in the solid state. Different spherical tensor states $\mathbf{T}_{i,j}$ of the density matrix [319,320] can be generated and filtered from the total signal by spin-mode filters. For a spin-1 system, dipolar encoded longitudinal magnetization, dipolar order and

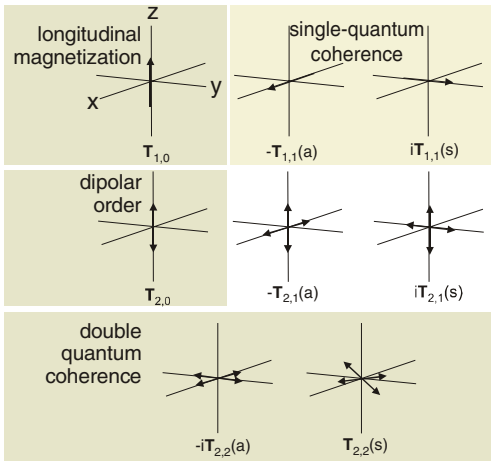

Fig. 19. Different tensorial components of the density matrix of a spin-1 system in vector notation (adapted from [319]). The symmetric and antisymmetric components $\mathbf{T}_{i,j}$ are denoted as (s) and (a), respectively. The decay of the single-quantum coherences can be observed directly in inhomogeneous fields by CPMG detection. Longitudinal magnetization, dipolar order, and double-quantum coherences can be filtered from the total signal with spin-mode filters. Their build-up and decay curves can be measured in inhomogeneous fields.

double-quantum coherences (Fig. 19) have been observed in the strongly inhomogeneous fields of the NMR-MOUSE [70,71].

Initially, multi-quantum Fourier NMR was applied to liquids in a 2D experiment [3,83]. Intra-molecular multi-quantum coherences between coupled protons are generated from longitudinal magnetization by at least two 90° pulses. To eliminate effects of chemical-shift and field inhomogeneity, these pulses preferably sandwich a 180° pulse (Fig. 20a). The multi-quantum coherences are then allowed to evolve for a multi-quantum evolution time t_{MQ} before they are converted back to longitudinal magnetization by the inverse of the multi-quantum excitation sequence, which can be obtained from the preparation sequence by a simple shift $\Delta\varphi = 90°$ of all the rf phases in the preparation propagator. A subsequent 90° pulse then converts the longitudinal magnetization modulated by the multi-quantum evolution during t_{MQ} back to observable single-quantum magnetization. It is not necessary to follow the path from multi-quantum coherence to single-quantum coherence via longitudinal magnetization, but this so called z-filter can be used in combination with appropriate cycling of the rf phases to eliminate stray signals from imperfect rf pulses and $\boldsymbol{B}_0$ inhomogeneities. Multi-quantum coherences of different order are selected by suitable phase cycles of the pulses in the preparation propagator [71,317].

The fact, that multi-quantum signals can be selected with such a pulse sequence by suitable choices of rf phases and not pulse flip angles makes this sequence amenable to use in strongly inhomogeneous magnetic fields. A further improvement in this case is to append the sequence by another 180° pulse centered in the t_{MQ} interval. With the resulting sequence (Fig. 20a), multi-quantum NMR signals have been observed with the NMR-MOUSE for differently cross-linked and differently strained rubber samples. For strong dipolar couplings in elastomers with high cross-link densities and in rigid polymers, higher order couplings perturb the postulated evolution of two-quantum coherences during the preparation and reconversion periods. Instead of the simple pulse scheme shown in Fig. 20a and in particular in homogeneous fields, better results are obtained by multi-pulse propagators for preparation and reconversion [321,322].

The same pulse sequence of Fig. 20a has also been used to select other multi-polar spin states such as dipolar encoded longitudinal magnetization and dipolar order [319,320] of rubber samples in the strongly inhomogeneous fields of the NMR-MOUSE (Fig. 21) [70,71]. If $\varpi_d \ll 1/\tau$ is the pre-averaged intra- and intergroup dipolar coupling constant in elastomers [323], the normalized signal in the initial time regime $\tau \ll T_{2eff}$ is given by

$$s_{DQ}(\tau)/s_0 \propto \langle \sin^4\theta \rangle_\theta 3/2 \langle (\varpi_d)^2 \rangle \tau^2 \quad (8)$$

for the double-quantum (DQ) build-up curve, and by

$$s_{DELM}(\tau)/s_0 \propto \langle \cos^4\theta \rangle_\theta + \langle \sin^4\theta \rangle_\theta (1 - 3/4 \langle (\varpi_d)^2 \rangle \tau^2) \quad (9)$$

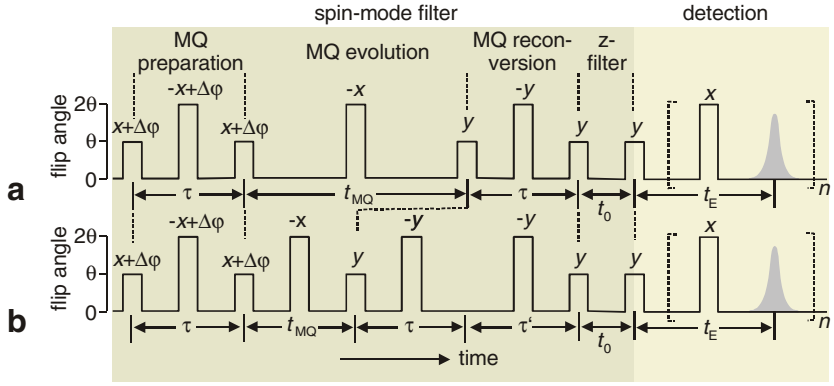

Fig. 20. Multi-quantum NMR in strongly inhomogeneous magnetic fields. (a) Pulse sequence to observe signals from different spin modes. Multi-quantum build-up and decay curves are obtained by systematic variation of the preparation and reconversion time τ. (b) Pulse sequence for observation of multi-quantum decay curves. A mismatch time τ' is added to the reconversion period which is varied at the value of τ fixed to the maximum in the build-up curve.

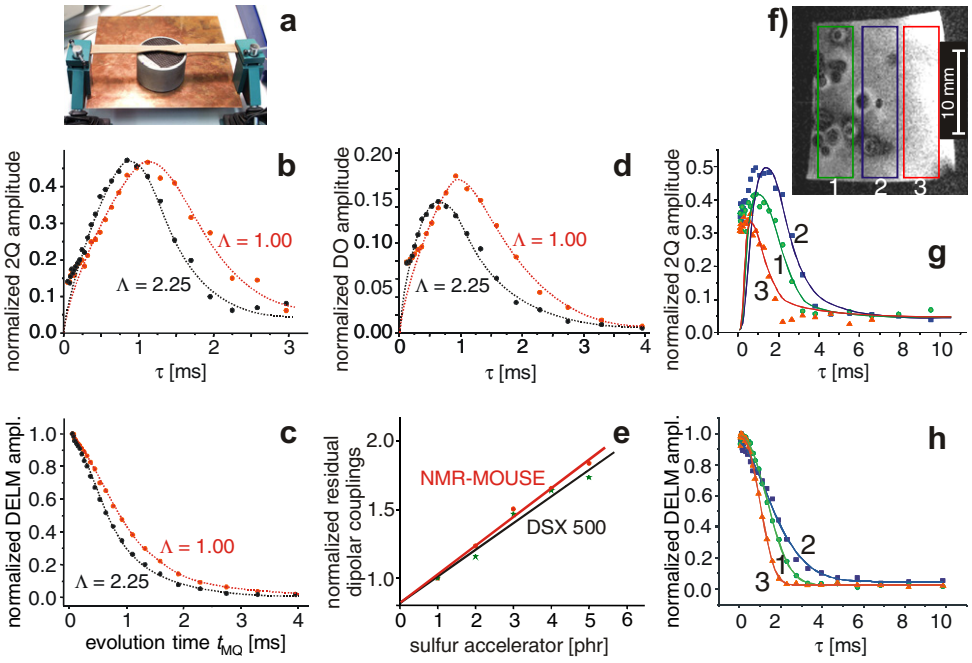

Fig. 21. Spin-mode filtered NMR signals from rubber. The drawn lines are guides for the eye. The initial values at short times are contaminated by dead-time effects of the sensor used. (a) Simple straining device for rubber bands to be used for measurements with the NMR-MOUSE. (b) Double-quantum (2Q) build-up and decay curves for two differently strained bands from unfilled, cross-linked natural rubber. The residual dipolar coupling increases with the elongation Λ. (c) Decay curves for dipolar encoded longitudinal magnetization (DELM). (d) Build-up and decay curves for dipolar order (DO). (e) Normalized residual dipolar couplings for unfilled natural rubber samples with different amounts of sulfur/accelerator given in parts per hundred rubber (phr). The values measured with the NMR-MOUSE agree well with those measured by conventional NMR at 500 MHz. (f) NMR image of a block of silicone rubber which shows an electrical tree from voltage overload. Three different measurement depths are framed and assigned to the DQ and DELM curves in (g and h). (g) DQ build-up and decay curves measured at the depths indicated in (f). (h) DELM curves measured at the depths indicated in (f).

for dipolar encoded longitudinal (DELM) magnetization [324]. Here the symbol $\langle \ldots \rangle_\theta$ denotes the statistical average over the flip-angle distribution in the sensitive volume, $\langle (\ldots) \rangle$ represents the average of the statistics of the distributions of lengths and orientations of the end-to-end vectors of the inter cross-link chains, and s_0 is the signal amplitude detected with a Hahn echo at a short echo time. Both signal contributions can be discriminated from each other and filtered from the detected total signal by specific phase cycling schemes [20]. Dipolar order (DO) can be measured with the same pulse sequence and approximately separated from dipolar encoded longitudinal magnetization by shifting the phase of the refocusing pulse in the dipolar evolution period t_{MQ} by 180°. An approximate separation from the DQ and DO signals can be achieved by exploring their different flip angle dependences [71]. In the short time limit

$$s_{DO}(\tau)/s_0 \propto 9/8\langle \sin^3\theta \rangle_\theta \langle (\varpi_d)^2 \rangle \rangle \tau^2. \quad (10)$$

A slightly reduced sensitivity to residual dipolar couplings is obtained when the double-quantum decay signal (DQD) is measured with the help of a mismatched reconversion propagator (Fig. 20b), extended in its timing by a variable time τ' with τ suitably fixed to the maximum of the build-up curve, so that only the decay from the maximum onwards is recorded as a function of τ' [70]. The benefit of this procedure is better sensitivity, as the DQ signal starts with a maximum instead of zero. In the short time limit

$$s_{DQD}(\tau)/s_0 \propto \langle \sin^4\theta \rangle_\theta (1 - 3/4\langle (\varpi_d)^2 \rangle \rangle \tau'^2). \quad (11)$$

The spin modes of dipolar coupled protons are sensitive probes for the time scale and geometry of molecular motion in soft matter, where the dipolar coupling is partially averaged by the motion. The anisotropy and time scale of segmental motion in cross-linked elastomers depends on the cross-link density and on the applied strain [323,325]. The NMR-MOUSE is particularly well suited for investigating strained rubber samples, as the straining device can be simple without a special, non-magnetic design that fits inside a magnet (Fig. 21a). DQ, DQD, DELM and DO curves have been measured for differently cross-linked and differently strained bands of unfilled natural rubber by the NMR-MOUSE [70,71]. The curves for unstrained samples ($\Lambda = 1$) and samples strained to 2.25 times their original length ($\Lambda = 2.25$) are depicted in Fig. 21b–d. The different states of strain clearly lead to well separated curves, indicating good contrast for discriminating residual dipolar couplings. These can be extracted with the help of Eqs. (8)–(11) from the initial parts of the curves. As the DQ (Fig. 21b) and DO (Fig. 21d) curves start at zero, the precision of the values determined by a polynomial fit in the initial time regime is better for DQD and DELM (Fig. 21c) which start at a maximum. While the

value of the mean square average residual dipolar coupling $\langle(\varpi_d)^2\rangle$ cannot readily be quantified from DELM curves due to the formation of an average over the distribution of flip angles θ (cf. Eq. (9)), a relative value can be obtained from the double-quantum decay curves by normalizing the data of a sample with unknown residual dipolar coupling to those of a sample with known coupling. This has been done for a series of natural rubber samples with different cross-link densities resulting from different amounts of sulfur/accelerator in the formulation. The values obtained with the NMR-MOUSE agree well with those obtained at high field with a conventional 500 MHz NMR spectrometer (Fig. 21e).

The excellent sensitivity of the spin-mode filters to differences in molecular motion in soft matter has been exploited to detect different stages of electrical aging in cable insulation material made from polydimetylsiloxane [132,134,326]. High voltage overload generates local discharges that form tree-like aggregates of cavities (Fig. 21f), which grow with time and eventually lead to failure of the material. The residual dipolar couplings change non-uniformly with increasing density of cavities, which leads to differences sensed consistently in the DQ (Fig. 21g) and DELM (Fig. 21h) curves. This effect is hard to observe by CPMG measurements. On the other hand, to acquire signals with spin-mode filters takes more time than CPMG measurements.

3.3. Diffusion

Diffusion is a phenomenon that is of fundamental interest in basic and the applied sciences [327]. NMR is unique in its capability of measuring the translational self-diffusion. This is important in understanding fluids and fluid mixtures as well as in studying diffusion under confinement in porous media such as biological cells [328], heterogeneous catalysts [329], and fluid bearing rock [175,330]. The spin positions are labeled by their precession phases in a spatially varying magnetic field and a concentration gradient is not required. Apart from hole burning experiments [278,311,331], there are two basic ways to quantify self-diffusion by NMR [247]. One uses pulsed gradient fields (PFG: pulsed field gradient) [69,332] and the other constant gradient fields (CFG) [7]. PFG-NMR requires rapid switching of magnetic gradient fields while the rf excitation proceeds in a homogeneous field to excite the sample uniformly in a large sensitive volume (Fig. 22, left). CFG NMR [247,333,334] uses time-invariant gradient fields

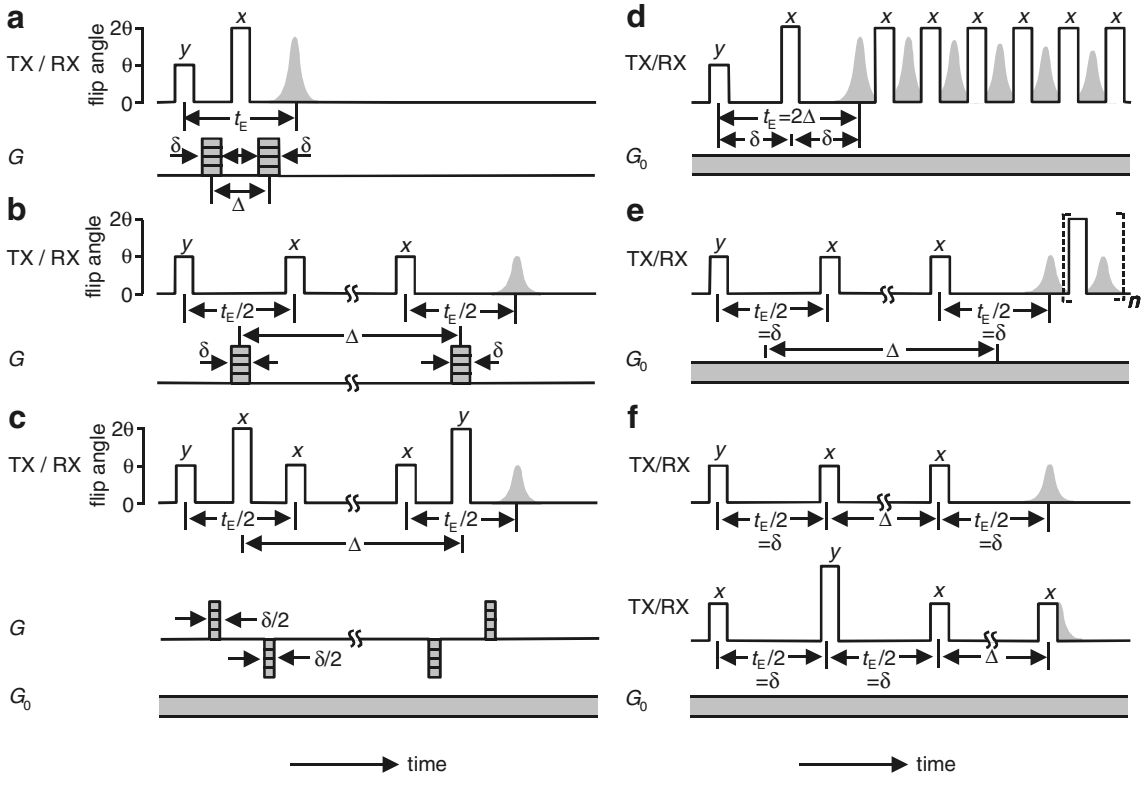

Fig. 22. Pulse sequences used to study diffusion with pulsed gradients G and with constant gradients G_0. TX denotes transmitter and RX denotes receiver. (a) Pulsed gradient spin–echo sequence. The diffusing spins carry transverse magnetization. (b) Pulsed-gradient stimulated-echo sequence. It allows for longer diffusion times as the diffusing spins carry longitudinal magnetization. (c) Pulsed-gradient stimulated spin–echo sequence with compensation of dephasing in linear background gradient fields. (d) Constant-gradient spin–echo sequence with CPMG detection. (e) Constant-gradient stimulated-echo sequence with CPMG detection. (f) Sequence for measuring diffusion in internal field gradients. The gradient field is a property of each pore and not of the sensor. A reference free induction decay signal is acquired (bottom) to subtract the effect of longitudinal relaxation from the echo acquired with diffusion weighting in the internal gradients (top).

and is less susceptible to instrument vibration from eddy currents (Fig. 22, right). The rf excitation is applied in the presence of the gradient, so that only the spins in a small sensitive volume such as a slice are excited. This is why CFG NMR is less sensitive than PFG-NMR. But it does not require sophisticated equipment [228,335,336], in particular, when high gradients of the order of several tens of Tesla per meter are in demand. Such gradients can easily be generated in the stray fields of superconducting [333] and permanent magnets [46,162].

In either case, the displacement of spins is measured in a time Δ determined by the parameters of the Hahn or stimulated echo sequences (Fig. 22a and b) [4,245,247]. In most cases the narrow-pulse approximation or slow motion limit is assumed [337,338]. Here the time δ during which initial and final positions are labeled, is short compared to the diffusion time Δ during which the spins change their position. Then the initial spin positions are marked instantaneously by a precession helix (cf. Fig. 15b) with wave number k_i just before the diffusion time. The final position is interrogated by instantaneously unwinding the magnetization helix immediately after the diffusion time. To observe a signal, the gradient action of the second position encoding period must correspond to a wave number $k_f = -k_i$, so that at the time of the echo $k_i + k_f = 0$. This argument is identical to the one given for observation of a Hahn echo (cf. Section 3.1.1 and Fig. 15a). The difference is that the observed echo is attenuated not only by relaxation, but also by spins changing from their initial positions with one value of the magnetic field to their final positions with another value of the magnetic field. In the case of diffusion, this process is incoherent and leads to an additional attenuation of the echo amplitude. For coherent flow, a phase shift of the echo amplitude is observed [245]. Motion fast enough to violate the slow motion limit requires a different experimental approach such as the analysis of the displacement power spectrum [339].

For gradient pulses which encode position according to wave number

$$k = \gamma \int_0^{t_E/2} G(t)\,dt, \tag{12}$$

the wave number q of displacement corresponding to the first order moment of the gradient modulation function from the first pulse to the first echo is given by

$$q = \gamma \int_0^{t_E} G(t)t\,dt/\Delta, \tag{13}$$

where Δ is the diffusion time (Fig. 22). For rectangular gradient pulses, one obtains $k = q$. The attenuation factors of the Hahn (Fig. 22a and d) and stimulated echoes (Fig. 22 b, e, and f) due to diffusion in pulsed (Fig. 22 a–c) and constant (Fig. 22 d–f) gradient fields are summarized in Table 2 [247]. The diffusion coefficients D can be extracted from a semi-logarithmic plot of the echo amplitude versus δ^3 or $\delta^2(\Delta - \delta/3)$ for constant gradient fields, respectively, or versus G^2 for pulsed gradient fields. For pulsed gradient fields usually the gradient strength is varied to maintain the same signal attenuation by relaxation for all echo amplitudes, while for constant gradients, δ is varied.

Table 2
Echo attenuation factors due to diffusion (cf. Fig. 22 for Δ and δ)

	Hahn echo	Stimulated echo
Pulsed gradient fields	$\exp\{-\gamma^2 G^2 D\delta^2 (\Delta - \delta/3)\}$	$\exp\{-\gamma^2 G^2 D\delta^2 (\Delta - \delta/3)\}$
Constant gradient fields	$\exp\{-\gamma^2 G^2 D\, 2\, \delta^3/3\}$	$\exp\{-\gamma^2 G^2 D\delta^2 (\Delta - \delta/3)\}$

Fig. 23a and b report some experimental data measured with the Profile NMR-MOUSE. Given the strong and uniform field gradient in the sensitive volume, diffusion coefficients from bulk fluids are conveniently measured with unilateral NMR devices by positioning beakers containing the fluids on top of the sensor [220,336,340]. The agreement between the diffusion coefficients of *n*-hexane, ethanol and methanol measured by the Hahn echo (Fig. 23d) and stimulated echo methods (Fig. 23e) is very good [336]. In the strong gradients of the Profile NMR-MOUSE, the echo attenuation by diffusion is much stronger than by relaxation, so that the influence of relaxation can be neglected in the analysis of the data. The reduced sensitivity of the Hahn and stimulated echo sequences in constant gradient fields is largely recovered by detecting the diffusion modulated, Hahn or stimulated echo with a CPMG sequence at short echo times with the added benefit of reducing the sensitivity of the detection sequence to diffusion.

In porous media, the diffusing spins experience not only the pulsed or time-invariant applied gradient field but also internal gradient fields from susceptibility differences [341]. The gradients of these fields are often referred to as background gradients, and their influence on the measured echo can be eliminated to a good degree by splitting each gradient pulse in the simple PFG-NMR scheme into a pair of anti-phase gradient pulses which sandwich a 180° refocusing pulse (Fig. 22c) [342]. This sequence is amazingly effective and has subsequently been refined for higher order corrections [343–345]. Yet these sequences are optimized for linear gradient fields. If the diffusing spins explore non-linear fields such as curved fields, the echo attenuation is more difficult to quantify in terms of the translational diffusion coefficient [346,347]. In principle it is possible to extend the elementary pulse sequence that compensates dephasing in linear gradient fields to quadratic and higher order gradient fields at the expense of extended encoding and decoding periods before and after the diffusion time [157].

On the other hand, the internal gradient fields which arise within heterogeneous samples from susceptibility differences when applying a homogeneous external field can be exploited as well to analyze pore sizes and their distributions [348–352]. As no pulsed gradient fields are applied, very short diffusion times can be probed. To measure

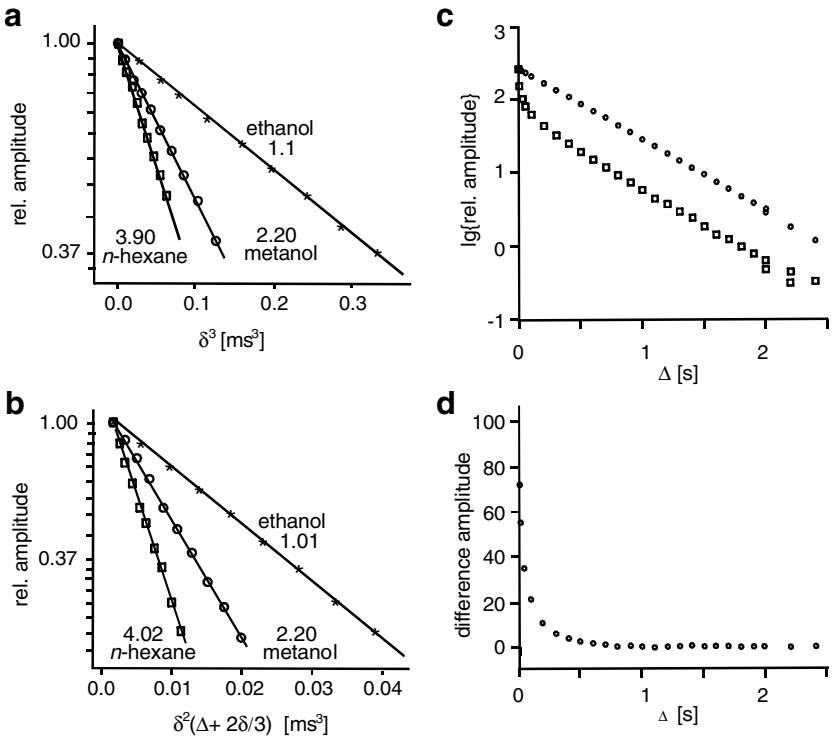

Fig. 23. Signals measured by single-sided NMR in time-invariant gradients. (a) Diffusion curves for organic liquids obtained with the Profile NMR-MOUSE by the Hahn-echo sequence with CPMG detection and extracted diffusion coefficients in 10^{-9} m^2/s [336]. (b) Diffusion curves obtained with the Profile NMR-MOUSE by the stimulated-echo sequence with CPMG detection and extracted diffusion coefficients in 10^{-9} m^2/s [336]. (c) Echo and reference signals of water measured with the sequences of Fig. 22f in the internal gradients of packed glass beads (adapted from [348]). (d) Difference signal of the curves shown in (c). It displays the effect of diffusive attenuation in the internal gradients only (adapted from [348]).

diffusion in such gradients, a stimulated echo sequence is employed with variable diffusion time (Fig. 22f). The effect of T_1 relaxation on the acquired signal is measured in a second experiment, and the signal difference from both experiments provides the echo attenuation from diffusion only [350,351]. The signals measured for water in the interstitial volume of randomly packed, 50 μm diameter glass beads are depicted in Fig. 23c and their difference is shown in Fig. 23d. The effects of internal gradients on the measured signal are less at low field [353] and can be eliminated altogether, if diffusion is probed in a $\boldsymbol{B}_1$ field gradient [354,355].

In porous media, the bulk diffusion coefficient D_0 is observed only in the short time limit. At long diffusion times, the diffusion length is restricted by the pore network structure [356,357], and an apparent diffusion coefficient D_{app} smaller than D_0 is obtained which relates to the tortuosity $\tau = D_0/D_{\mathrm{app}}$ of the medium. In the case of restricted diffusion, the apparent diffusion coefficient maps the pore size d at short diffusion times as it scales with the surface-to volume-ratio S/V according to [358,359]

$$D_{\mathrm{app}}(\Delta) = D_0\left[1 - 4/(9\pi^{1/2})(D_0\Delta)^{1/2}S/V\right]. \qquad (14)$$

Pore-size distributions can be derived by Laplace transformation of the diffusive echo decay as a function of the diffusion time. The resultant spectrum of decay-times T_{D} transforms into the distribution of pore sizes by rescaling the axis of decay times according to $d = \pi(DT_{\mathrm{D}})^{1/2}$ [351]. The extraction of the pore structure from diffusion in porous media interrogated by CFG-NMR [347,360–363] with CPMG-like sequences and by PFG-NMR [364–366] is a subject of great importance in geophysics and oil exploration.

Different methods used to measure diffusion in time-invariant gradient fields have been designed. One method with good signal-to-noise ratio is steady-state free precession [367]. Various coherence pathways are accessed by the magnetization components during a long series of many rf pulses. As longitudinal magnetization is affected differently from transverse magnetization by translational diffusion in an inhomogeneous magnetic field, the magnetization components exploring different coherence pathways are affected differently as well [368–370]. Investigation of this phenomenon has led to the design of sequences with multiple modulation multiple echoes (MMME) that use suitable cycling of the pulse phases to select particular coherence pathways [58,65,272] for fast measurements of diffusion [68,284,286] and coherent flow [72]. In combination with pulsed gradients, even the diffusion tensor can be determined rapidly [287,288]. In a novel approach to single-shot measurements in grossly inhomogeneous fields, diffusion and T_1 are encoded simultaneously in the CPMG echo shape exploring at least two different coherence pathways [285].

Early studies of diffusion by single-sided sensors with strong gradients like the NMR-MOUSE have shown, that even in curved fields with a gradient strength varying in the sensitive volume, diffusion coefficients can be determined on the basis of an effective gradient strength and used for discriminating between different materials [62,314,371]. A more accurate estimation of the diffusion coefficient can be achieved with knowledge of the $\boldsymbol{B}_0$ and $\boldsymbol{B}_1$ field profiles across the sensitive volume [372,373]. Effects of relaxation during the diffusion time can be accounted for in different ways. For example, in a stimulated echo experiment, the amplitude of the stimulated echo can be normalized to that of the Hahn echo [25,335], or the time variables in the pulse sequence are varied in such a way, that the signal attenuation by transverse relaxation does not change. This principle has been applied to the stimulated echo [374], the Hahn echo [373], and the CPMG [375] sequence.

3.4. 2D inverse Laplace transform NMR

A remarkable breakthrough in the development of NMR was the introduction of joint probability densities of relaxation times and diffusion constants in terms of two- and multi-dimensional distributions [79,80,273, 376,377]. While the principle of two-dimensional time-domain NMR for correlation of relaxation components in heterogeneous media had been known for some time [312,313], the inversion of the time-domain data to multi-dimensional distribution functions had been hampered by the lack of a suitable algorithm for rapid 2D inverse Laplace transformation [376,377], which became available in 2000 [79,378].

The basic measurement scheme is outlined in Fig. 2. An initial non-equilibrium magnetization is prepared by use of some filter [4] such as a T_1 filter, a T_2 filter, or a diffusion filter. This magnetization state is subsequently detected typically by means of a CPMG sequence either immediately following the filter sequence or following a mixing time for exchange of magnetization components. The scheme is repeated in a 2D fashion with a systematic variation of the filter parameter, which may simply be an echo time, and the resulting data set is inverted to a distribution of parameters like relaxation times or diffusion coefficients [274,379]. The intriguing part of this scheme is that it is simple, and most applications of the scheme work in inhomogeneous fields without much effort.

Some useful pulse sequences for 2D inverse Laplace transform NMR [380] are depicted in Fig. 24. As in multi-dimensional Fourier NMR spectroscopy [3], there are correlation (a and b) and exchange (c and d) experiments. Exchange experiments are characterized by a mixing time t_m during which magnetization components prepared in the evolution period exchange by coherent coupling or incoherent processes such as diffusion and cross-relaxation. These components are then identified in the detection period. Any exchange experiment becomes a correlation experiment for vanishing mixing time, and any correlation experiment can be expanded into an exchange experiment by incorporating a mixing time in between evolution and detection periods.

A simple experiment is the T_1–T_2 correlation experiment (Fig. 24a), which can also be realized with a saturation recovery filter for the T_1 evolution and a CPMG detection [79,80,274]. A constant T_1/T_2 ratio in relaxation time distributions of porous media indicates identical relaxation mechanisms in large and small pores [274]. As the measurement of T_1 is not prone to error by signal attenuation from diffusion like that of T_2, T_1–T_2 correlation maps also serve to assess the effect of diffusion in internal gradients on T_2 distributions from fluids in porous media (Fig. 25a) [79,222]. This appears to be one way to separate the signals from the wetting and the non-wetting phases of multi-component fluids such as gas, water, and oil in rocks. Another way of doing that is by means of diffusion–relaxation cor-

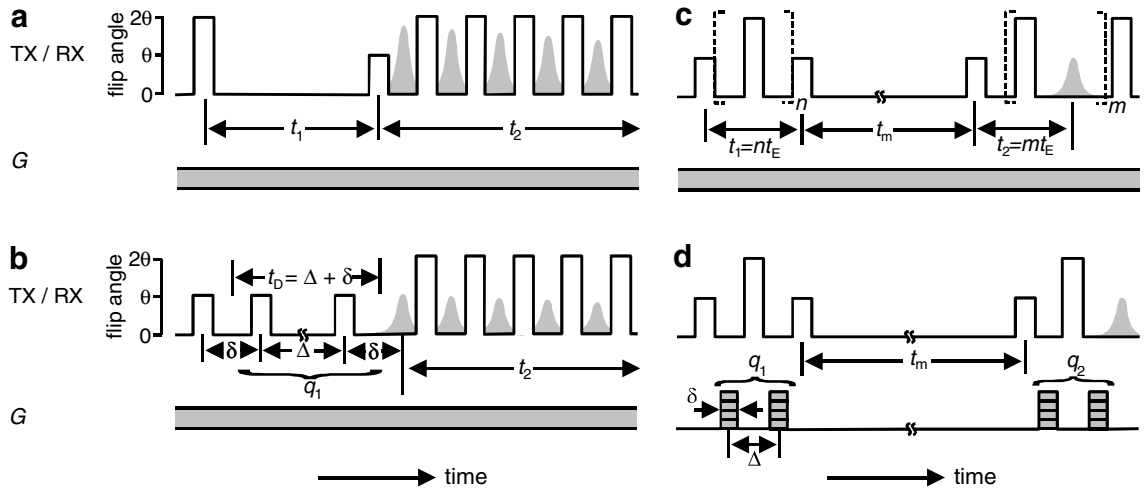

Fig. 24. Some pulse sequences for 2D inverse Laplace transform NMR. TX denotes transmitter and RX denotes receiver. (a) T_1–T_2 correlation experiment. (b) Diffusion-T_2 correlation experiment. (c) T_2–T_2 exchange experiment. (d) Diffusion–diffusion PFG exchange experiment. Schemes (a–c) refer to CFG NMR, while scheme (d) refers to PFG-NMR. CFG NMR schemes are simpler to implement on mobile devices.

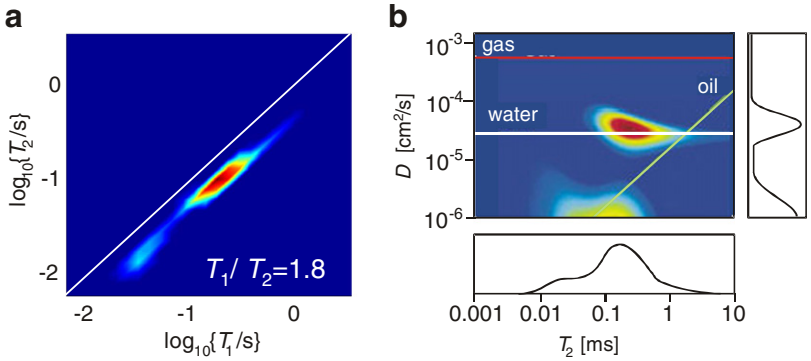

Fig. 25. Joint probability densities of fluids in rocks. (a) T_1–T_2 correlation map of water in sandstone measured with a mobile Halbach scanner by a saturation-recovery CPMG method with an echo time of 60 μs [222]. The constant T_1/T_2 ratio for all values of relaxation times reveals a uniform pore environment for small and large pores. (b) 2D D–T_2 map of a mixture of water and mineral oil in Brea sandstone together with projections along orthogonal directions that show the distributions of diffusion coefficients and of relaxation times (adapted from [273]).The water and oil signals overlap in the T_2 dimension but can be separated in the D dimension so that the water and oil saturations can be determined. The drawn lines show average correlations for gas, water and oil.

relations (Fig. 25b) [67,80,273,274,381,382]. Clearly, diffusion–relaxation correlation maps provide a direct way to study internal gradients in porous media [383,384]. As they essentially correlate translational and rotational properties of molecular dynamics, they establish a new and powerful means of identifying and separating the NMR response of mobile molecules without resorting to spectroscopic techniques. Both, the T_1–T_2 and the D–T_2 correlation experiments have been shown to provide detailed and novel insights into food such as dairy products and candy, respectively [274,385]. As the relaxation–relaxation and diffusion–relaxation experiments can be conducted in constant gradient fields, they are of great value for mobile NMR, in particular, for well-logging applications [380,381,383].

Relaxation and diffusion exchange maps are sensitive means of probing molecular dynamics on long time scales, as slowly relaxing longitudinal magnetization prevails during the mixing time t_m (Fig. 24c and d). Such dynamics may refer to translation motion in fluids such as the water transport in plants and the heterogeneity of rotational molecular motion in glassy polymers [377,379,386]. The relaxation–relaxation exchange experiment (Fig. 24c) does not require pulsed gradient fields nor is it sensitive to moderate field inhomogeneities. It has been tested first with the proton exchange between urea and water [377]. The diffusion–diffusion correlation and exchange experiments bear great promise in unraveling the pore connectivity in porous media and the anisotropic environment of fluids in ordered structures such as lyotropic liquid crystals [386] and plants [387].

3.5. Imaging

Imaging by mobile NMR involves imaging at low and inhomogeneous fields. The disadvantage is low sensitivity as the signal-to-noise ratio scales approximately with the square of the Larmor frequency. But there are also some advantages [388]: the longitudinal relaxation time T_1 decreases for many materials shortening the repetition time between scans, the relaxation time contrast improves, chemical-shift and susceptibility artifacts are scaled down, and the instrumentation becomes smaller and less expensive.

3.5.1. Depth profiling

In stray fields with strong gradients, images can be acquired with unilateral sensors by following the principles of stray-field imaging (STRAFI) [47,48,50,57,248,389]. This means, that the sensitive volume is shifted through the sample by displacing the sensor laterally [62] and in the depth direction [77,220], by changing the B_0 field profile [244], or by varying the rf excitation frequency [212]. As the shape of the sensitive volume is defined by the spatial dependence of the magnetic field, special attention has been paid to designing magnets which generate fields with uniform gradients along the depth direction over a laterally extended region. Such field profiles facilitate slice selection at well-defined depths within the object to acquire high-resolution depth profiles, that is, 1D-images along the depth direction. Examples of such sensors are the Profile NMR-MOUSE [77,220] and the GARfield magnet [211,212]. Depth resolution across the thickness of the sensitive volume can be obtained by Fourier transforming the echo shape [214,220,227].

Fig. 26a depicts the Profile-MOUSE mounted on a precision lift controlled by a step motor. The maximum slice thickness Δz which can be excited by the sensor is defined by the excitation bandwidth and the gradient strength. Structures within Δz are resolved by Fourier transforming the echo. Larger depth ranges are scanned by moving the sensitive volume across the sample depth. This is achieved by changing the distance between the sensor and the sample surface in increments of Δz and combining the partial Δz profiles into one profile as shown in Fig. 26b. Besides providing superior resolution, the procedure of shifting

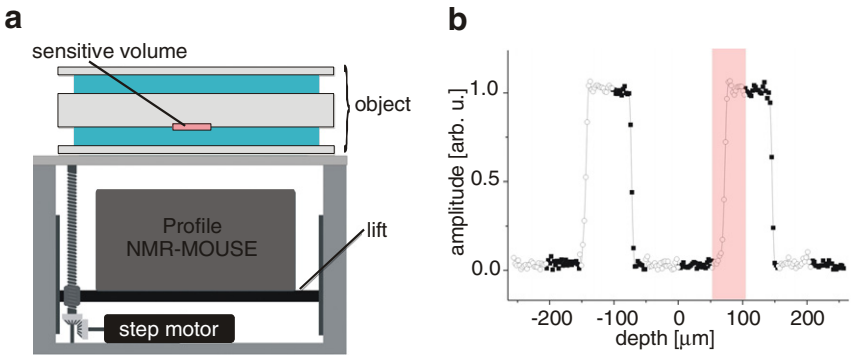

Fig. 26. (a) The Profile-MOUSE which possesses a flat sensitive volume at a given distance external to the sensor. It is useful for depth profiling. (a) The sensor is mounted on a precision lift which shifts the sensitive volume through the object. (b) Profile across two 50 µm thick latex layers separated by a 160 µm thick glass sheet. The complete profile is constructed as combination of partial profiles (open and closed symbols) covering 50 µm depth intervals. Each of the partial profiles is the Fourier transform of an echo signal.

the sensitive volume mechanically through the sample is advantageous compared to shifting it by retuning the rf frequency, as the sensitivity remains the same at all accessible depths.

3.5.2. *Slice-selective imaging in a strongly inhomogeneous magnetic field*

Lateral resolution across the sensitive volume of a stray-field NMR-sensor can be achieved by pulsing additional gradient fields [73,74,145] in phase encoding schemes (Fig. 27a) [390]. 3D images over larger distances in depth direction can so far be obtained only in strongly inhomogeneous fields by using multi-slice techniques (Fig. 27b) [76,217], that is, by scanning depth by changing the excitation frequency [76] or by mechanically moving the sensitive volume through the sample following the concept of the profile NMR-MOUSE [220]. To this end, field profiles are advantageous, that are linear in the depth direction over the full extension of the sensitive volume [200,216,217].

Sensitivity is a major issue in imaging with sensors that are characterized by field gradients of the order of 10 T/m and more, as the achievable slice thickness is limited to less than 0.1 mm which is much smaller than in standard medical imaging applications. For this reason, multi-echo acquisition is essential (Fig. 27a) along with suitable addition of echoes to enhance the total amplitude of the detected signal [75]. In this way, a factor of two to three orders of magnitude can be recovered in single-sided imaging of soft matter. But off-resonance effects due to magnetization evolving in strongly inhomogeneous fields require separate experiments to acquire quadrature echo trains of space encoded transverse magnetization [75,76]. In the more homogeneous fields of closed magnets, conventional imaging techniques can be applied [150,169,170], which may account for weak field inhomogeneity [391].

For moderately inhomogeneous fields, fast sequences for 2D [392] and 3D imaging [393] can be designed, that explore novel principles of ultra-fast multi-dimensional spectroscopy [394]. The basic concept is that the sequence accommodates the field inhomogeneities at the time of excitation of the spatially dependent magnetization components to allow for the effects that the field distortions will

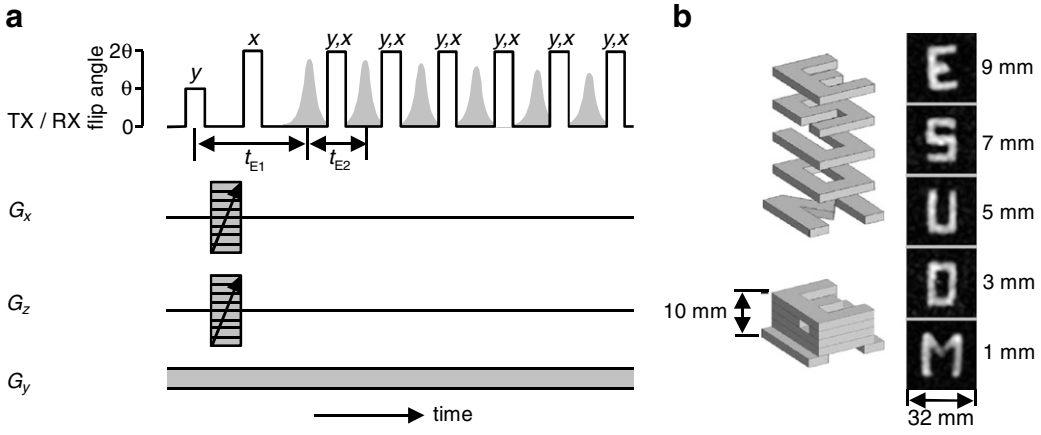

Fig. 27. Imaging in time-invariant gradient fields. (a) 2D imaging with phase encoding in x- and z-directions and with CPMG detection. All pulses are slice selective in strong gradients G_y. (b) Slice-selective images through a stack of rubber letters acquired with the tomograph of Fig. 13c (adapted from [76]). As the sensitivity decreases with depth, the number of scans per slice increases with depth. The acquisition times per slice were 45, 45, 90 and 180 s from bottom to top.

have on the detected signal, rather than correcting the field inhomogeneities themselves by shimming the magnet. This can be achieved by manipulation of the amplitudes and phases of the longitudinal and transverse magnetization components through manipulations of the rf excitation either alone [393] or aided by suitable gradient modulation [249]. The latter concept is known by the name of "shimpulses", as the excitation is chosen to stroboscopically generate a response in inhomogeneous fields corresponding to that generated by single-pulse excitation in fields shimmed to homogeneity.

The compensation of effects of field profiles deviating from linear ones relies on imparting the spins with an initial space-dependent phase. In the ideal case of a perfect field profile, the spins may be excited with a 90° rf pulse, the frequency of which is swept by changing the offset frequency in the presence of a gradient field at constant sweep rate. Then transverse magnetization will be generated at a different time at each position in the direction of the gradient. The position-dependent phases of the transverse magnetization components accumulate over the course of the sweep on account of their different excitation times and their rotation in the $\boldsymbol{B}_1$ field of the continuing rf pulse. By formation of an echo for acquisition, the spatial information of the signal is decoded in an analog fashion when recording the data in the presence of an acquisition gradient. Known, non-linear field profiles that arise in arbitrarily inhomogeneous fields can be accommodated in this scheme by simply introducing, for example, a time-dependent excitation rate or off-set modulation of the rf excitation. This basic concept can be applied in different ways and in two and three dimensions for spectroscopy as well as for imaging. For example, k-space can be scanned in a single shot in parallel traces, zig-zag, and spiral traces [393].

3.5.3. Imaging at ultra-low field

Ultra-low magnetic fields are less expensive and simpler to generate than high fields. But conventional NMR at micro-Tesla fields suffers from a lack of sensitivity. This can be recovered by hyperpolarization of nuclear spins [395], or detectors such as super-conducting quantum interference devices (SQUIDs) [396–398], and optical detectors [102] which are more sensitive than regular coils, or by the combined use of both [399]. At ultra-low fields, the field distortions from susceptibility differences become so small that distortion-free NMR images can be acquired even in the presence of conducting metal, and the skin depth becomes large enough that with a low rf excitation frequency, NMR images can be acquired even through an aluminum beverage can [400]. But at such low fields, the gradient field may be of the same order or even higher than the polarization field, so that the gradient field tensor can no longer be truncated to a vector, and imaging schemes need to be designed, that account for the full tensor field of the gradient coils [401] by either eliminating or correcting for the so called concomitant gradients [402,403] or by making use of them [404]. In the Earth's magnetic field, this issue may be ignored, and simple mobile equipment developed, that uses prepolarization of the object by an electromagnet together with experimental conditions that accommodate the temporal fluctuations in the magnitude of the Earth's magnetic field [405].

3.6. Velocity measurements

Velocity images and velocity distributions can be measured in strongly inhomogeneous magnetic fields similar to measurements of displacement by diffusion (Section 3.3). Displacement by coherent flow can be encoded with a stimulated echo in constant gradients (cf. Fig. 22e) [406], and the Cotts sequence can be employed for phase encoding by pulsed field gradients according to Eqs. (12) and (13) in the presence of time-invariant background gradients (Fig. 28a, cf. Fig. 22c) [77,78]. The signal is preferably detected directly with a CPMG sequence at short echo time.

The depth direction y is resolved in a multi-slice approach, as each excitation pulse is selective in the strong gradients of the sensor. Similar to imaging in strong gradients, artifacts from off-resonance excitation are cancelled by detecting both quadrature components of the transverse magnetization in separated experiments and by suitable phase cycling. In each slice, the velocity distribution can readily be measured by acquiring the CPMG signal for different values of the velocity encoding gradient G_v (Fig. 28b). Each slice produces a different distribution. For laminar flow through a circular pipe, the sum distribution reproduces the familiar hat function. A grey-scale representation of the stacked distributions provides a velocity image along the depth direction y.

Lateral resolution is obtained by pulsing a further gradient G_r along a direction parallel to the sensor surface. In combination with multi-slice imaging in the depth direction, a 2D image of a velocity component such as v_x is obtained (Fig. 28c). To speed up the measurement, an average velocity component can be determined in a single phase-encoding step at the expense of gathering information about the velocity distribution in many phase encoding steps. The orthogonal cross-sections through such an image (Fig. 28c) reveal good agreement of the measured velocity profiles with the theoretical, parabolic ones.

A fast method for measuring flow in the presence of a static field gradient has been developed based on the analysis of signals from selected coherence pathways by multi-echo excitation [72]. Because all coherence pathways are resolved in the time domain by multiple modulation multiple echoes from suitably adjusted pulse separations, there is no need to use repetitive scans for phase cycling, and the method is a true one-scan experiment. The same approach can be used to measure the velocity vector in a single scan [289].

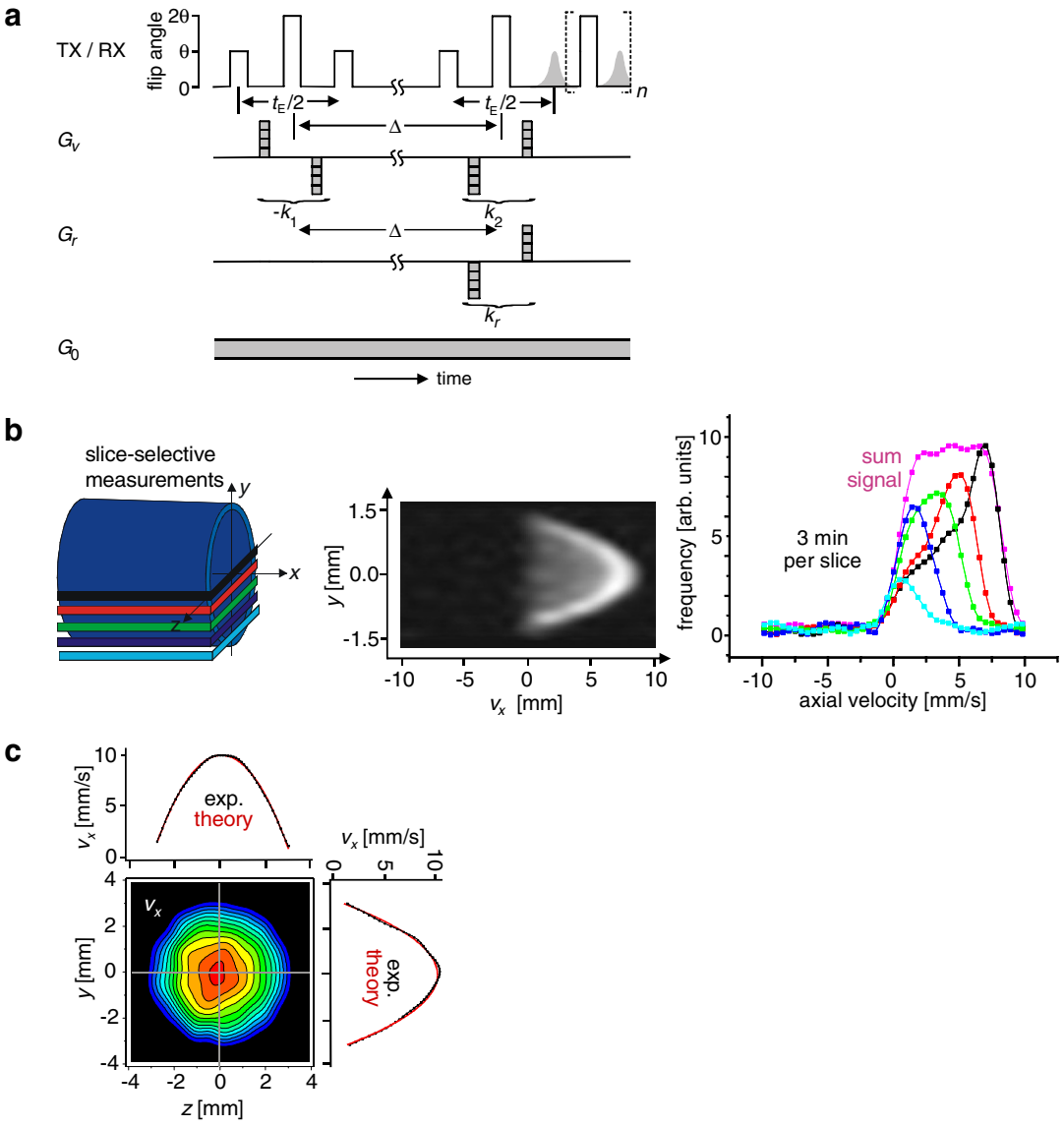

Fig. 28. Velocity images and velocity distributions for laminar water flow through a circular pipe measured with a single-sided NMR tomograph (cf. Fig. 13c). (a) Pulse sequence for measuring coherent flow in time-invariant background gradients with CPMG detection. The space-encoding gradient G_r provides lateral resolution in the z direction parallel to the sensor surface. Spatial resolution in the depth direction y is achieved by multi-slice imaging. The pulsed gradients G_v encode displacement. (b) Slice-selective velocity distributions in a 3 mm diameter pipe measured with $G_r = 0$ by stepping the velocity-encoding gradients G_v. Each slice produces a different distribution. The sum distribution reproduces the familiar hat function for the velocity distribution of laminar flow through a circular pipe. A grey scale representation of the stacked distributions provides a 1D velocity image in the depth direction y. (c) 2D transverse velocity image of flow through a 6 mm diameter pipe measured with a single phase encoding step of velocity. The orthogonal cross-sections through the image compare the measured velocity profiles with the theoretical, parabolic profiles.

3.7. Spectroscopy

Portable and open NMR magnets are convenient tools for non-destructive inspection of valuable objects from which samples cannot be drawn. However, the convenience is bought at the expense of magnetic field homogeneity that affords high chemical-shift resolution in conventional NMR. Spectroscopic resolution concerning bilinear spin interactions such as dipolar and quadrupolar splittings in solids can be obtained in strongly inhomogeneous magnetic fields as the Fourier transform over the envelope of a series of Hahn echoes as has been demonstrated with the NMR force microscope [162]. But the possibility to access chemical information seemed impossible for more than four decades because the field variations across objects outside a magnet are usually orders of magnitude larger than those created by the structure of the molecules to be detected. Several attempts to recover high-resolution spectra in inhomogeneous magnetic fields can be found in the literature. Encouraged by the fact that the Hahn echo is modulated by the homo-nuclear indirect coupling in fields sufficiently inhomogeneous to obscure the chemical-shift [407], multiple-quantum coherence transfer echoes have been explored to gain access to spectroscopic

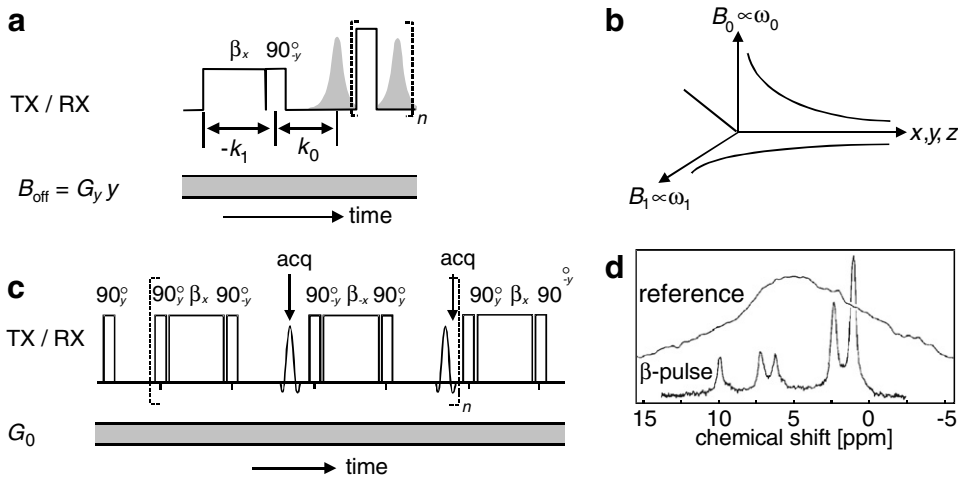

Fig. 29. Chemical-shift resolved spectroscopy by field matching. (a) Mixed echo with a dephasing period in the $\boldsymbol{B}_1$ field and a rephasing period in the $\boldsymbol{B}_0$ field. It maintains the chemical-shift information in the echo maximum and is preferably detected indirectly via a CPMG train. (b) In the absence of spatial resolution, field matching requires the perpendicular components of $\boldsymbol{B}_0$ and $\boldsymbol{B}_1$ to show the same proportionality across the sensitive volume. (c) Pulse sequence to generate a series of mixed echoes in the presence of matched $\boldsymbol{B}_0$ and $\boldsymbol{B}_1$ fields. The echo maxima are sampled as a function of the pulse length β. (d) High-field, 180 MHz, ^{1}H NMR spectrum of trans-2-pentenal acquired in a deshimmed magnetic field by single-pulse excitation and the β-pulse technique *c* (adapted from [82]).

resolution [408,409]. They take advantage of the fact that the total spin coherence of order p_{max} evolves only under the Zeeman interaction, while coherences of lower order $p = \Delta m$, where m is the magnetic quantum number, experience the field inhomogeneity $\Delta \boldsymbol{B}_0$ across the sample as $p\,\Delta \boldsymbol{B}_0$. Echoes involving different coherence orders in the dephasing and rephasing periods can be combined to cancel the effect of field inhomogeneity. A related approach explores inter-molecular multi-quantum coherences [410,411]. High-resolution spectroscopic information can be obtained as long as the field variations can be neglected over a length of about 10 μm of the dipolar correlation [412–414]. This and the low signal amplitudes, however, have so far prevented application of the approach to single-sided and to low-field NMR.

A brute-force approach is to reduce the sample size relative to the magnet size. An extreme example is Earth's field NMR which can provide milli-Hertz resolution [94]. Another concept is hole-burning, which somehow makes use of the combination of both, restriction of the sensitive volume and spin manipulation. This has been utilized in a clever way to obtain high-resolution spectra of solute molecules interacting with solvent molecules by the nuclear Overhauser effect [415]. Only the solute spins interacting with the solvent molecules at the narrow frequency range of the hole are measured. Unfortunately, these approaches to high-resolution NMR in inhomogeneous fields are limited to a particular class of systems, and are not suited to use at low field.

3.7.1. Field matching and ex situ NMR

A breakthrough in the development of NMR spectroscopy in inhomogeneous magnetic fields was the discovery, that the mixed echo, which is generated by combining an evolution under nutation of the magnetization in the $\boldsymbol{B}_1$ field with precession in the $\boldsymbol{B}_0$ field [416], preserves the chemical-shift information [82]. The pulse sequence (Fig. 29a) involves an extended rf pulse of duration β for nutation of the transverse magnetization about the x axis of the rotating frame to build up a magnetization helix, followed by reorientation of the magnetization helix along the z axis with a subsequent unwinding of the helix. With reference to Fig. 15b and linear gradient fields for $\boldsymbol{B}_1$ and $\boldsymbol{B}_0$, the helix is characterized by a wave number k_1 for the nutation in the $\boldsymbol{B}_1$ field and a wave number k_0 for the precession in the $\boldsymbol{B}_0$ field. The mixed echo forms at the time, when the condition $k_1 = -k_0$ is fulfilled. If $\kappa = k_1/k_0$ and τ is the duration of the β pulse, the echo is formed at an evolution time $\kappa\tau$ in the $\boldsymbol{B}_0$ field. As the echo condition must be fulfilled at all positions within the sensitive volume to observe the maximum echo amplitude, each vector component of the $\boldsymbol{B}_1$ field must show the same proportionality to its corresponding vector component of the $\boldsymbol{B}_0$ field (Fig. 29b). This concept of field matching can be extended from linear correlations to non-linear ones, as long as there is a one-to-one mapping of the $\boldsymbol{B}_1(\boldsymbol{r})$ and $\boldsymbol{B}_0(\boldsymbol{r})$ fields over an appreciable volume of the sample (cf. Fig. 30c) [417,418]. The key point of the sequence is that the chemical-shift is not resolved for the precession of the magnetization in the $\boldsymbol{B}_1$ field but only for the precession in the $\boldsymbol{B}_0$ field. This modulates the phase of the echo maximum by the effective chemical-shift evolution for a period $\kappa\tau$. A pseudo-FID is acquired by sampling the echo maxima as a function of $\kappa\tau$ by incrementing either κ or τ from echo to echo in a repetitive fashion (Fig. 29a) in a multi-echo train (Fig. 29c), and the Fourier transform of the stroboscopically sampled echo maxima is the chemical-shift resolved NMR spectrum (Fig. 29d).

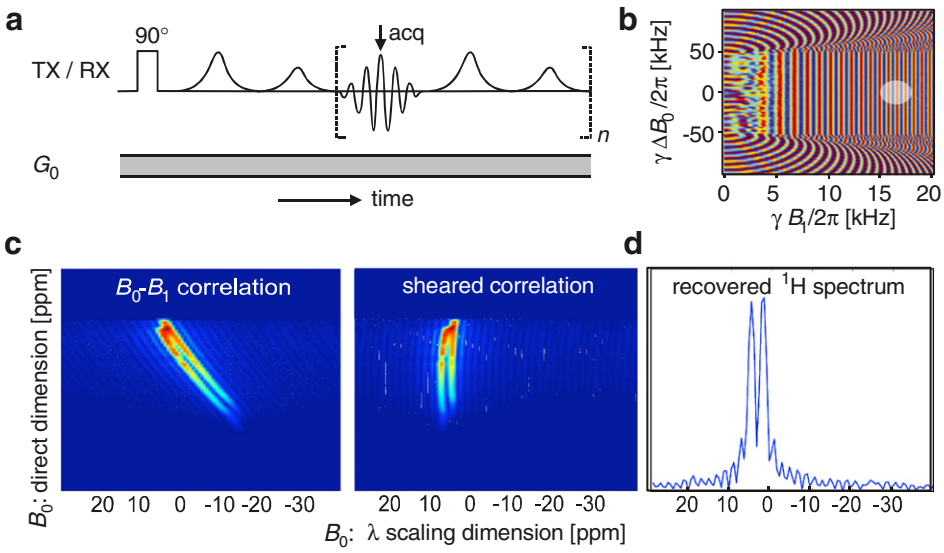

Fig. 30. *Ex situ* methodology for high-resolution NMR in inhomogeneous fields. (a) Broad-band, double adiabatic passage on transverse magnetization (bell-shaped pulses). The stroboscopically sampled echo contains the chemical-shift information. (b) Transverse component M_x of the magnetization in a sample of uncoupled spins 1/2, generated by the double-passage technique as a function of B_0 and B_1 offset. A wide region of off-set independent phase modulation is obtained as a function of the offset from resonance of the central frequency of the sweep and the peak amplitude of the first pulse with the second pulse adjusted to half that value ($\lambda = 0.5$, adapted from [422]). The light region marks the region accessible by composite z pulses. (c) The spectra of the acquired signal as a function of the acquisition time and the scaling factor λ are correlated in this region (adapted from [420]). (d) High-resolution 1D spectrum extracted from the 2D data set (adapted from [420]).

The pseudo-FID decays with a characteristic time, which converges to T_2 in the ultimate case of perfect matching between **rf** and static gradients. While in conventional NMR spectroscopy the characteristic decay time T_2^* of the FID is determined by the quality of shimming $\boldsymbol{B}_0$ to homogeneity, in this case it is determined by the quality of shimming $\boldsymbol{B}_0$ and $\boldsymbol{B}_1$ to match their profiles in 3D space. This condition imposes a constraint on both $\boldsymbol{B}_0$ and $\boldsymbol{B}_1$, while conventional NMR can deal with slight $\boldsymbol{B}_1$ inhomogeneities and constrains only $\boldsymbol{B}_0$.

The field matching technique can be extended to multidimensional NMR spectroscopy [240], and it has been shown to be suitable also for measurements of diffusion by using a pair of mixed echoes [419]. Since Meriles et al. [82] first reported this method the general approach to NMR with simple instruments producing inhomogeneous fields has evolved to the understanding of being a hierarchical one consisting of different steps. This philosophy is known as *ex situ* NMR [85,420], a name that, for historical reasons, refers to NMR with the sample outside the magnet. These steps comprise (a) optimization of the $\boldsymbol{B}_0(\boldsymbol{r})$ and $\boldsymbol{B}_1(\boldsymbol{r})$ fields to suitable but not necessarily homogeneous profiles; (b) fine tuning by the use of electronic shims; (c) spin manipulation by rf excitation together with gradient field manipulations.

In an inhomogeneous $\boldsymbol{B}_0$ field, the nuclear Larmor frequencies are distributed over a wide range. Any spin manipulation should affect as many of these spins as possible to boost the sensitivity through a large sensitive volume. One promising way of manipulating spins over a broad range of frequencies is by using the full adiabatic passage through resonance [421] by which an inversion of the longitudinal magnetization is achieved, independent of the strength of the $\boldsymbol{B}_1$ field, as the longitudinal magnetization follows the effective field. If such a field sweep is applied to transverse magnetization, the magnetization components will continue to precess around the effective field during the sweep. In a double passage with different B_1 amplitudes for each passage, the magnetization components will experience a phase shift determined by the B_1 amplitude of the first sweep and the amplitude ratio λ between both sweeps over a broad range of offsets of the Larmor frequency from the center frequency of the passage (Fig. 30a) [422]. The region accessible to excitation-dependent phase manipulation of the spins is much larger than the one that could be covered by z-pulses, that is, by composite pulses which perform rotations around the axis of the $\boldsymbol{B}_0$ field with compensation of $\boldsymbol{B}_0$ and $\boldsymbol{B}_1$ inhomogeneities (Fig. 30b) [423]. The spectra of the acquired echoes as a function of the acquisition time and the scaling factor λ are correlated in this region (Fig. 30c), and a high-resolution 1D spectrum can be extracted from the 2D data set (Fig. 30d) [418,420].

A further improvement in spectroscopic resolution can be obtained by extending the concept of uniform broad-band excitation to an excitation which adjusts for residual magnetic field imperfections by prescribing an individual phase to each magnetization component so that the phase acquired by evolution in a homogeneous magnetic field is obtained stroboscopically at the observation points. This corresponds to shimming the spins instead of shimming the magnet and can be realized with so-called shim-pulses (Fig. 31a and b) [249]. Such pulses constitute the most general form of NMR excitation. They require phase and

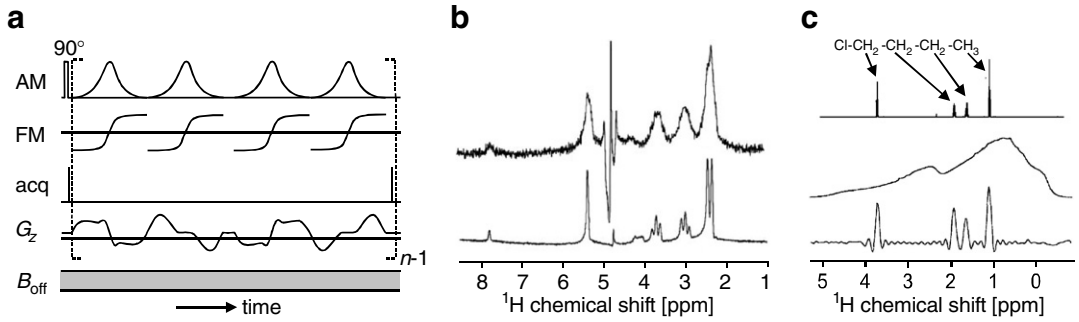

Fig. 31. High-resolution NMR-spectroscopy in inhomogeneous fields by manipulation of the spins. (a) Shim pulse designed from adiabatic sweeps through resonance with modulation of the pulse amplitude (AM), the pulse frequency (FM), and the gradient G_z in the z direction. The data are acquired stroboscopically similar to multi-echo NMR (adapted from [249]). (b) ^{1}H NMR spectra of vitamin B_1 in ^2H_2O acquired in a magnetic field with linear profiles in the x and y directions without (top) and with (bottom) the shim-pulse method (adapted from [249]). (c) ^{1}H NMR spectra acquired at 11.75 T in a homogeneous field (top), in a homogeneity spoiled field (middle), and with phase-adjusted, spatially encoded rf excitation pulses (bottom, adapted from [424]).

amplitude modulation of the rf excitation together with a modulation of the gradient tensor.

A related approach makes use of the segmentation of the probe volume into different compartments together with excitation by frequency-swept pulses in the presence of modulated gradients [424,425]. The magnetization of each compartment is modulated in a way to account for the known field inhomogeneity by a different evolution time t_1 so that the entire spectrum can subsequently be detected in a single scan (Fig. 31c).

The shim-pulse and rapid-encoding methodologies have also been demonstrated to be applicable to spectroscopic imaging [230,420] and self-diffusion measurements [426]. In fact, conventional spectroscopic imaging is a very straight forward way to arrive at high-resolution spectra in weakly inhomogeneous fields by adding the spectra acquired for each phase-encoded voxel of the sensitive volume [427]. A far more demanding issue is the narrowing of lines broadened by tensorial spin interactions with singe-sided NMR tools. A principal but not necessarily practical way is to rotate the field and not the sample about the magic angle [428–430]. As only angles more shallow than the magic angle can conveniently be accessed by single-sided devices, schemes with rotations away from the magic angle are of interest. It has been shown, that projections across 2D correlations of spectra acquired at different rotation angles reveal the isotropic and anisotropic line shapes [431,432]. This constitutes one route towards high-resolution solid-state NMR spectroscopy by single-sided devices. In the end, combinations of different approaches are likely to produce the best results just as combined multi-pulse excitation and magic-angle spinning does in conventional high-resolution, homo-nuclear, solid-state NMR spectroscopy [433].

The *ex situ* methodology applies to high-resolution NMR spectroscopy of both liquids and solids by simple, mobile NMR devices, with open and closed sensor geometries. It had largely been developed at high field with superconducting magnets and a continuous current was used in one of the gradient coils that generated a static gradient field to approximate the field inhomogeneities found in open magnets. Although such a set-up is extremely useful for testing a new technique, its implementation on open, low-field sensors presents several additional challenges. To quantify how close the high-field conditions are to those anticipated in single-sided sensors, one may consider the field strength and the magnitude of the gradient. The spectrum of Fig. 29d was measured with $\gamma B_0/2\pi = 180$ MHz and $G_0 = 0.012$ T/m [83], while $\gamma B_0/2\pi = 8$ MHz and $G_0 = 2.5$ T/m apply to the open tomograph with which the images in Fig. 27b have been measured [76]. Taking into account that the frequency difference associated with the chemical-shift is proportional to the external field and that the line width defined by the mismatch between the rf and the static magnetic fields is proportional to the gradient strength, the spectroscopic resolution is proportional to the field strength and inversely proportional to the gradient. Given the same matching quality as in [82], the spectroscopic resolution attainable with the open tomograph would be 4600 times lower. Furthermore, contrary to the high-field test case, the stray magnetic field of a single-sided sensor varies not only in magnitude, but also in direction.

While the initial idea for matching focused on shaping the $\boldsymbol{B}_1$ field to match the known inhomogeneity of the $\boldsymbol{B}_0$ field, it turned out to be more efficient to match the $\boldsymbol{B}_0$ field to an optimized $\boldsymbol{B}_1$ field by varying the geometry of a shim unit from permanent magnets (Fig. 32a). Here "shimming" is used in the general sense of "matching" a given field profile and not in the special sense of adjusting to a perfectly homogeneous field profile. To boost the sensitivity, the individual mixed echoes were acquired indirectly with a CPMG sequence for direct detection (Fig. 29a). Addition of the echoes [76] reduced the measurement time by a factor of 500. The performance of the method was tested by measuring different fluorinated compounds in a capillary sample tube 1 mm in diameter and 3 mm long. Within a measurement time of a few minutes, ^{19}F spectra could be acquired with a resolution of 8 ppm (Fig. 32b) [81,158].

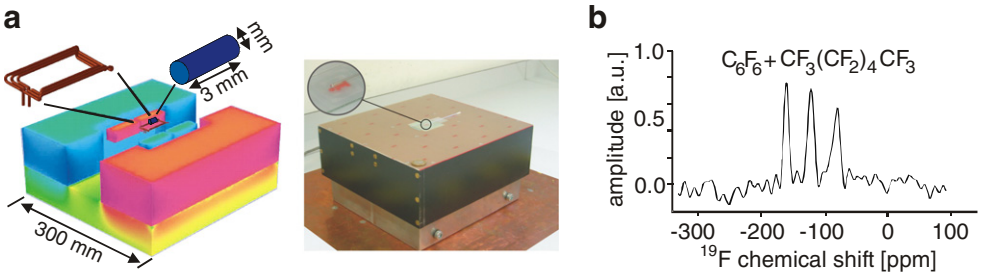

Fig. 32. Single-sided chemical-shift resolved NMR spectroscopy by matching $\boldsymbol{B}_0$ and $\boldsymbol{B}_1$ profiles [78,81]. (a) The field matching was achieved by adjusting the shape of the rf coil and the field profile of the magnet. (b) A high-resolution, 8 MHz, ^{19}F spectrum was obtained in this way from fluids contained in a capillary positioned in the region of matched fields over the sensor.

While this work demonstrated the feasibility of measuring chemical-shift resolved spectra with a single sided sensor at low field, the sample size was artificially restricted to remain within the volume of matched fields.

3.7.2. Spectroscopy in a highly homogeneous magnetic stray field

Magnetic fields generated by open magnets are believed to be inherently inhomogeneous. This perception is at the root of designing the ingenious *ex situ* methodology based on the formation of mixed nutation echoes [83], shim pulses [249], and the like [424] for use in high-resolution NMR in inhomogeneous magnetic fields. However, this assumption is misleading as was demonstrated recently by shimming the magnetic stray field in a limited region external to the magnet to a homogeneity of a few parts in 10^7 sufficient to measure chemical-shift resolved ^{1}H NMR spectra of liquids [89]. Conventional NMR magnets, which enclose the sample, are equipped with shim coils to adjust the polarizing magnetic field to extreme homogeneity for narrow lines in the NMR spectrum. The straightforward adaptation of this approach to shimming the stray field of a single-sided sensor must be discarded simply because of excessive requirements for the shim currents. However a current loop of 1000 A can be replaced by an approximately 1 mm thick NdFeB permanent magnet block, and single-sided shim unit can be constructed simply by a suitable arrangement of such magnet blocks. In fact, the current distribution needed for electrical single-sided shims can be replaced by pairs of magnet blocks with opposite polarization, suitably arranged with respect to the main magnet. In this way, the stray field of a conventional u-shaped, single-sided magnet has been adjusted by means of a simple shim unit, which generates eight shim components (Fig. 7g) [89]. Supplementary shimming is achieved by three single-sided coils that generate additional x, y and z gradient fields for fine tuning which are not shown in Fig. 7g.

The magnetic fields generated either by conventional closed magnets or by the open sensor presented here possess the required degree of homogeneity only in a limited volume. In conventional NMR, this limitation is often not important simply because the sample size is restricted

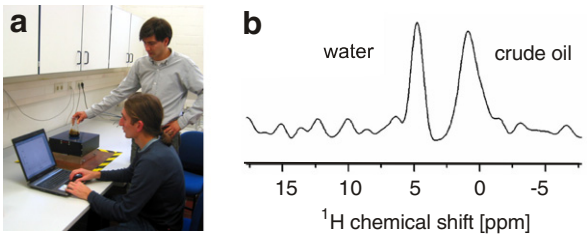

Fig. 33. High-resolution spectroscopy by single-sided NMR. (a) The fluid is placed in a beaker on top of the sensor. (b) Chemical-shift resolved, 8.33 MHz, ^{1}H NMR spectrum of water and crude oil measured in a few seconds.

to fit into this volume, but the main motivation for single-sided NMR is to investigate arbitrarily large samples (Fig. 33a). Hence, the sensitivity of the sensor must be limited to the region of homogenous field. This is achieved using a soft 90°-pulse for slice-selective excitation in the presence of a pulsed gradient field.

For the sensor depicted in Fig. 7g, the volume selected inside the object measures 5×5 mm^2 in the lateral directions and 0.5 mm across. It is situated 2 mm above the rf coil surface. The line-width obtained was 2.2 Hz, corresponding to a spectral resolution of about 0.25 ppm. This is better by a factor of 30 than the resolution obtained by field matching. At the same time, the sensitive volume could be enlarged by a factor of 5 with an associated increase in sensitivity. The sub ppm resolution of the single-sided sensor is sufficient to resolve a number of molecular structures including the peaks of water and crude oil (Fig. 33b) [89]. From the line integrals, the water/oil ratio can be quantified, a result of interest for use in well-logging in the oil industry. Given the homogeneous field of this sensor, the complete and well elaborated methodology of NMR in a homogeneous field can be applied for non-destructive testing, including sophisticated multidimensional schemes.

The availability of high-resolution spectroscopy to portable, single-sided NMR opens the door for new applications. ^{1}H spectroscopy can be employed, for example, for non-invasive screening of molecular composition, control of chemical reactions, and the identification of target compounds. An interesting figure of merit in the further development of single-sided NMR sensors is the ratio of the accessible sample volume and the total volume of the

sensor. A common goal of different ongoing research activities is the development of hardware and methods of mobile NMR to achieve a high value of this figure. The *ex situ* NMR methodology provides a number of novel concepts along this way.

3.7.3. High-resolution NMR with portable, closed magnets

Apart from open magnets for non-destructive testing, small and closed magnets are being developed for applications demanding high sample throughput or instrument mobility. Magnetic fields up to two Tesla can readily be produced with small permanent magnets to resolve the spread in chemical-shift. An ingenious way to arrange permanent magnets to generate multi-polar fields either inside or outside a magnet array is due to Halbach [86] who subsequently extended his original concept of ring-shaped magnet arrays to flat magnet arrays [218]. This concept has become popular in mobile NMR as such magnet arrays are inexpensive and comparatively easy to manufacture [88,434–436]. Several studies have been published describing the optimization of the production and homogeneity of such magnets [222,437–440]. As the magnetic field of a dipolar Halbach magnet can be made zero outside and transverse to the axis inside, simple solenoids can be used as rf coils. If magnets with a hexagonal cross-section are used, a space filling array can be produced from identical, discrete elements. The most simple dipolar Halbach magnet that can be manufactured from such hexagonal bar magnets is depicted in Fig. 34a and b. Given regular NdFeB material, fields of about 1 T can be produced with fist-size arrays. Several such rings from hexagonal or quadratic bar magnets can be aligned with optimized gaps to improve the axial homogeneity. Also other small magnets are now becoming available for NMR spectroscopy (Fig. 34c) [441]. The field homogeneity required for good spectral resolution and low-power operation can be achieved with micro-coils that limit the spatial extent of the sensitive volume and with it the width of the effective field distributions. For example, a ^{1}H NMR line-width of 2.5 Hz has been obtained in this way at 44 MHz from a water-filled capillary surrounded by a 0.55 mm diameter solenoidal rf coil at 0.25 mW rf power for a 200 μs 90° excitation pulse with a signal-to-noise ratio of 137 in a single shot with a magnet similar to that shown in Fig. 34c [441]. As an example, Fig. 34d shows the ethanol spectrum acquired in about 6 min [442]. The novel aspect here is that the hardware is small, simple, and inexpensive, making NMR technology available to a variety of new applications where conventional high-field instruments are out of question.

4. Applications

Mobile NMR was initially driven by the need for NMR well-logging [11–13,53] which today is the most important area of application [5,175,382,443–446]. The development of mobile NMR equipment for well-logging NMR went hand in hand with the development and application of NMR for process and quality control [26,27,29,32,125–127,131,135–138,150,447,448] with product streams passing the NMR sensor [16,30,125,127,449–451]. Such a set-up is closely related to early approaches to NMR imaging in real space with sensitive-point methods [4,452,453], where an NMR image was composed of grey-scale values derived from NMR signals acquired separately for each voxel. In fact, the old FONAR (field-focusing nuclear magnetic resonance) imaging method required the patient to be physically repositioned through the sweet spot of the device [454]. The concept of a sweet spot implies good field homogeneity within the sensitive volume. Inside-out or unilateral NMR devices with such a sweet spot are preferably applied to measure moisture in building materials [19,24,42,129], soil [19,20,22,23,129] and food [27,455], as low gradients reduce signal attenuation by translational diffusion, which is commonly perceived as undesirable. On the other hand, various methods of imaging of solids [4,156,456–460] including stray-field imaging [50,51,212] have shown that solid matter can be investigated in strong field gradients with a broad range of different contrast features [461–463]. This observation gave rise to the development of unilateral NMR sensors with high gradients, such as the NMR-MOUSE and also the GARfield magnet [209–211]. Such high-gradient NMR devices opened up a diverse range of new applications. As stray-field NMR by the

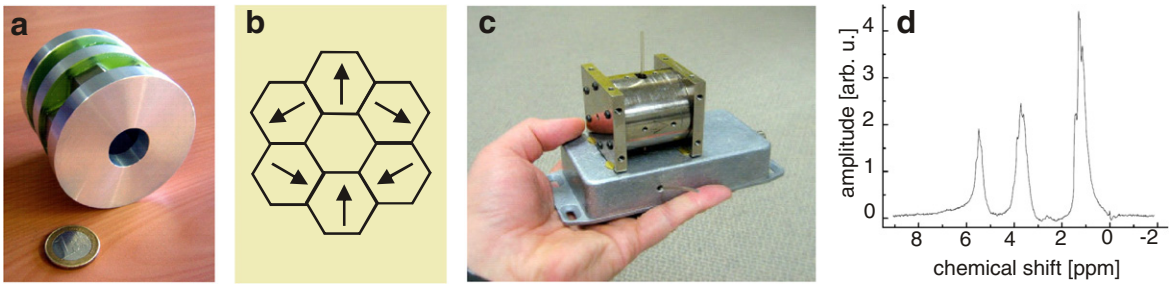

Fig. 34. Closed magnets for mobile NMR. (a) Halbach magnet built from identical bar magnets with hexagonal cross-section. (b) Orientation of the magnets to produce a homogeneous field inside the Halbach array transverse to the main axis. (c) Portable 2 T miniature magnet for NMR spectroscopy with outer dimensions of about (5 cm)^3 [442]. (d) Ethanol spectrum acquired at 44.2 MHz in 64 scans with a magnet related to the one shown in (c) (adapted from [441]).

GARfield technology is essentially applied in the laboratory to thin films and has been exhaustively reviewed elsewhere [212] it is addressed only partially in the following.

Mobile unilateral NMR sensors are suitable for a variety of applications in materials testing [4,121,156,464], in particular of rubber [126,464–467], and other polymer products, such as solid polymers [301,315,468]. The use of such sensors [42] had been published before in the context of inspecting solid rocket motor bond-lines nondestructively [469–471]. More recently, the mobile inside-out NMR technology has been complemented by mobile outside-in magnets [88,434,435] which bear great promise for analysis of cylindrical objects such as geophysical drill cores [222,434,472,473], of food produce and other objects on conveyor belts passing through the magnet [150,155,474], and of capillaries bearing fluids for chemical analysis by nano-liter spectroscopy [441]. Today, applications of mobile NMR are found, for example, in the analysis of food [136,314,455,475,476], biomedical diagnostics [216,468,477,478], the inspection of rubber [132,133,216,241,276,457,467,468,478–480], polymer products [301,477,481–483], and objects of cultural heritage [276,484–491], in investigations of porous media [25,145–148,241,335,492], and as sensors in testing laboratories and manufacturing plants. Novel applications are continuously being explored. The steady progress in NMR technologies at low magnetic field in terms of polarization enhancement and detection sensitivity and in terms of unconventional NMR methods that address the issues of field inhomogeneity and field stability are strong indicators of mobile NMR becoming a more common method of instrumental analysis in the future [14,120,275,493,494].

4.1. Food

Analysis and quality control of food is an important application area for NMR [150,495,496]. For example, NMR spectroscopy has been shown to reveal the composition and origin of fatty acids and their derivatives like olive and hazelnut oil [497], and of beverages like wine [498]. Low-field desk-top NMR is a validated method for determining the fat content in seeds [499] via the spin–echo amplitude at a specified echo time according to international standards [500]. Different 1D methods of time-domain NMR without and with diffusion weighting are used for example to determine the fat content in meat [501], the solid/liquid content in fats and oils [502], the droplet-size distribution of emulsions [136,503,504], the maturing of fruit and vegetables [505], and to study the baking process of bread [506]. While a single- or multiple-point analysis of the free induction decay or echo envelope has been the routine approach in the past, multivariate methods of analysis following chemometric principles improve the discrimination accuracy among similar samples [497,501,506,507].

Free water and oil are difficult to separate in 1D measurements as their relaxation times do not differ much unless diffusion weights are applied [455,503] or 2D methods are employed that correlate distributions of relaxation times and diffusion coefficients [274,385,508]. Such 2D methods show great promise in studies of sweets and dairy products and their aging. Internal magnetic field gradients in plant-based materials are sufficiently strong to affect the signal decay in measurements of the self-diffusion coefficient and can be utilized to assess the cell structure [509].

The merits of low-field time-domain NMR with desk-top instruments are low-cost [168,266,267], simplicity [32,155,436] and high accuracy. However, as samples need to be withdrawn, packaged food, intact plants, and process control are largely excluded from such an analysis unless strategies related to imaging are employed. Low-field NMR methods including the NMR-MOUSE [510] find application in monitoring and optimizing the processing of complex food stuffs [26,27,251,507,511] as well as the detection of foreign bodies [512]. Heterogeneous foods such as chocolates, fruit, vegetable, and fish are investigated by imaging for effects of ripening, storage, freezing, thawing, and cooking and baking [86,150,513–519]. More recently, mobile imagers have been designed to analyze food produce in the field, on the farm, or in the factory [150,168,496,516]. Stationary magnets have been built with product streams such as boxed yogurt containers passing through [32,474]. Each box is analyzed in an imaging mode by placing one voxel into each container in the box. The current voxel contrast is referenced against a moving average so as to identify containers with spoiled food [474]. Although moving samples pose new challenges to NMR, sample translation relative to the sensor through a region with time-invariant rf excitation provides a simple way to generate transverse magnetization and leads to more simple and robust instrumentation [155].

The concept of placing one voxel into the container for analysis is essentially also followed in measurements with single-sided sensors as they measure through the packaging into the product or through the shell into the produce [214,520,521]. As the sensitive volume is smaller than with desk-top instruments, the signal-to-noise ratio is smaller. Nevertheless, accuracies of 1% and better can be obtained in measurement times shorter than one minute. High-gradient devices like the NMR-MOUSE introduce a diffusion weight into the CPMG signal decay, which inverts the contrast between water and oil. In a homogeneous field, the FID from oil relaxes faster than that of water (Fig. 35a), while in a strong field gradient, the CPMG envelope of water decays faster than that of oil due to faster diffusion (Fig. 35b). This diffusion weight makes the NMR-MOUSE a suitable instrument for quantifying the oil/water ratios (Fig. 35c) [455,475]. The diffusion weight is also important when characterizing damage to the cell structures in plant material [314,509]. The envelope of the Hahn echoes decays faster for a bruised potato than for an intact one as the confinement to water diffusion is destroyed in the bruise one (Fig. 35d). Furthermore, single-sided NMR can be used to determine the fat content [510,520], for example,

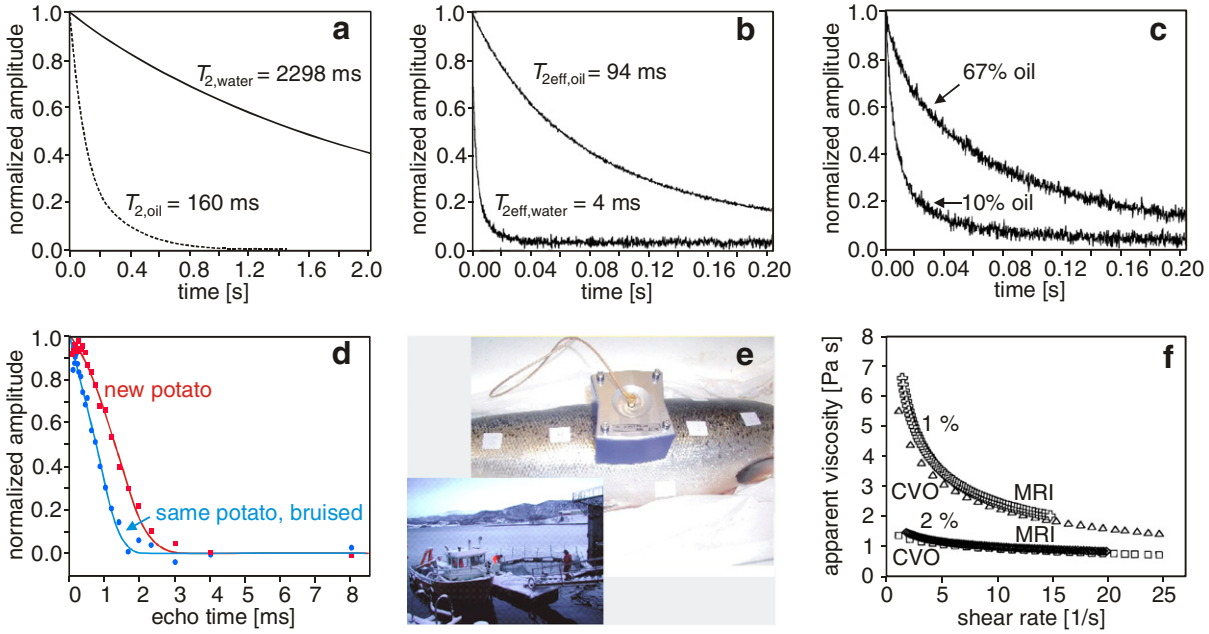

Fig. 35. Applications of mobile NMR to food. (a) The effective transverse relaxation decays of water and oil in homogeneous and inhomogeneous fields differ. In a homogeneous field, the water signal decays slower than the oil signal. (b) In an inhomogeneous field, diffusion accelerates the signal decay. In high field gradients the water signal decays faster than the oil signal. (c) The combined effect of relaxation and diffusion identifies single-sided NMR with CPMG excitation in high gradients as an interesting tool to quantify water/oil emulsions ((a–c) adapted from [455]). (d) Damage to the cell structures in plant material can be identified by similar means. The envelope of the Hahn echoes decays faster for a bruised potato than for an intact one as the confinement to water diffusion is destroyed in the bruise [314]. (e) Single-sided NMR can be used for detection of the fat content of live fish as a measure to select fish for breeding (photos with permission by SINTEF, Norway) [476]. (f) The structural viscosity of fluid food intermediates can be determined by NMR imaging with mobile NMR magnets mounted on an extruder (adapted from [526]). The apparent MRI viscosities refer to carboxymethyl cellulose in water and are compared to values determined with a commercial creep–viscosity–oscillation (CVO) rheometer.

in live fish as a measure for selecting fish for breeding (Fig. 35e) [476] and promises to be of interest for the analysis of a variety of packed foods [135,136,504] as well as for determining droplet size distributions [522].

Small Halbach magnets have found use in the construction of capillary rheometers using micro-coils for rf and for gradient pulses [523,524]. Such magnets can be mounted in the production line for process control [525] or on the tip of an extruder in order to study the complex rheology of food pastes and fluids and to control and optimize the processing of food [154,526,527]. The viscosities determined by NMR imaging are in good agreement with those determined by conventional capillary rheometry (Fig. 35f). A larger, portable Halbach system has been built to assess freeze damage in oranges [150]. A further intriguing area of applications for mobile NMR is the study of plant systems in their natural environment [168,269, 528,529].

4.2. Biomedicine

One area of applications for mobile NMR which comes to mind first is Biomedicine, drawing on the outstanding success of medical MRI. Yet any new NMR technology in medicine will have to compete with the established MRI technology and the community representing it. Certainly, the public interest in biomedical NMR applications is much higher than that in materials applications. This should be expected also for unilateral NMR [16,120,530]. When dealing with patients and living species, the measurement times need to be short. This is why portable or even single-sided imaging has not yet found any application in the medical community [216]. More promising are integral measurements which analyze a sizable sensitive volume by a CPMG-type scheme in a matter of seconds up to a minute or so. As biological matter is heterogeneous on many space scales, spatial resolution in at least one dimension is helpful. Given also the demand for a large sensitive volume to arrive at short acquisition times, the single-sided NMR sensors with good depth resolution [220,531] and dedicated limb imagers [165–167,179] bear great potential for biomedical applications. As limb imagers are established devices in the medical community and can be described as transportable rather than portable, they are excluded in the following.

4.2.1. Tendon

Single-sided NMR sensors with the field parallel to the surface are well suited to studies of angle dependences of NMR parameters in large objects (Fig. 36a), in particular of relaxation rates, which are difficult to study by conventional medical MRI as the patient is difficult to reorient perpendicular to the magnet axis. Tendon is a high performance biological material of exceptional strength with a

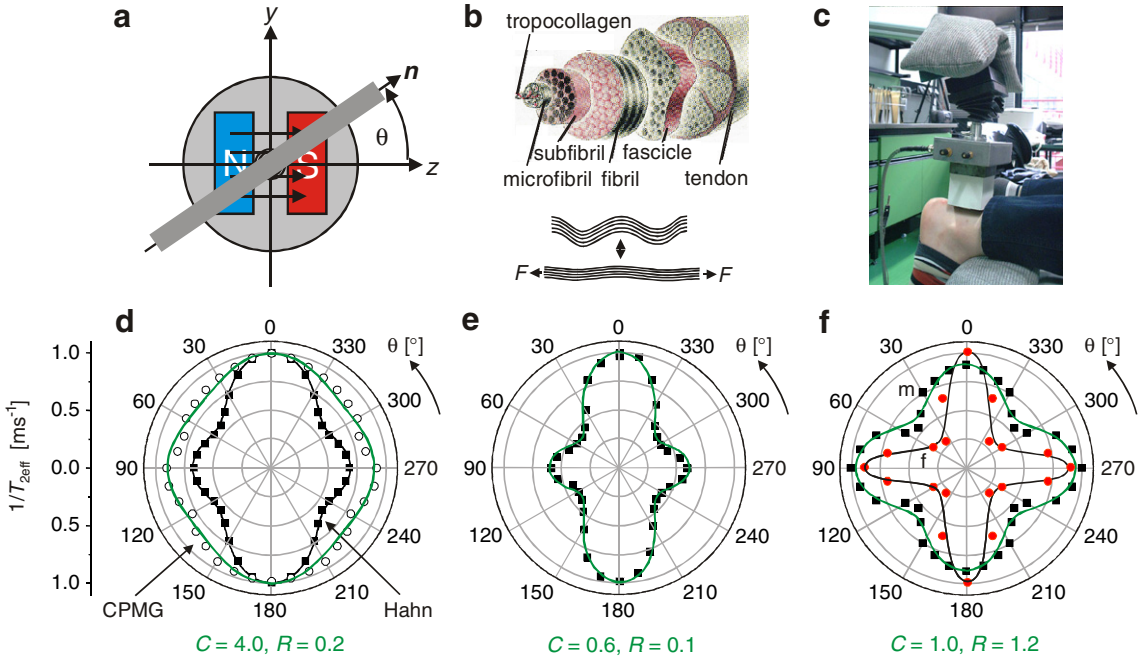

Fig. 36. Angle-dependent relaxation rates normalized to 1 ms at $\theta = 0°$ and measured with CPMG sequences at echo times of 0.1 ms. (a) Definition of the orientation angle θ. (b) Schematic showing the hierarchical structure of tendon and the crimps which provide elasticity. (c) Set-up for measuring human Achilles tendon *in vivo* with the NMR-MOUSE. (d) Angle dependences of transverse relaxation rates for a rat tail acquired with the CPMG and the Hahn echo sequences. (e) Angle dependence of the CPMG relaxation rate for sheep Achilles tendon *in vitro*. (d) Angle dependences of CPMG relaxation rates of the Achilles tendons of a male (m) and a female (f) volunteer. In (e–f), the points correspond to measured data, the drawn curves are fits according to Eq. (16) [549] with the fit values given underneath each graph, except for the inner curve in (f) which is just a guide to the eye. All measurements were conducted in 4–5 mm depth, and the acquisition of the data for one orientation lasted 5 min.

high degree of macroscopic molecular order, which has been studied in detail by different NMR methods [195,532–540]. It consists mainly of collagen triple helices which are arranged in bundles in a hierarchical structure with crimps and twists to provide optimum mechanical stability (Fig. 36b) [541]. Due to the high order, the magic-angle effect is observed by medical imaging in tendon as well as in cartilage, as a result of reduced tensorial spin interactions for fibres oriented at the magic angle [542–544]. In medical NMR imaging, tissue anisotropy [532] can be followed *in vivo* only by investigations of the anisotropy of translational diffusion with pulsed gradient fields [545,546], while the relaxation anisotropy can only be studied successfully on dead samples [533–535].

The Achilles tendon is easy to access with the NMR-MOUSE *in vivo* and is thick enough to cover most of the sensitive volume (Fig. 36c). The anisotropy of human Achilles tendon was studied *in vivo* (Fig. 36f) and compared to that of sheep Achilles tendon (Fig. 36e) and a rat tail (Fig. 36d). A smaller transverse relaxation rate is observed near the magic angle. As the relaxation in collagen is dipolar in nature [547] and the spins near resonance are locked in a CPMG sequence [55,61,62,184,548], the dipolar interaction is partially averaged by the CPMG excitation but not by the Hahn echo excitation, so that the apparent anisotropy is reduced in CPMG measurements (Fig. 36d). Furthermore, the anisotropy of the effective relaxation rate may be reduced due to signal attenuation by diffusion. Yet the CPMG sequence is preferred for *in vivo* studies as the measurements are much faster than with Hahn echoes.

In objects with perfect uniaxial order, the transverse relaxation is expected to scale with the square of the second Legendre polynomial [533–535]. A fit of the angle dependence of the observed CPMG relaxation rates $1/T_{2\mathrm{eff}}$ by an isotropic and an anisotropic contribution [549] according to

$$1/T_{2\mathrm{eff}} = 1/T_{2\mathrm{eff},0}\{C + [1/2(3\cos^2(\theta) - 1)]^2\} \tag{15}$$

was not successful for human Achilles tendon. To account for the crimps and twists in the collagen fibrils, a weighted sum of two functions of the form

$$1/T_{2\mathrm{eff}} = 1/T_{2\mathrm{eff},0}\Big\{C + \big[1/2(3\cos^2(\theta) - 1)\big]^2 + R\Big(C + \big[1/2(3\cos^2(\theta + 90°) - 1)\big]^2\Big)\Big\} \tag{16}$$

was used with one function phase shifted by 90°. The corresponding fitted curves and parameters are depicted in Fig. 36d–f for the three types of tendon studied, rat tail, sheep Achilles tendon, and human Achilles tendon *in vivo*, respectively. The weight C of the isotropic relaxation rate is the larger the more disordered tissue there is in the sensitive volume. The highest value of C is found for the rat tail (Fig. 36d), which consists of several collagen bundles embedded in connective tissue. Different values of C apply to the two human volunteers (Fig. 36f, only one fit is shown). This is likely to be due to shortcomings in the

accuracy of positioning the sensitive volume completely inside the Achilles tendon. Interestingly, both, the rat tail and the sheep Achilles tendon can be fitted reasonably well with a predominantly uniaxial fiber orientation as the R values are low (Fig. 36d and e) while the anisotropy pattern of the human Achilles tendon is much more star like and is biaxial with both orthogonal orientations nearly equally populated ($R = 1.2$, Fig. 36f) [541]. A possible explanation is that the tendon structure has changed upon sacrificing the animals.

The anisotropy of tendon has also been probed *in vitro* by diffusion studies with the bar-magnet NMR-MOUSE [188] using a constant-time relaxation method [373] to eliminate the relaxation weight on the measured echo amplitudes. Similar to the Profile NMR-MOUSE, the bar-magnet NMR-MOUSE exhibits a nearly linear $\boldsymbol{B}_0$ field profile as a function of distance from the magnet in a region close to the magnet, so that it is well suited for diffusion measurements. The data are in agreement with measurements of the diffusion anisotropy at high field [536] although different diffusion processes can more readily be differentiated at high field due to better sensitivity.

In an early clinical study with the original, u-shaped NMR-MOUSE [193] on patients with different types of Achilles tendon problems, a uniform distribution of the relaxation times measured at 5 mm depth was found that precluded a simple correlation with the medical condition (Fig. 37a), but the relaxation times of the tendon were always lower than those of the skin including the subcutaneous tissue [194]. Also the tendon relaxation times $T_{2\mathrm{eff}}$ of athletes and healthy young adults were observed to be in the same range, including that of an Achilles tendon healed after rupture (Fig. 37b). This indicates, that methods more refined than simple measurements of the effective transverse relaxation times of Achilles tendon at 0° orientation angle need to be found to differentiate between different tendon conditions. Instead of applying straight-forward CPMG sequences, anisotropy parameters, diffusion weights, relaxation-weighted, and double-quantum filtered signal amplitudes could be measured [528] possibly in combination with volume selection to eliminate signal from surrounding tissue. However, the relaxation times of the skin covering the tendon differed for both feet of the individual with the healed tendon fracture (Fig. 37b), demonstrating that one can discriminate scarred and healthy skin by simple relaxation measurements. Furthermore, differences in $T_{2\mathrm{eff}}$ of the skin but not the Achilles tendon were found for two individuals before and directly after bicycling (Fig. 37c). These early observations suggested that skin is well suited for investigations with the NMR-MOUSE.

4.2.2. Skin

While the different layers of the skin cannot be resolved with the curved sensitive volume of the original, u-shaped NMR-MOUSE (cf. Figs. 6b and 7a) [62], the Profile NMR-MOUSE (Figs. 7d and 26) [220] provides the necessary flat and thin sensitive volume needed for such investigations in addition to convenient access to nearly all parts of the human body. Other *in vivo* NMR studies of skin need to employ tomographs fitted with surface gradient coils and a surface rf coil to obtain an acceptable depth resolution of 70 μm [550,551]. Also, the stray-field technology with the GARfield magnet has been used to study the skin *in vitro* and *in vivo* of body extremities like the finger or the arm which are compatible with the geometrical constrains imposed by the semi-open magnet geometry [210–212,552–554] with a high depth resolution of up to 5 μm comparable to that of the Profile NMR-MOUSE [477]. Topics of interest are the characterization of effects on skin due to age [550], hydration [212,554], and skin care products [50,212,477,552].

Some representative depth profiles through human skin acquired *in vivo* are depicted in Fig. 38 [477]. The contrast is adjusted by proper choice of the parameter w defined in Eq. (6) or signal amplitudes and relaxation times are extracted from exponential fits of the CPMG decays. Profiles through the palm of the hand demonstrate the excellent reproducibility of the measurements. The profiles show very small deviations when taken at the same spot

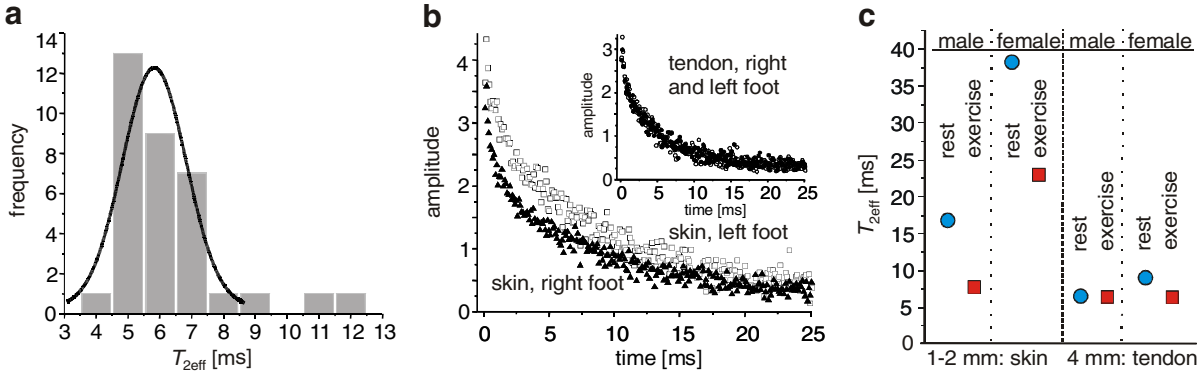

Fig. 37. *In vivo* analysis of human Achilles tendon and the skin above it. (a) Distribution of relaxation times in 4–5 mm depth at $\theta = 0°$ of athletes and healthy young adults [194]. (b) CPMG signals of the right and the left foot from a person with a rupture of the left Achilles tendon after healing. Differences are seen in the signals from scarred and normal skin. (c) The effect of bicycling for a male and a female young adult. There is no change in $T_{2\mathrm{eff}}$ at $\theta = 0°$ of the Achilles tendon but in $T_{2\mathrm{eff}}$ of the skin.

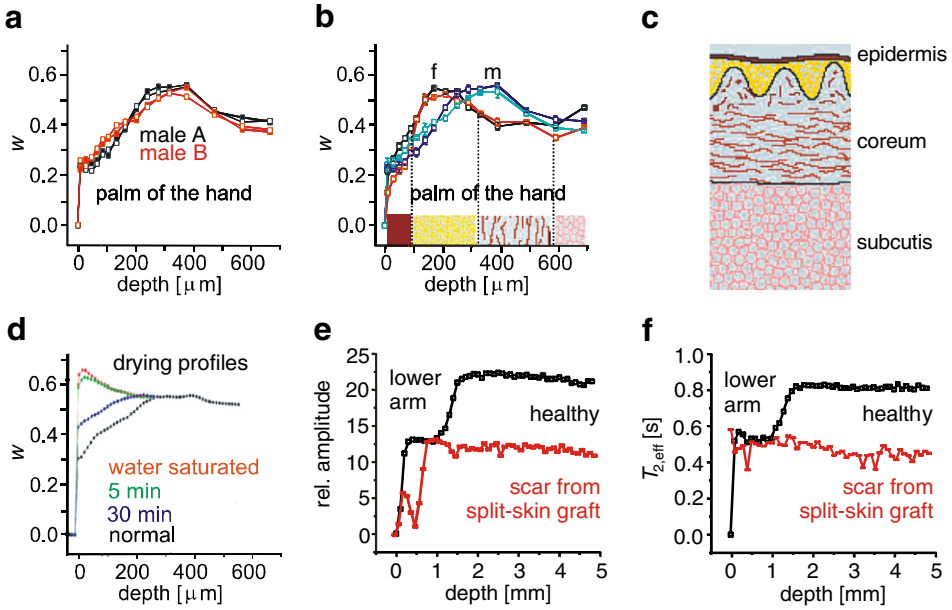

Fig. 38. Depth profiles through skin measured with the Profile NMR-MOUSE. (a) Palms of the hands of two male individuals, two profiles for each, demonstrating the excellent reproducibility. (b) Palms of two young adult females and two young adult males. The skin is thinner for the females than for the males. Different skin layers can be differentiated. (c) Schematic drawing of the skin structure with the major layers named. (d) Drying study of the skin on the palm. Only the epidermis takes up a significant amount of water and dries on a time scale of half an hour. Profiles a through (e) are calculated as the ratio w of echo sums derived from the CPMG decay curve (cf. Eq. (6)). (e) Comparison of CPMG amplitude profiles through the skin of both lower arms of a patient where skin has been split off from one arm for replacement at another part of the body. (f) T_{2eff} profiles corresponding to (e).

of one person, but larger deviations when taken at similar spots for different persons (Fig. 38a). A comparison of the profiles from two young male adults with those of two young female adults reveals thinner skin on the palm of the hand for the females (Fig. 38b). From the shape of the profile, different skin layers can be differentiated and assigned to the stratigraphy of the skin (Fig. 38c). The uptake and residence time of water and cosmetics [50,212,477,552,554] are of great interest to commercial applications. Drying of the water-soaked skin on the palm takes of the order of half an hour (Fig. 38d), while the moisturizing effect of skin cream may last for even shorter times [477].

Medical applications of the Profile NMR-MOUSE are facilitated by the small size of the instrument providing access to the skin at most parts of the body. An interesting subject of study is the formation and treatment of scars [555]. The signal amplitude (Fig. 38e) and the relaxation time T_{2eff} (Fig. 38f) follow similar modulations through the depth of the skin. Both are able the clearly discriminate between healthy skin and skin scarred from taking a split-skin graft, although the CPMG amplitude is more sensitive than T_{2eff} to the structure of the outer layer of the scar.

In a skin study with the original, u-shaped NMR-MOUSE of three patients with severe breast cancer, the signal recovery following magnetization saturation of the affected skin and subcutaneous fatty tissue was followed before and after administering a contrast agent [556]. Malignant tissue exhibits a faster signal recovery than scar tissue and healthy tissue, which only differ slightly.

4.2.3. Further studies

As the NMR-MOUSE provides a local NMR analysis at a given depth, silicone breast implants can be probed with it for indications of rupture. A ruptured implant will leak into the surrounding tissue, but also the body fluids of the surrounding tissue will seep into the implant giving rise to a change in the relaxation time of the gel inside. The validity of this hypothesis has been supported in a laboratory study with the bar-magnet NMR-MOUSE (Fig. 3e) [557], suggesting the use of the NMR-MOUSE for screening of patients with breast implants. Also, the multi-layer structure of the implant can be resolved with the Profile NMR-MOUSE, providing a means of quality control before implantation by measuring the depth profiles of the shell of the sterile implant sealed in a plastic bag [557].

Single-sided NMR devices can be miniaturized to dimensions smaller than 2 mm to serve as intravascular endoscopes (Fig. 3f) [163,181]. The inhomogeneities in the $\boldsymbol{B}_0$ and $\boldsymbol{B}_1$ can be used to construct coarse-grained high-resolution depth profiles within the sensitive sector of the device [181]. Such a self-contained MRI probe has been shown to be suitable for characterizing plaque morphology in the aorta and in coronary arteries [182]. Angular profiles can be obtained by rotation of the probe in a point-by-point approach.

Such a point-by-point approach was also followed in constructing the first 2D images from measurements with the NMR-MOUSE [62], and images with different contrasts were acquired by a steady-state saturation recovery sequence which allows the simultaneous and rapid determination of

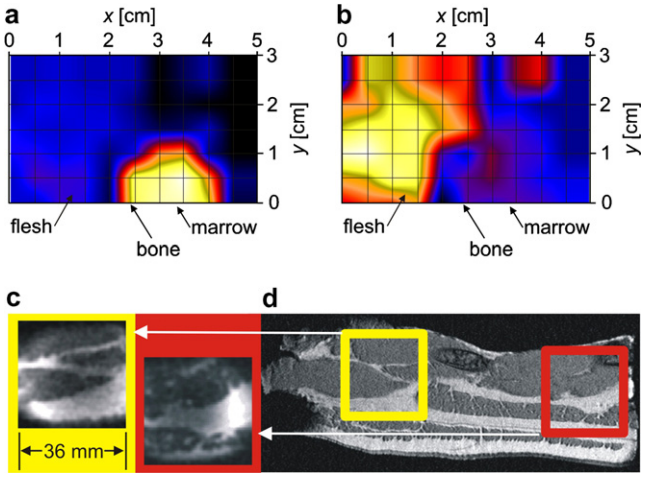

Fig. 39. NMR images of meat. (a) T_2-parameter image and (b) T_1-weighted image of a cross-section through a pork leg bought at a butcher. The images were derived from measurements of individual pixels selected by displacing the NMR-MOUSE [62]. (c) 32×32 pixel images measured with a single-sided tomograph [216]. The acquisition time per image was nine minutes. (d) NMR image of a piece of raw bacon measured in a conventional medical tomograph with the positions marked where the images were taken with the single-sided tomograph.

T_1 and T_2. The T_2-parameter image in Fig. 39a highlights the bone and the marrow, and the T_1-weighted image in Fig. 39b highlights a muscle part of a pork leg. The spatial resolution is low, because it is determined by the extension of the sensitive volume, but the contrast is excellent.

Images with better resolution are obtained by Fourier imaging techniques with pure phase encoding (Section 3.5) using pulsed gradient fields that null the signal dephasing in the background gradient of the inhomogeneous polarization field at the time of the echo acquisition. A single-sided tomograph with pulsed gradient fields has been built to acquire slice-selective images parallel to the sensor surface (Fig. 13c) and tested for materials and bio-medical applications [216,494]. Images of biological tissues with 32×32 pixels at a resolution of about 1 mm^3 can be measured in about ten minutes (Fig. 39c). The quality is acceptable compared to that of an image measured with a conventional instrument (Fig. 39d). Similar quality images were obtained as cross-sections through a finger [242,494] and the mandibula of a rat head *in vitro* [478]. But despite CPMG detection and echo addition, the imaging time is still too long for routine use in medicine. This is largely due to the low slice thickness defined by the high background gradient of about two Tesla, suggesting, that low-gradient sensors are better suited for mobile NMR imaging.

4.3. Elastomers

Elastomers are organic matter similarly soft as biological tissues. As MRI is highly successful in analyzing biological tissues [2], NMR also plays an important role in analyzing rubbery materials such as elastomers [325,465]. Elastomers can be stretched reversibly to multiples of their initial length. The reversibility is ensured by chemical cross-links between the macromolecular chains of rubber molecules. The cross-link density is the most important quantity for characterization of elastomer materials, and conventionally it is determined on test samples by mechanical deformation or swelling in solvents like benzene [558]. Similarly, it can be determined from the NMR relaxation decays and related parameters [465,559]. While this is an established procedure for desk-top NMR instruments [252,264,371] similar results can be obtained non-destructively by mobile single-sided NMR at different parts and different depths of a product (Fig. 40), and in the production line [4,46,126,132,133,156,275,276,466,480,560].

Commonly the envelope of a CPMG train is parameterized (cf. Fig. 17) to compare material properties of different samples or measurement positions. Absolute values of material properties such as cross-link density are obtained by calibration with NMR data of reference samples with known cross-link densities [46,561]. As time-domain NMR probes molecular mobility similar to dynamic mechanical relaxation, the effect that dominates $T_{2\text{eff}}$ is chain stiffness [314,561,562], and the effects of cross-link density, strain, and temperature are hard to separate if more than one of these parameters vary [133]. To discriminate between different samples near room temperature, a stability better than 1 °C is needed [215], or the NMR data measured from samples at different temperatures need to be extrapolated to a reference temperature by means of known temperature coefficients [133,560–563].

4.3.1. Parameter statistics

Most natural products and many synthetic ones are inhomogeneous on different space scales. Elastomers are three-dimensional networks of macromolecular chains cured from a formulation of different compounds and filled with carbon black or other fine grained materials. The distributions of cross-links and filler particles are statistical, and some of the components may aggregate (Fig. 41a) [133,276,564]. Most technical elastomer materials are heterogeneous to a degree which is determined by the economic pressure to keep mixing and curing times short yet long enough to meet consumer specifications (Fig. 41b). In addition to that, the product quality may vary due to wear and tear of the processing equipment and errors in the composition of the formulations.

The consequences are twofold: first, continuous product monitoring is required for comparison of the current product quality with that of a chosen reference product (Fig. 40c) in order to assure equal product quality over long times with varying quality of raw compounds, wear-down of equipment, and changing personnel. Often this is done by mechanical testing of a sample (Fig. 40b) with a rubber process analyzer [565]. Second, due to the statistical nature of the cross-links, filler, and defect distributions, a single measurement of a product property like the hardness of a rubber part at a selected spot is insufficient. Rather the property should be tested at different equivalent

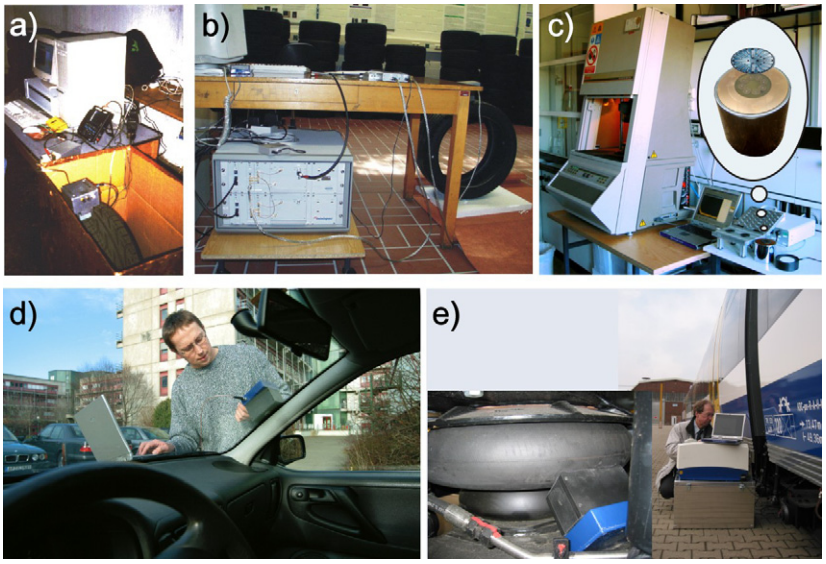

Fig. 40. Rubber product testing with the NMR-MOUSE. (a) Testing of a steel-belted car tire in a garage at the Nürburgring race track in 1998 [132]. (b) Tire sorting in the laboratory at RWTH Aachen University in 1999. (c) Proposed set-up for combining mechanical rheometry on standard test samples and NMR relaxometry with a dedicated NMR-MOUSE [188] to match the geometry of the circular test sample. The samples to be measured are stored in a heating unit upon leaving the rheometer and are then tested at elevated temperature with an NMR-MOUSE covered by a temperature-stabilization hood [133]. The resultant NMR data can serve for reference in non-destructive product testing with the NMR-MOUSE. (d) Testing the rubber gasket of a windshield in a passenger car [563]. (e) Measuring the air-spring bellows of a passenger train. Condensation water can be detected within a few seconds of measuring time [121,448].

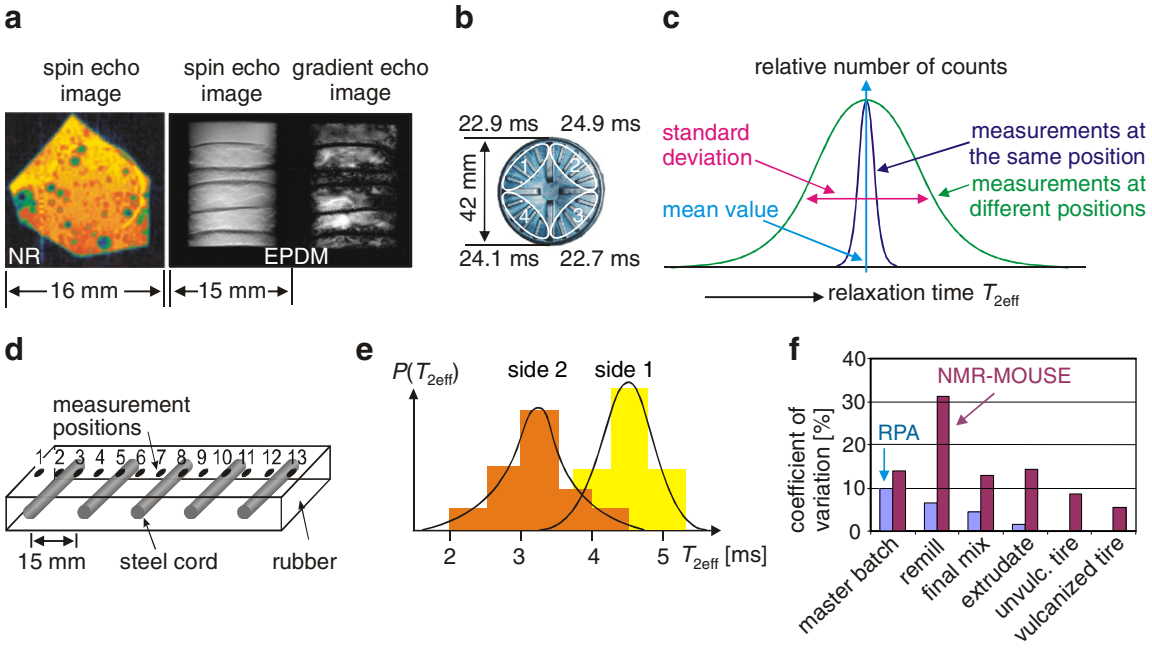

Fig. 41. Statistical analysis of NMR data from heterogeneous products. (a) NMR images of an unfilled sheet of natural rubber showing aggregates of zinc oxide due to improper processing (adapted from [276]) and images of stacks of EPDM sheets filled with carbon black (adapted from [564]). (b) Test sample from the rubber process analyzer RPA [565] showing variations in T_{2eff} at different positions [448]. (c) Distribution of relaxation times acquired by repetitive scans at one position and at different positions (adapted from [276]). (d) Schematic drawing of a conveyor belt with steel cords and measurement positions [126]. (e) Distributions of relaxation times acquired from both sides of the belt (adapted from [134]). (f) Coefficients of variation for several measurements on different intermediate products in the tire manufacturing process for the rheometer moment (RPA, left bars with light shades) determined on test samples and T_{2eff} obtained non-destructively with the NMR-MOUSE (right bars with dark shades) [560]. Measurements on the intact tire can only be done by the NMR-MOUSE.

spots (Fig. 41b and d) [126,134] and its distribution should be analyzed (Fig. 41c, e, and f) for example in terms of the statistical mean and its standard deviation or coefficient of variation (Fig. 41f) [133,276,473,481]. For repetitive measurements at the same spot, the distribution function is often much narrower than for measurements at different spots (Fig. 41c). The standard deviation and the coefficient of variation for measurements at different spots are measures of the heterogeneity of the product, and the mean is a measure of the average material property tested, for example the cross-link density in terms of $T_{2\mathrm{eff}}$ (Fig. 41e). Similar considerations apply to other technical polymer products which are formulated from a number of different compounds and subsequently processed to achieve, for example, particular average crystallinities and average segmental orientations. Again, the local properties may deviate from the overall average due to the statistical nature of the product [566].

4.3.2. Cross-link density

The cross-link density of elastomers can be determined simply by mechanical deformation such as shear or elongation. The shear modulus G correlates with the cross-link density n and the average molecular weight M_c between two cross-links,

$$G = nRT = RT\rho/M_c, \tag{17}$$

where R is the gas constant, T the absolute temperature, and ρ the density of the material [558]. The shear modulus is routinely tested for different formulations by curing circular rubber sheets (Fig. 41b) between the counter-oscillating hot plates in a rheometer (Fig. 40c) [565]. Alternatively, the cross-link density can be determined from recording stress σ versus strain Λ and fitting the curve by the Mooney–Rivlin equation

$$\sigma/(\Lambda - \Lambda^{-2}) = 2C_1 + 2C_2/\Lambda, \tag{18}$$

where $\Lambda = L/L_0$ is the elongation ratio defined as the ratio of final over initial lengths, and C_1 and C_2 are constants. C_1 is associated with physical entanglements. For small Λ, $C_2 = n\ R\ T/2$ correlates with the chemical cross-link density n. Cross-link density can also be determined via the glass temperature T_g (Fig. 42a) [59,276,464,561,567] and the degree Q of swelling. The latter specifies the volume ratio of solvent-saturated and dry samples, and n scales with $Q^{-5/3}$ [558]. T_2 and Q are observed to be proportional to each other (Fig. 42b), suggesting that n should scale with $T_2^{-5/3}$ or approximately T_2^{-2} [324,568]. However, in sufficiently small ranges, any function can be approximated linearly, and also T_2 is often found to depend linearly on cross-link density n (Fig. 42c and d) [46,480,557].

As the transverse relaxation can conveniently and accurately be measured with desk-top and mobile NMR instruments, NMR relaxometry is a useful method of determining cross-link density [59,465,559,569]. Portable sensors like the NMR-MOUSE allow such measurements to be carried out non-invasively and at room temperature for testing of intermediate and final elastomer products (cf. Fig. 41f). Moreover, the CPMG amplitude scales with the material density (Fig. 42e), so that cross-link density and material density can be determined simultaneously for elastomer foams in a single measurement at a given depth and profiled by using measurements at different depths [570].

With increasing curing time, cross-link density increases as the cross-linking reaction proceeds leading to a decrease in T_2 (Fig. 42a) [61,184,563,569–571] and the degree of swelling (Fig. 42b). This feature is used, for example, to assess the state of curing of adhesives (Fig. 40d) [133,213,276,563,567,571]. Some rubber types show reversion, i.e. a decrease in the shear modulus at high curing times due to chain scission starting to dominate cross-linking (Fig. 42f). In this regime, the simple relationship between $T_{2\mathrm{eff}}$ and the shear modulus changes (Fig. 42g) [133,276], as the chemical reactions that compete with the cross-linking reactions also modify the polymer chain structure and with it the molecular mobility so that mechanical testing, swelling, and NMR relaxation change their dependencies on chemical cross-link density in different ways. Another way used to probe chain stiffness and cross-link density is by measuring multi-quantum build-up curves (cf. Section 3.2). This methodology has been shown to work in the inhomogeneous fields of the NMR-MOUSE (Fig. 21) [70,71,138] as well as in the low and homogeneous field of desk-top NMR spectrometers [322,572].

4.3.3. Strain

Multi-quantum coherences can be generated in elastomer networks, because there is a residual dipolar interaction between neighboring spins in the chain due to the anisotropic motion of the chain segments between the cross-links [465,559]. This interaction also determines the magnitude of the relaxation times and it depends on the orientation of the magnetic field with respect to the end-to-end vector of the intercross-link chains, which align under strain. Consequently, all kinds of relaxation rates and multi-quantum signals in strained samples depend on the orientation angle θ of the magnetic field $\boldsymbol{B}_0$ with respect to the strain direction $\boldsymbol{n}$ (Fig. 43) [71,196,197,538] similar to the transverse relaxation rate of tendon (Fig. 36).

With increasing sample elongation Λ, the orientation distribution of chain segments narrows and the angular dependence of the transverse relaxation rate $R_{2\mathrm{eff}} = 1/T_{2\mathrm{eff}}$ becomes more pronounced (Fig. 43b) [196,197]. By fitting the observed relaxation rates with a distribution of anisotropic relaxation rates following Eq. (15)

$$R_{2\mathrm{eff}}(\theta) = R_{2\mathrm{eff,iso}} + R_{2\mathrm{eff,aniso}} \int P(\theta - \theta')[(3\cos^2\theta' - 1)/2]^2 \mathrm{d}\theta', \tag{19}$$

the isotropic and anisotropic relaxation rates $R_{2\mathrm{eff},iso} = 1/T_{2\mathrm{eff,iso}}$ and $R_{2\mathrm{eff,aniso}} = 1/T_{2\mathrm{eff,iso}}$ are extracted

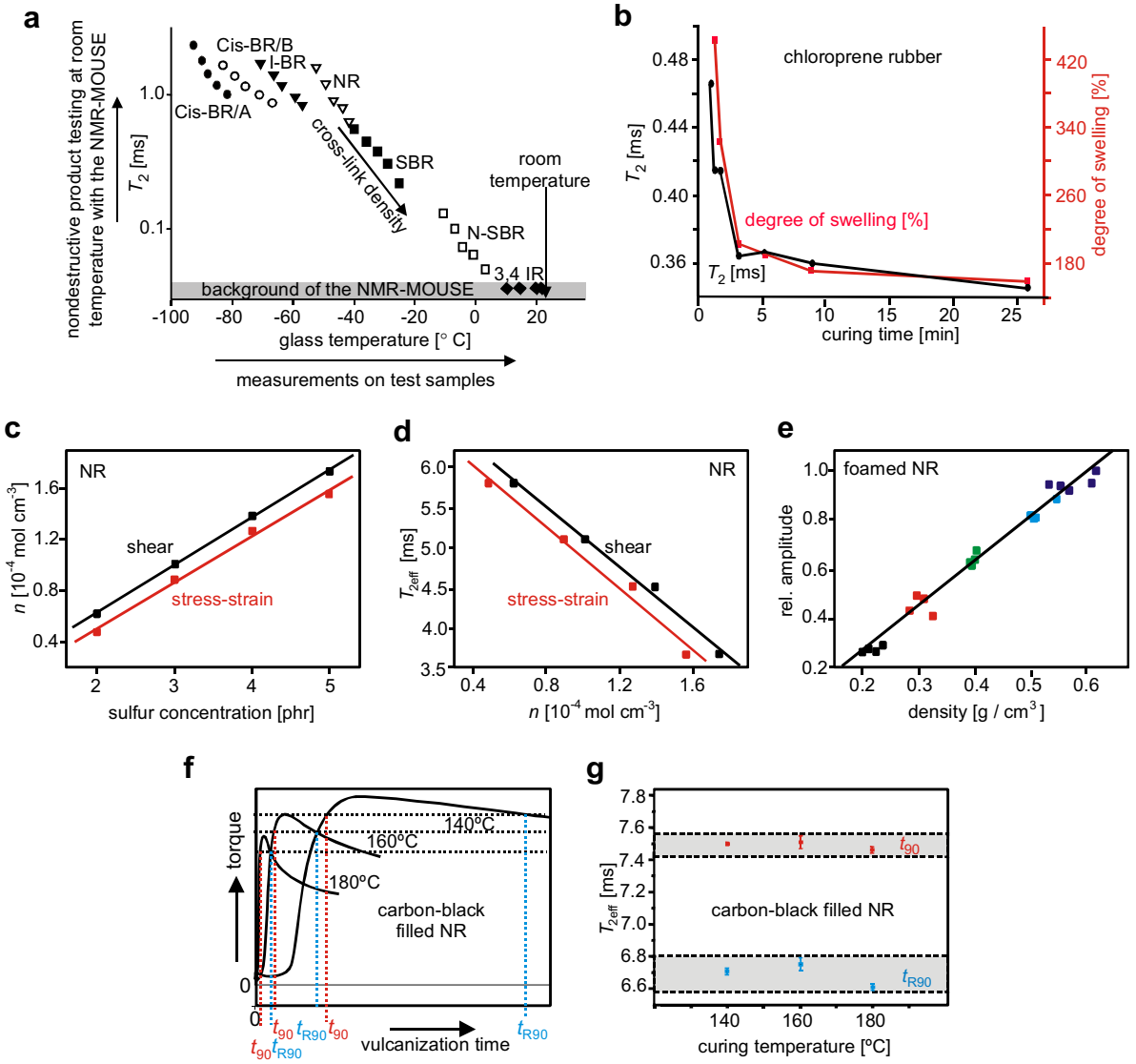

Fig. 42. (a) Transverse relaxation time T_2 of different types of unfilled rubber samples with different cross-link densities as a function of the glass temperature T_g [561]. T_2 was measured at room temperature in a short time, and the determination of T_g required lengthy temperature-dependent measurements. (b) The degree of swelling for chloroprene samples decreases in proportion to T_2 with increasing curing time. (c) Correlation of cross-link density for natural rubber (NR) versus sulfur concentration in parts per hundred rubber according to stress–strain and rheometer measurements [570]. (d) Linear correlation of T_{2eff} with cross-link density for NR [570]. (e) The CPMG amplitude for foamed NR samples scales linearly with the gravimetrically determined density [570]. (f) Rheometer curves of NR determined at different curing temperatures. The temperatures t_{90} and t_{R90} at 90% of the torque before and after the rheometer maximum are indicated [276]. (g) T_{2eff} can discriminate between curing states before and after the rheometer maximum with the same torque [276].

(Fig. 43c and d), where $P(\theta - \theta')$ is the orientation distribution of end-to-end vectors [549]. The dependencies on elongation Λ are approximately linear for natural rubber [46,480] in both cases, but change differently in the vicinity of $\Lambda = 3$, where NR is known to crystallize.

Mobile, single-sided sensors with $\boldsymbol{B}_0$ parallel to the surface are well suited to analyze chain ordering due to local strain in thin test samples, while devices with $\boldsymbol{B}_0$ perpendicular to the surface cannot sense the orientation dependence. The distribution of strain in a natural rubber band with a hole in the center and strained to $\Lambda = 2.9$ is mapped in Fig. 43e by the anisotropy of $R_{eff} = 1/T_{2eff}$ [196]. The observed anisotropy values $[R_{2eff}(0°) - R_{2eff}(\theta_m)]/R_{2eff}(0°)$ agree with the symmetry of the sample. Strain effects in rubber have also been studied by double-quantum NMR (Fig. 21), T_2 instead of T_{2eff}, and $T_{1\rho}$, as well as by unilateral NMR imaging [242].

4.3.4. Degradation

Degradation or aging denotes the change of material properties with time. Degradation studies are an integral part of efforts to arrive at reliable life-time predictions. Chemical aging and physical aging are differentiated. The former is also called corrosion and involves a chemical attack, often by oxygen and free radicals, the latter concerns reordering of polymer chains as a result of

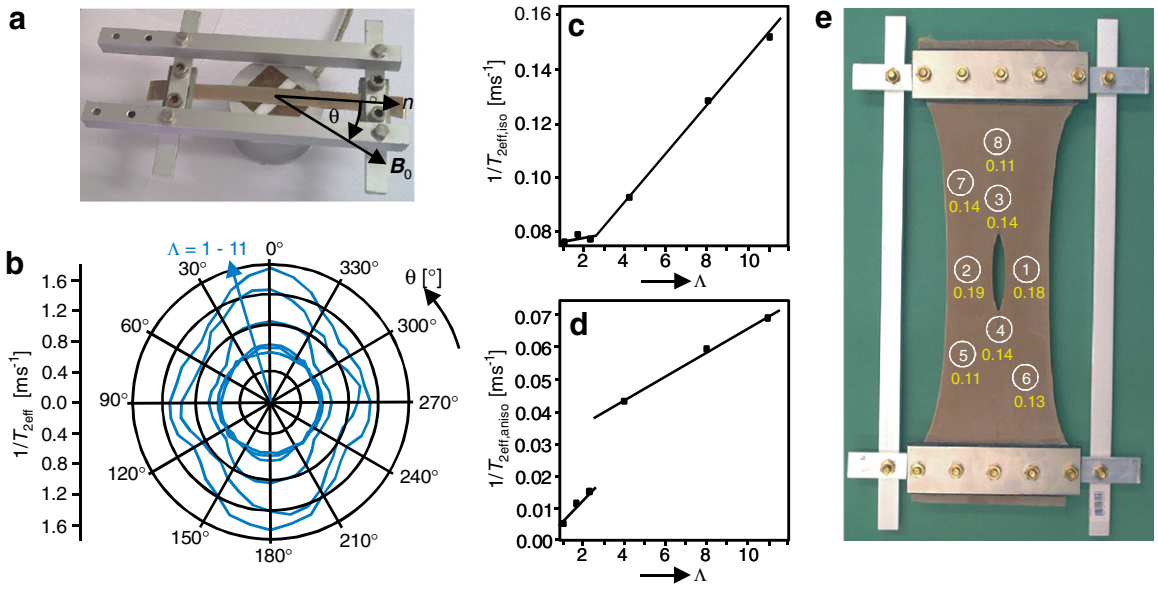

Fig. 43. Anisotropy of relaxation rates in strained rubber samples due to macroscopic chain ordering. (a) Simple straining device to investigate strain effects in rubber bands with the NMR-MOUSE. (b) Orientation-dependent relaxation rates for a natural rubber band strained to different elongations Λ [196]. These experimental data were fitted with Eq. (19) to extract the isotropic and anisotropic relaxation rates, using a Gaussian distribution $P(\theta)$ of average chain orientations with a variance of 10° [549]. (c) Strain dependence of the isotropic relaxation rate. The drawn line is a guide to the eye. (d) Strain dependence of the anisotropic relaxation rate. The drawn lines are guides to the eye. (e) Relaxation anisotropies of a strained natural rubber band with a hole in the centre [196].

mechanical load, temperature, and wetting over time. Both mechanisms affect the segmental mobility of the polymer chains and lead to changes in residual dipolar couplings and relaxation times.

The effect of different additives to the rubber formulation on the aging resistance can easily be probed with the NMR-MOUSE (Fig. 44a), and the time-dependent degradation of the sample can be followed (Fig. 44b) [215,242,573,574]. However, in originally homogeneous samples, the aging process may generate layer structures as oxygen diffuses into the sample or if one surface is exposed to UV light (Fig. 44c) [575,576]. Depending on the aging conditions, different aging mechanisms dominate in different depths such as chain scission and cross-linking, leading to a softening or a hardening of the elastomer, respectively. Circulating air while aging rubber sheets in temperature chambers may invoke asymmetric depth profiles, and as different aging mechanisms dominate in different regions across the sheet diameter, the characteristic aging times differ as well [215].

Thermo-oxidative and light aging typically start at the surface of the sheet, and single-sided NMR sensors are well suited to map their depth profiles. The sensors can be optimized to low penetration depths [189] and for curved surfaces [138]. Depending on the area of application different degradation effects arise. For example, silicone pads used in aerospace applications have been analyzed by NMR imaging and single-sided NMR to assess the impact of the fabrication process, the service conditions, and the effect of γ irradiation [577]. NMR relaxation is sufficiently sensitive to discriminate between formulation errors and effects of prolonged mixing of rubber formulations. Furthermore, the effects of mechanical strain and electrical overload on shells of high power electrical cable joints have been studied with the NMR-MOUSE (Fig. 21f–h) [326,448,571], and an on-line detection system for moisture contamination of raw rubber has been proposed [578].

When exposed to liquids and gases, diffusion, swelling, and drying of rubber need to be assessed. The diffusion fronts of solvents ingressing into polymer and rubber sheets can be followed with the Profile NMR-MOUSE (Fig. 45a and b) [575]. For example, the uptake of gasoline by natural rubber (NR) proceeds much faster than the uptake of oil by EPDM rubber. The uptake of cyclohexane vapor by a PDMS membrane has been followed with a bar-magnet NMR-MOUSE fitted with a meander coil to optimize the sensitivity near the coil surface [189]. The MOUSE was covered by the membrane and positioned in a desiccator together with an open container of cyclohexane. $T_{2\mathrm{eff}}$ follows a mono-exponential law for the uptake of the solvent vapor (Fig. 45c) but a bi-exponential law for drying (Fig. 45d). The latter is explained with the formation of a dry surface layer which slows down the drying of the membrane core. The same set-up has been used to study the drying of a spray adhesive [189].

Non-destructive testing by single-sided NMR opens a window for probing mechanical deformation at a molecular scale [314]. Fatigue due to excessive mechanical stress is routinely tested by cyclic loading of test bodies such as rubber stripes. A small NMR sensor based on the classical permanent magnet configuration (Fig. 6a) has been built to fit a stress–strain device for rubber stripes (Fig. 45e) [478].

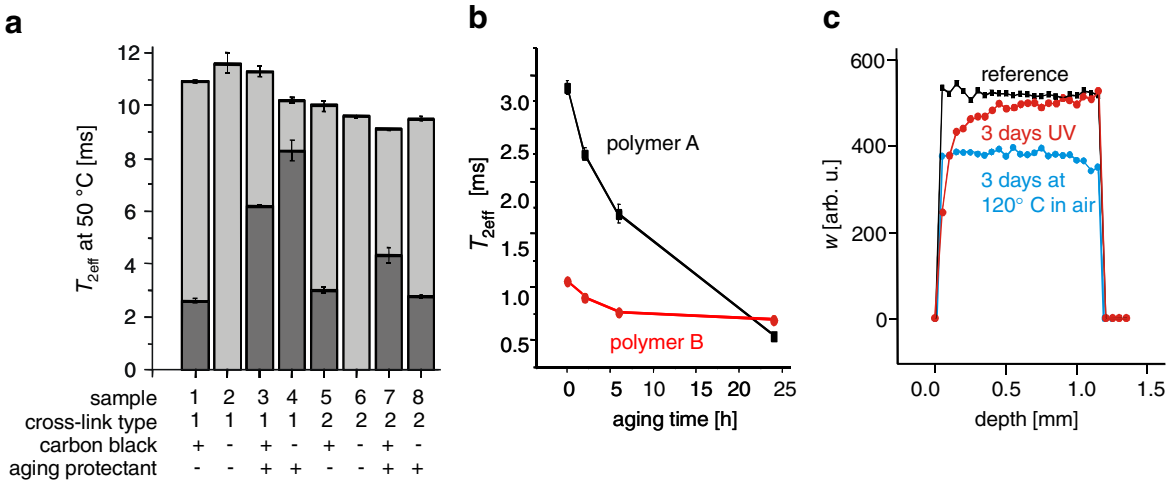

Fig. 44. Thermo-oxidative aging of rubber sheets investigated with single-sided NMR. (a) Relaxation times of fluorine rubber sheets with different formulations before (light grey) and after aging in air at 120 °C (dark grey) measured with the u-shaped NMR-MOUSE. Sample 4 shows the highest aging resistance. (b) Transverse relaxation times of two rubber sheets aged under the same conditions as a function of the aging time measured with the u-shaped NMR-MOUSE. Polymer A ages faster than polymer B [215]. (c) Depth profile across natural rubber sheets new, aged in air, and aged under UV irradiation, measured with the Profile NMR-MOUSE [575]. UV aging produces an aged surface layer.

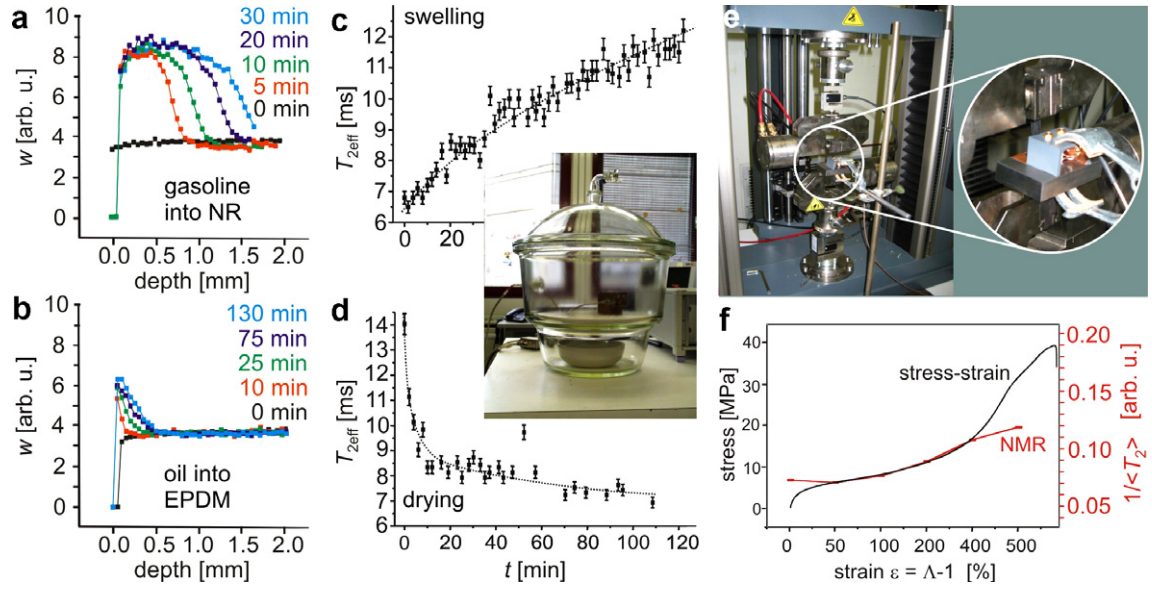

Fig. 45. Testing of rubber sheets. (a) Profiles mapping the migration of a gasoline-diffusion front in natural rubber [575]. (b) Profiles mapping the migration of an oil-diffusion front in EPDM rubber [575]. (c) Uptake of cyclohexane vapor by a poly(dimethylsiloxane) film [189]. (d) Drying of a cyclohexane saturated poly(dimethylsiloxane) film [189]. (e) Stress–strain testing device supplemented by an NMR sensor to acquire NMR data during straining of a rubber test stripe. (f) Stress–strain curve and $1/\langle T_{2eff}\rangle$ curve for carbon black-filled natural rubber [478].

The stress–strain curve could be mapped simultaneously with the mechanical measurement by recording CPMG decay curves at different strains $\varepsilon = \Lambda - 1$. As expected from the proportionality of NMR relaxation rates and elongation Λ, the inverse of the average relaxation time $\langle T_{2eff}\rangle$ obtained from summing all the echoes of the normalized CPMG decay (Eq. (5)) parallels the stress–strain curve up to about $\Lambda = 4$ (Fig. 45f). Such a set-up promises to be of use for predicting the time of failure based on NMR relaxation measurements in cyclic loading tests. Mobile NMR sensors also promise to be of use for in-line monitoring of the polymer extrusion process [154]. Similar to well-logging instruments, they can be constructed from temperature resistant magnet material such as samarium cobalt alloy so that they can be in contact with the hot polymer melt [153].

4.3.5. Defects in elastomer composites

Most rubber products are composites of different types of rubber and other materials such as reinforcing textile

fibers in rubber tubes and sheets, and steel belts and cords in tires and conveyor belts. Single-sided NMR can be used to profile the layer structure of such products [4,59,479,573]. The Profile NMR-MOUSE has been employed to scan depth profiles through composite rubber tubes with different types of defects. Despite the planar sensitive slice of the device, meaningful amplitude and relaxation time profiles were obtained, which reveal the structure of the composite and provide information about the type of defect (Fig. 46) [241]. Differences in cross-link density or the formulation are revealed by changes in $T_{2\text{eff}}$ with respect to a reference, and a hole in the lining gives rise to a lower signal amplitude (Fig. 46a), while $T_{2\text{eff}}$ remains unaffected if the defect is smaller than the sensitive volume of the device (Fig. 46b).

In rubber-textile composites critical for safety, the accurate positioning of the reinforcing fibers and defects in the rubber matrix (Fig. 12e) [76,216,242] are important to know. The use of NMR instruments is not impeded by the same safety regulations required for X-ray instruments. Low-field, single-sided imaging with lateral resolution (Section 3.5) [73–76] was first explored for imaging the fiber positions in an air-spring bellows (Fig. 13a). With the development of the unilateral tomograph [76,216,561], the crossed fiber layers in the bellows could be resolved slice-selectively (Fig. 47a) and the accuracy of the fiber spacing analyzed from the imaging data (Fig. 47b and c) [216,494]. As the unilateral imager works with the inhomogeneous stray field just like the NMR-MOUSE, some distortion of the field due to the presence of steel is acceptable, as long as these distortions are accounted for in a quantitative evaluation [314]. This is why intact tires with steel belts can be investigated by single-sided NMR devices in terms of depth profiles [4,59] and images (Fig. 47d and e).

4.4. Solid polymers

Solid polymers are more challenging to investigate by mobile NMR than is soft matter, as the transverse relaxation times are shorter, and significant portions of the signal may decay within the dead time of the sensor. Short inter-echo times of 20 μs can be achieved with the bar-magnet NMR-MOUSE (Fig. 6c), so that semi-crystalline and other hard polymers can be studied [42,46,184,241,275,301,481–483,566,579] including glass-fiber reinforced epoxy [42,481,482]. Carbon-fiber reinforced material is hard to measure as it is conducting and shields rf, and the sensitivity of the NMR-MOUSE in the $T_{1\rho}$ measurements needed for identification of thermal damage is too low [315,580]. On the other hand, the sensor can be used in the vicinity of steel, as some distortions of the magnetic measuring field can be tolerated [469,525,579].

One of the most common mass products from thermoplastic polymers are pipes. The most popular material is polyethylene (PE), which consists of macromolecular chains packed in disordered amorphous and ordered crystalline domains which constitute the polymer morphology. The magnetization of the chain segments in the amorphous domains relaxes slowly with $T_{2\text{eff,long}}$, and those in the crystalline domains relax rapidly with $T_{2\text{eff,short}}$. In contrast to X-ray scattering the crystalline and amorphous domains are distinguished with NMR by their molecular mobility and not by their state of order. The NMR crystallinity defined as the relative amplitude $A_{\text{short}}/(A_{\text{long}} + A_{\text{short}})$ of the rapidly relaxing magnetization component includes

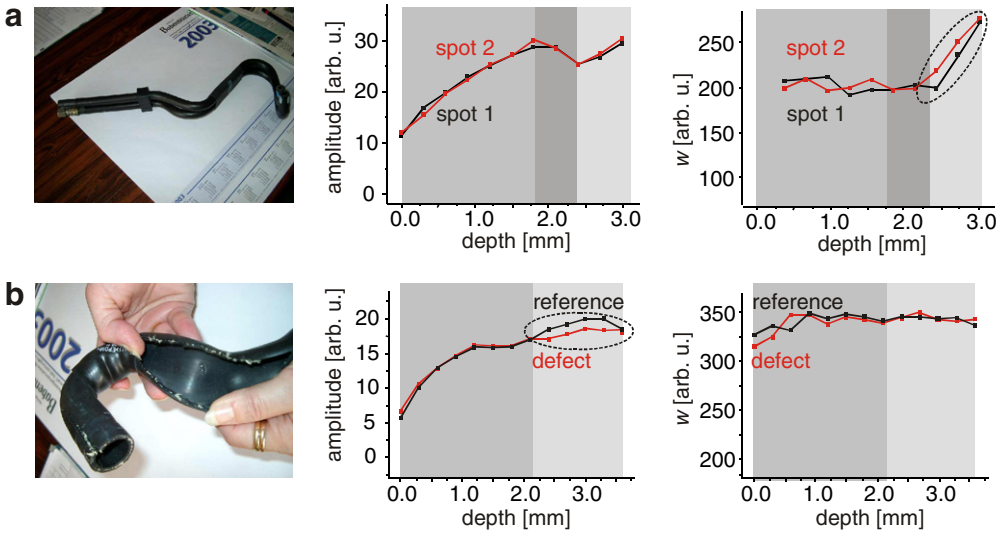

Fig. 46. Depth profiling of rubber tubes with the Profile NMR-MOUSE [241]. (a) A pair of textile reinforced rubber tubes. The position of the textile fibers is revealed in the amplitude signal. The rubber formulation of the outer liner penetrates the textile layer as $T_{2\text{eff}}$ begins to change with the inner liner at the inner side of the textile layer. $T_{2\text{eff}}$ of the inner liner is not constant, revealing a gradient in the modulus of the liner. Both inner liners differ in their $T_{2\text{eff}}$ profiles due to different formulations or exposure to different solvents. (b) Profiles through a defect rubber tube at the position of the defect and a reference position. $T_{2\text{eff}}$ is constant across the entire tube wall indicating the same formulation for the inner and the outer sides of the tube. The defect is a hole in the inner tube wall (cf. Fig. 13c) and manifests itself in reduced signal amplitude.

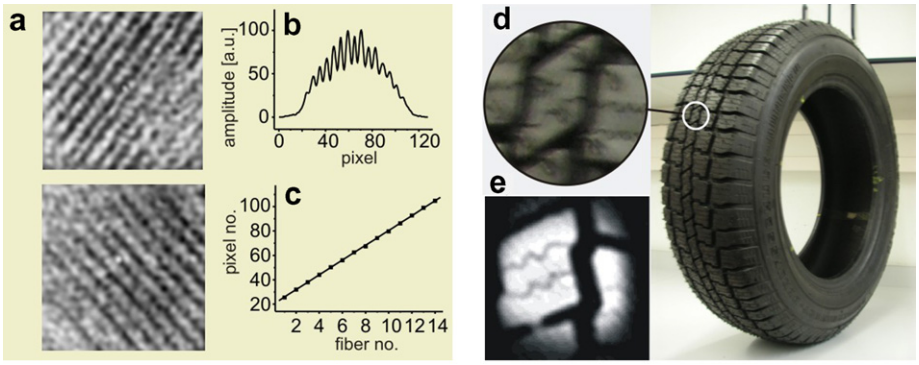

Fig. 47. Images from rubber composites taken with the open tomograph depicted in Fig. 13c. (a) Slice-selective images of the crossed fiber layers in an air spring bellows [216,494]. The layers are 1 mm apart. The field of view (fov) is 14×14 mm^2, the spatial resolution is about 200 μm, and the acquisition time per image was 2 h. (b) 1D projection along the diagonal of one of these 2D images and (c) fiber position versus fiber number to assess the fiber spacing. (d) Photo and (e) image of a section of the tire tread from an intact car tire with a steel belt. The 35×35 mm^2 image consists of 32^2 pixels and was acquired in 4 h.

the signal from the rigid amorphous chains in the interface between crystalline and amorphous domains and gives rise to the particular sensitivity of NMR to aging and annealing effects in semi-crystalline thermoplastics [581]. This feature is explored in non-destructive testing of polyethylene pipes to understand the effects that production, deformation, chemical aging, and annealing have on the morphology of the material with the final goal of predicting the residual lifetime of a pipe in service [301,481–483,566].

PE pipes are produced by extrusion of a melt into pipe form and subsequent cooling to room temperature. The temperature gradient during cooling leads to a gradient in crystallinity through the pipe wall, which can be traced by measuring NMR relaxation data at different depths (Fig. 48a) [481,482,566]. In the lateral directions, the crystallinity is not constant but changes statistically as revealed by maps of the NMR parameter w defined in Eq. (6) [301,481,482,566]. These fluctuations can be mapped systematically point by point (Fig. 48b) and the resultant data plotted in image form (Fig. 48c) or analyzed in terms of parameter distributions (Fig. 48d and f). The effect of annealing is summarized well in terms of distributions of w. Already 55° C below the glass transition temperature T_g, a significant effect of annealing and crystallization is observed in an uncorroded high-density polyethylene (HDPE) pipe (Fig. 48d) [566]. Such annealing effects were also observed in mechanically deformed PE pipes [241,275,301,483]. These observations indicate validity limits of established laboratory tests conducted at 80 °C for life-time prediction of HDPE pipes. Also a chemically corroded low-density PE (LDPE) steel-pipe shell (Fig. 48e) shows a dramatic effect of annealing well below T_g in the distributions of the NMR parameter w, which goes along with an increase of the elongation at break from 24% to 264% (Fig. 48f). As the chemical attack starts from the outside, a heterogeneous layer structure develops in the aging polymer sheet, which can be resolved by the Profile NMR-MOUSE [566].

Single-point measurements for reference with known data can serve to assess the state of material deterioration, for example, in weathering studies (Fig. 49a) [184,579], and to identify defects by probing at suspicious positions, such as in glass-fiber reinforced components (Fig. 49b) [481,482,566] and solid rocket motor bond-lines [469,525]. Also the quality of processing could be identified, for example, on intact spools of synthetic fibers [582]. Lateral scans across a sample can identify fracture zones in round pipes and planar sheets (Fig. 49c) [46] as well as welding lines (Fig. 49d) [301,483]. The latter bears promise for developing a tool to asses the quality of welding lines for PE pipes. Depth profiles through layers of polymers reveal the composition of the object and the functioning of the layers in degradation studies. For example, different polyurethane and epoxy layers can be identified by means of signal amplitudes (Fig. 49e) and relaxation times (Fig. 49f) in polymer coatings of cement walls and floors [477].

Time-dependent degradation and fluid absorption studies on polymers and polymer products are performed with considerable ease using single-sided NMR [42,583]. Such studies may concern the uptake of oil in inner polymer liners of steel pipes as a function of temperature (Fig. 50a) [61,62], the swelling of polymers in solvents under extreme pressure and temperature conditions (Fig. 50b and c) [491], the moisture profiles through a polymer sheet changing with the wetting time of the sheet in a water bath (Fig. 50d) [275,477], and the water moisture profile through a polymer sheet after drying and subsequent exposure to the humidity of air at room temperature (Fig. 50e) [275,477]. The barrier function to diffusion of gasoline through a composite polymer tank wall has been probed with the Profile NMR-MOUSE in a laboratory set up (Fig. 50f). The time-dependent diffusion profiles show, how the progressive uptake of gasoline is blocked by the barrier layer [220,242,477,481,482]. Other investigations concern the quality and curing kinetics of adhesive joints [211,213,567] and the curing of coatings [210,212,584].

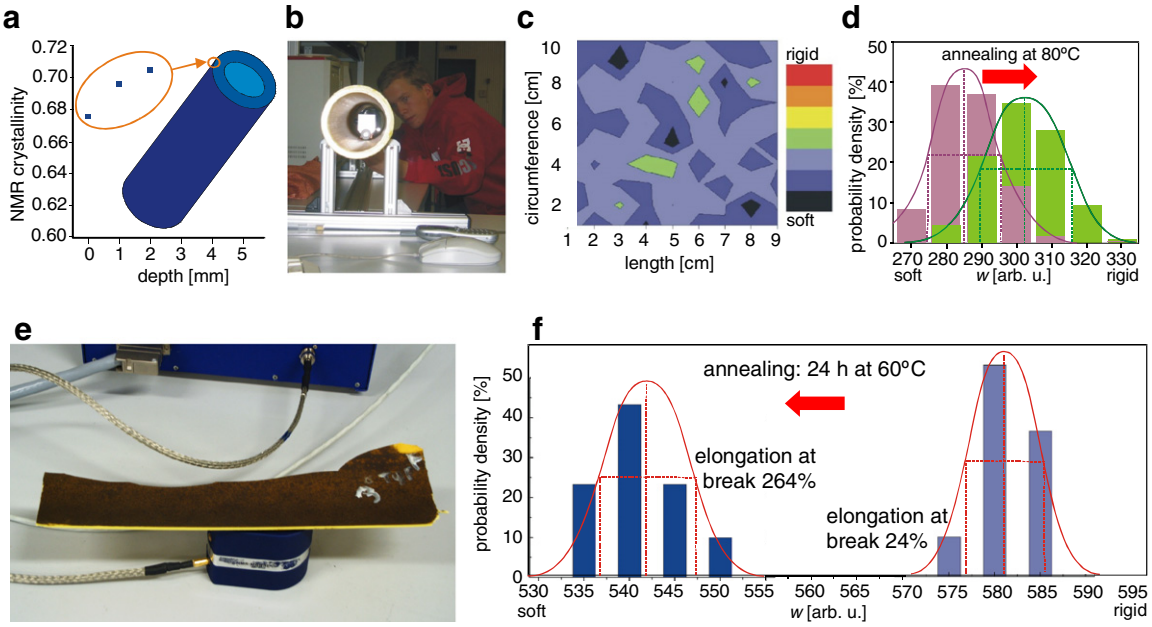

Fig. 48. Applications of the NMR-MOUSE to the characterization of PE used with gas and water pipes [566]. (a) Crystallinity gradient in the outer part of a PE pipe. (b) Device for mapping the inside of PE pipes by a special NMR-MOUSE having a surface curved to fit the shape of the pipe. (c) Map of the NMR parameter w (Eq. (6)) on a 1 cm^2 grid from the inside of a PE pipe. (d) Statistics of w acquired for a pipe section before and after annealing at 80 °C for 36 h. The material becomes more brittle, (e) Section of a steel-pipe shell from LDPE which had been in the ground for 20–30 years. (f) Effect of annealing of the LDPE sample at 60 °C for 24 h. The material becomes more elastic.

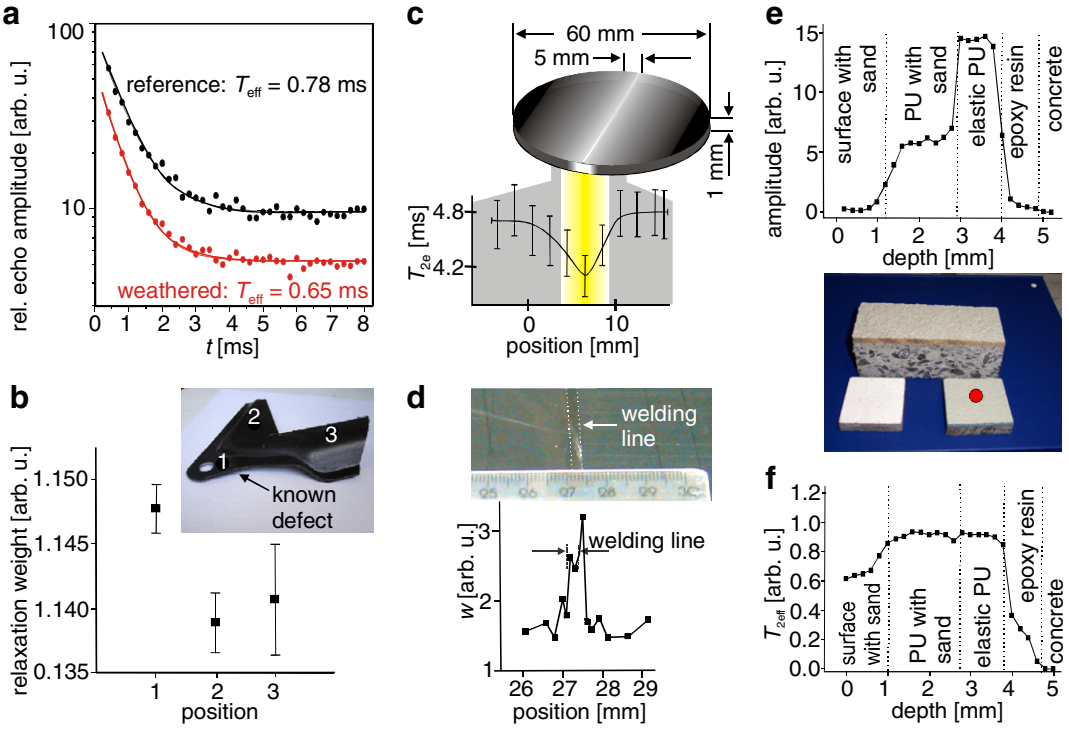

Fig. 49. Quality control and defect detection by single-sided NMR. (a) Weathering of a 0.5 mm PVC coating on a 1 mm iron sheet. The weathered material has a shorter transverse relaxation time [579]. (b) Identification of a defect in a section of a glass-fiber reinforced epoxy bottom-floor cover of a passenger car [482]. (c) Scan across a line of stress whitening in a sheet from impact modified polystyrene caused by bending [46]. (d) Detection of a welding line in two joined sheets of carbon-black filled PE [301]. (e) CPMG amplitude profile of different polymer layers on a cement sample [477]. (f) T_{2eff} profile of different polymer layers on a cement sample [477].

Such studies can be conducted with mobile single-sided NMR devices like the Profile NMR-MOUSE on intact objects and on laboratory specimens.

Several studies on thin films concerning solvent diffusion, drying and film formation have been conducted using the GARfield magnet. These studies are reviewed in [210] and [212]. The GARfield magnet is particularly well suited to measure NMR parameter profiles by 1D Fourier imaging techniques. The film is aligned perpendicular to the gravity direction which coincides with the direction of the strong gradient, so that high-resolution profiles across films are obtained as Fourier transforms of echoes. Such profiles serve, for example, to analyze and model the drying and cross-linking of coatings and adhesives, the photo-initiated curing of latex dispersions, the film formation of alkyd emulsions and other colloidal layers upon drying, the swelling of polyvinylchloride upon ingress of acetone vapor, and the water ingress into starch amylase or sodium polyacrylate [210,212].

4.5. Moisture and porous media

The characterization of porous media was the original challenge that gave rise to the development of mobile NMR for well-logging [5,175,585]. As the moisture content of the sensitive volume inside objects with proton-bearing fluids can most easily be quantified just by the amplitude of the echo envelope, or equivalently by the integral of the relaxation time distribution function, the detection and quantification of moisture content in diverse products by dedicated NMR sensors was rapidly developed [18–24,27,124,128,129,139–141,269,583,586]. However, surface relaxation of fluids in pores and diffusion in internal gradients of porous media provide a wealth of information that can be probed with a variety of relaxation, diffusion and correlation experiments (Section 3) and modeled by analytical and numerical methods [587–590]. The low magnetic fields of mobile NMR sensors alleviate signal distortions from diffusion in background gradients, and low-gradient sensors with a sweet spot are preferred for analysis of fluid-filled porous media [185,208,223,224,226,229], unless diffusion itself is to be measured [25,314,336,372–374].

Relaxation time distributions derived from CPMG echo envelopes measured with high-gradient devices suffer from diffusive attenuation, which practically cannot be eliminated even at echo times as short as 20 μs (Fig. 51a) [372,375,485]. Compared to T_2 distributions measured at

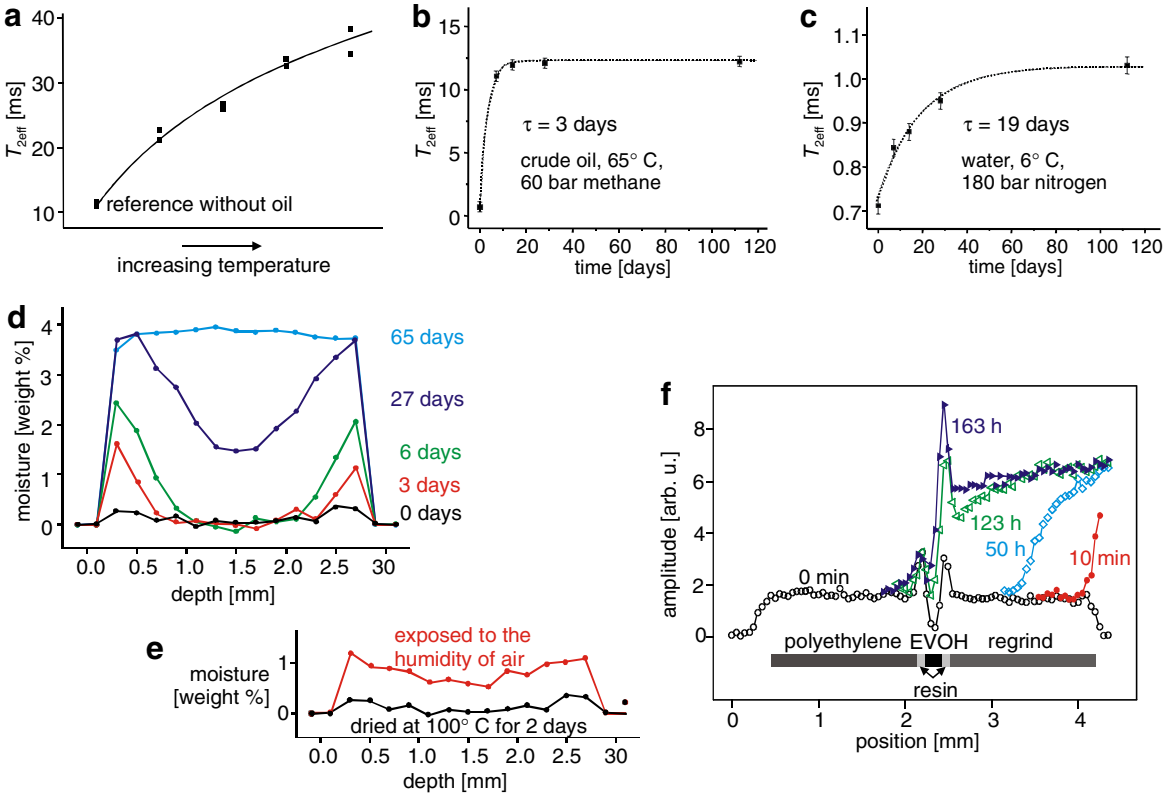

Fig. 50. Swelling studies of polymers and polymer products with single-sided NMR. (a) Effect of T_{2eff} on the uptake of oil in an inner polymer liner of a steel pipe as a function of temperature [61]. (b) Effect of T_{2eff} on the uptake of crude oil in medium-density polyethylene (MDPE) over time measured after taking the sample out of the autoclave [491]. (c) Effect of T_{2eff} on the uptake of water in MDPE [491]. (d) Water moisture profiles through a polymer sheet as a function of the immersion time in water [477]. (e) Water moisture profile through a polymer sheet after drying and exposition to the humidity of air at room temperature [477]. (f) Time-dependent profiles through the composite polymer wall of a gasoline tank showing how the progressive uptake of gasoline is blocked by the barrier layer [220,242].

homogeneous field (Fig. 51b), the distribution of apparent relaxation times T_{2eff} is compressed at constant area towards shorter relaxation times [485,591]. This effect may be quite pronounced in some geophysical samples (cf. Fig. 53a below) [175]. Building materials such as bricks and concrete have strong internal gradients and sometimes even ferromagnetic impurities, which mask this effect by spoiling the homogeneity of the applied field (cf. Fig. 51a and b) [485,592,593]. In fact, the relaxation time distributions measured in inhomogeneous fields may match conventional differential mercury injection pressure curves (Fig. 51c) accidentally quite well. Nevertheless, mercury intrusion porosimetry (MIP) measures the throat-size distribution, while NMR measures the relaxation time distribution, and both match only under favorable conditions.

Most applications of mobile NMR to porous media reported at conferences [20,21,146,147,594] and in the literature concern soil, building materials such as concrete, mortar, and bricks, down-hole well-logging, laboratory core analysis, and wood. Others address moisture content for example in coal and cokes [586] and reduction-grade aluminum oxide [45]. Mobile NMR can provide unique data for modeling the processes of moisture uptake, migration and drying [595]. Partial saturation of porous media with fluids, however, is a complex process which depends on the distribution of paramagnetic centers [596] and on the wetting properties of the pore walls so that relaxation time distributions for different saturation states cannot simply be interpreted in terms of a pore-radius distribution [241,275,276,597–599]. More sophisticated experiments like 2D correlation NMR may help to reveal the physics at the pore scale [381]. Chemical processes such as ion migration and salt outcropping [600] associated with wetting and drying of building materials have been investigated in laboratory studies with dedicated instruments [139] that are sufficiently sensitive to detect other nuclei like ^{23}Na [600,601]. The direct detection of ^{23}Na with a sensor embedded in the concrete matrix has not yet been realized [602].

4.5.1. Soil

Soil moisture is part of the water cycle that defines our climate and agricultural productivity. To calibrate satellite data, a single-sided NMR sensor with an u-shaped electromagnet [23] was developed at the Southwest Research Institute in San Antonio, Texas, over 20 years ago. This was be pulled across a field at a speed of up to 18 km/ h while acquiring moisture concentrations from the ^{1}H signal amplitude at about 3 MHz at a depth of 62 mm (Fig. 1b) [30,129]. The NMR data were shown to correlate highly with volumetric soil-water content [22]. A similar sensor was built to measure evaporable moisture in bridge decks with an accuracy of $\pm$ 0.4% for depths ranging from 70 to 95 mm (Fig. 1a) [30,44,129].

In a later study, the NMR-MOUSE was shown to be suitable for characterizing oil contaminations in soil. The transverse relaxation time was found to correlate linearly with the mass concentration of oil in water-dry soil [314,371]. Single-sided NMR has also been used to measure relaxation time distributions in unconsolidated soils with different grain distributions. The relaxation time distributions were interpreted in terms of their distributions of open pores, from which values of porosity and permeability were calculated [603–605]. Stray-field NMR was shown to be applicable to image plant tissue in soil [606] and to study water transport in soil [607]. Furthermore, the anisotropic diffusion of water in Antarctic sea ice has been probed by mobile Earth's field NMR with pulsed gradient fields [608]. As mobile NMR is becoming a less expensive commodity, and given the remarkable advances in the NMR methodology at low and inhomogeneous fields, it is to be expected, that NMR studies of moisture and water transport in soil will become an increasingly attractive field of research.

4.5.2. Concrete and other building materials

NMR of cement-based materials is a field of broad interest due to the great economic importance of cement and the considerable details that can be learned from NMR measurements about chemical structure and pro-

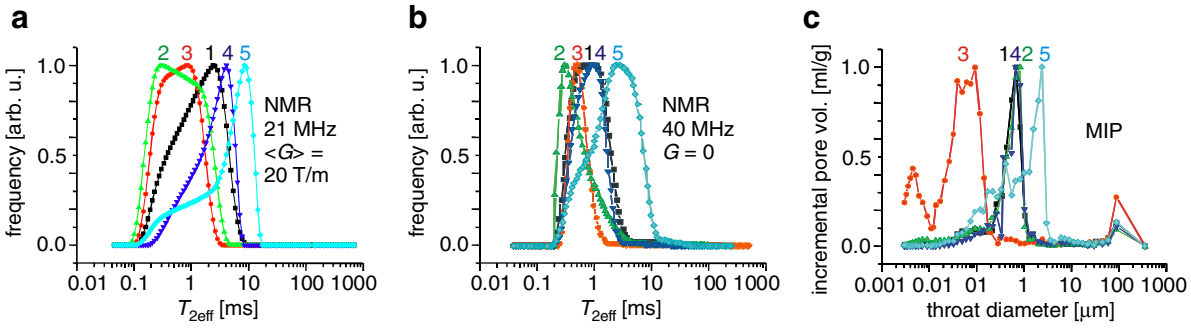

Fig. 51. Comparison of distributions functions for historic Roman brick samples 1–5 [485]. (a) Distributions of apparent transverse relaxation times measured with a u-shaped NMR-MOUSE. (b) Distributions of transverse relaxation times measured with a low-field desk-top NMR spectrometer. (c) Differential pressure curves from conventional mercury injection claimed to measure the pore-size distribution. The shapes agree misleadingly well. Sample 2 is an exception. It was strongly ferromagnetic.

cesses of hardening, the role of water, and the pore structures [609,610]. The early single-sided NMR device employed by Southwest Research Institute to study moisture in bridge decks (Fig. 1a) [30,129] used an electro-magnet and weighted about 300 kg. Later on, single-sided sensors with permanent magnets were also developed (Fig. 1c and d) [32,42,129]. The technology was subsequently optimized at the Fraunhofer Institute of Non-destructive Testing in Saarbrücken, Germany, with the primary focus on the inspection of concrete and other building materials [25,204]. They developed the NMR-INSPECT system consisting of a mobile spectrometer and a single-sided NMR sensor (Fig. 52a) [25,148] based on a u-shaped magnet weighting 38.5 kg with a field gradient of about 3 T/m. The resonance frequencies for ^{1}H can be tuned to frequencies between 5.2 and 9 MHz to access depths up to several centimeters. This non-destructive testing technology by one-sided access (OSA) NMR was shown to be useful for measuring the water content of concrete, the water mobility during concrete hardening, water profiles during drying (Fig. 52b), and the water permeability of the hardened concrete [148,149,340,603–605, 611,612]. A related study has been conducted with the NMR-MOUSE and by stray-field imaging [591].

A single-sided sensor with a field gradient of about 10 T/m operating at ^{1}H frequencies between 6 and 14 MHz (Fig. 7b) has been built by Quantum Magnetics and its operation demonstrated with measurements of moisture content and concrete hardening (Fig. 52c) [145,217]. The new surface GARfield magnet operating at 3.2 MHz to access depth up to 5 cm has been employed for a comparative curing study of two different types of cement pastes by 2D T_2–T_2 correlation experiments [613]. The OSA sensor, the Quantum-Magnetics sensor, and the surface GARfield magnet have magnetic fields parallel to the sensor surface. A barrel-type portable NMR sensor with the field perpendicular to the sensor surface, the NMR-MOLE (Fig. 10b) has been designed with a low gradient of 0.2 T/m at 3.3 MHz in a sweet spot for moisture measurements. The use of this 6 kg sensor has been demonstrated by measurements of curing of cement pastes [229].

The moisture transport over distances longer than those accessible to single-sided NMR is possible with dedicated NMR instruments that accommodate long samples. To scan the sample in length, either the sample is moved through the magnet [139], or the magnet is moved along the sample [222]. Such a device with a fixed magnet and a moving sample was built over 10 years ago to analyze moisture transport in building materials with paramagnetic impurities at spatial resolution of better than 1 mm in a gradient of 0.4 T/m [139]. This sensor has been employed to analyze the water absorption and drying of bricks [139,141–144], the water extraction out of mortar during brick laying [614] and drying [615], and the moisture transport [616] and the composition of mortar [617] over the

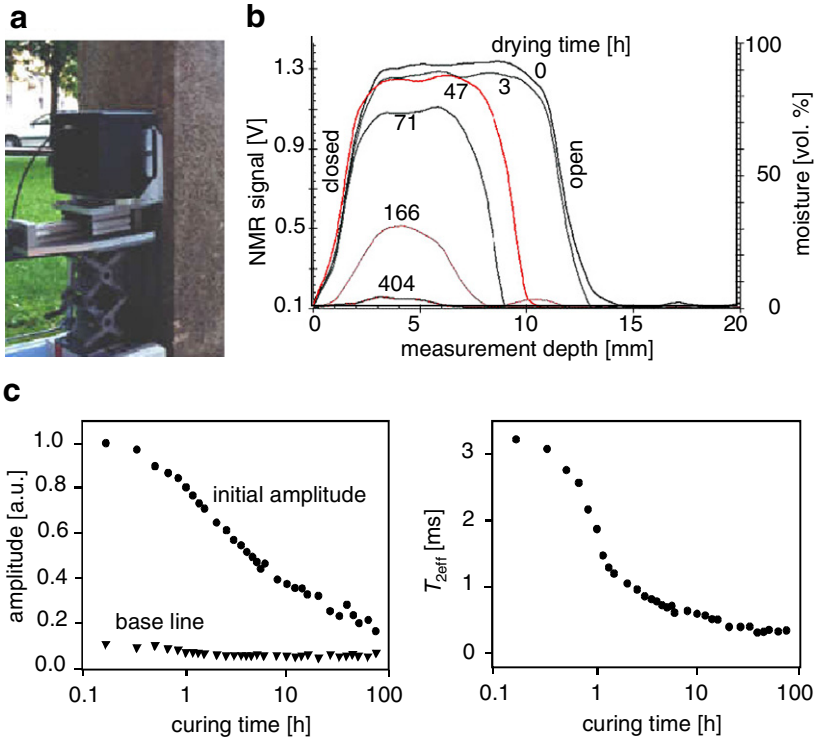

Fig. 52. Measuring water in concrete by single-sided NMR. (a) Single-sided NMR sensor of the NMR-INSPECT system measuring moisture in concrete [340]. The sensor [25] has a sensitive plane at a given distance from the sensor surface. Depth profiles are scanned by adjusting the distance between the sensor surface and the object. (b) NMR depth profiles of a bentonite test body covered from five sides, which is drying from the surface [340]. The profiles reveal shrinking of the object while drying. (c) Amplitudes and relaxation times plotted as a function of the curing time of rapid-set cement [145].

brick–mortar interface. The instrument has subsequently been adapted to observe the transport of sodium ions in bricks during one-sided drying of acid saturated samples [618–620] to gain a better understanding of salt crystallization as a damage mechanism in porous building materials [600,621]. For example, the NMR data indicate, that excessive pressure is generated by the crystallization of sodium sulfate in nanometer pores.

4.5.3. Wood

Wood is an organic building material which is employed as boards and beams cut from solid trunks or produced as chip boards. In both cases, the content and distribution of moisture during fabrication, storage, and transport are important factors that determine product quality and strength. A moisture meter for wood chips, pulp and paper has been built and successfully tested as a bench-top instrument with a permanent magnet [622]. Pore moisture and surface moisture can be differentiated using this meter. High-resolution depth profiles of surface moisture have been determined during drying of wood from NMR measurements with the GARfield magnet [623].

Single-sided NMR has been used to follow the moisture content of poplar heartwood during drying [145] and to measure profiles of density, volumetric and gravimetric moisture content through differently treated chip boards. Although accurate results could be obtained, the measuring speed of 0.5 mm/s was found to be too slow for online quality control in the factory [603,624]. However, the measurement method is believed to be of use for investigating wooden objects of cultural heritage [492].

4.5.4. Applications to geophysics

The applications of mobile NMR to geophysics are in well-logging [5,175], subsurface water identification [124] and laboratory core analysis [222,625–627]. Well-logging uses wire-line tools which are lowered into the borehole after the drilling process and tools for logging while drilling, which are part of the drill string (Fig. 10) [443,445,446,628]. The latter demands more sophisticated NMR technology, as the drill mud has to pass the sensor, and the NMR magnet rotates with the drill. However, as the time available for a scan is often longer, more demanding experiments can be performed, and the information can be used to change the drilling direction upon demand.

CPMG relaxation curves are routinely measured and converted to distributions of relaxation times. Such distributions are interpreted in terms of pore-size distributions, which are evaluated for porosity, permeability, and fluid typing [382,629]. In the fast diffusion limit, the relaxation rate is proportional to the surface-to-volume ratio, that is, the relaxation time is proportional to the pore diameter. In contrast to the longitudinal relaxation rate, the transverse relaxation rate is affected by translational diffusion in inhomogeneous fields with a gradient G. The field gradients can arise from the external applied field and from susceptibility differences caused by the heterogeneity of the porous medium. Information about the pore size is also obtained from the restrictions in molecular self-diffusion imposed by the pore walls.

The CPMG amplitude corresponds to the integral of the relaxation time distribution. It provides mineralogy-independent porosity. A model-bound analysis of the relaxation time distribution yields irreducible water saturation from clay-bound and capillary-bound water, permeability estimates, hydrocarbon type, and oil viscosity estimates. By 2D NMR methods such as diffusion–relaxation correlation NMR, the often overlapping signals from oil and water can be separated to provide valuable information for fluid typing (Fig. 25) [274,380,630]. The possibility to separate signals from different fluids in a porous rock matrix by 2D correlation NMR has also been demonstrated with the NMR-MOUSE [631]. NMR well-logging tools have been tested for determining unfrozen water at grain interfaces in permafrost regions [632] and for probing gas hydrate deposits [444,633,634]. But the short relaxation times present a serious challenge to the direct detection of the gas hydrate signal.

Subsurface fluids like water can be localized by NMR in the Earth's magnetic field by sing surface coils over 100 m in diameter, which can excite and collect signals from up to 100 m depth [124,635–637]. Water bearing formations can be characterized by modeling the response based on a priori knowledge of the geophysical layer structure. This approach has been evaluated for use in subsurface water detection on Mars [638].

Well-logging measurements are routinely accompanied by laboratory measurements of drill cores from the bore hole. Low magnetic fields are preferred to avoid complications due to internal field gradients from susceptibility differences [222,625–627]. The resultant loss in sensitivity can be recovered by hyperpolarization techniques [627]. With laser-polarized noble gas NMR, rock permeability and effective porosity can be probed simultaneously. A further advantage of low-field NMR is the low cost of the magnet and the mobility of the instrumentation. The latter has been the motivation to use single-sided NMR in measuring the water distribution of different sandstones [612] and estimating porosity and permeability of soils [603–605]. A prerequisite for this approach is the complete fluid saturation of the porous medium, which is hard to achieve for initially dry stone [434,473], but comes for free if drill cores are investigated with mobile NMR equipment immediately after recovery at the drilling platform or onboard a ship. The large gradient of the NMR-MOUSE, however, causes diffusive attenuation of the fluid signal, and the associated distribution of effective relaxation times appears compressed at long times compared to distributions measured in homogeneous field (Fig. 53a, cf. Fig. 51) [472]. Nevertheless, the device is a convenient tool to determine porosity from the signal amplitude, as volume calibration is not needed as long as the core completely encloses the sensitive volume during measurement.

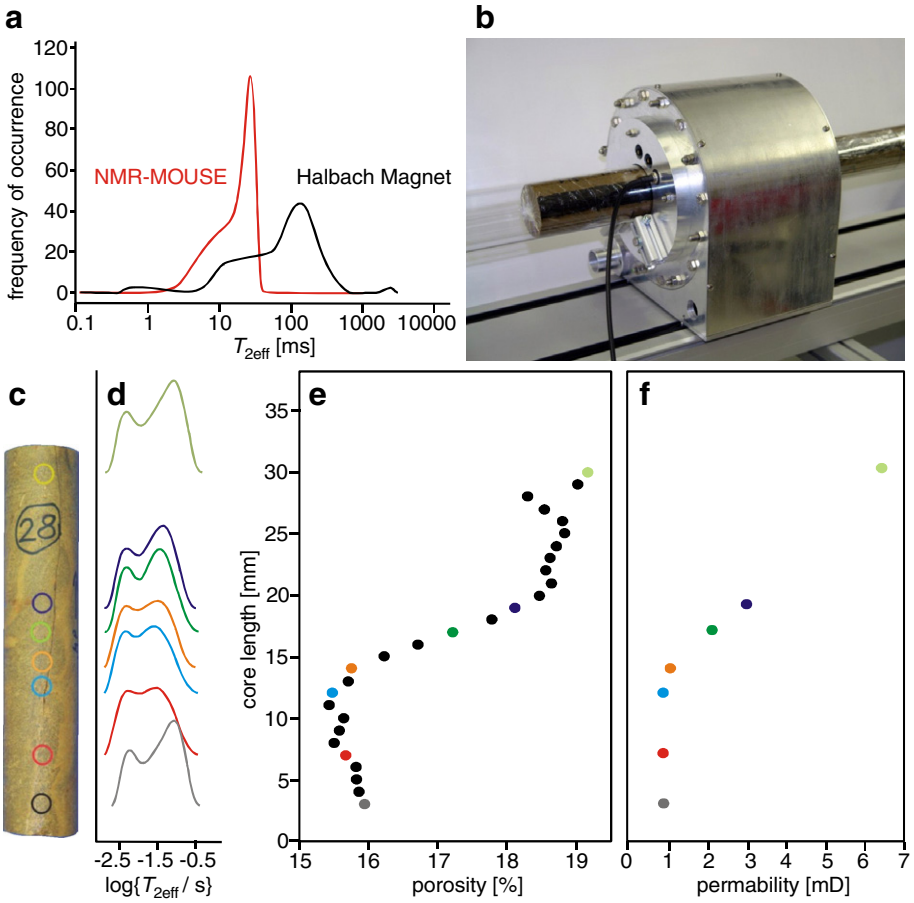

Fig. 53. Drill core analysis by mobile NMR with a Halbach scanner. (a) Relaxation time distributions for a limestone core measured in the inhomogeneous field of the NMR-MOUSE and the homogeneous field of a Halbach Magnet [472]. (b) Halbach magnet holding a drill core. The magnet is positioned relative to the stationary core by a stepper motor [222]. (c) Sandstone drill core. (d) Relaxation time distributions at the positions marked on the core. (e) Porosity from integrals of the relaxation time distribution. (f) Permeability predicted from the relaxation time distributions.

However, the small sensitive volume of the NMR-MOUSE restricts its use to samples with porosities greater than 10% [472].

But as drill cores are cylindrical, they are suited for analysis by conventional magnet geometries. The Halbach magnet (Fig. 34a and b) is ideal for mobile, on-site NMR analysis of drill cores. Its homogeneous field provides performance superior to the NMR-MOUSE in terms of sensitivity and a correct representation of the relaxation time distribution [222,434,472]. It is suitable also for performing 2D correlation NMR experiments (Fig. 25a) [222]. Such a Halbach magnet has recently been optimized for homogeneity and mounted on a sliding table (Fig. 53b) to scan drill cores (Fig. 53c) lengthwise in terms of relaxation time distributions (Fig. 53d) which can subsequently be further analyzed to investigate porosity (Fig. 53e) and to estimate permeability (Fig. 53f) and other parameters of interest [222].

4.6. Cultural heritage

Objects of cultural heritage are precious and often cannot be moved. As a consequence, their analysis needs to be entirely non-destructive and requires mobile analytical instruments. This is why single-sided mobile NMR receives increasing attention by art historians and art conservators [639–641]. So far, the original NMR-MOUSE including the Bruker Profiler [486] and the Profile NMR-MOUSE [220] have been applied successfully to different types of historical objects to analyze stone conservation [241,275,276,485,639–642], wall paintings [276,489,643], wood and paper [185,484,487,488,490–492,644], old master paintings [477,531] and mummies [645]. For the automated point-by-point analysis of large surfaces, a 2D lateral translation stage has been developed and tested [646].

4.6.1. Stone

The time-dependent water uptake and drying of stone can be followed by the evolution of various NMR parameters such as relaxation times [641], the signal amplitude, and the relaxation time spectrum [276]. The spectra of the transverse relaxation decays from water saturated samples are known to be affected by an apparent shortening of the relaxation time at long times due to signal attenuation by diffusion in the inhomogeneous

field of the single-sided NMR sensor as well as by the field inhomogeneities generated by paramagnetic impurities and the internal pore structure of the sample (Figs. 51 and 53a) [485,642]. Nevertheless, the relaxation time distributions are signatures of the material and change with the treatment of the stones during stone conservation [485,599]. Depth profiles through water saturated sandstone treated with stone strengthener have been measured with the u-shaped NMR-MOUSE at a fixed frequency by varying the distance between the scanner surface and the object. Both relaxation times extracted from a bi-exponential fit of the CPMG envelopes increase at the same depth of about 5 mm indicating a reduction in the pore size or a change in wetting properties due to the penetration of the strengthener into the stone (Fig. 54a) [485]. When large objects are analyzed, full fluid saturation is hard to achieve (Fig. 54c), yet the relaxation time distributions of treated and untreated sandstone differ (Fig. 54b), indicating that the effects of stone treatment of large objects can indeed be followed by single-sided NMR [241,275,599]. These differences are consistent with laboratory studies of partially and fully water saturated stones by single-sided NMR [647] and NMR imaging [599,647,648].

4.6.2. Wall paintings

Buildings are naturally moist. As the moisture breathing of walls determines the fate of wall paintings, moisture maps can give important information to restorers on the state of a wall painting. This has been demonstrated by an analysis of the frescoes in Vasari's house in Florence from the 16th century [489] and by systematic moisture maps of frescoes by Pellegrino degli Aretusi in the Cappella Serra of the church of Nostra Signora del Sacro Cuore in Rome. The latter (Fig. 55a) were painted between 1517 and 1519 and suffer from humidity rising from underground. The moisture was mapped in terms of the Hahn echo amplitude (Fig. 55b) [643]. A shift of the T_{2eff} distribution was observed in places with outcropping salts [600] (Fig. 55c), and the values of the transverse relaxation time were found to be correlated with past cleansing and restoration efforts [489].

The mobility and high depth resolution of the Profile NMR-MOUSE lend themselves to the investigation of hidden wall paintings. To prove the point, a covered painting (Fig. 55d) was fabricated in the secco and fresco techniques of medieval Byzantine art (Fig. 55e) at the Pratt Institute in Brooklyn [649]. A measurable signal was generated by spraying water on the surface and measuring the moisture profiles immediately after spraying and three hours later. The combined action of binder and pigments inhibit the moisture transport through the hidden secco in ways that differ for different paint formulations (Fig. 55f). This demonstrates that not only the position, but also some information about the color of hidden paintings can be accessed by NMR depth profiles.

4.6.3. Paper and wood

Old paper is made mainly from cellulose while wood consists mainly of cellulose and lignin. Both materials contain bound and free water. The organic host material as well as the water can be measured by ^{1}H NMR. Paper and wood are damaged by chemical and biological mechanisms, which change the amounts of water, the molecular weight, and the crystallinity of the cellulose molecules. As all of these factors affect the NMR relaxation times [650], the state of conservation of wood and paper can be probed by single-sided NMR. To observe the solid cellulose signal in paper, a NMR-MOUSE with a short dead-time is needed [185]. Increasing paper damage has been shown to lead to decreasing relaxation times of both the cellulose and the water [484,487]. In an artificial aging study, the results obtained by single-sided NMR have been shown to be in good agreement with those obtained by NMR in homogeneous fields [488]. Corrosive effects of iron gall ink on paper were detected in the Codex Major of the Collectio Altaemsiana [491]. Different inks have different effects on the NMR relaxation times. Even faded inks can in some cases be detected [644]. Moisture [492] and degradation [490] in wooden objects have also been studied by single-sided NMR.

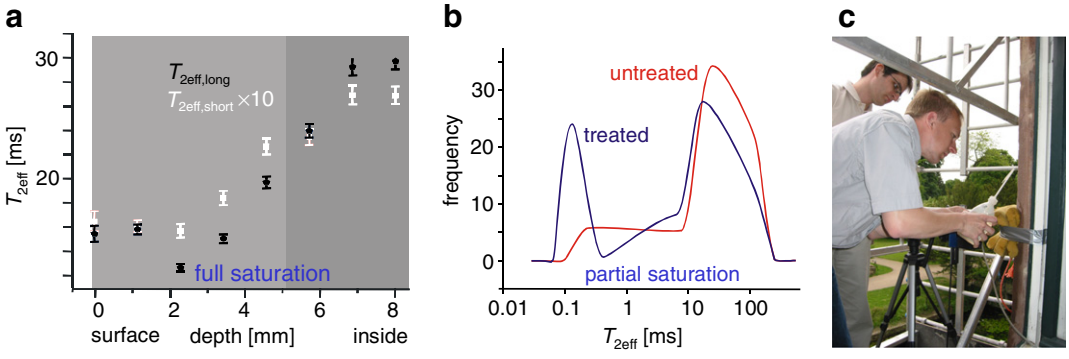

Fig. 54. Inspection of stone treatment with the NMR-MOUSE. (a) Relaxation time parameter depth profiles through fully water-saturated sandstone treated with stone strengthener [485]. (b) Relaxation time distributions of partially wet sandstone window frames from Paffendorf castle untreated and treated with stone strengthener [241]. (c) Wetting of a sandstone window frame before measurement [275].

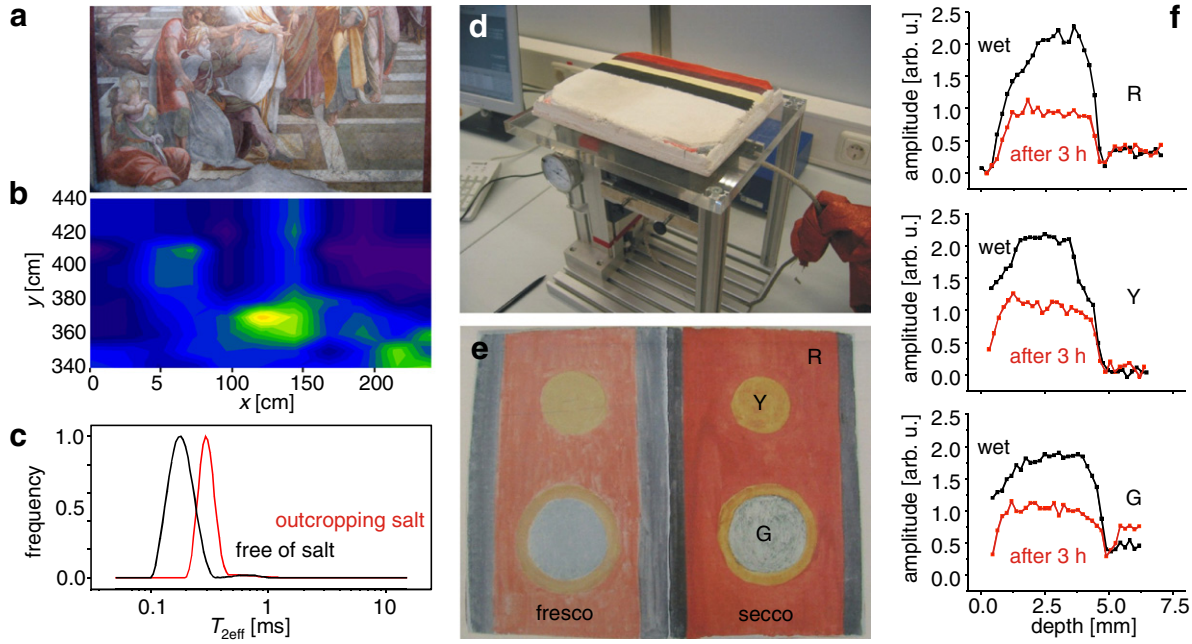

Fig. 55. (a) Photo of a fresco by Pellegrino degli Aretusi in the Cappella Serra of the church of Nostra Signora del Sacro Cuore in Rome, which suffers from degradation due to moisture rising from the ground. (b) Contour plot of the Hahn-echo amplitude which maps the moisture content. Dark denotes dry and light denotes wet. (c) Outcropping salts invoke a shift of the apparent distribution of relaxation times towards higher values [643]. (d) Phantom of hidden wall paintings on the Profile NMR-MOUSE for analysis by monitoring moisture depth profiles after spraying the surface with water. (e) A secco and a fresco painted in the techniques of medieval Byzantine art [649]. (f) The time-dependent moisture profiles through different sections of the hidden secco reveal the position of the hidden painting as well as information about different colors.

4.6.4. Old master paintings

Many old masters have produced their paintings on wooden panels, which were strengthened with a textile layer and smoothed with a gypsum base before applying the paint layers (Fig. 56a). These different layers can nicely be differentiated by the high-resolution depth profiles [477,531] acquired in a museum with the Profile NMR-MOUSE (Fig. 36b) [651]. Differences in the stratigraphy can be detected at different spots (Fig. 36c) which are unobservable by other means. It turns out, that one can even differentiate between different colors in different paint layers based on their differing transverse relaxation properties [477,531]. The longitudinal relaxation time appears to be suitable to discriminate between oil and tempera binders in old master paintings, while in more recent paintings differences are also found in T_{2eff}. A combined analysis of T_1 and T_{2eff} may help to distinguish recent from old paintings, as real-time aging over several centuries results in chemical and physical changes of paint and binder different from accelerated laboratory aging, for example, by UV light.

4.6.5. Mummies

Mummies are another subject of interest for non-destructive analysis by the NMR-MOUSE, as they may not be allowed to leave the museum or need to be chilled as the 5300-year-old glacier mummy in the Archeological

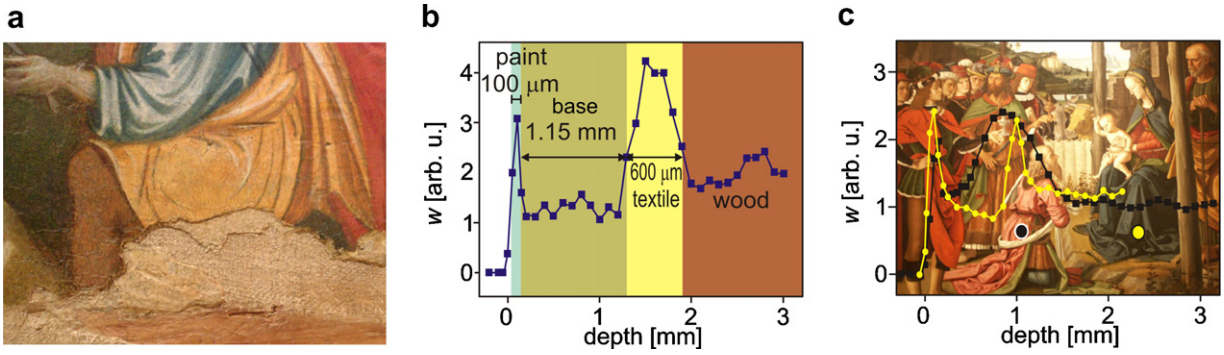

Fig. 56. Depth profiling of paintings. (a) Close-up of a damaged part of an altar frontal by Maestro del Farneto from 1290 AD in the National Gallery of Umbria in Perugia showing the stratigraphy of master paintings [651]. (b) Depth profile identifying the thickness of each layer, paint, base, and canvas on wood [531]. (c) Depth profiles at the two marked positions through Adoration of the Magi by Perugino from 1470 AD revealing differences in the thickness of the textile layer [531].

Museum in Bozen (Fig. 57a) [645]. Depth profiles can discriminate between textile wrapping from tissue and bone in Egyptian mummies, the thickness of the ice layer, tissue layers and bone structure in the glacier mummy and the density of bones in different states of decay (Fig. 37b). The bone density is the amplitude of the signal component that relaxes with the relaxation time of the bone, as long as the sensitive volume resides entirely inside the bone. The NMR-MOUSE can sample signal from solid bone rapidly and non-destructively, in contrast to the conventional and destructive way of determining bone density by mercury injection. Another way of determining bone density non-destructively is by using low-field NMR of fluids in the bone [653]. The bone density is an important indicator for the state of conservation of the bone material. This is corroborated by the observation, that an Egyptian mummy head and a 1000-year-old skull give NMR depth profiles with amplitudes significantly lower than those of profiles through a modern skull and through the forehead of one of the authors of this review. The state of bone conservation is a quantity in demand in the search for historic DNA: the higher the bone density, the higher the chance to find DNA.

5. Outlook

The idea of the pioneers of mobile NMR was to measure the signal from fluids and moisture in boreholes, soil, building materials, food and the like [129]. Single-sided sensors as small as the NMR-MOUSE were envisioned in the mid eighties to be buried in soil, silos and piles of grain to monitor moisture and drying processes [32]. In the fabrication of powdery chemicals like laundry detergents, molecular sieves, etc., this is a topic of continuing technical importance (Fig. 58a and b) [595,654–656]. So is process control with NMR sensors installed in the production line [61,127,131,447], which gains further momentum by the recent advances in the development of methods and hardware for mobile NMR.

Current hardware developments concern three avenues. One is the miniaturization of the spectrometer to laptop-size devices (Fig. 14) and smaller entities like single-chip spectrometers [270]. The latter is a development born out of the need for sensitive magnetometers based on the principles of NMR [91]. While such small devices cannot include a powerful rf amplifier, the output power may be sufficient to drive micro-coils [523,524] for chemical identification of substances [441] or characterization of single cells [657,658]. Along with such extreme miniaturization, the technology for massive, parallel NMR evolves for combinatorial studies, high throughput analysis [659], and online sensing of chemical and physical processes, for example, in micro-reactors [660,661].

A second avenue is the development of single-sided magnets following the open Halbach magnet [210,212,219] and related concepts [202,203], and the barrel magnet [222–226], to arrive at an accessible depth of more than just one or two centimeters together with a favorable figure of merit for the ratio of the accessible volume over the magnet size.

The third avenue concerns the development of specialized magnets with open or closed geometries that provide favorable field profiles for new and emerging NMR methodologies. The most conventional profile is that of a magnetic field homogeneous across the sample volume or within a certain region of the sample. The first can be achieved by shimming Halbach-type and similar closed magnets to maximum homogeneity [88,222] and by reducing the size of the sensitive volume [431]. The second one is achieved by adjusting the field profiles of open sensors like the NMR-MOUSE [89] to local homogeneity external to the sensor for localized spectroscopy and imaging by use of conventional NMR methodology. A more general view of this is the concept of *ex situ* NMR [85,230], where a

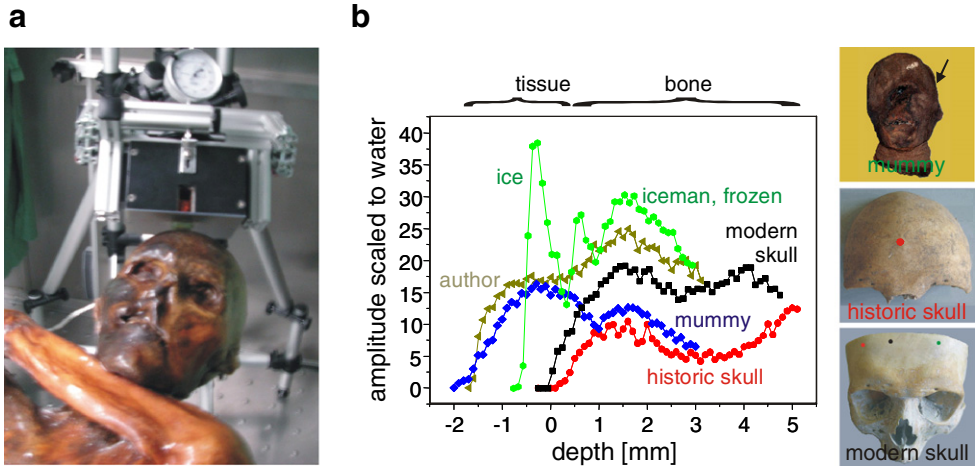

Fig. 57. Depth profiling of foreheads [645]. (a) Photo of the frozen glacier mummy from the Archaeological Museum in Bozen, Tyrol with the Profile NMR-MOUSE mounted near the forehead to measure a depth profile. (b) Depth profiles through the foreheads of the iceman, a modern skull, a 1000-year-old historic skull [652], a skull of an Egyptian mummy [652], and Bernhard Blümich.

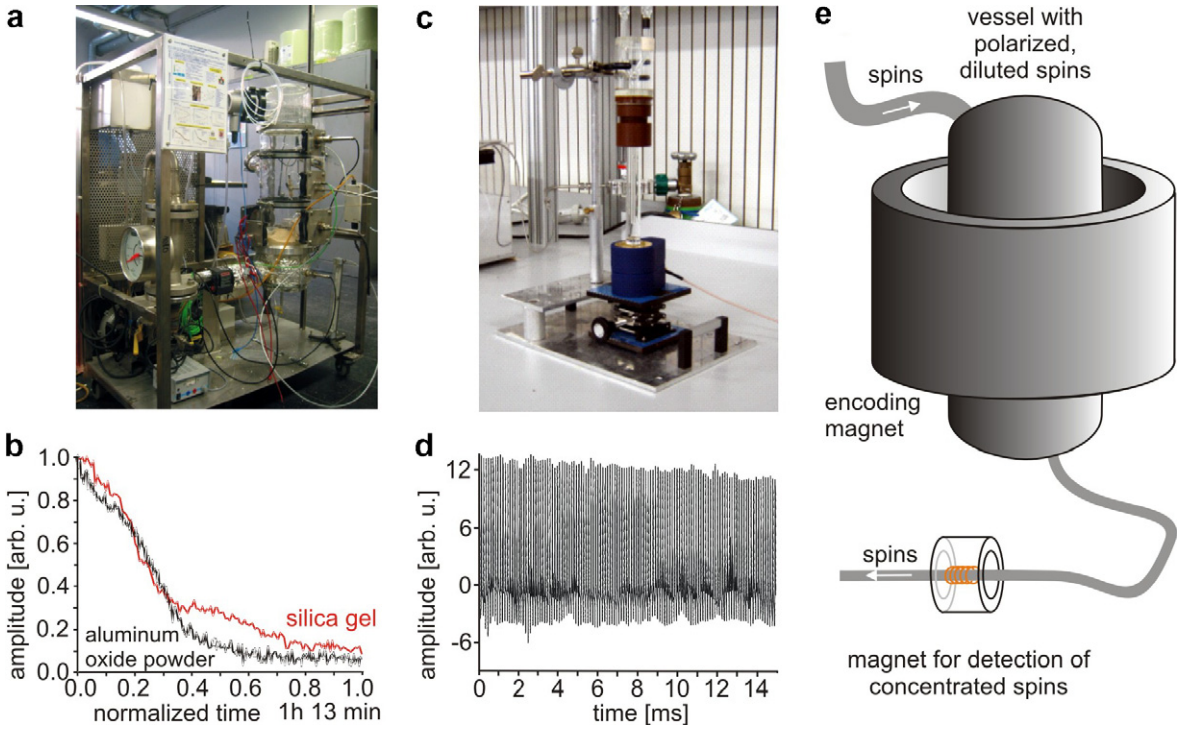

Fig. 58. Some applications of mobile NMR. (a) Setup for monitoring the drying of powders by a bar-magnet NMR-MOUSE embedded in a powder inside the round glass container to the right. (b) Drying curves of water-wet powders. The silica gel shows two drying processes, a fast one from interstitial water and a slower one from pore water. (c) Setup for measuring hyperpolarized ^{129}Xe passing through toluene with the bar-magnet NMR-MOUSE. (d) Beginning of a single-shot Xenon NMR CPMG echo train measured with the NMR-MOUSE at 4.9 MHz. (e) NMR with remote detection for flowing spins. The spins are encoded at high dilution and detected with high sensitivity at high concentration.

homogeneous field is not required, but one with a profile suitable for obtaining good images and spectra in combination with matched rf field profiles [82,158,240] and suitable rf excitation such as shim pulses for excitation of large sample volumes [249].

Current developments in the NMR methodology can be grouped into four areas. The first concerns the improvement of the measurement speed by clever pulse-sequence design. Here, multi-echo schemes provide a straightforward approach to improve the sensitivity in a conservative way for imaging, diffusion, and flow measurements. Here the inhomogeneous fields of single-sided sensors can be put to good use by the selection of coherence pathways [272] in single-shot measurements of relaxation, diffusion and flow. The spatial encoding inherent to NMR in an inhomogeneous field can further be utilized to measure images and spectra rapidly [392–394,424,425]. The practical use of such concepts, however, may suffer from a lack of sensitivity in polarization and detection.

The second area of methodological activity is the *ex situ* NMR concept mentioned above [85,230], i.e. the development of generalized concepts for NMR in inhomogeneous fields. It consists of shimming the $\boldsymbol{B}_0$ and $\boldsymbol{B}_1$ fields not necessarily to homogeneity but to match each other in their spatial dependences and then apply shim-pulses that impart an individual phase to the magnetization in each voxel, so that at the time of detection, the signal appears as if it had evolved in a homogeneous field.

The third area concerns sensitivity enhancement either by producing an initial polarization higher than the equilibrium polarization during detection or by boosting the detection sensitivity. Hyperpolarization can be induced, for example by prepolarization of the sample in a strong but inhomogeneous field prior to detection in a weak and inhomogeneous field such as the Earth's field [92,93,96,103], by the chemical reaction with para-hydrogen [109–112,662], laser polarization of noble gases [104–107,663], polarization transfer from the electrons [113–115,664,665] and by spin injection with solid state devices [666,667]. For example, hyperpolarized Xenon can be dissolved in toluene and detected in the more than 10 T/m gradient of the bar-magnet NMR-MOUSE (Fig. 58c and d). The detection sensitivity can be boosted at low field by the use of SQUIDS [96,98,99] and optical magnetometers [102,668]. All of these technologies bear great promise for use with portable NMR devices. One outstanding novel concept of use is remote detection NMR (Fig. 58e) [116–119,669]. In this method, the magnetization is encoded in a diluted state and then transported and concentrated for detection with high sensitivity. Such situations are likely to be encountered in chemical engineering [122], where the transport of matter [670–672] is a fundamental property of the discipline, so that the use of mobile NMR tools for encoding and detection can be anticipated, for example, in the analysis of porous media [673,674] and micro-fluidic devices [675,676].

The fourth area concerns NMR at ultra-low fields. This extreme approach is interesting, as such fields are either available for free in terms of the Earth's magnetic field, or can be produced with high homogeneity and at relatively low cost. The spin physics is quite different in that limit, as the chemical-shift cannot be resolved, but the spin–spin couplings are still active and bear chemical information [407,677]. Bio-magnetic signals can be of the same order of magnitude as NMR signals at ultra-low fields, and the same detection technology can be used in both cases [678,679]. In porous media, the field inhomogeneities due to susceptibility differences across interfaces become negligible, and metal containers become transparent to electromagnetic waves [400]. As bulky magnets are no longer needed, Earth's field and other low-field NMR investigations by spectroscopy [94–97,108,663,680,681] and imaging [168,396,397,405,439,682–684] can be performed with mobile instrumentation.

Mobile instrumentation for measuring relaxation times has been available for a while and is used most prominently in well-logging [5,175]. Mobile instruments are already available for high-resolution depth profiling [25,220], 2D and 3D imaging [76,78,242] as well as chemical-shift resolved spectroscopy [89,441] with closed and with open sensors: the technology will expand and be further refined driven by a wealth of new applications for NMR [493] and possibly extended to include ESR outside the laboratory [685,686]. Some key applications are non-destructive testing of food, art, medical implants, and devices with critical safety features. Other uses of mobile NMR are multifunctional NMR sensors in industrial fabrication processes and chemical plants. Some outstanding new uses at this time appear to be chemical NMR spectroscopy by inexpensive devices with the quality of the spectra in the 1970s, and portable imaging devices for use in developing countries, in emergency situations, and for screening of goods in high-security areas such as on airports. This approach will complement existing nuclear quadrupole resonance (NQR) technology [687–689] by providing better chemical sensitivity.

Acknowledgements

Foremost BB thanks Peter Blümler for the numerous creative ideas and valuable contributions that started the NMR-MOUSE line of work. Dan Demco joined the project at a later stage, and was the driving force in formulating the theoretical foundations of advanced experiments in inhomogeneous fields together with several PhD students from Aachen and visiting scientists from Cluj-Napoca. Gisela Zimmer-Guthausen was successfully leading the MOUSE team at the time when many new methods and material properties were explored. Andreas Guthausen, "Goody" is remembered for exploring many new applications and Flaviu Balibanu for his theoretical work in understanding single-sided NMR in inhomogeneous fields. Both have passed away but their names and achievements are remembered and honored in this review. We also thank the many other past and current members of the Aachen MOUSE group, in particular Ralf Savelsberg, Kidist Hailu, Ralf Eymael, Anette Wiesmath, Andrea Schwaiger, Martin Klein, Radu Fechete, Beatrice Lego, Kai Kremer, Nicolae Goga, Maria Baias and Jürgen Kolz, as well as the visiting scientists, Koji Saito, Sophia Anferova, Vladimir Anferov, Mihai Todica, and Vasiliki Demas. Eiichi Fukishima helped with comments and information on the development of mobile MR in the USA, Annalaura Segre introduced the NMR-MOUSE to Cultural Heritage, and Frank Rühli provided historic mummies and bones. Last but not least BB acknowledges the friendship and hospitality of Alex Pines and Jeff Reimer during the time of writing the overwhelming part of this review at the University of California at Berkeley, while the Miller Institute for Basic Research in Science is acknowledged for generous support of that stay. Most of the work in mobile NMR in Aachen was funded by grants from Deutsche Forschungsgemeinschaft DFG most notably the collaborative research initiative FOR333 "Surface NMR of Elastomers and Biological Tissues". Further support from Bundesministerium für Bildung und Forschung (BMBF) and Fonds der Chemischen Industrie is acknowledged. The work on Cultural Heritage was supported by the European Community projects Eureka Σ! 2214 MOUSE and EU-ARTECH. The authors are greatful to Andrew McDowell for providing Fig. 34c, to Jasper Jackson for proof reading the manuscript, and to Adrian Blümich, Gerlind Breuer, and Ingrid Schmitz for help with the literature and with editing.

References

[1] A. Abragam, The Principles of Nuclear Magnetism, Clarendon Press, Oxford, 1961.
[2] E.M. Haacke, R.W. Brown, M.R. Thompson, R. Venkatesan, Magnetic Resonance Imaging, Physical Principles and Sequence Design, Wiley-Liss, New York, 1999.
[3] R.R. Ernst, G. Bodenhausen, A. Wokaun, Principles of Nuclear Magnetic Resonance in One and Two Dimensions, Clarendon Press, Oxford, 1987.
[4] B. Blümich, NMR Imaging of Materials, Clarendon Press, Oxford, 2000.
[5] G.R. Coates, L. Xiao, M.G. Prammer, NMR Logging Principles and Applications, Halliburton Energy Services, Houston, 1999.
[6] R.L. Kleinberg, Well logging, in: D.M. Grant, R.K. Harris (Eds.), Encyclopedia of NMR, Wiley-Liss, New York, 1996, pp. 4960–4969.
[7] E.L. Hahn, Spin echoes, Phys. Rev. 80 (1950) 580–594.
[8] E.L. Hahn, Lille conference talk, J. Magn. Reson. 179 (2006) 9–19.
[9] H.Y. Carr, E.M. Purcell, Effects of diffusion on free precession in nuclear magnetic resonance experiments, Phys. Rev. 94 (1954) 630–638.
[10] S. Meiboom, D. Gill, Modified spin–echo method for measuring nuclear relaxation times, Rev. Sci. Instrum. 29 (1958) 688–691.
[11] R.J.S. Brown, Nuclear magnetism logging at the Coyote Institute, Magn. Reson. Imaging 14 (1996) 811–817.
[12] R.J.S. Brown, R. Chandler, J.A. Jackson, R.L. Kleinberg, M.N. Miller, Z. Paltiel, M.G. Prammer, The history of NMR well logging, Concepts Magn. Reson. 13 (2001) 340–411, Special issue.
[13] D.E. Woessner, The early days of NMR in the Southwest, Concepts Magn. Reson. 13 (2001) 77–102.

[14] L.J. Burnett, J.A. Jackson, Remote (inside-out) NMR. II. Sensitivity of NMR detection for external samples, J. Magn. Reson. 41 (1980) 406–410.
[15] R.K. Cooper, J.A. Jackson, Remote (inside-out) NMR. I. Remote production of a region of homgeneous magnetic field, J. Magn. Reson. 41 (1980) 400–405.
[16] J.A. Jackson, L.J. Burnett, F. Harmon, Remote (inside-out) NMR. III. Detection of nuclear magnetic resonance in a remotely produced region of homogeneous magnetic field, J. Magn. Reson. 41 (1980) 411–421.
[17] Southwest Research Institute, 6220 Culebra Road., San Antonio, Texas, USA, Available from: <http://www.swri.edu/>.
[18] C.I. Nicholls, A. De Los Santos, Hydrogen transient nuclear magnetic resonance for industrial moisture sensing, Drying Technol. 9 (1991) 849–873.
[19] Transportation Research Board, Development of prototype soil moisture sensors, NCHRP Research Results Digest 75, Transportation Research Board, Washington, 1975.
[20] G.A. Matzkanin, R.F. Paetzold, Measuring Soil Water Content Using Pulsed Nuclear Magnetic Resonance, ASAE Winter Mtg., Paper No. 82-2619, Chicago, Illinois, 1982.
[21] G.A. Matzkanin, W.L. Rollwitz, J.D. King, R.F. Paetzold, Principles of nuclear magnetic resonance for agricultural operations, in: Proceedings of the National Conference on Agricultural Electronics Applications, vol. l, ASAE 8-84, December 1984, pp. 309–318.
[22] R.F. Paetzold, G.A. Matzkanin, A. De Los Santos, Surface soil water content measurement using pulsed nuclear magnetic resonance techniques, Soil Sci. Soc. Am. J. 49 (1985) 537–540.
[23] R.F. Paetzold, A. De Los Santos, G.A. Matzkanin, Pulsed nuclear magnetic resonance instruments for soil–water content measurement: sensor configurations, Soil Sci. Soc. Am. J. 51 (1987) 287–298.
[24] G.A. Matzkanin, J.D. King, W.L. Rollwitz, Nondestructive measurement of moisture in concrete using pulsed NMR, in: Proceedings of the 13th Symposium on Nondestructive Evaluation, San Antonio, TX, April 21–23, 1981.
[25] A. Marko, B. Wolter, W. Arnold, Application of portable nuclear magnetic resonance surface probe porous media, J. Magn. Reson. 185 (2007) 19–25.
[26] R.M. Pearson, L.R. Ream, C. Job, J. Adams, Use of NMR spectrometers for process control, Cereal Foods World 32 (1987) 822–826.
[27] R.M. Pearson, Using industrial magnetic resonance for moisture monitoring, Cereal Foods World 32 (1987) 658.
[28] R.M. Pearson, D.I. Wetzel, Rapid on-line moisture determination of whole kernel wheat by pulsed nuclear magnetic resonance, Cereal Foods World 30 (1985) 563–564.
[29] G.A. Persyn, W.L. Rollwitz, Transient NMR quantitative measurements, JAOCS 48 (1971) 67–69.
[30] W.L. Rollwitz, G.A. Persyn, On-stream NMR measurements and control, JAOCS 48 (1971) 59–66.
[31] W.L. Rollwitz, J.D. King, G.A. Matzkanin, R.F. Paetzhold, Magnetic resonance: a versatile sensor for agricultural applications, Proceedings of the National Conference on Agricultural Electronics Applications ASAE, Chicago, Il, December 1983, pp. 766–772.
[32] W.L. Rollwitz, Using radiofrequency spectroscopy in agricultural applications, Agric. Eng. 66 (1985) 12–14.
[33] J. Derwin King, W.L Rollwitz, G.A. Matzkanin, Nuclear Magnetic Resonance Mine Detection Part I, USAEERD Contract No. DAAK02-72-C-0467, Final Report, AD 5225380, October 1973.
[34] J. Derwin King, W.L. Rollwitz, G.A. Matzkanin, Nuclear Magnetic Resonance Mine Detection Part II, USAEERD Contract No. DAAK02-72-C-0467, Final Report, AD 52 709L, December 1973.
[35] J.D. King, W.L. Rollwitz, G.A. Matzkanin, Nuclear Magnetic Resonance Techniques for Explosives Detection, U.S. Army Mobility Equipment Research and Development Center, Final Report, Contract No. DAAK02-74-C-0056, AD-C-003154, June 1975.
[36] J.D. King, W.L. Rollwitz, G.A. Matzkanin, Nuclear Magnetic Resonance Techniques for Explosives Detection Part III, U.S. Army Mobility Equipment Research and Development Center, Final Report Part III, Contract No. DAAK02-74-C-0056, AD-B026059, February 1977.
[37] J.D. King, W.L. Rollwitz, A. De Los Santos, J. Roland Gonano, Applications of nuclear magnetic resonance to the detection and identification of explosives, in: Proceedings of New Concepts Symposium and Workshop on the Detection and Identification of Explosives, Reston, VA, October 30–31, 1978.
[38] J.D. King, W.L. Rollwitz, GA.Matzkanin, Nuclear Magnetic Resonance Techniques for Explosives Detection, Part IV, U.S. Army Mobility Equipment Research and Development Center, Final Report Part IV, Contract No. DAAK02-74-C-0056, AD-B026430, February 1978.
[39] J.D. King, W.L. Rollwitz, A. De Los Santos, Nuclear magnetic resonance for explosives detection, in: Proceedings of the ASTM Symposium on Airport Security, Philadelphia, PA, April 22, 1982.
[40] J.D. King, W.L. Rollwitz, A. De Los Santos, J.R. Gonano, Application of Nuclear Magnetic Resonance to the detection and identification of explosives, in: Proceedings of New Concepts Symposium Workshop Detection Identification of Explosives, Reston, VA, 30 October–1 November 1978.
[41] L. Burnett, Single-sided NMR, Quantum Design Newslett. 4 (1994) 9.
[42] G.A. Matzkanin, A review of nondestructive testing of composites using NMR, in: P. Höller, G. Dobmann, C.O. Ruud, R.E. Green (Eds.), Nondestructive Characterization of Materials, Springer, Berlin, 1989, pp. 655–669.
[43] G.A. Matzkanin, A review of nuclear magnetic resonance for nondestructively characterizing materials, in: 11th International Symposium on Nondestructive Characterization of Materials, Berlin, Germany, 24–28 June, 2002.
[44] G.A. Matzkanin, Application of spatially localized NMR to nondestructive evaluation, in: Proceedings of 2nd World Conference NDT, 3–8, Las Vegas, NV, November 1985.
[45] M. Pearson, T.L. Parker, The use of nuclear magnetic resonance spectrometers as on-line analyzers for rotary kiln control, Light Metals, Los Angeles, 27 February–1 March 1984, pp. 81–89.
[46] G. Eidmann, R. Savelsberg, P. Blümler, B. Blümich, The NMR MOUSE: a mobile universal surface explorer, J. Magn. Reson. A122 (1996) 104–109.
[47] A.A. Samoilenko, D.Yu. Artemov, A.L. Sibel'dina, Application of NMR imaging to the investigation of the solid state, Bruker Rep. 2 (1987) 30–31.
[48] A.A. Samoilenko, D.Yu. Artemov, A.L. Sibel'dina, Formation of sensitive layer experiments on NMR subsurface imaging of solids, JETP Lett. 47 (1988) 417–419.
[49] M.J.D. Mallet, R.L. Halse, J.H. Strange, Stray field imaging by magnetic field sweep, J. Magn. Reson. 132 (1998) 172–175.
[50] P.J. McDonald, Stray field magnetic resonance imaging, Prog. Nucl. Magn. Reson. Spectr. 30 (1997) 69–99.
[51] P.J. McDonald, B. Newling, Stray field magnetic resonance imaging, Rep. Prog. Phys. 61 (1998) 1441–1493.
[52] A. Kumar, D. Welti, R.R. Ernst, NMR Fourier zeugmatography, J. Magn. Reson. 18 (1975) 69–83.
[53] D.E. Traficante (Ed.), History of NMR well logging, Concepts Magn. Reson., 13, Wiley, New York, 2001.
[54] J.G. Powles, P. Mansfield, Double-pulse nuclear-resonance transients in solids, Phys. Lett. 2 (1962) 58–59.
[55] E.D. Ostroff, J.S. Waugh, Multiple spin echoes and spin locking in solids, Phys. Rev. Lett. 16 (1966) 1097–1098.
[56] P. Mansfield, D. Ware, NMR spin dynamics in solids. I. Artificial line narrowing and Zeeman spin–spin relaxation in the rotating frame, Phys. Rev. 168 (1968) 318–334.
[57] F. Balibanu, K. Hailu, R. Eymael, D.E. Demco, B. Blümich, NMR in inhomogeneous magnetic fields, J. Magn. Reson. 145 (2000) 246–258.

[58] M.D. Hürlimann, D.D. Griffin, Spin dynamics of Carr–Purcell–Meiboom–Gill-like sequences in grossly inhomogeneous B_0 and B_1 fields and application to NMR well logging, J. Magn. Reson. 143 (2000) 120–135.
[59] G. Zimmer, A. Guthausen, B. Blümich, Characterization of technical elastomers by the NMR-MOUSE, Solid State Nucl. Magn. Reson. 12 (1998) 183–190.
[60] A. Sezginer, R.L. Kleinberg, M. Fukuhara, L.L. Latour, Very rapid simultaneous measurement of nuclear magnetic resonance spin–lattice relaxation time and spin–spin relaxation time, J. Magn. Reson. 92 (1991) 504–527.
[61] A. Guthausen, G. Zimmer, P. Blümler, B. Blümich, Analysis of polymer materials by surface NMR via the NMR MOUSE, J. Magn. Reson. 130 (1998) 1–7.
[62] A. Guthausen, G. Zimmer, R. Eymael, U. Schmitz, P. Blümler, B. Blümich, Soft-matter relaxation by the NMR MOUSE, in: P. Blümler, B. Blümich, R. Botto, E. Fukushima (Eds.), Spatially Resolved Magnetic Resonance, Wiley-VCH, Weinheim, 1998, pp. 195–209.
[63] R.L. Vold, J.S. Waugh, M.K. Klein, D.E. Phelps, Measurement of spin relaxation in complex systems, J. Chem. Phys. 48 (1968) 3831–3832.
[64] J.L. Markley, W.T. Horsley, M.P. Klein, Spin–lattice relaxation in slowly relaxing complex spectra, J. Chem. Phys. 55 (1971) 3604–3605.
[65] M.D. Hürlimann, Diffusion and relaxation effects in general stray field NMR experiments, J. Magn. Reson. 148 (2001) 367–378.
[66] M.D. Hürlimann, L. Venkataramanan, C. Flaum, P. Speier, C. Karmonik, R. Freedman, N. Heaton, Diffusion-editing: new NMR measurement of saturation and pore geometry, in: 43rd Annual SPWLA Meeting, Osio, Japan, June 2–5, 2002, pp. 1–14.
[67] G. Leu, E.J. Fordham, M.D. Hürlimann, P. Frulla, Fixed and pulsed gradient diffusion methods in low-field core analysis, Magn. Reson. Imaging 23 (2005) 305–309.
[68] Y.-Q. Song, M.D. Hürlimann, C. Flaum, A method for rapid characterization of diffusion, J. Magn. Reson. 161 (2003) 222–233.
[69] E.O. Stejskal, J.E. Tanner, Spin diffusion measurements: spin echoes in the presence of a time-dependent field gradient, J. Chem. Phys. 42 (1965) 288–292.
[70] A. Wiesmath, C. Filip, D.E. Demco, B. Blümich, Double-quantum-filtered NMR signals in inhomogeneous magnetic fields, J. Magn. Reson. 149 (2001) 258–263.
[71] A. Wiesmath, C. Filip, D.E. Demco, B. Blümich, NMR of multipolar spin states excited in strongly inhomogeneous magnetic fields, J. Magn. Reson. 154 (2002) 60–72.
[72] Y.-Q. Song, U.M. Scheven, An NMR technique for rapid measurement of flow, J. Magn. Reson. 172 (2005) 31–35.
[73] P.J. Prado, B. Blümich, U. Schmitz, One dimensional imaging with a palm-size NMR-probe, J. Magn. Reson. 144 (2000) 200–206.
[74] F. Casanova, B. Blümich, Two-dimensional imaging with a single-sided NMR probe, J. Magn. Reson. 163 (2003) 38–45.
[75] F. Casanova, J. Perlo, B. Blümich, K. Kremer, Multi-echo imaging in highly inhomogeneous magnetic fields, J. Magn. Reson. 166 (2004) 76–81.
[76] J. Perlo, F. Casanova, B. Blümich, 3D imaging with a single-sided sensor: an open tomograph, J. Magn. Reson. 166 (2004) 228–235.
[77] F. Casanova, J. Perlo, B. Blümich, Velocity distributions remotely measured with a single-sided NMR sensor, J. Magn. Reson. 171 (2004) 124–130.
[78] J. Perlo, F. Casanova, B. Blümich, Velocity imaging by ex situ NMR, J. Magn. Reson. 173 (2005) 254–258.
[79] Y.-Q. Song, L. Venkataramanan, M.D. Hürlimann, M. Flaum, P. Frulla, S. Straley, T_1–T_2 correlation spectra obtained using a fast two-dimensional laplace inversion, J. Magn. Reson. 154 (2002) 261–268.
[80] M.D. Hürlimann, L. Venkataramanan, Quantitative measurement of two-dimensional distribution functions of diffusion and relaxation in grossly inhomogeneous fields, J. Magn. Reson. 157 (2002) 31–42.
[81] J. Perlo, F. Casanova, B. Blümich, Single-sided sensor for high-resolution NMR spectroscopy, J. Magn. Reson. 180 (2006) 274–279.
[82] C.A. Meriles, D. Sakellariou, H. Heise, A.J. Moulé, A. Pines, Approach to high-resolution ex situ NMR spectroscopy, Science 293 (2001) 82–85.
[83] W.P. Aue, E. Bartholdi, R.R. Ernst, Two-dimensional spectroscopy. Application to nuclear magnetic resonance, J. Chem. Phys. 64 (1976) 2229–2246.
[84] P. Blümler, B. Blümich, Magnetization filters: applications to NMR imaging of elastomers, Magn. Reson. Imaging 10 (1992) 779–788.
[85] D. Sakellariou, C.A. Meriles, A. Pines, Advances in ex-situ nuclear magnetic resonance, C.R. Phys. 5 (2004) 337–347.
[86] K. Halbach, Design of permanent multipole magnets with oriented rare earth cobalt material, Nucl. Instrum. Methods 169 (1980) 1–10.
[87] K. Halbach, Strong rare earth cobalt quadrupoles, IEEE Trans. Nucl. Sci. NS-26 (1979) 3882–3884.
[88] H. Raich, P. Blümler, Design and construction of a dipolar Halbach array with a homogeneous field from identical bar magnets: NMR Mandhalas, Concepts Magn. Reson. B23 (2004) 16–25.
[89] J. Perlo, F. Casanova, B. Blümich, Ex situ NMR in highly homogeneous fields: ^{1}H spectroscopy, Science 315 (2007) 1110–1112.
[90] P.T. Callaghan, M. Le Gros, Nuclear spins in the Earth's magnetic field, Am. J. Phys. 50 (1982) 709–713.
[91] G.S. Waters, P.D. Francis, A nuclear magnetometer, J. Sci. Instrum. 35 (1958) 88–93.
[92] G.J. Bene, Nuclear magnetism of liquid systems in the earth field range, Phys. Rep. 58 (1980) 213–267.
[93] P.T. Callaghan, C.D. Eccles, J.D. Seymour, An Earth's field NMR apparatus suitable for pulsed gradient spin echo measurements of diffusion under Antarctic conditions, Rev. Sci. Instrum. 68 (1997) 4263–4270.
[94] S. Appelt, H. Kühn, F.W. Häsing, B. Blümich, Chemical analysis by ultrahigh resolution nuclear magnetic resonance in the Earth's magnetic field, Nat. Phys. 2 (2006) 105–109.
[95] S. Appelt, F.W. Häsing, H. Kühn, J. Perlo, B. Blümich, Mobile high resolution xenon nuclear magnetic resonance spectroscopy in the Earth's magnetic field, Phys. Rev. Lett. 94 (2005), 197602, 1–4.
[96] R. McDermott, A.H. Trabesinger, M. Mück, E.L. Hahn, A. Pines, J. Clarke, Liquid-state NMR and scalar couplings in microtesla magnetic fields, Science 295 (2002) 2247–2249.
[97] S. Appelt, From Photon Spin to Magnetic Resonance Imaging, habilitation thesis, section 5.1: Coil-based NMR spectrometer at low frequencies, RWTH Aachen University, 2004, p. 101.
[98] R. Kleiner, D. Koelle, F. Ludwig, J. Clarke, Superconducting quantum interference devices, state of the art and applications, Proc. IEEE 92 (2004) 1534–1548.
[99] N. Oukhanski, R. Stolz, V. Zakosarenko, H.-G. Meyer, Low-drift broadband directly coupled dc SQUID read-out electronics, Phys. C: Supercond. 368 (2002) 166–170.
[100] V.V. Yashchuk, J. Granwehr, D.F. Kimball, S.M. Rochester, A.H. Trabesinger, J.T. Urban, D. Budker, A. Pines, Hyperpolarized xenon nuclear spins detected by optical atomic magnetometry, Phys. Rev. Lett. 93 (2004), 160801, 1–4.
[101] I.M. Savukov, M.V. Romalis, NMR detection with an atomic magnetometer, Phy. Rev. Lett. 94 (2005), 123001, 1–4.
[102] D. Budker, M. Romalis, Optical magnetometry, Nat. Phys. 3 (2007) 227–234.
[103] A.M. Thayer, A. Pines, Zero-field NMR, Acc. Chem. Res. 20 (1984) 47–53.
[104] W. Happer, Optical pumping, Rev. Mod. Phys. 44 (1972) 169–249.
[105] B. Driehuys, G.D. Cates, E. Miron, K. Sauer, D.K. Walter, W. Happer, High-volume production of laser-polarized ^{129}Xe, Appl. Phys. Lett. 69 (1996) 1668–1670.
[106] S. Appelt, A. Ben-Amar Baranga, C.J. Erickson, M.V. Romalis, A.R. Young, W. Happer, Theory of spin-exchange optical pumping of ^{3}He and ^{129}Xe, Phys. Rev. A 58 (1998) 1412–1439.
[107] Y.-Q. Song, B.M. Goodson, A. Pines, NMR and MRI using laser-polarized xenon, Spectroscopy 14 (1999) 26–33.

[108] G. Navon, Y.-Q. Song, T. Room, S. Appelt, R.E. Taylor, A. Pines, Enhancement of solution NMR and MRI with laser-polarized xenon, Science 271 (1996) 1848–1851.
[109] C.R. Bowers, D.P. Weitekamp, Transformation of symmetrization order to nuclear-spin magnetization by chemical reaction and nuclear magnetic resonance, Phys. Rev. Lett. 57 (1986) 2645–2648.
[110] C.R. Bowers, D.P. Weitekamp, Parahydrogen and synthesis allow dramatically enhanced nuclear alignment, J. Am. Chem. Soc. 109 (1987) 5541–5542.
[111] T.C. Eisenschmid, R.U. Kirss, P.P. Deutsch, S.I. Hommeltoft, R. Eisenberg, J. Bargon, R.G. Lawler, A.L. Balch, Para hydrogen induced polarization in hydrogenation reactions, J. Am. Chem. Soc. 109 (1987) 8089–8091.
[112] J. Natterer, J. Bargon, Parahydrogen induced polarization, Prog. NMR Spectroscopy 31 (1997) 293–315.
[113] A.W. Overhauser, Polarization of nuclei in metals, Phys. Rev. 92 (1953) 411–415.
[114] T.R. Carver, C.P. Slichter, Polarization of nuclei spins in metals, Phys. Rev. 92 (1953) 212–213.
[115] K.H. Hausser, D. Stehlik, Dynamic nuclear polarisation in liquids, Adv. Magn. Reson. 3 (1968) 79–139.
[116] A.J. Moulé, M.M. Spence, S. Han, J.A. Seeley, K.L. Pierce, S. Saxena, A. Pines, Amplification of xenon NMR and MRI by remote detection, Proc. Natl. Acad. Sci. USA 100 (2003) 9122–9127.
[117] J. Granwehr, E. Harel, S. Han, S. Garcia, A. Pines, Time-of-flight flow imaging using NMR remote detection, Phys. Rev. Lett. 95 (2005), 075503, 1–4.
[118] S. Han, J. Granwehr, S. Garcia, E.E. McDonnell, A. Pines, Auxiliary probe design adaptable to existing probes for remote detection NMR, MRI, and time-of-flight tracing, J. Magn. Reson. 182 (2006) 260–272.
[119] S. Han, J. Granwehr, C. Hilty, Broadening the range of applications of NMR and MRI by remote detection, in: S. Stapf, S. Han (Eds.), NMR in Chemical Engineering, Wiley-VCH, Weinheim, 2006, pp. 139–163.
[120] J. Ferguson, The promise of portable MRI, Eng. Sci. 2 (2001) 29–33.
[121] B. Blümich, NMR-Bildgebung in den Materialwissenschaften, Nordrhein-Westfälische Akademie der Wissenschaften, Vorträge zur 483. Sitzung, Verlag Ferdinand Schöningh, München, 2004, pp. 33–54.
[122] L.F. Gladden, Magnetic resonance: ongoing and future role in chemical engineering research, AIChE J. 49 (2003) 2–9.
[123] J.G. Powles, The atomic nucleus as a magnetic top, New Sci. 5 (1959) 26–31.
[124] O.A. Shushakov, Groundwater NMR in conductive water, Geophysics 61 (1996) 998–1006.
[125] G.E. Maciel, NMR in industrial process control and quality control, in: G.E. Maciel (Ed.), Nuclear Magnetic Resonance in Modern Technology, Kluwer, Dordrecht, 1994, pp. 225–276.
[126] P. Prado, B. Blümich, B.J. Balcom, Magnetic resonance techniques in process analysis, in: J.M. Chalmers (Ed.), Spectroscopy in Process Analysis, Sheffield Academic Press, Sheffield, 1999, pp. 234–283.
[127] A. Nordon, C.A. McGill, D. Littlejohn, Process NMR spectrometry, Analyst 126 (2001) 260–272.
[128] W.L. Rollwitz, A nuclear magnetic resonance moisture meter, Proc. Natl. Electron. Conf. 12 (1957) 113–125.
[129] B.J. Hogan, One-sided NMR sensor system measures soil/concrete moisture, Design News (1986).
[130] The Foxboro Company, 33 Commercial Street, Foxboro, MA 02035, USA, Available from: <http://www.foxboro.com/>.
[131] A.K. Roy, S.A. Marino, NMR in Process, American Laboratory, October 1999, 32–33.
[132] B. Blümich, NMR for product and quality control of elastomers, KGK Kautschuk Gummi Kunststoffe 54 (2001) 188–190.
[133] B. Blümich, M. Bruder, Mobile NMR zur Qualitätskontrolle von Elastomerprodukten, KGK Kautschuk Gummi Kunststoffe 56 (2003) 90–94.
[134] R. Eymael, B. Blümich, NMR in der Prozesskontrolle: Bildgebende und unilaterale NMR in weicher Materie, Sonderheft Prozesstomographie "Technisches Messen", tm 69 (2002) 340–346.
[135] G. Guthausen, H. Todt, W. Burk, A. Guthausen, A. Kamlowksi, Industrial quality control with time-domain NMR, Bruker Rep. 150/151 (2002) 53–55.
[136] G. Guthausen, J. König, A. Kamlowski, Comprehensive quality control of food, Bruker Spin Rep. 154/155 (2004) 41–44.
[137] G. Guthausen, H. Todt, W. Burk, A. Kamlowski, D. Schmalbein, Quality control with NMR: selected examples and applications in polymer industry, KGK Kautschuk Gummi Kunststoffe 11 (2003) 578–581.
[138] H. Kühn, M. Klein, A. Wiesmath, D.E. Demco, B. Blümich, J. Kelm, P.W. Gold, The NMR-MOUSE®: quality control of elastomers, Magn. Reson. Imaging 19 (2001) 497–499.
[139] K. Kopinga, L. Pel, One-dimensional scanning of moisture in porous materials with NMR, Rev. Sci. Instrum. 65 (1994) 3673–3681.
[140] T. Ohkawa, Compact Open NMR Systems for In Situ Measurement of Moisture, Salinity, and Hydrocarbons, US patent 5,095,271, 10 March 1992.
[141] L. Pel, K. Kopinga, G. Bertram, G. Lang, Water absorption in fired-clay brick observed by NMR scanning, J. Phys. D: Appl. Phys. 28 (1995) 675–680.
[142] L. Pel, K. Kopinga, H. Brocken, Moisture transport in porous building materials, Heron 41 (1996) 95–105.
[143] W.-Y. Chiang, C.-H. Hu, L. Pel, H. Brocken, K. Kopinga, Determination of moisture diffusivity in porous media using moisture concentration profiles, Int. J. Heat Mass Transfer 39 (1996) 1273–1280.
[144] L. Pel, K. Hazrati, K. Kopinga, J. Marchand, Water absorption in mortar determined by NMR, Magn. Reson. Imaging 16 (1998) 525–528.
[145] P.J. Prado, NMR hand-held moisture sensor, Magn. Reson. Imaging 19 (2001) 505–508.
[146] B. Wolter, G. Dobmann, N. Surkowa, F. Kohl, Kernresonanz in Aufsatztechnik (nuclear magnetic resonance in one-sided access technique), Technisches Messen 69 (2002) 43–48.
[147] B. Wolter, G. Dobmann, H.-R. Herzer, U. Laub, P.J.C. Bloem, One-Sided Access NMR for Concrete Inspection, The ECNDT, Copenhagen, May 26–29, 1998.
[148] B. Wolter, NMR in Aufsatztechnik – Ein zerstörungsfreies Verfahren zur Feuchtemessung, Betonwerk + Fertigteil-Technik 67 (2001) 117–118.
[149] B. Wolter, Schadensdiagnose: Doppelt magnetisch, B+B 7 (2000) 64–66.
[150] M.J. McCarthy, P.N. Gambhir, A.G. Goloshevsky, NMR for food quality control, in: S. Stapf, S. Han (Eds.), NMR in Chemical Engineering, Wiley-VCH, Weinheim, 2006, pp. 471–490.
[151] A.L. Weekley, P. Bruins, M. Sisto, M.P. Augustine, Using NMR to study full intact wine bottles, J. Magn. Reson. 161 (2003) 91–98.
[152] D.N. Sobieski, G. Mulvihill, J.S. Broz, M.P. Augustine, Towards rapid throughput NMR studies of full wine bottles, Solid State Nucl. Magn. Reson. 29 (2006) 191–198.
[153] A. Gottwald, U. Scheler, Extrusion monitoring of polymer melts using a high-temperature surface-NMR probe, Macromol. Matter Eng. 290 (2005) 438–442.
[154] R.L. Powell, J.E. Maneval, J.D. Seymour, K.L. McCarthy, M.J. McCarthy, Nuclear magnetic resonance imaging for viscosity measurements, J. Rheol. 38 (1994) 1465–1470.
[155] B.P. Hills, K.M. Wright, Motional relativity and industrial NMR sensors, J. Magn. Reson. 178 (2006) 193–205.
[156] B. Blümich, Essential NMR for Scientists and Engineers, Springer, Berlin, 2005.
[157] B. Blümich, S. Han, C. Heine, R. Eymael, M. Bertmer, S. Stapf, Analysis of slow motion by multidimensional NMR, in: J. Fraissard, O. Lapina (Eds.), Magnetic Resonance in Colloid and Interface Science, Kluwer, Dordrecht, 2002, pp. 3–14.

[158] J. Perlo, V. Demas, F. Casanova, C.A. Meriles, J. Reimer, A. Pines, B. Blümich, High-resolution NMR spectroscopy with a portable single-sided sensor, Science 308 (2005) 1278.
[159] D. Rugar, C.S. Yannoni, J.A. Sidles, Mechanical detection of magnetic resonance, Nature 360 (1992) 563–566.
[160] M. Barbic, A. Scherer, Stray field magnetic resonance tomography using ferromagnetic spheres, J. Magn. Reson. 181 (2006) 223–228.
[161] C.L. Degen, Q. Lin, A. Hunkeler, U. Meier, M. Tomaselli, B.H. Meier, Microscale localized spectroscopy with a magnetic resonance force microscope, Phys. Rev. Lett. 94 (2005), 207601, 1–4.
[162] Y. Zur, An algorithm to calculate the NMR signal of a multi spin–echo sequence with relaxation and spin-diffusion, J. Magn. Reson. 171 (2004) 97–106.
[163] M.T. Vlaardingerbroek, J.A. den Boer, Magnetic Resonance Imaging, Springer, Berlin, 2003.
[164] A. Trequattrini, G. Coscia, S. Pittaluga, Double-cavity open permanent magnet for dedicated MRI, IEEE Trans. Appl. Supercond. 10 (2000) 756–758.
[165] Easote S. p. A., Via Siffredi 58, 16153 Genova, Italy, Available from: www.esaote.com.
[166] MagneVu, 1916 Palomar Oaks Way, Suite 150, Carlsbad, CA 92008, USA, Available from: www.magnevu.com.
[167] Odin Medical Technologies, Inc., 826 Coal Creek Circle, Louisville, CO 80027, USA, Odinmed, Available from: www.odinmed.com.
[168] M. Rokitta, E. Rommel, A. Zimmermann, A. Haase, Portable nuclear magnetic resonance imaging system, Rev. Sci. Inst. 71 (2000) 4257–4261.
[169] K. Kose, Y. Matsuda, T. Kurimoto, S. Hashimoto, Y. Yamazaki, T. Haishi, S. Utsuzawa, H. Yoshioka, S. Okada, M. Aoki, T. Tsuzaki, Development of a compact MRI system for trabecular bone volume fraction measurements, Magn. Reson. Med. 52 (2004) 440–444.
[170] K. Kose, Compact MRI for chemical engineering, in: S. Stapf, S. Han (Eds.), NMR in Chemical Engineering, Wiley-VCH, Weinheim, 2006, pp. 77–89.
[171] N. Iita, S. Handa, S. Tomiha, K. Kose, Development of a compact MRI system for measuring the trabecual bone microstructure of the finger, Magn. Reson. Med. 57 (2007) 272–277.
[172] M. Todica, R. Fechete, B. Blümich, Selective NMR excitation in strongly inhomogeneous magnetic fields, J. Magn. Reson. 164 (2003) 220–227.
[173] M. Todica, R. Fechete, B. Blümich, Selective saturation in strongly inhomogeneous magnetic fields, Appl. Magn. Reson. 29 (2005) 655–667.
[174] D.I. Hoult, Rotating frame zeugmatography, J. Magn. Reson. 33 (1979) 183–197.
[175] K.-J. Dunn, D.J. Berman, G.A. Latorraca, Nuclear Magnetic Resonance Petrophysical and Logging Applications, Pergamon Press, Amsterdam, 2002.
[176] R.J. Alvarado, A. Damgaard, P. Hansen, M. Raven, R. Heidler, R. Hoshun, J. Kovats, C. Morriss, D. Rose, W. Wendt, Nuclear magnetic resonance logging while drilling, Oilfield Rev. 15 (2003) 40–51.
[177] R.L. Kleinberg, A. Sezginer, D.D. Griffin, M. Fukuhara, Novel NMR apparatus for investigating an external sample, J. Magn. Reson. 97 (1992) 466–485.
[178] J. Tabary, M. Fleury, M. Locatelli, J.P. Martin, A high resolution NMR logging tool: concept validation, Magn. Reson. Imaging 19 (2001) 573–574.
[179] M. Locatelli, H. Mathieu, S. Bobroff, G. Guillot, B. Ziszner, Comparative measurements between a new logging tool and a reference instrument, Magn. Reson. Imaging 16 (1998) 593–596.
[180] S. Shtrikman, Nuclear magnetic resonance sensing apparatus and techniques, US Patent 4,710,713, December 1, 1987.
[181] A. Blank, G. Alexandrowicz, L. Muchnik, G. Tidhar, J. Schneiderman, R. Virmani, E. Golan, Miniature self-contained intravascular magnetic resonance (IVMI) probe for clinical applications, Magn. Reson. Med. 54 (2005) 105–112.
[182] J. Schneiderman, R.L. Wilensky, A. Weiss, E. Samouha, L. Muchnik, M. Chen-Zion, M. Ilovitch, E. Golan, A. Blank, M. Flugelman, Y. Rozenman, R. Virmani, Diagnosis of thin fibrous cap atheromas by a self-contained intravascular magnetic resonance imaging probe in ex-vivo human aortas and in-situ coronary arteries, J. Am. Coll. Cardiol. 45 (2005) 1961–1969.
[183] J. Mauler, NMR-Tomographie unter Berücksichtigung der Dipol-Dipol-Kopplung, Diploma thesis, RWTH Aachen University, Aachen, 2006.
[184] B. Blümich, P. Blümler, G. Eidmann, A. Guthausen, R. Haken, U. Schmitz, K. Saito, G. Zimmer, The NMR MOUSE: construction, excitation, and applications, Magn. Reson. Imaging 16 (1998) 479–484.
[185] S. Anferova, V. Anferov, M. Adams, P. Blümler, K. Hailu, K. Kupferschläger, M.J.M. Mallett, G. Schroeder, S. Sharma, B. Blümich, Construction of an NMR-MOUSE with short dead time, Concepts Magn. Reson. 15 (2002) 15–25.
[186] E.U. Purcell, H.C. Torrey, R.V. Pound, Resonance absorption by nuclear magnetic moments in a solid, Phys. Rev. 69 (1946) 37–38.
[187] F. Bloch, W.W. Hansen, M. Packard, Nuclear induction, Phys. Rev. 69 (1946) 127.
[188] B. Blümich, V. Anferov, S. Anferova, M. Klein, R. Fechete, M. Adams, F. Casanova, Simple NMR-MOUSE® with a Bar Magnet, Concepts Magn. Reson. 15B (2002) 255–261.
[189] B. Blümich, V. Anferov, S. Anferova, M. Klein, R. Fechete, An NMR-MOUSE® for analysis of thin objects, Macromol. Mat. Eng. 288 (2003) 312–317.
[190] D.V. Trushkin, O.A. Shushakov, A.V. Legchenko, The potential of a noise-reducing antenna for surface NMR groundwater surveys in the earth's magnetic field, Geophys. Prospect. 42 (1994) 855–862.
[191] Y.M. Pulyer, M.I. Hrovat, An open magnet utilizing ferro-refraction current magnification, J. Magn. Reson. 154 (2002) 298–302.
[192] R. Haken, B. Blümich, Anisotropy in tendon investigation in vivo by a portable NMR scanner, the NMR-MOUSE, J. Magn. Reson. 144 (2000) 195–199.
[193] O. Miltner, A. Schwaiger, C. Schmidt, A. Bücker, C. Kölker, C.H. Siebert, K.W. Zilkens, F.U. Niethard, B. Blümich, Mobile NMR-MOUSE®: eine neue Methode und erste Anwendung an der Achillessehne, Z. Orthop. 140 (2002) 148–152.
[194] O. Miltner, A. Schwaiger, C. Schmidt, B. Blümich, F.U. Niethard, Vergleichende Untersuchung der Achillessehne von Leistungssportlern mit einer mobilen NMR Mouse, Z. Orthop. 140 (2002) 472–474.
[195] G. Navon, U. Eliav, D.E. Demco, B. Blümich, Study of order and dynamic processes in tendon by NMR and MRI, J. Magn. Reson. Imaging 25 (2007) 362–380.
[196] K. Hailu, R. Fechete, D.E. Demco, B. Blümich, Segmental anisotropy in strained elastomers detected with a portable NMR scanner, Solid State Nucl. Magn. Reson. 22 (2002) 327–343.
[197] K. Hailu, R. Fechete, D.E. Demco, B. Blümich, Anisotropy of transverse ^{1}H magnetization relaxation in strained elastomers by the NMR-MOUSE®, in: J. Fraissard, O. Lapina (Eds.), Magnetic Resonance in Colloid and Interface Science, NATO Science Series, Series II: Mathematics, Physics and Chemistry, vol. 76, Kluwer, Dordrecht, 2002, pp. 525–530.
[198] Y.M. Pulyer, M.I. Hrovat, Generation of remote homogeneous magnetic fields, IEEE Trans. Magn. 38 (2002) 1553–1563.
[199] Y.M. Pulyer, Planar Open Magnet MRI System, US patent 5,744,960, 28 April, 1998.
[200] H. Popella, G. Henneberger, Design and optimization of the magnetic circuit of a mobile nuclear magnetic resonance device for magnetic resonance imaging, COMPEL: Int. J. Comput. Math. Elec. Elec. Eng. 20 (2001) 269–279.
[201] H. Popella, G. Henneberger, Object-oriented genetic algorithms for two-dimensional design optimization of the magnetic circuit of a mobile magnetic resonance device, Int. J. Appl. Electromagn. Mech. 15 (2001/2002) 219–223.

[202] A.E. Marble, I.V. Mastikhin, B.G. Colpitts, B.J. Balcom, An analytical methodology for magnetic field control in unilateral NMR, J. Magn. Reson. 174 (2005) 78–97.
[203] A.E. Marble, I.V. Masthikin, B.G. Colpitts, B.J. Balcom, A constant gradient unilateral magnet for near-surface MRI profiling, J. Magn. Reson. 183 (2006) 228–234.
[204] N. Surkova, B. Wolter, G. Dobmann, Optimierung von Sensoren auf der Basis von Permanentmagneten, DGzfP-Jahrestagung, Mainz, 26–28 May, 2003.
[205] Y. Zhang, D. Xie, A new development of fully open MRI magnet by a hybrid FEM-NESM computation, J. Electrom. Waves App. 20 (2006) 747–760.
[206] J.C. Goswami, A. Sezginer, B. Luong, On the design of NMR sensor for well-logging applications, IEEE Trans. Ant. Propag. 48 (2000) 1393–1401.
[207] B. Luong, J.C. Goswami, A. Sezginer, D. Davies, Optimal control technique for magnet design in inside-out nuclear magnetic resonance, IEEE Trans. Magn. 37 (2001) 1015–1023.
[208] A.E. Marble, I.V. Masthikin, B.G. Colpitts, B.J. Balcom, A compact permanent magnet array with a remote homogeneous field, J. Magn. Reson. 186 (2007) 100–104.
[209] P.M. Glover, P.S. Aptaker, J.R. Bowler, E. Ciampi, P.J. McDonald, A novel gradient permanent magnet for profiling of planar films and coatings, J. Magn. Reson. 139 (1999) 90–97.
[210] P. Doughty, P.J. McDonald, Drying of coatings and other applications with GARField, in: S. Stapf, S. Han (Eds.), NMR in Chemical Engineering, Wiley-VCH, Weinheim, 2006, pp. 89–107.
[211] G. Bennett, J.-P. Gorce, J.L. Keddie, P.J. McDonald, H. Bergling, Magnetic resonance profiling studies of the drying of film-forming aqueous dispersions and glue layers, Magn. Reson. Imaging 21 (2003) 235–241.
[212] J. Mitchell, P. Blümler, P.J. McDonald, Spatially resolved nuclear magnetic resonance studies of planar samples, Prog. Nucl. Magn. Reson. Spectr. 48 (2006) 161–181.
[213] A. Hartwig, B. Wolter, NMR – Aufsatztechnik: Neue Online – Methode zum zerstörungsfreien Prüfen? Adhäsion 11 (2001) 25–29.
[214] W.-H. Chang, J.-H. Chen, L.-P. Hwang, Single-sided mobile NMR with a Halbach magnet, Magn. Reson. Imaging 24 (2006) 1095–1102.
[215] S. Anferova, V. Anferov, M. Adams, R. Fechete, G. Schroeder, B. Blümich, Thermo-oxidative aging of elastomers: a temperature control unit for operation with the NMR-MOUSE®, Appl. Magn. Reson. 27 (2004) 361–370.
[216] B. Blümich, C. Kölker, F. Casanova, J. Perlo, J. Felder, Kernspintomographie für Medizin und Materialforschung: Ein mobiler und offener Kernspintomograph, Physik in unserer Zeit 36 (2005) 236–242.
[217] P.J. Prado, Single sided imaging sensor, Magn. Reson. Imaging 21 (2003) 397–400.
[218] K. Halbach, Physical and optical properties of rare earth cobalt magnets, Nucl. Instrum. Methods 187 (1981) 109–117.
[219] P.J. McDonald, P.S. Aptaker, J. Mitchell, M. Mulheron, A unilateral NMR magnet for sub-structure analysis in the built environment: the surface GARField, J. Magn. Reson. 185 (2007) 1–11.
[220] J. Perlo, F. Casanova, B. Blümich, Profiles with microscopic resolution by single-sided NMR, J. Magn. Reson. 176 (2005) 64–70.
[221] N.R. Routley, K.J. Carlton, The HALO system – a light weight portable imaging system, Magn. Reson. Imaging 22 (2004) 1145–1151.
[222] S. Anferova, V. Anferov, J. Arnold, E. Talnishnikh, M.A. Voda, K. Kupferschläger, P. Blümler, C. Clauser, B. Blümich, Improved Halbach sensor for NMR scanning of drill cores, Magn. Reson. Imaging 25 (2007) 474–480.
[223] E. Fukushima, J.A. Jackson, Unilateral Magnet Having a Remote Uniform Region for Nuclear Magnetic Resonance, US patent 6,489,872, 3 December, 2002.
[224] E. Fukushima, J.A. Jackson, Unilateral Magnet Having a Remote Uniform Field Region for Nuclear Magnetic Resonance, US patent 6,828,892, 7 December, 2004.
[225] E. Fukushima, A.R. Rath, S.B.W. Roeder, Apparatus for Unilaterally Generating a Region of Uniform Magnetic Field, US patent 4,721,914, 26 January, 1988.
[226] S. Utsuzawa, Unilateral NMR for Water Detection, Masters Thesis, Institute of Applied Physics, University of Tsukuba, Ibaraki, Japan, 2003, Available from: <utsuzawa@mrlab.bk.tsukuba.ac.jp/>.
[227] S. Rahmatallah, Y. Li, H.C. Seton, I.S. Mackenzie, J.S. Gregory, R.M. Aspden, NMR detection and one-dimensional imaging using the inhomogeneous magnetic field of a portable single-sided magnet, J. Magn. Reson. 173 (2005) 23–28.
[228] A.R. Rath, S.B.W. Roeder, E. Fukushima, Opposed coil magnet calculations for large sample unilateral nuclear magnetic resonance, Rev. Sci. Instrum. 56 (1985) 402–410.
[229] B. Manz, A. Coy, R. Dykstra, C.D. Eccles, M.W. Hunter, B.J. Parkinson, P.T. Callaghan, A mobile one-sided NMR sensor with a homogeneous magnetic field: the NMR-MOLE, J. Magn. Reson. 183 (2006) 25–31.
[230] V. Demas, C. Meriles, D. Sakellariou, S.-I. Han, J. Reimer, A. Pines, Toward ex situ phase-encoded spectroscopic imaging, Concepts Magn. Reson. B29 (2006) 137–144.
[231] B.H. Suits, A.N. Garroway, Optimizing surface coils and the Self-Shielded Gradiometer, J. Appl. Phys. 94 (2003) 4170–4178.
[232] B.H. Suits, A.N. Garroway, J.B. Miller, Surface gradiometer coils near a conducting body: the lift-off effect, J. Magn. Reson. 135 (1998) 373–379.
[233] B.H. Suits, A.N. Garroway, J.B. Miller, Noise-immune coil for unshielded magnetic resonance measurements, J. Magn. Reson. 131 (1998) 154–158.
[234] B.H. Suits, A.N. Garroway, J.B. Miller, K.L. Sauer, ^{14}N magnetic resonance for materials detection in the field, Solid State Nucl. Magn. Reson. 24 (2003) 123–136.
[235] S.A. Bogacz, J.B. Ketterson, NMR in normal ^{3}He with a Meander-line coil, Phys. Rev. Lett. 57 (1986) 591–594.
[236] R. Kemmer, Coil-design for unilateral NMR with the barrel magnet, Report, New Mexico Research, Albuquerque, 2002.
[237] S. Utsuzawa, Study of Unilateral NMR, Report, New Mexico Research, Albuquerque, 2002.
[238] V. Demas, D. Sakellariou, C. Meriles, S. Han, J. Reimer, A. Pines, 3D phase encoded chemical shift MRI in the presence of inhomogeneous fields, Proc. Natl. Acad. Sci. USA 101 (2004) 8845–8847.
[239] V. Demas, Ex-Situ NMR: Single Sided and Portable Magnetic Resonance Sensors, Dissertation, UC Berkeley, Berkeley, 2006.
[240] H. Heise, D. Sakellariou, C.A. Meriles, A.J. Moulé, A. Pines, Two-dimensional high-resolution NMR spectra in matched B_0 and B_1 field gradients, J. Magn. Reson. 156 (2002) 146–151.
[241] B. Blümich, F. Casanova, J. Perlo, S. Anferova, V. Anferov, K. Kremer, N. Goga, K. Kupferschläger, M. Adams, Advances of unilateral, mobile NMR in nondestructive materials testing, Magn. Reson. Imaging 23 (2005) 197–201.
[242] J. Kolz, N. Goga, F. Casanova, T. Mang, B. Blümich, Spatial localization with single-sided NMR sensors, Appl. Magn. Reson. 32 (2007) 71–184.
[243] B. Blümich, P. Prado, Vorrichtung zur Untersuchung von Flächenware aus polymeren Werkstoffen mit eingebetteten textilen Festigkeitsträgern, Patent PCT WO 00/79253, 28 December, 2000.
[244] M.C.A. Brown, D.A. Verganelakis, M.J.D. Mallett, J. Mitchell, P. Blümler, Surface normal imaging with a hand-held NMR device, J. Magn. Reson. 169 (2004) 308–312.
[245] P.T. Callaghan, Principles of Nuclear Magnetic Resonance Microscopy, Clarendon Press, Oxford, 1991.
[246] E. Fukushima, S.B.W. Roeder, Experimental Pulse NMR: A Nuts and Bolts Approach, Addison Wesley, New York, 1986.
[247] R. Kimmich, NMR Tomography, Diffusometry, Relaxometry, Springer, Berlin, 1997.
[248] R. Halse, J.H. Strange, Stray field imaging by magnetic field sweep, J. Magn. Reson. 132 (1998) 172–175.

[249] D. Topgard, R.W. Martin, D. Sakellariou, C.A. Meriles, A. Pines, "Shim pulses" for NMR spectroscopy and imaging, Proc. Natl. Acad. Sci. USA 101 (2004) 17576–17581.
[250] V. Vegh, H. Zhao, G.J. Galloway, D.M. Doddrell, I.M. Brereton, The design of planar gradient coils. Part I: a winding path correction method, Concepts Magn. Reson. B27 (2005) 17–24.
[251] A. Métais, F. Mariette, Determination of water self-diffusion coefficient in complex food products by low field ^{1}H PFG-NMR: comparison between the standard spin–echo sequence and the T_1-weighted spin–echo sequence, J. Magn. Reson. 165 (2003) 265–275.
[252] Bruker BioSpin GmbH, Silberstreifen 4, D-76287 Rheinstetten, Germany, Available from: www.minispec.com/products/mouse.html.
[253] Oxford Instruments, Tubney Woods, Abingdon, Oxfordshire OX13 5QX, United Kingdom, Available from: <http://www.oxford-Instruments.com/>.
[254] Resonance Instruments; Oxford Instruments, Tubney Woods, Abingdon, Oxfordshire, OX13 5QX, UK, Available from: <http://www.resonance.co.uk/>.
[255] NMR-MOUSE® is a registered trademark of RWTH Aachen University.
[256] TeachSpin Inc., 45 Pnehurst Park, Buffalo, NY 14222, USA, Available from: <http://www.teachspin.com/>.
[257] Magritek Ltd., 32 Salamanca Road, Wellington 6005, New Zealand, Available from: www.magritek.com.
[258] Stelar s.r.l., Via Enrico Fermi 4, 27035 Mede, Italy, Available from: www.stelar.com.
[259] Macromolecular Chemistry, RWTH Aachen University, D-52056 Aachen, Germany, Available from: www.mc.rwth-aachen.de.
[260] ACT GmbH, Bergstr. 31, D-52159 Roetgen, Germany, Available from: www.act-aachen.com.
[261] Tecmag Inc., 10161 Harwin 150, Houston TX 77036, USA, Available from: <http://www.tecmag.com/>.
[262] D.D. Griffin, R.L. Kleinberg, M. Fukuhara, Low-frequency NMR spectrometer, Meas. Sci. Technol. 4 (1993) 968–975.
[263] T. Haishi, R. Uematsy, Y. Yoshimasa, K. Kose, Development of a 1.0 T MR microscope using Nd–Fe–B permanent magnet, Magn. Reson. Imaging 19 (2001) 875–880.
[264] Innovative Imaging Corporation, Talstrasse 88, D-66440 Blieskastel, Germany, Available from: <http://www.iic-nmr.com/>.
[265] K. Kose, T. Haishi, A. Caprihan, E. Fukushima, Real-time NMR imaging system using personal computers, J. Magn. Reson. 124 (1997) 35–41.
[266] R.M. Pearson, C. Job, Instrumentation for the home builder, in: D.M. Grant, R.K. Harris (Eds.), Encyclopedia of NMR, Wiley-Liss, New York, 1996, pp. 2569–2575.
[267] C. Job, R.M. Pearson, M.F. Brown, A personal computer-based nuclear magnetic resonance spectrometer, Rev. Sci. Instrum. 65 (1994) 3354–3362.
[268] T.N. Rudakov, A.V. Belyakov, V.T. Mikhaltsevich, A low-frequency instrument for remote nuclear quadrupole resonance experiments, Meas. Sci. Technol. 8 (1997) 444–448.
[269] H. Van As, J.E.A. Reinders, P.A. de Jager, P.A.C.M. van de Sanden, T.J. Schaafsma, In situ plant water balance studies using a portable NMR spectrometer, J. Exp. Bot. 45 (1994) 61–67.
[270] G. Boero, J. Frounchi, B. Furrer, P.-A. Besse, R.S. Popovic, Fully integrated probe for proton nuclear magnetic resonance magnetometry, Rev. Sci. Instrum. 72 (2001) 2764–2768.
[271] G. Boero, P.-A. Besse, R. Popovic, Hall detection of magnetic resonance, Appl. Phys. Lett. 79 (2001) 1498–1500.
[272] Y.-Q. Song, Categories of coherence pathways for the CPMG sequence, J. Magn. Reson. 157 (2002) 82–91.
[273] M.D. Hürlimann, L. Venkataramanan, C. Flaum, The diffusion–spin relaxation time distribution function as an experimental probe to characterize fluids in porous media, J. Chem. Phys. 117 (2002) 10223–10232.
[274] Y.-Q. Song, Novel two-dimensional NMR of diffusion and relaxation for material characterization, in: S. Stapf, S. Han (Eds.), NMR in Chemical Engineering, Wiley-VCH, Weinheim, 2006, pp. 163–183.
[275] B. Blümich, F. Casanova, Mobile NMR, in: G.A. Webb (Ed.), Modern Magnetic Resonance, Springer, Berlin, 2006, pp. 369–378.
[276] B. Blümich, S. Anferova, K. Kremer, S. Sharma, V. Herrmann, A. Segre, Unilateral NMR for quality control: The NMR-MOUSE®, Spectroscopy 18 (2003) 18–32.
[277] F. Bloch, Nuclear induction, Phys. Rev. 70 (1946) 460–474.
[278] N. Bloembergen, E.M. Purcell, R.V. Pound, Relaxation effects in nuclear magnetic resonance absorption, Phys. Rev. 73 (1948) 679–712.
[279] W.P. Halperin, F. D'Orazio, S. Bhattacharja, C.J. Tarczon, Magnetic resonance relaxation in porous media, in: J. Klafter, J.M. Drake (Eds.), Molecular Dynamics in Restricted Geometries, Wiley, New York, 1989, pp. 311–350.
[280] R.L. Kleinberg, W.E. Kenyon, P.P. Mitra, Mechanism of NMR relaxation of fluids in rock, J. Magn. Reson. A 108 (1994) 206–214.
[281] S. Davies, K.J. Packer, Pore size distribution from NMR spin–lattice relaxation measurements of fluid-saturated porous solids. I. Theory and simulation, J. Appl. Phys. 67 (1990) 3163–3170.
[282] N. Nestle, B. Walaszek, M. Nolte, Reduced apparent longitudinal relaxation times in slice-selective experiments in strong magnetic field gradients, J. Magn. Reson. 168 (2004) 46–52.
[283] G. Goelman, M.G. Prammer, The CPMG pulse sequence in strong magnetic field gradients with applications to oil-well-logging, J. Magn. Reson. A113 (1995) 11–18.
[284] Y.-Q. Song, Multiple modulation multiple echoes: a one-shot method, Magn. Reson. Imaging 23 (2005) 301–303.
[285] M.D. Hürlimann, Encoding of diffusion and T_1 in the CPMG echo shape: single-shot D and T_1 measurements in grossly inhomogeneous fields, J. Magn. Reson. 184 (2007) 114–119.
[286] Y.-Q. Song, X. Tang, A one-shot method for measurement of diffusion, J. Magn. Reson. 170 (2004) 136–148.
[287] X.-P. Tang, E.E. Sigmund, Y.-Q. Song, Simultaneous measurement of diffusion along multiple directions, J. Am. Chem. Soc. 126 (2004) 16336–16337.
[288] H. Cho, X.-H. Ren, E.E. Sigmund, Y.-Q. Song, A rapid measurement of a 3D diffusion tensor, J. Chem. Phys. 126 (2007) 154501-1–154501-4.
[289] H. Cho, X.-H. Ren, E.E. Sigmund, Y.-Q. Song, A single-scan method for measuring flow along multiple directions, J. Magn. Reson. 186 (2007) 11–16.
[290] H. Cho, L. Chavez, E.E. Sigmund, D.P. Madio, Y.-Q. Song, Fast imaging with the MMME sequence, J. Magn. Reson. 180 (2006) 18–28.
[291] T.B. Benson, P.J. McDonald, The application of spin echoes to stray-field imaging, J. Magn. Reson. B109 (1995) 314–317.
[292] A.D. Bain, E.W. Randall, Hahn spin echoes in large static gradients following a series of 90° pulses, J. Magn. Reson. A 123 (1996) 49–55.
[293] T.B. Benson, P.J. McDonald, Profile amplitude modulation in stray-field magnetic-resonance imaging, J. Magn. Reson. A112 (1995) 17–23.
[294] M.D. Hürlimann, Optimization of timing in the Carr–Purcell–Meiboom–Gill sequence, Magn. Reson. Imaging 19 (2001) 375–378.
[295] M.H. Levitt, Composite pulses, in: D.M. Grant, R.K. Harris (Eds.), Encyclopedia of Nuclear Magnetic Resonance, Wiley, New york, 1996, pp. 1396–1411.
[296] S. Wimperis, Broadband, narrowband, and passband composite pulses for use in advanced NMR experiments, J. Magn. Reson. A109 (1994) 221–231.
[297] M.D. Hürlimann, Carr–Purcell sequences with composite pulses, J. Magn. Reson. 152 (2001) 109–123.
[298] K. Schmidt-Rohr, H.W. Spiess, Multidimensional Solid-State NMR and Polymers, Academic Press, London, 1994.
[299] J.B. Miller, A.N. Garroway, Dipolar decoupled inversion pulses for NMR imaging in solids, J. Magn. Reson. 85 (1989) 432–437.

[300] M. Peyron, G.K. Pierens, A.J. Lucas, L.D. Hall, R.C. Stewart, The modified stretched exponential model for characterization of NMR relaxation in porous media, J. Magn. Reson. A 118 (1996) 214–220.
[301] B. Blümich, F. Casanova, A. Buda, K. Kremer, T. Wegener, Mobile NMR for analysis of polyethylene pipes, Acta Phys. Pol. A 108 (2005) 13–23.
[302] E.W. Randall, T.G. Nunes, G. Guillot, P.R. Bodart, T_1-weighting of Hahn echo-trains in the stray-field for deuterium: prospects for imaging using long echo-train summation, Solid State Nucl. Magn. Reson. 14 (1999) 165–172.
[303] S.W. Provencher, A constrained regularization method for inverting data represented by linear algebraic or integral equations, Comp. Phys. Commun. 27 (1982) 213–227.
[304] S.W. Provencher, CONTIN: a general purpose constrained regularization program for inverting noisy linear algebraic and integral equations, Comp. Phys. Commun. 27 (1982) 229–242.
[305] G.C. Borgia, R.J.S. Brown, P. Fantazzini, Uniform-penalty inversion of multiexponential decay data, J. Magn. Reson. 132 (1998) 65–77.
[306] G.C. Borgia, R.J.S. Brown, P. Fantazzini, Uniform-penalty inversion of multiexponential decay data II: data spacing, T_2 data, systematic data errors, and diagnostics, J. Magn. Reson. A 146 (2000) 273–285.
[307] G.C. Borgia, R.J.S. Brown, P. Fantazzini, Examples of marginal resolution of NMR relaxation peaks using UPEN and diagnostics, Magn. Reson. Imaging 19 (2001) 473–475.
[308] R. Lamanna, On the inversion of multi-component NMR relaxation decays in heterogeneous systems, Concepts Magn. Reson. A26 (2005) 78–90.
[309] B. Sun, K.-J. Dunn, Methods and limitations of NMR data inversion for fluid typing, J. Magn. Reson. 169 (2004) 118–128.
[310] B. Sun, K.-J. Dunn, A global inversion method for multi-dimensional NMR logging, J. Magn. Reson. 172 (2005) 152–160.
[311] M. Todica, B. Blümich, Hole-burning NMR in strongly inhomogeneous fields, Solid State Nucl. Magn. Reson. 32 (2007) 66–70.
[312] H. Peemoeller, M.M. Pintar, Two-dimensional NMR time evolution approach for resolving a composite free induction decay, J. Magn. Reson. 41 (1980) 358–360.
[313] H. Peemoeller, NMR spin grouping, Bull. Magn. Reson. 11 (1989) 19–30.
[314] G. Guthausen, A. Guthausen, F. Balibanu, R. Eymael, K. Hailu, U. Schmitz, B. Blümich, Soft-matter analysis by the NMR-MOUSE, Macromol. Mater. Eng. 276/277 (2000) 25–37.
[315] S.K. Brady, M.S. Conradi, C.M. Vaccaro, NMR detection of thermal damage in carbon fiber reinforced epoxy resins, J. Magn. Reson. 172 (2005) 342–345.
[316] E.E. Sigmund, N. Caudal, Y.-Q. Song, Rapid T_1 measurement via decay–recovery decomposition: applications in fringe-field and distributed relaxation experiments, Solid State Nucl. Magn. Reson. 29 (2006) 232–241.
[317] M. Munowitz, A. Pines, Principles and applications of multiple-quantum NMR, Adv. Chem. Phys. 66 (1987) 1–145.
[318] K. Wüthrich, NMR of Proteins and Nucleic Acids, Wiley, New York, 1986.
[319] G.J. Bowden, W.D. Hutchison, Tensor operator formalism of multiple-quantum NMR. 1. Spin-1 nuclei, J. Magn. Reson. 67 (1986) 403–414.
[320] G.J. Bowden, W.D. Hutchison, J. Khachan, Tensor operator formalism of multiple-quantum NMR. 1. Spins 3/2, 2, and 5/2 and general I, J. Magn. Reson. 67 (1986) 415–437.
[321] J. Baum, A. Pines, NMR studies of clustering in solids, J. Am. Chem. Soc. 108 (1986) 7447–7454.
[322] K. Saalwächter, Detection of heterogeneities in dry and swollen polymer networks by proton low-field NMR spectroscopy, J. Am. Chem. Soc. 125 (2003) 14684–14685.
[323] J.P. Cohen Addad, NMR and fractal properties of polymeric liquid crystals and gels, Prog. Nucl. Magn. Reson. Spectr. 25 (1993) 1–316.
[324] M. Schneider, L. Gasper, D.E. Demco, B. Blümich, Residual dipolar couplings by ^{1}H dipolar encoded longitudinal magnetization, double- and triple-quantum nuclear magnetic resonance in cross-linked elastomers, J. Chem. Phys. 111 (1999) 402–415.
[325] V.M. Litvinov, P. Dee (Eds.), Spectroscopy of Rubber and Rubbery Materials, Rapra Press, Sheffield, 2002.
[326] C. Cornelissen, A. Schnettler, A. Wiesmath, B. Blümich, Ultraschall und Kernspinresonanz: Nicht-destruktive Verfahren zur Zustandsbewertung von Kabelsystemen, Das Magazin für die Energiewissenschaften ew 101 (2002) 38–43.
[327] P. Heitjans, J. Kärger (Eds.), Diffusion in Condensed Matter: Methods, Materials, Models, Springer, Berlin, 2005.
[328] K.R. Brownstein, C.E. Tarr, Importance of classical diffusion NMR studies of water in biological cells, Phys. Rev. A 19 (1979) 2446–2453.
[329] J. Kärger, Diffusion under confinement, Sitzungsberichte der Sächsischen Akademie der Wissenschaften zu Leipzig, vol. 128 (6), S. Hirzel, Leipzig, 2003.
[330] P.T. Callaghan, Some perspectives on dispersion and the use of ensemble-averaged PGSE NMR, Magn. Reson. Imaging 23 (2005) 133–137.
[331] E.E. Sigmund, W.P. Halperin, Hole-burning diffusion measurements in high magnetic field gradients, J. Magn. Reson. 163 (2003) 99–104.
[332] J. Kärger, W. Heink, The propagator representation of molecular transport in microporous crystallites, J. Magn. Reson. 51 (1983) 1–7.
[333] R. Kimmich, W. Unrath, G. Schnur, E. Rommel, NMR measurement of small self-diffusion coefficients in the fringe field of superconducting magnets, J. Magn. Reson. 91 (1991) 136–140.
[334] R. Kimmich, E. Fischer, One- and two-dimensional pulse sequences for diffusion experiments in the fringe field of superconducting magnets, J. Magn. Reson. A106 (1994) 229–235.
[335] A. Marko, B. Wolter, Diffusion Studies in porous media with the "Inside-Out" technique, Magn. Reson. Imaging 21 (2003) 363–364.
[336] D.G. Rata, F. Casanova, J. Perlo, D.E. Demco, B. Blümich, Self-diffusion measurement by a mobile single-sided NMR sensor with improved magnetic field gradient, J. Magn. Reson. 180 (2006) 229–235.
[337] W.S. Price, P. Stilbs, O. Söderman, Determination of pore space shape and size in porous systems using NMR diffusometry. Beyond the short gradient pulse approximation, J. Magn. Reson. 160 (2003) 139–143.
[338] C. Malmborg, D. Topgaard, O. Söderman, NMR diffusometry and the short gradient pulse limit approximation, J. Magn. Reson. 169 (2004) 85–91.
[339] S. Lasic, J. Stepisnik, A. Mohoric, Displacement power spectrum measurement by CPMG in constant gradient, J. Magn. Reson. 182 (2006) 208–214.
[340] B. Wolter, G. Dobmann, N. Surkowa, F. Kohl, A. Marko, Neue Anwendungsmöglichkeiten der NMR-Aufsatztechnik, DGZfP Jahrestagung, Weimar, 6–8 May, 2002.
[341] K.-J. Dunn, Enhanced transverse relaxation in porous media due to internal field gradients, J. Magn. Reson. 156 (2002) 171–180.
[342] R.M. Cotts, M.J.R. Hoch, T. Sun, J.T. Marker, Pulsed field gradient stimulated echo methods for improved NMR diffusion measurements in heterogeneous systems, J. Magn. Reson. 83 (1989) 252–266.
[343] Ph.Z. Sun, J.G. Seland, D. Cory, Background gradient suppression in pulsed gradient stimulated echo measurements, J. Magn. Reson. 161 (2003) 168–173.
[344] S. Vasenkov, P. Galvosas, O. Geier, N. Nestle, F. Stallmach, J. Kärger, Determination of genuine diffusivities in heterogeneous media using stimulated echo pulsed field gradient NMR, J. Magn. Reson. 149 (2001) 228–233.
[345] P. Galvosas, F. Stallmach, J. Kärger, Background gradient suppression in stimulated echo NMR diffusion studies using magnetic pulsed field gradient ratios, J. Magn. Reson. 166 (2004) 164–173.

[346] P. Le Doussal, P.N. Sen, Decay of nuclear magnetization by diffusion in a parabolic magnetic field: an exactly solvable model, Phys. Rev. B46 (1992) 3465–3485.
[347] L.J. Zielinski, P.N. Sen, Relaxation of nuclear magnetization in a non-uniform magnetic field gradient and in a restricted geometry, J. Magn. Reson. 147 (2000) 95–103.
[348] Y.-Q. Song, Determining pore sizes using an internal magnetic field, J. Magn. Reson. 143 (2000) 397–401.
[349] Y.-Q. Song, S. Ryu, P.N. Sen, Determining multiple length scales in rocks, Nature 406 (2000) 178–181.
[350] Y.-Q. Song, Pore sizes and pore connectivity in rocks using the effect of internal field, Magn. Reson. Imaging 19 (2001) 417–421.
[351] Y.-Q. Song, Using internal magnetic fields to obtain pore size distributions of porous media, Concepts Magn. Reson. A18 (2003) 97–110.
[352] Y.-Q. Song, E.E. Siegmund, N.V. Lisitza, NMR pore size measurements using an internal magnetic field in porous media, in: S. Stapf, S. Han (Eds.), NMR in Chemical Engineering, Wiley-VCH, Weinheim, 2006, pp. 340–358.
[353] P.M. Singer, G. Leu, E.J. Forham, P.N. Sen, Low magnetic fields for flow popagators in permeable rocks, J. Magn. Reson. 183 (2006) 167–177.
[354] R. Raulet, J.M. Escanye, F. Humbert, D. Canet, Quasi-immunity of B_1 gradient NMR microscopy to magnetic susceptibility distortions, J. Magn. Reson. A119 (1996) 111–114.
[355] G. Farrher, I. Ardelean, R. Kimmich, Probing four orders of magnitude of the diffusion time in porous silica glass with unconventional NMR techniques, J. Magn. Reson. 182 (2006) 215–220.
[356] P.N. Sen, L.M. Schwartz, P.P. Mitra, B.I. Halperin, Surface relaxation and the long-time diffusion coefficient in porous media: periodic geometries, Phys. Rev. B 49 (1994) 215–225.
[357] P.N. Sen, Time-dependent diffusion coefficient as a probe of geometry, Concepts Magn. Reson. A23 (2004) 1–21.
[358] P.P. Mitra, P.N. Sen, L.M. Schwartz, Short-time behavior of the diffusion coefficient as a geometrical probe of porous media, Phys. Rev. B 47 (1993) 8565–8574.
[359] M. Hürlimann, K. Helmer, L. Latour, L.C. Sotak, Restricted diffusion in sedimentary rocks. determination of surface-area-to-volume-ratio and surface relaxivity, J. Magn. Reson. A111 (1994) 169–178.
[360] D.S. Grebenkov, Multiexponential attenuation of the CPMG spin echoes due to a geometrical confinement, J. Magn. Reson. 180 (2006) 118–126.
[361] L.J. Zielinski, P.N. Sen, Restricted diffusion in grossly inhomogeneous fields, J. Magn. Reson. 164 (2003) 145–153.
[362] L.J. Zielinski, M.D. Hürliman, Short-time restricted diffusion in a static gradient and the attenuation of individual coherence pathways, J. Magn. Reson. 171 (2004) 107–117.
[363] L.J. Zielinski, M.D. Hürliman, Probing short length scales with restricted diffusion in a static gradient using the CPMG sequence, J. Magn. Reson. 172 (2005) 161–167.
[364] D. van Dusschoten, P.A. de Jager, H. van As, Extracting diffusion constants from echo-time-dependent PFG NMR data using relaxation-time information, J. Magn. Reson. A116 (1995) 22–28.
[365] L.J. Zielinski, P.N. Sen, Effects of finite-width pulses in the pulsed-field gradient measurement of the diffusion coefficient in connected porous media, J. Magn. Reson. 165 (2003) 153–161.
[366] C. Vogt, P. Galvosas, N. Klitsch, F. Stallmach, Self-diffusion studies of pore fluids in unconsolidated sediments by PFG NMR, J. Appl. Geophys. 50 (2002) 455–467.
[367] R. Bradford, C. Clay, E. Strick, A steady-state transient technique in nuclear induction, Phys. Rev. 84 (1951) 157–158.
[368] R. Kaiser, E. Bartholdi, R.R. Ernst, Diffusion and field-gradient effects in NMR fourier spectroscopy, J. Chem. Phys. 60 (1974) 2966–2979.
[369] D.E. Freed, U.M. Scheven, L.J. Zielinski, P.N. Sen, M.D. Hürlimann, Steady-state free precession experiments and exact treatment of diffusion in a uniform gradient, J. Chem. Phys. 115 (2001) 4249–4258.
[370] D.E. Freed, M.D. Hürlimann, U.M. Scheven, The equivalence between off-resonance and on-resonance pulse sequences and its application to steady-state free precession with diffusion in inhomogeneous fields, J. Magn. Reson. 162 (2003) 328–335.
[371] G. Guthausen, R. Eymael, A. Guthausen, B. Blümich, The NMR-MOUSE: taking the probe to the sample, Bruker Rep. 148 (2000) 20–21.
[372] C. Casieri, S. Bubici, F. De Luca, Self-diffusion coefficient by single-sided NMR, J. Magn. Reson. 162 (2003) 348–355.
[373] M. Klein, R. Fechete, D.E. Demco, B. Blümich, Self-diffusion measurements by a constant-relaxation method in strongly inhomogeneous magnetic fields, J. Magn. Reson. 164 (2003) 310–320.
[374] E. Fischer, R. Kimmich, Constant time steady gradient NMR diffusometry using the secondary stimulated echo, J. Magn. Reson. 166 (2004) 273–279.
[375] C. Casieri, F. De Luca, P. Fantazzini, Pore-size evaluation by single-sided nuclear magnetic resonance measurements: compensation of water self-diffusion effect on transverse relaxation, J. Appl. Phys. 97 (2005) 043901-1–043901-10.
[376] A.E. English, K.P. Wittall, M.L.G. Joy, R.M. Henkelman, Quantitative two-dimensional time-correlation relaxometry, Magn. Reson. Med. 22 (1991) 425–434.
[377] J.-H. Lee, C. Labadie, C.S. Springer Jr., G.S. Harbison, Two-dimensional inverse laplace transform NMR: altered relaxation times allow detection of exchange correlation, J. Am. Chem. Soc. 115 (1993) 7761–7764.
[378] L. Venkataramanan, Y.-Q. Song, M.D. Hürlimann, Solving Fredholm integrals of the first kind with tensor product structure in 2 and 2.5 dimensions, IEEE Trans. Sign. Proc. 50 (2002) 1017–1026.
[379] P.T. Callaghan, S. Godefroy, B.N. Ryland, Use of a second dimension in PGSE NMR studies of porous media, Magn. Reson. Imaging 21 (2003) 243–248.
[380] B. Sun, K.-J. Dunn, Two-dimensional nuclear magnetic resonance petrophysics, Magn. Reson. Imaging 23 (2005) 259–262.
[381] M.D. Hürlimann, M. Flaum, L. Venkataramanan, C. Flaum, R. Freedman, G.J. Hirasaki, Diffusion–relaxation distribution function of sedimentary rocks in different saturation states, Magn. Reson. Imaging 21 (2003) 305–310.
[382] R. Freedman, N. Heaton, Fluid characterization using nuclear magnetic resonance logging, Petrophysics 45 (2004) 241–250.
[383] R.C. Wilson, M.D. Hürlimann, Relationship between susceptibility induced field inhomogeneities, restricted diffusion, and relaxation in sedimentary rocks, J. Magn. Reson. 183 (2006) 1–12.
[384] P. Callaghan, S. Godefroy, B.N. Ryland, Diffusion-relaxation correlation in simple pore structures, J. Magn. Reson. 162 (2003) 320–327.
[385] M.D. Hürlimann, L. Burcaw, Y.-Q. Song, Quantitative characterization of food products by two-dimensional D-T_2 and T_1-T_2 distribution functions in a static gradient, J. Colloid Interface Sci. 297 (2006) 303–311.
[386] P. Callaghan, I. Furó, Diffusion-diffusion correlation and exchange as a signature for local order and dynamics, J. Chem. Phys. 120 (2004) 4032–4038.
[387] Y. Qiao, P. Galvosas, P.T. Callaghan, Diffusion correlation NMR spectroscopic study of anisotropic diffusion of water in plant tissues, Biophys. J. 89 (2005) 2899–2905.
[388] D.M. Kramer, L. Kaufman, Low-field 3-DFT MRI: conceptual, analytical, and experimental aspects, IEEE Trans. Med. Imaging 10 (1991) 382–386.
[389] J. Godward, E. Ciampi, M. Cifelli, P.J. McDonald, Multidimensional imaging using combined stray field and pulsed gradients, J. Magn. Reson. 155 (2002) 92–99.
[390] S. Emid, J.H.N. Creighton, High resolution NMR imaging in solids, Physica B 128 (1985) 81–83.
[391] C.E. Epstein, J. Magland, A novel technique for imaging with inhomogeneous fields, J. Magn. Reson. 183 (2006) 183–192.

[392] Y. Shrot, L. Frydman, Spatially encoded NMR and the acquisition of 2D magnetic resonance images within a single scan, J. Magn. Reson. 172 (2005) 179–190.
[393] A. Tal, L. Frydman, Spatial encoding and the single-scan acquisition of high definition MR images in inhomogeneous fields, J. Magn. Reson. 182 (2006) 179–194.
[394] L. Frydman, Single-scan multidimensional NMR, C.R. Chim. 9 (2006) 336–345.
[395] C.H. Tseng, G.P. Wong, V.R. Pomeroy, R.W. Mair, D.P. Hinton, D. Hoffmann, R.E. Stoner, F.W. Hersman, D.G. Cory, R.L. Walsworth, Low-field MRI of laser polarized noble gas, Phys. Rev. Lett. 81 (1998) 3785–3788.
[396] K. Schlenga, R. McDermott, J. Clarke, R.E. de Souza, A. Wong-Foy, A. Pines, Low-field magnetic resonance imaging with a high-T_c dc superconducting quantum interference device, Appl. Phys. Lett. 75 (1999) 3695–3697.
[397] M. Mößle, W.R. Myers, S.-K. Lee, N. Kelso, M. Hatridge, A. Pines, J. Clarke, SQUID-detected in vivo MRI at microtesla magnetic fields, IEEE Trans. Appl. Supercond. 15 (2005) 757–760.
[398] A.N. Matlachov, P.L. Volegov, M.A. Espy, J.S. George, R.H. Kraus Jr., SQUID detected NMR at microtesla fields, J. Magn. Reson. 170 (2004) 1–7.
[399] M.P. Augustine, A. Wong-Foy, J.L. Yarger, M. Tomaselli, A. Pines, D.M. TonThat, J. Clarke, Low field magnetic resonance images of polarized noble gases obtained with a dc superconducting quantum interference device, Appl. Phys. Lett. 72 (1998) 1908–1910.
[400] M. Mößle, S.-I. Han, W.R. Myers, S.-K. Lee, N. Kelso, M. Hatridge, A. Pines, J. Clarke, SQUID-detected microtesla MRI in the presence of metal, J. Magn. Reson. 179 (2006) 146–151.
[401] C.A. Meriles, D. Sakellariou, A.H. Trabesinger, Theory of MRI in the presence of zero to low magnetic fields and tensor imaging field gradients, J. Magn. Reson. 182 (2006) 106–114.
[402] W.R. Myers, M. Mößle, J. Clarke, Correction of concomitant gradient artifacts in experimental microtesla MRI, J. Magn. Reson. 177 (2005) 274–284.
[403] P.L. Volegov, J.C. Mosher, M.A. Espy, R.H. Kraus Jr., On concomitant gradients in Low-field MRI, J. Magn. Reson. 175 (2005) 1003–1113.
[404] L.-S. Bouchard, Unidirectional magnetic-field gradients and geometric-phase errors during Fourier encoding using orthogonal ac fields, Phys. Rev. B 74 (2006), 054103, 1–11.
[405] M.E. Halse, A. Coy, R. Dykstra, C. Eccles, M. Hunter, R. Ward, P.T. Callaghan, A practical and flexible implementation of 3D MRI in the Earth's magnetic field, J. Magn. Reson. 182 (2006) 75–83.
[406] U.M. Scheven, Stray field measurements of flow displacement distributions without pulsed gradient fields, J. Magn. Reson. 174 (2005) 338–342.
[407] E.L. Hahn, D.E. Maxwell, Spin echo measurements pf nuclear spin coupling in molecules, Phys. Rev. 88 (1952) 1070–1084.
[408] D.P. Weitekamp, J.R. Garbow, J.B. Murdoch, A. Pines, High-resolution NMR spectra in inhomogeneous magnetic fields: application to total spin coherence transfer echoes, J. Am. Chem. Soc. 103 (1981) 3578–3579.
[409] J.R. Garbow, D.P. Weitekamp, A. Pines, Total spin coherence transfer echo spectroscopy, J. Chem. Phys. 79 (1983) 5301–5310.
[410] S. Vathyam, S. Lee, W.S. Warren, Homogeneous NMR spectra in inhomogeneous fields, Science 272 (1996) 92–96.
[411] Y.-Y. Lin, S. Ahn, N. Murali, W. Brey, C.R. Bowers, W.S. Warren, High-Resolution, >1 GHz NMR in unstable magnetic fields, Phys. Rev. Lett. 277 (1997) 367–374.
[412] Q. He, W. Richter, S. Vathyam, W.S. Warren, Intermolecular multiple-quantum coherences and cross-relaxations in solution nuclear magnetic resonance, J. Chem. Phys. 98 (1993) 6779–6800.
[413] S. Lee, W. Richter, S. Vathyam, W.S. Warren, Quantum treatment of the effects of dipole–dipole interactions in liquid nuclear magnetic resonance, J. Chem. Phys. 105 (1996) 874–900.
[414] R. Bowtell, P. Robyr, Structural investigations with the dipolar demagnetization field in solution NMR, Phys. Rev. Lett. 76 (1996) 4971–4974.
[415] J.J. Balbach, M.S. Conradi, D.P. Cistola, C. Tang, J.R. Garbow, W.C. Hutton, High-Resolution NMR in inhomogeneous fields, Chem. Phys. Lett. 277 (1997) 367–374.
[416] I. Ardelean, R. Kimmich, A. Klemm, The nutation spin echo and its use for localized NMR, J. Magn. Reson. 146 (2000) 43–48.
[417] S. Antonijevic, S. Wimperis, High-resolution NMR spectroscopy in inhomogeneous B_0 and B_1 fields by two-dimensional correlation, Chem. Phys. Lett. 381 (2003) 634–641.
[418] D. Topgaard, D. Sakellariou, A. Pines, NMR spectroscopy in inhomogeneous B_0 and B_1 fields with non-linear correlation, J. Magn. Reson. 175 (2005) 1–10.
[419] A. Scharfenecker, I. Ardelean, R. Kimmich, Diffusion measurements with the aid of nutation spin echoes appearing after two inhomogeneous radiofrequency pulses in inhomogeneous magnetic fields, J. Magn. Reson. 148 (2001) 363–366.
[420] V. Demas, Ex-Situ NMR: Single-Sided and Portable Magnetic Resonance Sensors, Dissertation, UC Berkeley, 2006.
[421] C.P. Slichter, Principles of Magnetic Resonance, third ed., Springer, Berlin, 1990.
[422] C.A. Meriles, D. Sakellariou, A. Pines, Broadband phase modulation by adiabatic pulses, J. Magn. Reson. 164 (2003) 177–181.
[423] D. Sakellariou, C.A. Meriles, A. Moulé, A. Pines, Variable rotation composite pulses for high resolution nuclear magnetic resonance using inhomogeneous magnetic and radiofrequency fields, Chem. Phys. Lett. 363 (2002) 25–33.
[424] B. Shapira, L. Frydman, Spatial encoding and the acquisition of high-resolution NMR spectra in inhomogeneous magnetic fields, J. Am. Chem. Soc. 126 (2004) 7184–7185.
[425] B. Shapira, L. Frydman, Spatially encoded pulse sequences for the acquisition of high resolution NMR spectra in inhomogeneous fields, J. Magn. Reson. 182 (2006) 12–21.
[426] D. Topgaard, A. Pines, Self-diffusion measurements with chemical shift resolution in inhomogeneous magnetic fields, J. Magn. Reson. 168 (2004) 31–35.
[427] M.E. Halse, P.T. Callaghan, Imaged deconvolution: a method for extracting high-resolution NMR spectra from inhomogeneous fields, J. Magn. Reson. 185 (2007) 130–137.
[428] E.R. Andrew, R.G. Eades, Possibilities for high-resolution nuclear magnetic resonance spectra of crystals, Disc. Farad. Soc. 34 (1962) 38–42.
[429] C.A. Meriles, D. Sakellariou, A. Moulé, M. Goldman, T.F. Budinger, A. Pines, High-resolution NMR of static samples by rotation of the magnetic field, J. Magn. Reson. 169 (2004) 13–18.
[430] C. Meriles, D. Sakellariou, A. Pines, Resolved magic angle spinning of anisotropic samples in inhomogeneous fields, Chem. Phys. Lett. 358 (2002) 391–395.
[431] D. Sakellariou, C.A. Meriles, R.W. Martin, A. Pines, High-resolution NMR of anisotropic samples with spinning away from the magic angle, Chem. Phys. Lett. 377 (2003) 333–339.
[432] D. Sakellariou, C.A. Meriles, R.W. Martin, A. Pines, NMR in rotating magnetic fields: magic angle field spinning, Magn. Reson. Imaging 23 (2005) 295–299.
[433] B.C. Gerstein, C.R. Dybowski, Transient Techniques in NMR of Solids, Academic Press, New York, 1985.
[434] S. Anferova, V. Anferov, D.G. Rata, B. Blümich, J. Arnold, C. Clauser, P. Blümler, H. Raich, Mobile NMR device for measurements of porosity and pore size distributions of drilled core samples, Concepts Magn. Reson. 23B (2004) 26–32.
[435] G. Moresi, R. Magin, Miniature permanent magnet for table-top NMR, Concepts Magn. Reson. B19 (2003) 35–43.
[436] B.P. Hills, K.M. Wright, D.G. Gillies, A low-field, low-cost Halbach magnet array for open access NMR, J. Magn. Reson. 175 (2005) 336–339.
[437] H.A. Leupold, E. Potenziani II, M.G. Abele, Applications of yokeless flux confinement, J. Appl. Phys. 64 (1988) 5994–5996.

[438] H.A. Leupold, G.F. McLane, Fabrication of multipolar magnetic field sources, J. Appl. Phys. 76 (1994) 6253–6255.
[439] A. Podol'skii, Permanent-magnet assemblies for magnetic resonance imaging devices for various purposes, IEEE Trans. Magn. 38 (2002) 2–5.
[440] X.N. Xu, D.W. Lu, Q. Yuan, Y.S. Han, X. Jin, Studies of strong magnetic field produced by permanent magnet array for magnetic refrigeration, J. Appl. Phys. 95 (2004) 6302–6307.
[441] L.O. Sillerud, A.F. McDowell, N.L. Adolphi, R.E. Serda, D.P. Adams, M.J. Vasile, T.M. Alam, ^{1}H NMR detection of superparamagnetic Nanoparticles at 1 T using a microcoil and novel tuning circuit, J. Magn. Reson. 181 (2006) 181–190.
[442] Aster Enterprises, Inc., 6 Eastern Road, Acton, MA 01720, USA.
[443] B. Clark, R. Kleinberg, Physics in oil exploration, Phys. Today (2002) 48–53.
[444] R.L. Kleinberg, P.G. Brewer, Probing gas hydrate deposits, Am. Sci. 89 (2001) 244–251.
[445] R.L. Kleinberg, C. Flaum, Review: NMR detection and characterization of hydrocarbons in subsurface earth formations, in: B. Blümich, P. Blümler, R. Botto, E. Fukushima (Eds.), Spatially Resolved Magnetic Resonance, Wiley-VCH, Weinheim, 1998, pp. 555–573.
[446] D. Allen, Ch. Flaum, T.S. Ramakrishnan, J. Bedford, K. Castelijns, D. Fairhurst, G. Gubelin, N. Heaton, C.C. Minh, M.A. Norville, M.R. Seim, T. Pritchard, R. Ramamoorthy, Trends in NMR logging, Oilfield Rev. 12 (2000) 2–19.
[447] I.L. Pyckett, NMR – a powerful tool for industrial process control and quality assurance, IEEE Trans. Appl. Supercond. 10 (2000) 721–723.
[448] B. Blümich, S. Anferova, F. Casanova, K. Kremer, J. Perlo, S. Sharma, Unilateral NMR: principles and applications to quality control of elastomer products, KGK Kautschuk Gummi Kunststoffe 57 (2004) 346–349.
[449] Process Control Technology Corporation, 3620 Soderburg Drive, Ft. Collins, CO 80526, USA, Available from: <http://www.pctnmr.com/>.
[450] Process NMR Associates, 87A Sand Pit Rd, Danbury, CT 06810, USA, Available from: <http://www.process-nmr.com/>.
[451] Progression Inc., 15 Foundation Avenue, Haverhill, MA 01835, USA, Available from: <http://www.progression-systems.com/>.
[452] P. Mansfield, P.G. Morris, NMR Imaging in Biomedicine, Adv. Magn. Reson. Suppl. 2, Academic Press, New York, 1982.
[453] W.S. Hinshaw, Spin mapping: the application of moving gradients to NMR, Phys. Lett. A 48 (1974) 87–88.
[454] R. Damadian, L. Minkoff, M. Goldsmith, M. Stanford, J. Koutcher, Field focusing nuclear magnetic resonance (FONAR): visualization of a tumor in a live animal, Science 194 (1976) 1430–1432.
[455] H.T. Pedersen, S. Ablett, D.R. Martin, M.J.D. Mallett, S.B. Engelsen, Application of the NMR MOUSE to food emulsions, J. Magn. Reson. 165 (2003) 49–58.
[456] P. Blümler, B. Blümich, NMR imaging of solids, NMR – Basic Principles and Progress 30 (1994) 209–281.
[457] B. Blümich, P. Blümler, K. Saito, NMR imaging and spatial information, in: I. Ando, T. Asakura (Eds.), Solid-State NMR of Polymers, Elsevier, Amsterdam, 1998, pp. 123–163.
[458] G.C. Chingas, J.B. Miller, A.N. Garroway, NMR images of solids, J. Magn. Reson. 66 (1986) 530–535.
[459] D. Demco, B. Blümich, Solid-state NMR imaging methods – Part I: strong field gradients, Concepts Magn. Reson. 12 (2000) 188–206.
[460] D. Demco, B. Blümich, Solid-state NMR imaging methods – Part II: line narrowing, Concepts Magn. Reson. 12 (2000) 269–288.
[461] B. Blümich, Contrast in solid-state NMR imaging. Part I: principles, Concepts Magn. Reson. 10 (1998) 19–31.
[462] B. Blümich, Contrast in solid-state NMR imaging IIa: basic filters, Concepts Magn. Reson. 11 (1999) 71–87.
[463] B. Blümich, Contrast in solid-state NMR imaging IIb: advanced filters, spectroscopic parameters, and sample manipulation, Concepts Magn. Reson. 11 (1999) 147–164.
[464] B. Blümich, P. Blümler, L. Gasper, A. Guthausen, V. Göbbels, S. Laukemper-Ostendorf, K. Unseld, G. Zimmer, Spatially resolved NMR in polymer science, Macromol. Symp. 141 (1999) 83–93.
[465] P. Blümler, B. Blümich, NMR imaging of elastomers: a review, Rubber Chem. Tech. (Rubber Rev.) 70 (1997) 468–518.
[466] B. Blümich, D.E. Demco, NMR imaging of elastomers, in: V.M. Litvinov, P.P. De (Eds.), Spectroscopy of Rubbers and Rubbery Materials, Rapra Technology Limited, Shawbury, 2002, pp. 247–289.
[467] U. Netzelmann, G. Walle, B. Wolter, C. Skalrczyk, M. Mais, Prüfung von Elastomeren mit Hilfe neuer zerstörungsfreier Prüfverfahren, KGK Kautschuk Gummi Kunststoffe 11 (2001) 586–591.
[468] R. Eymael, K. Hailu, B. Blümich, Mobile NMR mit der NMR-MOUSE®, CLB Chemie in Labor und Biotechnik 52 (2001) 124–127.
[469] L.J. Burnett, D.R. McKay, E.M. Magnuson, E.J. VanderHeiden, Solid rocket motor NDE using nuclear magnetic resonance, Rev. Prog. Quant. Nondestr. Eval. 12 (1993) 663–670.
[470] L.J. Burnett, E.E. Magnuson, E.J. VanderHeiden, NDE using nuclear magnetic resonance, Rev. Prog. Quant. Nondestr. Eval. 14 (1995) 1521–1528.
[471] E.J. VanderHeiden, Applications of NMR imaging on solid rocket motor materials, Rev. Prog. Quant. Nondestr. Eval. 11 (1992) 663–670.
[472] J. Arnold, C. Clauser, R. Pechnig, S. Anferova, V. Anferov, B. Blümich, Porosity and permeability from mobile NMR core-scanning, Petrophysics 47 (2006) 306–314.
[473] B. Blümich, S. Anferova, R. Pechnig, H. Pape, J. Arnold, C. Clauser, Mobile NMR for porosity analysis of core sections, J. Geophys. Eng. 1 (2004) 177–180.
[474] T.W. Schenz, B. Dauber, C. Nicholls, C. Gardner, V.A. Scott, S.P. Roberts, M.J. Hennesy, Online MR imaging for detection of spoilage in finished packages, Food Sci. Technol. Today 13 (1999) 92–96.
[475] D.R. Martin, S. Ablett, H.T. Pedersen, J.M.D. Mallett, The NMR MOUSE: its applications to food science, in: P.S. Belton, A.M. Gill, G.A. Webb, D. Rutledge (Eds.), Magnetic Resonance in Food Science: Latest Developments, RCS, Cambridge, pp. 54–61.
[476] E. Veliyulin, C. van der Zwaag, W. Burk, U. Erikson, In vivo determination of fat content of atlantic salmon (Salmo Salar) with a mobile NMR spectrometer, J. Sci. Food Agric. 85 (2005) 1299–1304.
[477] F. Casanova, J. Perlo, B. Blümich, Depth profiling by single-sided NMR, in: S. Stapf, S. Han (Eds.), NMR in Chemical Engineering, Wiley-VCH, Weinheim, 2006, pp. 107–123.
[478] N.O. Goga, A. Pirnau, L. Szabo, R. Smeets, D. Riediger, O. Cozar, B. Blümich, Mobile NMR: applications to materials and biomedicine, J. Optoelectr. Adv. Mat. 8 (2006) 1430–1434.
[479] A. Guthausen, G. Zimmer, S. Laukemper-Ostendorf, P. Blümler, B. Blümich, NMR-Bildgebung und Materialforschung, Chemie in unserer Zeit 32 (1998) 73–82.
[480] B. Blümich, P. Blümler, A. Guthausen, C. Fülber, G. Eidmann, R. Savelsberg, Ortsaufgelöste Abbildung von Vernetzungsdichten mit NMR, Kautschuk, Gummi, Kunststoffe 50 (1997) 560–563.
[481] B. Blümich, A. Buda, K. Kremer, Non-destructive testing with mobile NMR, RFP 1 (2006) 34–37.
[482] B. Blümich, A. Buda, K. Kremer, Zerstörungsfreies Prüfen mit mobiler NMR, GAK Gummi Fasern Kunststoffe 59 (2006) 290–293.
[483] B. Blümich, F. Casanova, A. Buda, K. Kremer, T. Wegener, Anwendungen der mobilen NMR zur Zustandsbewertung von Bauteilen aus Polyethylen, 3R Int. 44 (2005) 349–354.
[484] B. Blümich, S. Anferova, S. Sharma, A.L. Segre, C. Federici, Degradation of historical paper: nondestructive analysis by the NMR-MOUSE®, J. Magn. Reson. 161 (2003) 204–209.
[485] S. Sharma, F. Casanova, W. Wache, A.L. Segre, B. Blümich, Analysis of historical porous building materials by the NMR-MOUSE®, Magn. Reson. Imaging 21 (2003) 249–255.
[486] G. Bizzaro, R. Melzi, F. Tedoldi, M. Kloza, D. Maier, G. Guthausen, Single-sided NMR with the MQ-ProFiler: latest devel-

opments in cultural heritage investigations, Bruker Spin Rep. 156 (2005) 8–22.
[487] C. Casieri, S. Bubici, I. Viola, F. De Luca, A low-resolution non-invasive NMR characterization of ancient paper, Solid State Nucl. Magn. Reson. 26 (2004) 65–73.
[488] N. Proietti, D. Capitani, E. Pedemonte, B. Blümich, A.L. Segre, Monitoring degradation in paper: non-invasive analysis by unilateral NMR. Part II, J. Magn. Reson. 170 (2004) 113–120.
[489] N. Proietti, D. Capitani, R. Lamanna, F. Presciutti, E. Rossi, A.L. Segre, Fresco paintings studied by unilateral NMR, J. Magn. Reson. 177 (2005) 111–117.
[490] S. Viel, D. Capitani, N. Proietti, F. Ziarelli, A.L. Segre, NMR spectroscopy applied to cultural heritage: a preliminary study on ancient wood characterization, Appl. Phys. A 79 (2004) 357–361.
[491] I. Viola, S. Bubici, C. Casieri, F. De Luca, The codex major of the Collectio Altaempsiana: a non-invasive NMR study of paper, J. Cult. Heritage 5 (2004) 257–261.
[492] C. Casieri, L. Senni, M. Romagnoli, U. Santamaria, F. De Luca, Determination of moisture fraction in wood by mobile NMR device, J. Magn. Reson. 171 (2004) 364–372.
[493] B. Goodson, Mobilizing magnetic resonance, Phys. World 19 (2006) 28–33.
[494] J. Perlo, F. Casanova, B. Blümich, Advances in Single-Sided NMR, in: G.A. Webb (Ed.), Modern Magnetic Resonance, Springer, Berlin, 2006, pp. 1503–1507.
[495] P.S. Belton, A.M. Gil, G.A. Webb, D. Rutledge, Magnetic Resonance in Food Science: Latest Developments, R. Soc. Chem. London, 2003.
[496] S. Bank, Some principles of NMR spectroscopy and their novel applications, Concepts Magn. Reson. 9 (1996) 83–93.
[497] L. Mannina, A.P. Sobolev, A.L. Segre, Olive oil as seen by NMR and chemometrics, Spectrosc. Eur. 15 (2003) 6–14.
[498] C. Guillou, G. Remaud, G.J. Martin, Trends Food Sci. Tech. 3 (1992) 197–201.
[499] P.N. Gambhir, Application of low-resolution pulsed NMR to the determination of oil and moisture in oil seeds, Trends Food Sci. Tech. 3 (1992) 191–196.
[500] AOCS Official Method Ak 4-95, ISO 10565, ISO 10632 for Residues, USDA, GIPSA Approval, FGIS00-11.
[501] H.T. Pedersen, H. Berg, F. Lundby, S.B. Engelsen, The multivariate advantage in fat determination in meat by bench-top NMR, Innov. Food Sci. Emerg. Tech. 2 (2001) 87–94.
[502] M.C.M. Gribnau, Determination of solid/liquid ratios of fats and oils by low-resolution pulsed NMR, Trends Food Sci. Tech. 3 (1992) 186–190.
[503] P.T. Callaghan, K.W. Jolley, R.D. Humphrey, Diffusion of fat and water in cheese as studied by pulsed field gradient nuclear magnetic resonance, J. Colloid Interface Sci. 93 (1983) 521–529.
[504] H. Todt, W. Burk, G. Guthausen, A. Guthausen, A. Kamlowski, D. Schmalbein, Eur. J. Lipid Sci. Technol. 103 (2001) 835–840.
[505] P. Chen, M.J. McCarty, R. Kauten, Y. Sarig, S. Han, Maturity evaluation of avocados by NMR methods, J. Agric. Eng. Res. 55 (1993) 177–187.
[506] S.B. Engelsen, M.K. Jensen, H.T. Pedersen, L. Norgaard, L. Munck, NMR-baking and multivariate prediction of instrumental texture parameters in bread, J. Cereal Sci. 33 (2001) 59–69.
[507] A.M. Haiduc, J. van Duynhoven, Correlation of porous and functional properties of food materials by NMR relaxometry and multivariate analysis, Magn. Reson. Imaging 23 (2005) 343–345.
[508] S. Godefroy, P.T. Callaghan, 2D relaxation/diffusion correlations in porous media, Magn. Reson. Imaging 21 (2003) 381–383.
[509] N. Nestle, A. Qadan, P. Galvosas, W. Süss, J. Kärger, PFG NMR and internal magnetic field gradients in plant-based materials, Magn. Reson. Imaging 20 (2002) 567–573.
[510] S. Martini, M.L. Herrera, A. Marangoni, New technologies to determine solid fat content on-line, J. Am. Oil Chem. Soc. 82 (2005) 313–317.
[511] R. Colsenet, O. Soderman, F. Mariette, Diffusion of polyethyleneglycols in casein solutions and gels as studied by pulsed field gradient NMR, Magn. Reson. Imaging 23 (2005) 347–348.
[512] B. Zion, M.J. McCarthy, P. Chen, Real-time detection of pits in processed cherries magnetic resonance projection, Food Sci. Technol. 27 (1994) 457–462.
[513] M.J. McCarthy, Magnetic Resonance Imaging in Foods, Chapman and Hall, London, 1994.
[514] B.P. Hills, Magnetic Resonance Imaging in Food Science, Wiley, New York, 1998.
[515] M.J. McCarthy, K.L. McCarthy, Applications of magnetic resonance imaging to food research, Magn. Reson. Imaging 14 (1996) 799–802.
[516] M. Koizumi, S. Naito, T. Haishi, S. Utsuzawa, N. Ishida, H. Kano, Thawing of frozen vegetables observed by a small dedicated MRI for food research, Magn. Reson. Imaging 24 (2006) 1111–1119.
[517] F. Mariette, Relaxation RMN et IRM: un couplage indispensable pour l'étude des produits alimentaires, C.R. Chim. 7 (2004) 221–232.
[518] G. Galed, M.E. Fernández-Valle, A. Martínez, A. Heras, Application of MRI to monitor the process of ripening and decay in citrus with chitosan solutions, Mag. Reson. Imaging 22 (2004) 127–137.
[519] M.E. Miquel, L.D. Hall, A general survey of chocolate confectionery by magnetic resonance imaging, Lebensm. Wiss. Technol. 31 (1998) 93–99.
[520] A. Guthausen, G. Guthausen, A. Kamlowski, H. Todt, W. Burk, D. Schmalbein, Measurement of fat content of food with single-sided NMR, J. Am. Oil Chem. Soc. 81 (2004) 727–731.
[521] S. Rahmatallah, Y. Li, H.C. Seton, J.S. Gregory, R.M. Aspden, Measurement of relaxation times NMR in foodstuffs using a one-sided portable magnetic resonance probe, Eur. Food Res. Tech. 222 (2006) 298–301.
[522] K.J. Carlton, M.R. Halse, A.M. Maphossa, M.J. Mallett, NMR stray-field analysis of oil droplet size distribution in peanut cotyledons, Eur. Biophys. J. 29 (2001) 574–578.
[523] A.G. Goloshevsky, J.H. Walton, M.V. Shukov, J.S. de Ropp, S.D. Collins, M.J. McCarthy, Development of low field nuclear magnetic resonance microcoils, Rev. Sci. Instrum. 76 (2005), 024101, 1–6.
[524] A.G. Goloshevsky, J.H. Walton, M.V. Shukov, J.S. de Ropp, S.D. Collins, M.J. McCarthy, Integration of biaxial planar gradient coils and an rf microcoil for NMR flow imaging, Meas. Sci. Technol. 16 (2005) 512–515.
[525] A. De Los Santos, J.D. King, D.C. Stead, Industrial magnetic resonance – food and other industries, in: G.A. Webb, P.S. Belton, A.M. Gil, I. Delgadillo, Magnetic Resonance in Food Science: Analysis, Monitoring and Authentication, R. Soc. Chem., Cambridge, 2001.
[526] A.G. Goloshevsky, J.H. Walton, M.V. Shukov, J.S. de Ropp, S.D. Collins, M.J. McCarthy, Nuclear magnetic resonance imaging for viscosity measurements of non-Newtonian fluids using a miniturized RF coil, Meas. Sci. Technol. 16 (2005) 513–518.
[527] K.L. McCarthy, R.J. Kauten, C.K. Agemura, Application of NMR imaging to the study of velocity profiles during extrusion processing, Trends Food Sci. Tech. 3 (1992) 215–219.
[528] L. van der Weerd, T. Ruttink, D. van Dusschoten, F.J. Vergeldt, P.A. de Jager, H. Van As, Plant growth studies using low Field NMR, in: P. Blümler, B. Blümich, R. Botto, E. Fukushima (Eds.), Spatially Resolved Magnetic Resonance, Wiley-VCH, Weinheim, 1998, pp. 473–479.
[529] L. Van der Weerd, M.M.A.E. Claessens, C. Efdé, H. Van As, Nuclear magnetic resonance imaging of membrane permeability changes in plants during osmotic stress, Plant Cell Environ. 25 (2002) 1539–1549.
[530] The Whitaker Foundation 2001 Annual Report, Biomedical Engineering and the Practice of Medicine, Available from: <www.whitaker.org/01_annual_report/practice.html/>.

[531] J. Perlo, Single-Sided NMR Tomography, Dissertation, RWTH Aachen University, 2006.
[532] R.M. Henkelman, G.J. Stanisz, J.K. Kim, M.J. Bronskill, Anisotropy of NMR properties of tissues, Magn. Reson. Med. 32 (1994) 592–601.
[533] Y. Xia, Relaxation anisotropy in cartilage by NMR microscopy (μMRI) at 14 μm resolution, Magn. Reson. Med. 39 (1998) 941–949.
[534] Y. Xia, Relaxation anisotropy as a possible marker for macromolecular orientations in carticular cartilage, in: P. Blümler, B. Blümich, R. Botto, E. Fukushima (Eds.), Spatially Resolved Magnetic Resonance, Wiley-VCH, Weinheim, 1998, pp. 351–362.
[535] Y. Xia, J.B. Moody, H. Alhadlaq, Orientational dependence of T_2 relaxation in articular cartilage: a microscopic MRI (μMRI) study, Magn. Reson. Med. 48 (2002) 460–469.
[536] R. Fechete, D.E. Demco, U. Eliav, B. Blümich, G. Navon, Self-diffusion anisotropy of water in sheep Achilles tendon, NMR Biomed. 18 (2005) 577–586.
[537] R. Fechete, D.E. Demco, B. Blümich, U. Eliav, G. Navon, Anisotropy of collagen fiber orientation in sheep tendon by ^{1}H double-quantum filtered NMR signals, J. Magn. Reson. 162 (2003) 166–175.
[538] R. Fechete, D.E. Demco, B. Blümich, Segmental anisotropy in strained elastomers by ^{1}H NMR of multipolar spin states, Macromolecules 35 (2002) 6083–6085.
[539] R. Fechete, D.E. Demco, B. Blümich, Parameter maps of ^{1}H residual dipolar couplings in tendon under mechanical load, J. Magn. Reson. 165 (2003) 9–17.
[540] J. Wellen, K.G. Helmer, P. Grigg, C.H. Sotak, Application of porous-media theory to the investigation of water ADC changes in rabbit achilles tendon caused by tensile loading, J. Magn. Reson. 170 (2004) 49–55.
[541] J. Kastelic, A. Galeski, E. Baer, The multicomposite structure of tendon, Connect. Tissue Res. 6 (1978) 11–23.
[542] G.D. Fullerton, I.L. Cameron, V.A. Ord, Orientation of tendon in the magnetic field and its effect on relaxation times, Radiology 155 (1985) 433–435.
[543] S.J. Erickson, I.H. Cox, J.S. Hyde, G.F. Carrera, J.A. Strandt, L.D. Estkowski, Effect of tendon orientation on mr imaging signal intensity: a manifestation of the "Magic Angle" phenomenon, Radiology 181 (1991) 389–392.
[544] M.E. Timins, S.J. Erckson, L.D. Estkowski, G.F. Carrera, R.A. Komorowski, Increased signal in the normal supraspinatus tendon on MR imaging: diagnostic pitfall caused by the magic-angle effect, Am. J. Radiol. 164 (1995) 109–114.
[545] T.L. Chenevert, J.A. Brunberg, J.G. Pipe, Anisotropic diffusion in human white matter: demonstration with MR techniques in vivo, Radiology 177 (1990) 401–405.
[546] P.J. Basser, J. Mattiello, D. LeBihan, Diffusion tensor spectroscopy and imaging, Biophys. J. 66 (1994) 259–267.
[547] V. Mlynarik, P. Szomolanyi, R. Toffanin, F. Vittur, S. Trattnig, Transverse relaxation mechanisms in articular cartilage, J. Magn. Reson. 169 (2004) 300–307.
[548] G.E. Santyr, R. Mark Henkelman, M.J. Bronskill, Variation in measured transverse relaxation in tissue resulting from spin locking with the CPMG sequence, J. Magn. Reson. 79 (1988) 28–44.
[549] A. Blümich, B. Blümich, unpublished results.
[550] S. Richard, B. Querleux, J. Bittoun, O. Jolivet, I. Idy-Peretti, O. de Lacharriere, J.-L. Lévêque, Characterization of the skin *in vivo* by high resolution magnetic resonance imaging: water behavior and age-related effects, J. Investig. Derm. 100 (1993) 705–709.
[551] S. Richard, B. Querleux, J. Bittoun, I. Idy-Peretti, O. Jolivet, E. Cermakova, J.-L. Lévêque, In vivo proton relaxation time analysis of the skin layers by magnetic resonance imaging, J. Investig. Derm. 97 (1991) 120–125.
[552] L. Backhouse, M. Dias, J.P. Gorce, K. Hadgraft, P.J. McDonald, J.W. Wiechers, GARField magnetic resonance profiling of the ingress of model skin-care product ingredients into human skin *in vitro*, J. Pharm. Sci. 93 (2004) 2274–2283.
[553] P.J. McDonald, A. Akhmerov, L.J. Backhouse, S. Pitts, Magnetic resonance profiling of human skin *in vivo* using GARField magnets, J. Pharm. Sci. 94 (2005) 1850–1860.
[554] M. Dias, J. Hadgraft, P.M. Glover, M.J. McDonald, Stray field magnetic resonance imaging: a preliminary study of skin hydration, J. Phys. D: Appl. Phys. 36 (2003) 364–368.
[555] N. Pallua, E. Demir, M. Schröder, P. von Oppell, J. Perlo, F. Casanova, B. Blümich, unpublished.
[556] F. Heller, A. Schwaiger, R. Eymael, R. Schulz-Wendtland, B. Blümich, Messung der Kontrastmittelanreicherung in der Haut und im subkutanen Fettgewebe mit der NRM-MOUSE® – eine Machbarkeitsstudie, RöFo 177 (2005) 1412–1416.
[557] M. Krüger, A. Schwarz, B. Blümich, Investigations of silicone breast implants with the NMR-MOUSE, Magn. Reson. Imaging 25 (2007) 215–218.
[558] J.M.G. Cowie, Polymers: Chemistry & Physics of Modern Materials, second ed., Blackie Academic & Professional, London, 1991.
[559] V.M. Litvinov, Characterization of chemical and physical networks in rubbery materials using proton NMR magnetization relaxation, in: V.M. Litvinov, P. Dee (Eds.), Spectroscopy of Rubber and Rubbery Materials, Rapra Press, Sheffield, 2002, Chapter 10.
[560] N.O. Goga, K. Kremer, B. Blümich, Zerstörungsfreie Qualitätskontrolle in der Reifenproduktion: Die, NMR-MOUSE, GAK 58 (2005) 104–108.
[561] V. Herrmann, K. Unseld, H.-B. Fuchs, B. Blümich, Molecular dynamics of elastomers investigated by DMTA and the NMR-MOUSE®, Colloid Polym. Sci. 280 (2002) 758–764.
[562] V. Hermann, T. Böhner, B. Blümich, Application of NMR in the tire industry, KGK Kautschuk Gummi Kunststoffe 57 (2004) 22–27.
[563] K. Kremer, H. Kühn, B. Blümich, J. Seitzer, F.-P. Schmitz, NMR-MOUSE® ermöglicht Online-Qualitätskontrolle im KFZ-Bau, Adhäsion 46 (2002) 32–36.
[564] P. Blümler, V. Litvinov, H.G. Dikland, M. van Duin, Detection of interfacial layers in elastomer samples by NMR imaging, Kautschuk Gummi Kunststoffe 51 (1998) 865–867.
[565] C.A. Stevens, Factory testing and control of raw natural rubber and mixed batches using the rubber process analyzer, Kautschuk Gummi Kunststoffe 54 (2001) 29–35.
[566] B. Blümich, A. Adams-Buda, M. Baias, Alterung von Polyethylen: Zerstörungsfreise Prüfen mit mobiler magnetischer Resonanz, Gas Erdgas 148 (2007) 95–98.
[567] A. Hartwig, B. Wolter, Zerstörungsfreie NMR-Aufsatztechnik: Anwendungsbeispiele und Möglichkeiten, Adhäsion 12 (2001) 34–38.
[568] R. Fechete, D.E. Demco, B. Blümich, Chain orientation and slow dynamics in elastomers by mixed magnetic Hahn echoe decays, J. Chem. Phys. 118 (2003) 2411–2421.
[569] V.M. Litvinov, M. van Duin, Real-time ^{1}H NMR relaxation study of EPDM vulcanization, KGK Kautschuk Gummi Kunststoffe 55 (2002) 460–463.
[570] J. Kolz, J. Martins, K. Kremer, T. Mang, B. Blümich, Investigation of the elastomer-foam production with Single-Sided NMR, Kautschuk Gummi Kunststoffe 60 (2007) 179–183.
[571] K. Kremer, B. Blümich, F.-P. Schmitz, J. Seitzer, Nondestructive testing of adhesive curing in glass-metal compounds by unilateral NMR, in: W. Possart (Ed.), Adhesion – Current Research and Applications, Wiley-VCH, Weinheim, 2005, pp. 435–443.
[572] K. Saalwächter, M. Gottlieb, R. Liu, W. Oppermann, Gelation as studied by proton multiple-quantum NMR, Macromolecules 40 (2007) 1555–1561.
[573] B. Wolter, E. Köller, Prüfung von Elastomeren mit NMR, DGzfP-Jahrestagung 2001, 21–23 May, Berlin.
[574] A.E. Somers, T.J. Barstow, M.I. Burgar, M. Forsyth, A.J. Hill, Quantifying rubber degradation using NMR, Polym. Degrad. Stab. 70 (2000) 31–37.

[575] I.H. Gocan, Sample Profiling by Unilateral NMR, Thesis, RWTH Aachen University, Aachen, 2006.
[576] P. Blümler, B. Blümich, Aging and phase separation of elastomers investigated by NMR imaging, Macromolecules 24 (1991) 2183–2188.
[577] J.L. Herberg, S.C. Chinn, A.M. Sawvel, E. Gjersing, R.S. Maxwell, Characterization of local deformation in filled-silicone elastomers subject to high strain – NMR MOUSE and Magnetic Resonance Imaging as a diagnostic tool for detection of inhomogeneities, Polym. Degrad. Stab. 91 (2006) 1701–1710.
[578] T.W. Skloss, M.J. Hennessy, I. Pykett, Magnetic Resonance Inspection of Synthetic Rubber, Meeting of the Rubber Division, American Chemical Society Orlando, Florida, September 21–24, 1999.
[579] G. Zimmer, A. Guthausen, U. Schmitz, K. Saito, B. Blümich, Weathering investigation of PVC coatings on iron sheets by the NMR MOUSE, Adv. Mater. 9 (1997) 987–989.
[580] A.E. Marble, I.V. Mastikhin, R.P. MacGregor, M. Akl, G. LaPlante, B.G. Colpitts, P. Lee-Sullivan, B.J. Balcom, Distortion-free single point imaging of multi-layered composite sandwich panel structures, J. Magn. Reson. 168 (2004) 164–174.
[581] V.M. Litvinov, M. Soliman, The effect of storage of poly(propylene) pipes under hydrostatic pressure and elevated temperatures on the morphology, molecular mobility and failure behavior, Polymer 46 (2005) 3077–3089.
[582] D. Knittel, R. Benken, E. Schollmeyer, Niedrigauflösende NMR-Analysen zur Bestimmung textiler Veredelungsparameter, Melliand Textilberichte 7–8 (2002) 550–555.
[583] G.A. Matzkanin, A. De Los Santos, NDE of moisture absorption in composites using nuclear magnetic resonance, Defense Technical Information Center Add328178, September 1987.
[584] S.J.F. Erich, J. Laven, L. Pel, H.P. Huinink, K. Kopinga, Comparison of NMR and confocal Raman microscopy as coatings research tools, Prog. Org. Coatings 52 (2005) 210–216.
[585] W.E. Kenyon, Nuclear magnetic resonance as a petrophysical measurement, Nucl. Geophys. 6 (1992) 153–171.
[586] L.A. Kirk, W.R. Ladner, H.B. Taylor, Some physical methods for moisture determination, Proc. Soc. Anal. Chem. 1 (1964) 82–84.
[587] R.M.E. Valckenborg, H.P. Huinink, J.J.V.D. Sande, K. Kopinga, Random-walk simulations of NMR dephasing effects due to uniform magnetic-field gradients in a pore, Phys. Rev. E 65 (2002), 021306, 1–8.
[588] R.M.E. Valckenborg, H.P. Huinink, K. Kopinga, Nuclear magnetic resonance dephasing effects in a spherical pore with a magnetic dipolar field, J. Chem. Phys. 118 (2003) 3243–3251.
[589] G.Q. Zhang, G.J. Hirasaki, CPMD relaxation by diffusion with constant magnetic field gradient in a restricted geometry: numerical simulation and application, J. Magn. Reson. 163 (2003) 81–91.
[590] J. Petkovic, H.P. Huinink, L. Pel, K. Kopinga, Diffusion in porous building materials with high internal magnetic field gradients, J. Magn. Reson. 167 (2004) 97–106.
[591] J. Boguszynska, M.C.A. Brown, P.J. McDonald, J. Mitchell, M. Mulheron, J. Tritt-Goc, D.A. Verganelakis, Magnetic resonance studies of cement based materials in inhomogeneous fields, Cement Concrete Res. 35 (2005) 2033–2040.
[592] N. Nestle, P. Galvosas, M. Dakkouri, C. Zimmermann, J. Kärger, NMR studies of water diffusion and relaxation in hydrating slag-based construction materials, Magn. Reson. Imaging 19 (2001) 547–548.
[593] N. Nestle, NMR relaxometry study of cement hydration in the presence of different oxidic fine fraction materials, Solid State Nucl. Magn. Reson. 25 (2004) 80–83.
[594] F. Kohl, B. Wolter, One-sided access ^{1}H-nuclear magnetic resonance (Osa-^{1}H NMR) as a versatile tool for industrial application, Defektoskopie 2002 (2002) 93–100.
[595] O. Dicoi, P. Walzel, B. Blümich, W. Rähse, Untersuchungen des Trocknungsverhaltens von Feststoffen mit kernmagnetischer Resonanz, Chemie Ingenieur Technik 76 (2004) 94–99.
[596] R.M.E. Valckenborg, L. Pel, K. Kopinga, NMR relaxation and diffusion measurements on iron(III)-doped kaolin clay, J. Magn. Reson. 151 (2001) 291–297.
[597] P. Kinchesh, A.A. Samoilenko, A.R. Preston, E.W. Randall, Stray field nuclear magnetic resonance of soil water, J. Environ. Qual. 31 (2002) 494–499.
[598] M. Alesiani, S. Capuani, B. Maraviglia, NMR studies on the early stages of hydration of a porous carbonate stone, Magn. Reson. Imaging 21 (2003) 333–335.
[599] V. Bortolotti, M. Camaiti, C. Casieri, F. De Luca, P. Fantazzini, C. Terenzi, Water absorption kinetics in different wettability conditions studied at pore and sample scales in porous media by NMR with portable single-sided and laboratory imaging devices, J. Magn. Reson. 181 (2006) 287–295.
[600] L.A. Rijniers, L. Pel, H.P. Huinink, K. Kopinga, Salt crystallization as damage mechanism in porous building materials – a nuclear magnetic resonance study, Magn. Reson. Imaging 23 (2005) 273–276.
[601] L.A. Rijners, P.C.M.M. Magusin, H.P. Huinink, L. Pel, K. Kopinga, Sodium NMR relaxation in porous materials, J. Magn. Reson. 167 (2004) 25–30.
[602] H. Yun, M.E. Patton, J.H. Garrett, G.K. Fedder, K.M. Frederick, J.-J. Hsu, I.J. Lowe, I.J. Oppenheim, P.J. Sides, Detection of free chloride in concrete by NMR, Cement Concrete Res. 34 (2004) 379–390.
[603] B. Wolter, F. Kohl, N. Surkowa, G. Dobmann, Practical applications of NMR in civil engineering, in: International Symposium on Non-Destructive Testing in Civil Engineering, Berlin, 16–19 September, 2003.
[604] B. Wolter, G. Dobmann, F. Knapp, A. Marko, Nondestructive Characterization of Fresh Concrete and Other Porous Materials with One-Sided Access NMR, Adv. Test. Fresh Cement. Mat., Stuttgart, 3–4 August, 2006, pp. 131–138.
[605] B. Wolter, NMR Aquametry, in: G. Dobmann (Ed.), Electromagnetic Nondestructive Evaluation (VII), IOS Press, Amsterdam, 2006, pp. 29–37.
[606] P. Kinchesh, E.W. Randall, K. Zick, Magnetic susceptibility effects in imaging: distortion-free images of plant tissue in soil, Magn. Reson. Imaging 12 (1994) 305–307.
[607] A.R. Preston, N.R.A. Bird, P. Kinchesh, E.W. Randall, W.R. Whalley, STRAFI-NMR studies of water transport in soil, Magn. Reson. Imaging 19 (2001) 561–563.
[608] P.T. Callaghan, R. Dykstra, C.D. Eccles, T.G. Haskell, J.D. Seymour, A nuclear magnetic resonance study of antarctic sea ice by brine diffusivity, Cold Reg. Sci. 29 (1999) 153–171.
[609] P. Colombet, A.-R. Grimmer, Applications of NMR Spectroscopy to Cement Science, CRC Press, London, 1995.
[610] P. Colombet, A.-R. Grimmer, H. Zanni (Eds.), Nuclear Magnetic Resonance Spectroscopy of Cement-Based Materials, Springer, Berlin, 1998.
[611] G. Dobmann, M. Kroening, S. Surkowa, L. van Bernus, B. Wolter, The Potential of Nuclear Magnetic Resonance (NMR) to Non-Destructively Characterize Early-Age Concrete by an One-Sided Access (OSA) Technique, NDE2002, Chennai, 5–7 December, 2002.
[612] F. Kohl, B. Wolter, F. Knapp, Concrete hardening and moisture distribution in sandstones monitored by one-sided ^{1}H-Nuclear Magnetic Resonance, in: International Symposium on Non-Destructive Testing in Civil Engineering, Berlin, 16–19 September, 2003.
[613] P.J. McDonald, J. Mitchell, M. Mulheron, L. Monteilhet, J.-P. Korb, Two-dimensional correlation relaxation studies of cement pastes, Magn. Reson. Imaging 25 (2007) 470–473.
[614] H.J.P. Brocken, M.E. Spiekman, L. Pel, K. Kopinga, J.A. Larbi, Water extraction out of mortar during brick laying: a NMR study, Mater. Struct. 31 (1998) 49–57.
[615] R.M.E. Valckenborg, L. Pel, K. Hazrati, K. Kopinga, J. Marchand, Pore water distribution in mortar during drying as determined by NMR, Mater. Struct. 34 (2001) 599–604.
[616] H. Brocken, L. Pel, K. Kopinga, Moisture transport over the brick/mortar interface, in: P. Colombet, A.R. Grimmer, H. Zanni (Eds.),

Nuclear Magnetic Resonance Spectroscopy of Cement-Based Materials, Springer, Berlin, 1998, pp. 397–401.
[617] H.J.P. Brocken, J.A. Larbi, L. Pel, N.M. van der Pers, Composition of mortar as a function of distance to the brick-mortar interface: a study on the formation of cured mortar structure in masonry using NMR, PFM and XRD, Heron 44 (1999) 257–270.
[618] L. Pel, K. Kopinga, E.F. Kaasschieter, Saline absorption in calcium-silicate brick observed by NMR scanning, J. Phys. D: Appl. Phys. 33 (2000) 1380–1385.
[619] L. Pel, H.P. Huinink, K. Kopinga, L.A. Rijniers, E.F. Kaasschieter, Ion transport in porous media studied by NMR, Magn. Reson. Imaging 19 (2001) 549–550.
[620] L. Pel, H. Huinink, K. Kopinga, Ion transport and crystallization in inorganic building materials as studied by nuclear magnetic resonance, Appl. Phys. Lett. 81 (2002) 2893–2895.
[621] H.P. Huinink, L. Pel, M.A.J. Michels, How ions distribute in a drying porous medium: a simple model, Phys. Fluids 14 (2002) 1389–1395.
[622] P.J. Barale, C.G. Fong, M.A. Green, P.A. Luft, A.D. McInturff, J.A. Reimer, M. Yahnke, The use of a permanent magnet for water content measurement of wood chips, IEEE Trans Appl. Supercond. 12 (2002) 975–978.
[623] A. Rosenkilde, P. Glover, High resolution measurement of the surface layer moisture content during drying of wood using novel magnetic resonance imaging technique, Holzforschung 56 (2002) 312–317.
[624] B. Wolter, Determination of density and moisture distribution in chip boards with one-sided access nuclear magnetic resonance (OSA-NMR), in: Fourth International Conference on Electromagnetic Wave Interaction with Water and Moist Substances, Weimar, 13–16 May, 2001, pp. 318–324.
[625] M.K. Gingras, B. MacMillan, B.J. Balcom, T. Saunders, S.G. Pemberton, Using magnetic resonance imaging and petrographic techniques to understand the textural attributes and porosity distribution in macaronichnus-burrowed sandstone, J. Sediment. Res. 72 (2002) 552–558.
[626] M.K. Gingras, B. MacMillan, B.J. Balcom, Visualizing the internal physical characteristics of carbonate sediments with magnetic resonance imaging and petrography, Bull. Can. Petrol. Geol. 50 (2002) 363–369.
[627] R. Wang, R.W. Mair, M.S. Rosen, D.G. Cory, R.L. Walsworth, Simultaneous measurement of rock permeability and effective porosity using laser-polarized noble gas NMR, Phys. Rev. E 70 (2004), 026312, 1–7.
[628] M.G. Prammer, E. Drack, G. Goodman, P. Masak, S. Menger, M. Morys, S. Zannoni, B. Suddarth, J. Dudley, The Magnetic Resonance While-Drilling tool: Theory and operation, 2000 SPE Ann. Tech. Conf. Exhib., Dallas TX, 1–4 October, 2000.
[629] G. Hirasaki, NMR applications in petroleum reservoir studies, in: S. Stapf, S. Han (Eds.), NMR in Chemical Engineering, Wiley-VCH, Weinheim, 2006, pp. 321–340.
[630] B. Sun, In situ fluid typing and quantification with 1D and 2D NMR logging, Magn. Reson. Imaging 25 (2007) 521–524.
[631] G. Maddinelli, E. Peron, Characterization of sedimentary rocks with a single-sided NMR instrument, Appl. Magn. Reson. 29 (2005) 549–559.
[632] R.L. Kleinberg, D.D. Griffin, NMR measurements of permafrost: unfrozen water assay, pore-scale distributions of ice, and hydraulic permeability of sediments, Cold Reg. Sci. Technol. 42 (2005) 63–77.
[633] R.L. Kleinberg, C. Flaum, C. Straley, P.G. Brewer, G.E. Malby, E.T. Peltzer III, G. Friedrich, J.P. Yesinowski, Seafloor nuclear magnetic resonance assay of methane hydrate in sediment and rock, J. Geophys. Res. 108 (2003) 2, 1–13.
[634] R.L. Kleinberg, C. Flaum, D.D. Griffin, P.G. Brewer, G.E. Malby, E.T. Peltzer, J.P. Yesinowski, Deap sea NMR: methane hydrate growth habit in porous media and its implications for hydraulic permeability, deposit accumulation, and submarine slope stability, J. Geophys. Res. 108 (2003) 12, 1–17.
[635] M. Goldman, B. Rabinovich, M. Rabinovich, D. Gilad, I. Gev, M. Schirov, Application of the integrated NMR-TDEM method in groundwater exploration in Israel, J. Appl. Geophys. 31 (1994) 27–52.
[636] M.D. Schirov, A.V. Legchenko, J.G. Creer, New direct non-invasive groundwater detection technology for Australia, Explor. Geophys. 22 (1991) 333–338.
[637] U. Yaramanci, G. Lange, M. Hertrich, Aquifer characterisation using Surface NMR jointly with other geophysical techniques at the Nauen/Berlin test site, J. Appl. Geophys. 50 (2002) 47–65.
[638] R.E. Grimm, A comparison of time domain electromagnetic and surface nuclear magnetic resonance sounding for subsurface water on Mars, J. Geophys. Res. 108 (2003) 18, 1–10.
[639] A.L. Segre, B. Blümich, Progetto "MOUSE": Risonanza magnetica per i beni culturali, ricerca & futuro 25 (2002) 34–36.
[640] A.L. Segre, B. Blümich, Risonanza Magnetica Nucleare Unidirezionale e sua applicazione alla diagnostica conservativa dei beni culturali, Scienzaonline (2005). http://www.scienzaonline.com/archeologia/risonanza-magnetica-nucleare.html .
[641] F. Tedoldi, Il progetto Eureka-Mouse: un metodo di Risonanza Magnetica Nucleare al servizio del Patrimonio Artistico, Rend. Sci. Istituto Lombardo B136 (2002) 239–256.
[642] M. Brai, M. Camaiti, C. Casieri, F. De Luca, P. Fantazzini, Nuclear magnetic resonance for cultural heritage, Mag. Reson. Imaging 25 (2007) 461–465.
[643] N. Proietti, D. Capitani, E. Rossi, S. Cozzolio, A.L. Segre, Unilateral NMR study of a XVI century frescoed wall, J. Magn. Reson. 186 (2007) 311–318.
[644] W. Schoefberger, S.A. Centeno, A. Jerschow, L. Tyne, E. Del Federico, Characterization of iron gall and logwood inks, and oil stains on paper by using portable NMR devices, Poster, in: 47th Experimental NMR Conference, Asilomar, 23–28 April, 2006.
[645] F. Rühli, T. Böni, J. Perlo, F. Casanova, M. Baias, E. Egarter, B. Blümich, Noninvasive spatial tissue discrimination in ancient mummies and bones by in situ portable nuclear magnetic resonance, J. Cult. Heritage 8 (2007) 257–263.
[646] R. Cignini, R. Melzi, F. Tedoldi, C. Casieri, F. De Luca, Large surface mapping by a unilateral scanner, Magn. Reson. Imaging 24 (2006) 813–818.
[647] N. Proietti, D. Capitani, S. Cozzolino, M. Valentini, E. Pedemonte, E. Princi, S. Vicini, A.L. Segre, In situ and frontal polymerization for the consolidation of porous stones: a unilateral NMR and magnetic resonance imaging study, J. Phys. Chem. B 110 (2006) 23719–23728.
[648] M. Alesiani, S. Capuani, B. Maraviglia, NMR applications to low-porosity carbonate stones, Magn. Reson. Imaging 21 (2003) 799–804.
[649] E. Del Federico, Pratt Institute, 200 Willoughby Avenue, Brooklyn, NY 11205, USA.
[650] D. Capitani, M.C. Emanuele, J. Bella, A.L. Segre, D. Attanasio, B. Focher, G. Capretti, 1H NMR relaxation study of cellulose and water interaction in paper, TAPPI J. (1999) 117–124.
[651] A. Sgamellotti, F. Presciutti, Department of Chemistry, University of Perugia, 06123 Perugia, Italy.
[652] Private collection, F. Rühli.
[653] Q. Ni, J.D. King, X. Wang, The characterization of human compact bone structure changes by low-field nuclear magnetic resonance, Meas. Sci. Technol. 15 (2004) 58–66.
[654] S.B. Thoma, D.M. Smith, J. Boughton, R. Davies, On-line surface area measurement of concentrated slurries using low field spin–lattice relaxation NMR, Part. Part. Syst. Charact. 10 (1993) 246.
[655] A.A.J. Ketelaars, L. Pel, W.J. Coumans, P.J.A.M. Kerkhof, Drying kinetics: a comparison of diffusion coefficients from moisture concentration profiles and drying curves, Chem. Eng. Sci. 50 (1995) 1187–1191.
[656] H.P. Huinink, L. Pel, M.A.J. Michels, M. Prat, Drying processes in the presence of temperature gradients – pore-scale modelling, Eur. Phys. J. E9 (2002) 487–498.

[657] L. Ciobanu, A.G. Webb, C.H. Pennington, Magnetic resonance imaging of biological cells, Prog. Nucl. Magn. Reson. Spectr. 42 (2003) 69–93.
[658] L. Ciobanu, C.H. Pennington, 3D micron-scale MRI of single biological cells, Solid State NMR 25 (2004) 138–141.
[659] H. Wang, L. Ciobanu, A.S. Edison, A.G. Webb, An eight-coil high-frequency probehead design for high-throughput nuclear magnetic resonance spectroscopy, J. Magn. Reson. 170 (2004) 206–212.
[660] S. Ahola, F. Casanova, J. Perlo, K. Münnemann, B. Blümich, S. Stapf, Monitoring of fluid motion in a micromixer by dynamic NMR microscopy, Lab Chip 6 (2006) 90–95.
[661] H. Wensink, F. Benito-Lopez, D.C. Hermes, W. Verboom, H.J. Gardeniers, D.N. Reinhoudt, A. van den Berg, Measuring reaction kinetics in a lab-on-a-chip by microcoil NMR, Lab Chip 5 (2005) 280–284.
[662] L.T. Kuhn, U. Bommerich, J. Bargon, Transfer of parahydrogen-induced hyperpolarization to ^{19}F, J. Phys. Chem. A 110 (2006) 3521–3526.
[663] S. Appelt, F.W. Häsing, S. Baer-Lang, N.J. Shah, B. Blümich, Proton magnetization enhancement of solvents with hyperpolarized xenon in very low magnetic fields, Chem. Phys. Lett. 348 (2001) 263–269.
[664] E.R. McCarney, B.D. Armstrong, M.D. Lingwood, S. Han, Hyperpolarized water as an authentic magnetic resonance imaging contrast agent, Proc. Natl. Acad. Sci. USA 104 (2007) 1754–1759.
[665] W. Barros Jr., P. Loureiro de Sousa, M. Engelsberg, Low field intermolecular double-quantum coherence imaging via the Overhauser effect, J. Magn. Reson. 165 (2003) 175–179.
[666] M. Johnson, Dynamic nuclear polarization by spin injection, Appl. Phys. Lett. 77 (2000) 1680–1682.
[667] A.K. Paravastu, P. Coles, T.D. Ladd, R.S. Maxwell, J.A. Reimer, Photocurrent-modulated optical nuclear polarization in bulk GaAs, Appl. Phys. Lett. 87 (2005), 232109, 1–3.
[668] S. Xu, S.M. Rochester, V.V. Yashchuck, M.H. Donaldson, D. Budker, Construction an applications of an atomic magnetic greadiometer based on nonlinear magneto-optical rotation, Rev. Sci. Intrum. 77 (2006), 083106, 1–8.
[669] J. Granwehr, J.A. Seeley, Sensitivity quantification of remote detection NMR and MRI, J. Magn. Reson. 179 (2006) 280–289.
[670] P.T. Callaghan, Rheo-NMR: nuclear magnetic resonance and the rheology of complex fluids, Rep. Prog. Phys. 62 (1999) 599–668.
[671] A. Caprihan, E. Fukushima, Flow measurements by NMR, Phys. Rep. 4 (1990) 195–235.
[672] E. Fukushima, Nuclear magnetic resonance as a tool to study flow, Annu. Rev. Fluid Mech. 31 (1999) 95–123.
[673] J.A. Seeley, S.-I. Han, A. Pines, Remotely detected high-field MRI of porous samples, J. Magn. Reson. 167 (2004) 282–290.
[674] J. Granwehr, E. Harel, C. Hilty, S. Garcia, L. Chavez, P. Sen, Y.-Q. Song, A. Pines, Dispersion measurements using time-of-flight remote detection MRI, Magn. Reson. Imaging 25 (2007) 449–452.
[675] C. Hilty, E.E. McDonnell, J. Granwehr, K.L. Pierce, S.-I. Han, A. Pines, Microfluidic gas-flow profiling using remote detection NMR, Proc. Natl. Acad. Sci. USA 102 (2005) 14960–14963.
[676] E.E. McDonnell, S. Han, C. Hilty, K.L. Pierce, A. Pines, NMR analysis of microfluidic devices by remote detection, Anal. Chem. 77 (2005) 8109–8114.
[677] J. Stepisnik, Spectroscopy: NMR down to Earth, Nature 439 (2006) 799–801.
[678] M.A. Espy, A.N. Matlachov, P.L. Volegov, J.C. Mosher, R.H. Kraus Jr., SQUID-based simultaneous detection of NMR and biomagnetic signals at ultra-low magnetic fields, IEEE Trans. Appl. Supercond. 15 (2005) 635–639.
[679] P.L. Volegov, A.N. Matlachov, R.H. Kraus Jr., Ultra-low field NMR measurements of liquids and gases with short relaxation times, J. Magn. Reson. 183 (2006) 134–141.
[680] A. Wong-Foy, S. Saxena, A.J. Moule, H.-M.L. Bitter, J.A. Seeley, R. McDermott, J. Clarke, A. Pines, Laser-polarized Xe-129 NMR and MRI at ultralow magnetic fields, J. Magn. Reson. 157 (2002) 235–241.
[681] J. Bernarding, G. Buntkowski, S. Macholl, S. Hartwig, M. Burghoff, L. Trahms, *J*-Coupling nuclear magnetic resonance spectroscopy of liquids in nT fields, J. Am. Chem. Soc. 128 (2006) 714–715.
[682] J. Stepisnik, V. Erzen, M. Kos, NMR imaging in the Earth's magnetic field, Magn. Reson. Med. 15 (1990) 386–391.
[683] A. Mohoric, G. Planinsic, M. Kos, A. Duh, J. Stepisnik, Magnetic resonance imaging system bases on Earth's magnetic field, Instrum. Sci. Tech. 32 (2004) 655–667.
[684] O. Coeur-Joly, H. Saint-Jalmes, G. Soufflet, L. Darrasse, M. Sauzade, High resolution magnetic resonance imaging at low-field (0.1 Tesla), engineering in medicine and biology society, Proc. Ann. Int. Conf. IEEE 5 (1992) 1966–1967.
[685] M. Ikeya, Applied Electron Spin Resonance: ESR Dating, Dosimetry and Microscopy, World Scientific, Publishing, Singapore, 1993.
[686] Q. Ni, J.D. King, J.O. Parra, Development of Combined Electron Paramagnetic Resonance and Nuclear Magnetic Resonance Technologies for Reservoir Characterization, 15-9083, Southwest Research Institute, San Antonio, TX, 1999.
[687] V.S. Greshishikin, NQR device for detecting plastic explosives, mines, and drugs, Appl. Phys. A 55 (1992) 505–507.
[688] J.P. Yesinowski, M.L. Buess, A.N. Garroway, M. Ziegenweid, A. Pines, Detection of ^{14}N and ^{35}Cl in cocaine base and hydrochloride using NQR, NMR, and SQUID techniques, Anal. Chem. 67 (1995) 2256–2263.
[689] A.N. Garroway, M.L. Buess, J.B. Miller, B.H. Suits, A.D. Hibbs, G.A. Barrall, R. Mathews, L.J. Burnett, Remote sensing by nuclear quadrupole resonance, IEEE Trans. Geosci. Remote Sens. 39 (2001) 1108–1118.